

The 4th Japan – Greece Workshop

Seismic Design of Foundations, Innovations in Seismic Design, and Protection of Cultural Heritage

Special Issue: The 2011 East Japan Great Earthquake

October 6–7, 2011 Kobe, Japan



Volume 3

Edited by T. Tazoh and G. Gazetas

Co-chairperson: T. Okada
G. Gazetas

Secretariat General: T. Tazoh

Organizing Committee

Y. Goto	H. Kimata
K. Maebayashi	K. Horikoshi
T. Sato	M. Saitoh
K. Wakamatsu	N. Funaki
T. Kaneyoshi	P. Dakoulas
N. Yoshida	M. Panagiotou
T. Asano	N. Gerolymos
F. Miura	I. Anastasopoulos
A. Mikami	R. Kourkoulis

Organized by:

- Earthquake Engineering Committee of Japanese Society of Civil Engineers
- Kobe Gakuin University
- Hellenic Society for Earthquake Engineering, Technical Chamber of Greece
- Laboratory of Soil Mechanics of National Technological University of Athens
- Project DARE funded by ERC
- Project PERPETUATE funded by EC FP7

Supported financially by:

- Japan Society of Civil Engineers
- Kobe Gakuin University
- ATTIKES DIADROMES, ATTIKI ODOS, J&P AVAX, OMETE

Contents

Volume 1

- 01 *The impact of the March 11th 2011 Great East Japan Earthquake -- As a substitute for the welcome address*
K. Konagai i
- 02 *To our dear Japanese friends*
G. Gazetas iii

Invited papers

- 03 *Future Directions of Earthquake-Tsunami Disaster Reduction Based on the Lessons from the 2011 Great East Japan Earthquake,*
M. Hamada & N. Y. Yun 5
- 04 *Effectiveness of Polypropylene Fiber Reinforced Cement Composite for Enhancing the Seismic Performance of Bridge Columns*
K. Kawashima, R. Zafra, T. Sasaki, K. Kajiwara, & M. Nakayama 11
- 05 *The European research project SYNER-G: Systemic seismic vulnerability and risk analysis for buildings, lifeline networks and infrastructures safety gain*
K. Pitilakis 23
- 06 *PERPETUATE Project: the performance-based assessment for the earthquake protection of cultural heritage*
S. Lagomarsino et. al. 29
- 07 *Seismic Vulnerability Assessment and Retrofitting of the Historic Brooklyn Bridge*
M. K. Yegian, & S. G. Arzoumanidis 35
- 08 *Testing a cross vault and a two storey masonry building on the shaking table: Preliminary experimental results*
E. Vintzileou 63

Submitted papers

- 09 *Damage Analysis of Utatsu Bridge Affected by Tsunami due to Great East Japan Earthquake*
K. Kosa, L. Fu, H. Shimizu, & T. Sasaki 71
- 10 *Seismic Response Analysis Using Energy Transmitting Boundary in the Time Domain*
N. Nakamura 81
- 11 *Influence of the Embedded Length of Friction Pile on Seismic Isolation Effect of Elevated Railway Bridge Rigid Frame*
H. Kimata, P. Rungbanaphan, K. Fukutake, J. Jang, Y. Murono, A. Toyooka, & T. Nishimura 93
- 12 *Soil-water Coupling Analysis of Real-scale Field Test on Group-Pile Foundation Subjected to Cyclic Horizontal Loading*
Y. Jin, X. Bao, & F. Zhang 99
- 13 *Dynamic centrifuge tests to study the transient bending moments in piles during liquefaction*
S. Bhattacharya, S.R.Dash, D.Lombardi, N.A.Alexander, T. Tazoh, J.Jang, & M. Sato 107
- 14 *Parametric Study on Pile-Soil Interaction Analyses by Overlaying Mesh Method*
A. Ohta, & F. Miura 123
- 15 *On the Performance of a Mechanical System Emulating Dynamic Stiffness of Soil-Foundation Systems*
M. Saitoh, T. Saito, T. Hikima, M. Ozawa, & K. Imanishi 135
- 16 *Demand spectra for PBD in case of improved soils, existence of basements and shallow underground cavities*
K. Pitilakis, K. Trevelopoulos, & G. Tsinidis 141
- 17 *Normal and Reverse Fault Rupture Interaction with Caisson Foundations : Centrifuge Modeling and Numerical Simulation*
M. Loli, & I. Anastasopoulos 159
- 18 *1-g Experimental Investigation of the Metaplastic Rocking Response of 1-dof Oscillators on Shallow Footings*
I. Anastasopoulos, R. Kourkoulis, & E. Papadopoulos 169

Volume 2

- 19 *Earthquake-Resistant Tall Reinforced Concrete Buildings Using Seismic Isolation and Rocking Core-Walls*
V. Calugaru, & M. Panagiotou 183
- 20 *Seismic Behavior of Batter Pile Foundation: Centrifuge Tests and Analytical Study*
T. Tazoh, M. Sato, J. Jang, Y. Taji, H. Kimata, N. Kobayashi, & G. Gazetas 199
- 21 *Amplitude dependent response for three-story moment-resistant building during earthquakes*
S. Kataoka 217
- 22 *Shaking Table Test of Bridge Pile Foundation in Liquefied Ground Focused on Section Force to the Intermediate Part of Pile*
K. Uno, M. Mitou, & H. Otsuka 227
- 23 *Dynamic Centrifuge Model Test of Pile-Supported Building with Semi-Rigid Pile Head Connections in Liquefiable Soil*
S. Ishizaki, T. Nagao, & K. Tokimatsu 237
- 24 *Effects of inertial and kinematic interaction on vibration of an apartment building based on earthquake observation records*
M. Iiba, & K. Watanabe 247
- 25 *Cyclic Pushover and Shake Table Testing of Bridge Pier with Foundation Uplifting and Soil Yielding*
I. Anastasopoulos, M. Loli, V. Drosos, & G. Gazetas 261
- 26 *INSTED: Innovative Stiffness and Energy Dissipation System, Final Report*
Ph. S. Karydakis, I. Vagias, & G. Ioannidiss 271
- 27 *Earthquake Damage Estimating System in Hanshin Expressway Network*
A. Higatani, K. Sasaki, & N. Hamada 279
- 28 *Historic Liquefaction Sites in Japan, 745–2008*
K. Wakamatsu 287
- 29 *Physical Meaning of Phase in Earthquake Motions*
T. Sato 297
- 30 *New soil classification system and amplification factors for seismic code provisions*

	K. Pitilakis, A. Anastasiadis, & E. Riga	307
31	Seismic risk assessment and management of lifelines, utilities and infrastructures	
	K. Pitilakis, & K. Kakderi	323
32	The Christchurch 2011 Earthquake: Elastic and Perfectly-Plastic Response Potential of Selected Ground Motions	
	Ev. Garini, & G. Gazetas	349
33	Seismic vulnerability of ancient churches: damage observation after L'Aquila earthquake (2009)	
	S. Lagomarsino	359
34	Structural Stability and Bearing Capacity Analysis of the Tunnel-Entrance to the Stadium of Ancient Nemea	
	H. Alexakis, & N. Makris	377
35	Seismic Damage Evaluation on Full-scale Reinforced Concrete Bridge Columns based on Ambient Vibration Monitoring	
	S. Nagata, K. Kanazawa, & K. Kajiwara	393
36	Uncertainty effects on seismic response evaluations of ground pavement system	
	K. Kawano, & K. Nagafuchi	403
37	Development of MPS method for simulation of slope failure	
	I. Yoshida	413
38	Preliminary Study on Earthquake-induced Progressive Failure of Jointed Rock Foundation Supporting Arch Dam	
	H. Kimata, Y. Fujita, M.R. Okhovat, & M. Yazdani	421
39	Some notes on liquefaction analysis in simple two-dimensional formulation	
	N. Yoshida, & Y. Ohya	429
40	Development of New Liquefaction Countermeasure Aimed for Old Existing Structures	
	K. Horikoshi, H. Ishii, H. Matsui, & K. Higaki	435
41	Seismic Performance of an Integrated Steel Pipe Bridge Pier by Multi Steel Pipes with Hysteretic Shear Damper	
	M. Shinohara, & H. Kanaji	443
42	Shake Table Experiment on Damage Free RC Bridge Column Using E-Defense	
	M. Nakayama, T. Sasaki, R. Zafara, K. Kajiwara, & K. Kawashima	451

43	<i>Seismic Evaluation of a RC Rigid-Frame Arch Bridge Affected by Wenchuan Earthquake, May 12th, 2008, China</i> Z. Shi, K. Kosa, J. Zhang, & H. Shimizu	459
44	<i>Method of Evaluating Average Shear Wave Profiling for Levees by Using Microtremor Measurement</i> A. Mikami	471
45	<i>Seismic Performance of Buried Steel Pipelines Crossing Strike-Slip Seismic Faults</i> P. Vazouras, S. Karamanos, & P. Dakoulas	487

Volume 3

46	<i>An Estimation Method of Frequency Response Functions and Its Application to Vertical Array Earthquake Records</i> M. Nakamura, & J. Suzumura	501
47	<i>Strong Ground Motion and Damage to Large Scale Buildings by September 30, 2009 Earthquake in Padang, Indonesia</i> Y. Goto, M. H. Pradono, R. P. Rahmat, A. Hayashi, & K. Miyatake	513
48	<i>Seismic vulnerability of shallow tunnels. Application to the metro of Thessaloniki, Greece</i> S. Argyroudis, & K. Pitilakis	521
49	<i>Towards an analytical tool for quantifying vulnerability of simple RC buildings to permanent co-seismic slope deformation</i> S.D. Fotopoulou, & K.D. Pitilakis	539
50	<i>Estimation of Earthquake Induced Dry Settlements of CFR Dams</i> D. Egglezos	557
51	<i>Effect of Soil and Interface Nonlinearities on the Response of Caisson-Supported Bridge Piers</i> A. Zafeirakos, & N. Gerolymos	569
52	<i>Single Pile vs. Pile Group Lateral Response under Asymmetric Cyclic Loading</i> S. Giannakos, N. Gerolymos, & G. Gazetas	577
53	<i>Seismic Analysis of Reinforced-Earth Wall on Precarious Soil Improved with Stone Columns</i> P. Tasiopoulou, & G. Gazetas	589

54	<i>Correlation of Ground Motion Characteristics with Liquefaction in the Christchurch February 2011 earthquake</i>	
	<i>P. Tasiopoulou, E. Smyrou, & G. Gazetas</i>	601
55	<i>Parametric Dimensional Analysis on Rocking of 1-dof Systems</i>	
	<i>R. Kourkoulis, & P. Kokkali</i>	609
56	<i>Nonlinear Soil–Foundation Interaction: Numerical Analysis</i>	
	<i>I. Anastasopoulos, M. Loli, F. Gelagoti, R. Kourkoulis, & G. Gazetas</i>	621
57	<i>A Simplified Method to Assess the Toppling Potential of Ground Motions: Application to Rocking–Isolated Frame Structures</i>	
	<i>F. Gelagoti, & R. Kourkoulis</i>	633
58	<i>Rocking of Inelastic Frame on Two-Layered Inelastic Soil</i>	
	<i>R. Kourkoulis, F. Gelagoti, & V. Founta</i>	645
59	<i>Destructiveness of Earthquake Ground Motions: “Intensity Measures” versus Sliding Displacement</i>	
	<i>Ev. Garini, & G. Gazetas</i>	653

Submitted Papers

An Estimation Method of Frequency Response Functions and Its Application to Vertical Array Earthquake Records

Masataka Nakamura & Jun-ichi Suzumura

Department of civil engineering, College of science and technology, Nihon university, Tokyo, Japan

ABSTRACT: As vertical array earthquake records, noise with a normal distribution is added to response signals calculated by a numerical model and validity of FRF estimate values was discussed by the proposed method. With assuming the amount of noise proportional to the amount of each observation, even in the case the author examined the noise of a constant absolute quantity mixed in each observed value, estimated errors were small. A total amount of noise estimated by the proposed method is an effective index to discuss precision of FRF estimation.

1 INTRODUCTION

It is important to create a ground model precisely based on vertical array earthquake records for grasping ground properties. Generally, dynamic characteristics of the surface ground are studied with a focus on transfer characteristics in a depth direction under an assumption that plane waves propagate in a vertical direction. For an index that shows transfer characteristics, the frequency response function (FRF), which expresses a ratio of behaviors between observation points in a frequency domain, is referred and a linear ground model is examined so that FRF estimated by micro-earthquake motion records (observed FRF) and the FRF based on the one-dimensional multiple reflection theory (theoretical FRF) correspond each other (Sawada, T., et al., 1992). In the case of examining the non-linearity of ground properties, it is premised that a linear ground model is created with a good precision. Components except wave motions that propagates in a vertical direction is contained in the earthquake record and therefore it is required to extract precisely the wave motion components (signal components) that have properties coherent between observation points at the time of an estimation of observed FRF.

As methods to estimate FRF from observation records of multiple times, the non-parametric transfer function estimation methods (H_1 estimation, H_2 estimation, H_v estimation) (Bendat, J.S. & Piersol, A.G., 2000) of the single-input single-output (SISO) system, which captures relation between two observation points as input-output relations, is already known. In the SISO transfer function estimation method, correlativity between signals, and non-correlativity between signals and noises or between noises are treated structurally. Therefore the dynamic characteristics more sensitively receive an effect of the data processing method comparing with a Fourier spectrum ratio that treats observed values directly. It is assumed that noises are contained in output in H_1 , input in H_2 and both input and output in H_v . In a vertical array observation, the H_v estimation is often employed under the assumption that behavior in the deepest point is input, that in other point is outputs and noises are contained in both input and output. The SISO method has been studied. For example, Izumi et al. suggested that an estimation method must be selected depending on observation circumstances since the transfer function estimation method influenced the identification effects of damping, based on micro-tremor records at a building (Izumi, M., et al., 1990). It has been reported that in the case that constant noises are contained in input and output, amplitudes obtained by the H_v estimation is underestimated and it leads to overestimate of damping of the object system. It has been reported that signal components can

be extracted by improving the coherence function between two observation points of the underground and ground surface (Yamazaki, F., et al., 1991). Furthermore, an effect to identification value of ground properties by a windowing applied to observed FRF is examined (Tsujihara, O., et al., 1999).

On the other hand, the recent development of observation devices allows vertical array observation of multiple points set in the underground. For such observations of more than three points, highly precise FRF estimated results can be expected by collective processing of multi-point measurements. As a process method of multipoint simultaneous observation records, the authors have already proposed a new FRF estimation method for single-input multiple-output (SIMO) (hereinafter called " H_p estimation") (Nakamura, M., et al., 2005). The H_p estimation is a method to estimate non-parametrically relative behaviors between observation points and even if an input is unknown, it is possible to grasp relatively dynamic characteristic of an object system between observation points.

In earthquake observation, it is difficult to specify inputs to an object system. Therefore, in this paper, we aim at discussing on applicability of the H_p estimation, presuming that the multi-point vertical array observation system consists of a multiple-output system for single unknown input. Concretely, we estimate FRFs and quantity of noises with the values for which noises in normal distribution are added to response signals calculated with a numerical model as observation values and discuss on the result comparing with those obtained by the existing SISO methods.

2 FRF ESTIMATION METHOD

2.1 FRF of SIMO system

In the SIMO system shown in Figure 1, assuming $g_l(\omega)$ as a transfer function of an output signal $y_l(\omega)$ ($l = 1 \sim L$) for an input signal $x(\omega)$, the following equation is obtained.

$$y_l(\omega) = g_l(\omega) \cdot x(\omega) \quad (1)$$

Obtaining a ratio between outputs assuming a reference point voluntarily determined as observation point 1, the following relation is obtained.

$$y_l(\omega)/y_1(\omega) = g_l(\omega)/g_1(\omega) = h_l(\omega) \quad (2)$$

A ratio between output signals in the SIMO system is equal with a ratio of the transfer function and does not depend on an input. Equation (2) is not an input-output relation to the system but indicates relative behaviors between outputs. In this paper, a behavior ratio between observation points in a frequency domain is defined with the quantity expressed by Equation (2) as FRF of the object point for reference point 1. Since all the variables in this paper are assumed as a function of a frequency domain, (ω) is omitted below. Moreover, it is assumed that signals and noises contained and noises in different observation points are uncorrelated.

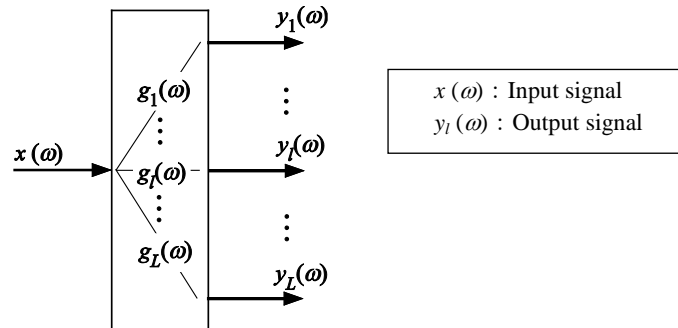


Figure 1 Single-input multiple-output system

2.2 Proposed method (H_p estimation)

In the H_p estimation, application to multipoint response observation is assumed as a base, with a focus on the total noise (quantity of all noises) in all observation points. Based on the two assumptions that the behaviors of all observation points are responses by one unknown input and the noise contained each observed value is considered independent, the feature of the H_p estimation is that an eigenvalue problem that corresponds FRF to eigenvectors is constituted with the quantity of all noises as an eigenvalue, and the quantity of all noises and FRF are obtained. In the system shown in Figure 2, the observation is carried out N times and an observed value in an observation point l is expressed as follows.

$$\left. \begin{aligned} \mathbf{w}_i &= \{w_i^{(1)} \quad w_i^{(2)} \quad \cdots \quad w_i^{(N)}\}^T \in C(N \times 1) \\ \mathbf{y}_i &= \{y_i^{(1)} \quad y_i^{(2)} \quad \cdots \quad y_i^{(N)}\}^T \in C(N \times 1) \\ \mathbf{v}_i &= \{v_i^{(1)} \quad v_i^{(2)} \quad \cdots \quad v_i^{(N)}\}^T \in C(N \times 1) \end{aligned} \right\} \quad (3)$$

Here, parenthetical numbers in upper right in Equation (3) indicate times of observation. In the H_p estimation, the following eigenvalue problem is solved

$$(\boldsymbol{\Sigma} - \lambda \mathbf{R}_0) \mathbf{g} = (\boldsymbol{\Sigma} - \lambda \mathbf{R}_0) \mathbf{h} = \mathbf{0} \quad (4)$$

FRF of the object point for the reference point is estimated by normalizing the eigenvector \mathbf{g} corresponding to the minimum eigenvalue with an element corresponding to the reference point. Here, $\boldsymbol{\Sigma}$, \mathbf{R}_0 , $\mathbf{S} \in C(L \times L)$, \mathbf{g} , $\mathbf{h} \in C(L \times 1)$ and * in upper right indicate conjugate transpose as below.

$$\boldsymbol{\Sigma} = \text{trace}(\mathbf{S}) \cdot \mathbf{I} - \text{conjg}(\mathbf{S}) \quad (5)$$

$$\mathbf{S} = [S_{ij}] \quad (i=1 \sim L, \quad j=1 \sim L) \quad (6)$$

$$S_{ij} = \mathbf{w}_i^* \mathbf{w}_j \quad (i=1 \sim L, \quad j=1 \sim L) \quad (7)$$

$$\mathbf{g} = \{g_1 \quad \cdots \quad g_l \quad \cdots \quad g_L\}^T \quad (8)$$

Assuming the observation point $l = 1$ as a reference point, FRF is expressed as follows.

$$\mathbf{h} = \{1 \quad h_2 \quad \cdots \quad h_l \quad \cdots \quad h_L\}^T \quad (9)$$

The opposite angle term in Equation (6) consists of power spectra and the non-opposite angle term consists of cross spectra. The opposite angle term of \mathbf{S} is expressed as the sum of observation power spectra except the concerned point l from all observation points. \mathbf{R}_0 is a parameter to relativize noises gathered in the opposite angle term of \mathbf{S} . Here, the sum of noise power spectra contained in all observation points is expressed in the form of a ratio against the sum of observed power spectra in all observation points and is expressed in the following equation.

$$\mathbf{R}_0 = \text{diag}(\boldsymbol{\Sigma}_{11} \quad \cdots \quad \boldsymbol{\Sigma}_{ll} \quad \cdots \quad \boldsymbol{\Sigma}_{LL}) \quad (10)$$

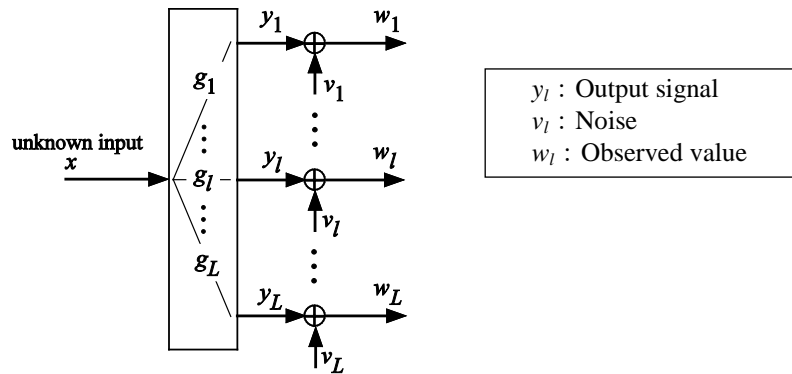


Figure 2 Unknown-input multiple-output system

2.3 Interpreting of noise in H_p estimation

The minimum eigenvalue obtained by solving Equation (4) indicates a ratio of noises contained in all observed points to observed values and is hereinafter called "noise ratio of the system". Since the noise property is expressed by Equation (9), the sum of noise power spectra sum contained in the sum of observed power spectra is approximated with the following equation with a noise ratio of the system.

$$\sum_{l=1}^L V_{ll} = \lambda \cdot \sum_{l=1}^L S_{ll} \quad (11)$$

2.4 Relational between H_p estimation and the SISO methods

In the system shown in Figure 2, when applying the H_p estimation as a single-unknown-input 2-output system ($L = 2$), the eigenvalue problem of Equation (4) is expressed as the following equation.

$$\begin{bmatrix} (1-\lambda)S_{22} & -S_{12} \\ -S_{21} & (1-\lambda)S_{11} \end{bmatrix} \begin{Bmatrix} g_1 \\ g_2 \end{Bmatrix} = \begin{Bmatrix} 0 \\ 0 \end{Bmatrix} \quad (12)$$

Equation (12) indicates that in the reference and object points, the noise power spectrum in proportion to each observed power spectra is set to the same noise ratio λ . Solving Equation (12), FRF is expressed by the following equation.

$$h_{2/1} = \frac{g_2}{g_1} = \sqrt{\frac{S_{12} \cdot S_{22}}{S_{11} \cdot S_{21}}} \quad (13)$$

Equation (13) corresponds with the H_v estimation equation for the SISO system in Figure 3. Here, the H_v estimation is expressed as a geometric mean of the H_1 and H_2 estimations. The amplitude is given as a square root of a power spectrum ratio of an input to output. These estimated amplitudes satisfy the following relation $|H_1| \leq |H_v| \leq |H_2|$. On the other hand, the minimum eigenvalue is a noise ratio and is given as the following equation.

$$\lambda = 1 - \sqrt{\frac{S_{12} \cdot S_{21}}{S_{11} \cdot S_{22}}} \quad (14)$$

Hanada summarized the system in Figure 3 in an eigenvalue problem directly and reached the conclusion same as that in this chapter theoretically (Hanada, K., 1988). Further, the following relation is satisfied for the noise ratio and coherence function of the system in Figure 3.

$$(1-\lambda)^2 = coh^2 \quad (15)$$

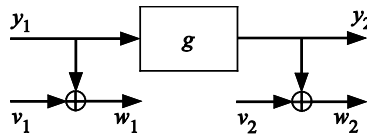


Figure 3 The Single-input single-output system with noise both in input and output

3 NUMERICAL MODEL AND ITS RESPONSES

It is assumed here that in the horizontally layered ground shown in Figure 4, observed values are obtained in the six observation points including the ground surface (● mark). Noises shown in Table 2 are contained in a time domain with response acceleration signals of each observation point linearly analyzed based on the one-dimensional multiple reflection theory and they are used as observed values. As an example, response signals in observation points 1 and 5, time history of the mixed noises and their power spectra are shown in Figures 5, 6 and 7. The

S/N ratio (response signal RMS value / noise RMS value) of each observation point are shown in Figure 8. As a noise property, constant and proportional noises assumed as below were used as study objects. The constant noise was expressed by multiplying random numbers having a mean value of zero and normal distribution with the standard deviation σ by RMS values of response signals in observation point 6. The noise amplitudes are approximately same regardless of observation points (Figure 6 (1)), and their frequency dependence is low and are close to white noises (Figure7). Since a response signal amplifies more as the observation point becomes close to the earth surface, the S/N ratios rise (Figure 8). To change sloppy loudness, three ways of σ value (0.1, 0.3, 0.5) was examined.

The proportion noises were expressed by multiplying random numbers having a mean value of zero and normal distribution of the standard deviation σ by Fourier amplitude values of each response signal and Fourier inverse transforming the obtained values. The noises accept various amplitudes of response signals (Figure 6 (2)), are the colored noises that depend on frequency (Figure 7) and the S/N ratios of each observation point are approximately same (Figure 8). The observation point mean values of the constant noise with $\sigma = 0.5$, and the proportional noise with $\sigma = 0.4$ almost correspond to each other (Figure 8) and therefore it is judged that noises at the approximately same level are contained for the observation system. Changing the values of those random numbers, ten times of observed values with different noises were created.

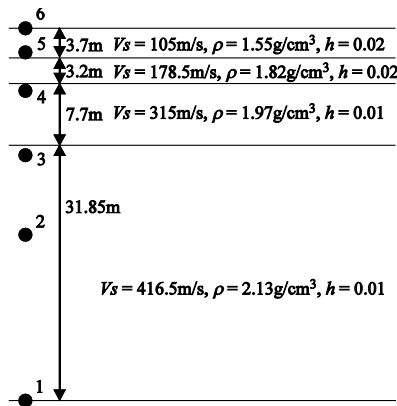
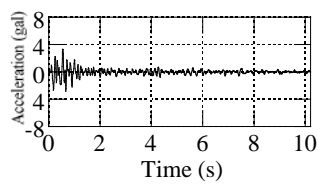


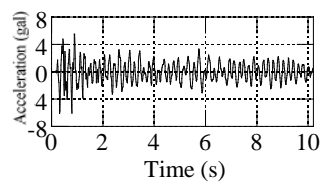
Figure 4 Ground model

Table 2 Noise property

	Noise property	Standard deviation σ
Constant noise	RMS value constant at all observations point (noise ratios of each observation point are different)	0.1, 0.3, 0.5
Proportional noise	Proportional to Fourier amplitude value of each response signal (noise ratios of each observation point are similar)	0.4



(a) Observation point 1



(b) Observation point 5

Figure 5 Response signal

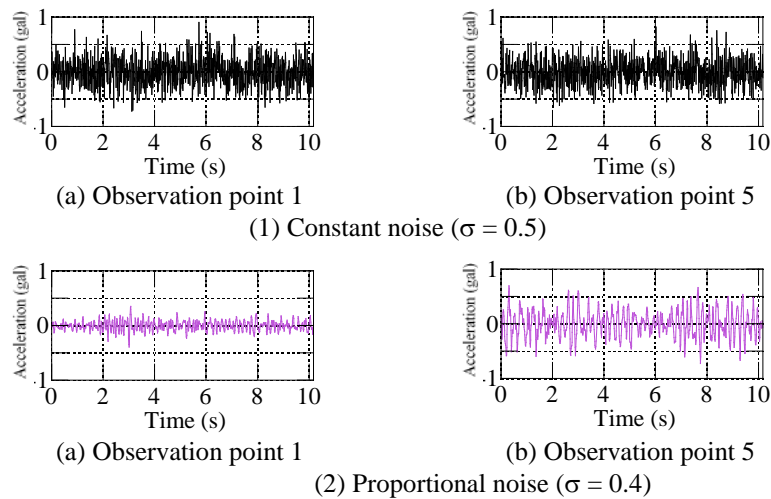


Figure 6 Example of noise (time history)

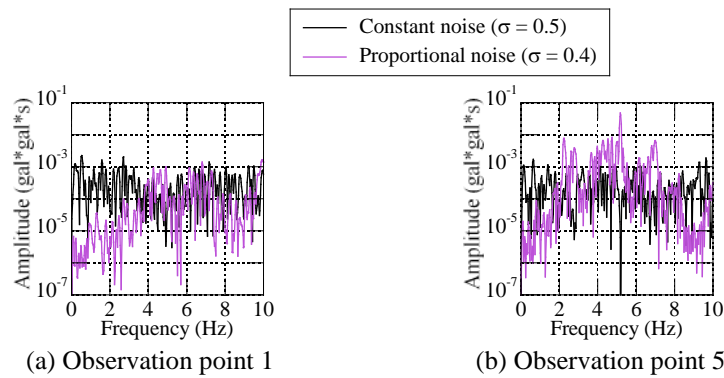


Figure 7 Example of noise (power spectra)

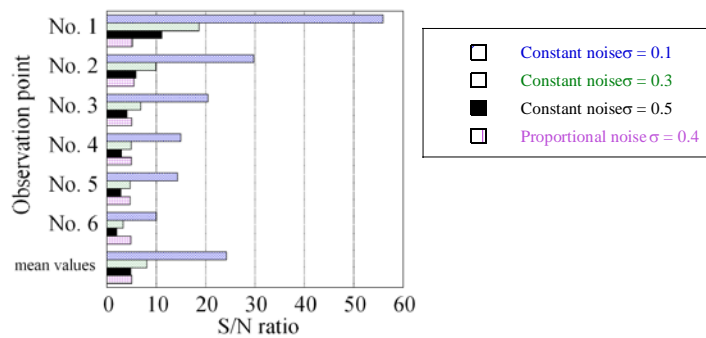


Figure 8 Set S/N ratio

4 ESTIMATION RESULT OF FRF BY EACH METHOD

For estimation results of FRF by each method, examples are shown with observation point 1 as a reference point and observation point 5 as an object point. A result when constant noise ($\sigma = 0.5$) and proportion noise ($\sigma = 0.4$) were used is shown in Figure 9. Moreover, for the noise ratio obtained at the same time as FRF, a noise ratio of the system obtained by H_p estimation is shown in Figure 10, and the noise ratio between two points of the reference point to object point obtained by the H_v estimation is shown in Figure 11. For the FRF phase, no significant differences are confirmed in each method. For the FRF amplitude, good estimate values close to set values were obtained in all methods when proportional noises were contained. In the case

of a constant noise, features of each method are confirmed. Therefore, each method is evaluated for the five items of three frequency bands (0-2Hz, 2-8Hz, 8-10Hz), 1st resonant amplitude and noise evaluation.

4.1 0-2Hz

The target signal is acceleration and the amplitude of the low frequency band is small. In this frequency band, the signal amplitude of the object point is equal to or slightly greater than that of the reference point (Figure 9 set value). Moreover, the noise ratio of the system is remarkably higher than those of other frequency bands (Figure 10 (1) set value) and the influence of the noise is strong. Therefore, as shown in Figure 9 (1), the amplitudes are underestimated by the H_1 estimation and overestimated by the H_2 estimation. The value obtained by the H_v estimation, which adopts a geometric mean of both estimates, is close to the set value as a result. Although there are many spikes in the H_p estimation, the spikes seem to occur around the set value and its mean precision is high.

4.2 2-8Hz

In this frequency band, the object point has signals that are greater than those of the reference point (Figure 9 set value). The noise ratio is smaller than those of other frequency bands (Figure 10 (1) set value) and the influence of the noise is weak. Therefore, as shown in Figure 9(1), FRF shapes are estimated almost well in all methods. However, as described later, in the vicinity of the 1st resonant frequency, some of the methods are affected by noise levels.

4.3 8-10Hz

This is a frequency band that includes an anti-resonant frequency for which signal amplitudes of the object point is extremely smaller than those of the reference point. Depending on how the reference point voluntarily chosen is adopted, the anti-resonant frequency of the object point is equivalent to the peaks of other points and therefore verification of estimate precision in an anti-resonant frequency is important, too. The noise ratio of the reference point is different from that of the object point. It is great at the object point (Figure 11(1) -(a), (b)) and the influence of the noises is strong. Therefore, as shown in Figure 9, precision of H_1 estimation to evaluate noises of the object point is high. On the other hand, precision of H_2 estimation, which does not consider noises of the object point is low and the H_v estimation adopts these means. Although spikes occurs in the H_p estimation, mean precision is high.

4.4 Resonant amplitude

In the resonant frequency, signal amplitudes of the object point is extremely greater than those of the reference point. FRF amplitude estimate values of the vicinity of the 1st resonant frequency (1.8-2Hz) are shown in Figure 12, with the noise levels as a parameter. While the H_2 and H_p estimations are appropriate since influences of noises are low, the H_1 and H_v estimations are strongly affected by noise levels. The signal component of the object point is great at the peak, the noise ratio of the reference point governs the FRF shapes. Therefore, precision of H_2 estimation for which the noise of the reference point is considered is high. Estimate precision of the H_p estimation is also high in the same way. Since noises contained in the reference point are not assumed for the H_1 estimation, estimate precision is extremely low and the peak value greatly varies depending on noise quantity. The H_v estimation shows the tendency similar to that of the H_1 estimation.

The amplitude distribution is an estimate value equivalent to a mode vector. Figure 13 shows depth of the observation points corresponded to FRF amplitude values in the 1st resonant frequency. The figure shows that description about peak estimate values for observation point 5 are satisfied equally for all observations points.

4.5 Noise evaluation

Here, we discuss on precision of each method comparing the noise ratios obtained by the H_v and H_p estimations with values set beforehand. For the set values of the noise ratios of the system shown in Figure 10, the H_p estimation performs estimation with sufficient precision. In the H_p estimation, since the noises of a real part and an imaginary part left in item non-opposite angle term of Σ in Equation (4) are expressed, plural spikes occur in FRF due to over-fitting. In noise ratios added to reference point 1 and object point 5 shown in Figure 11, the noise ratios by the H_v estimation are evaluated by averaging noise ratios of both observation points. In the SISO system estimations, FRF estimate values depend on noise ratios of two observations points.

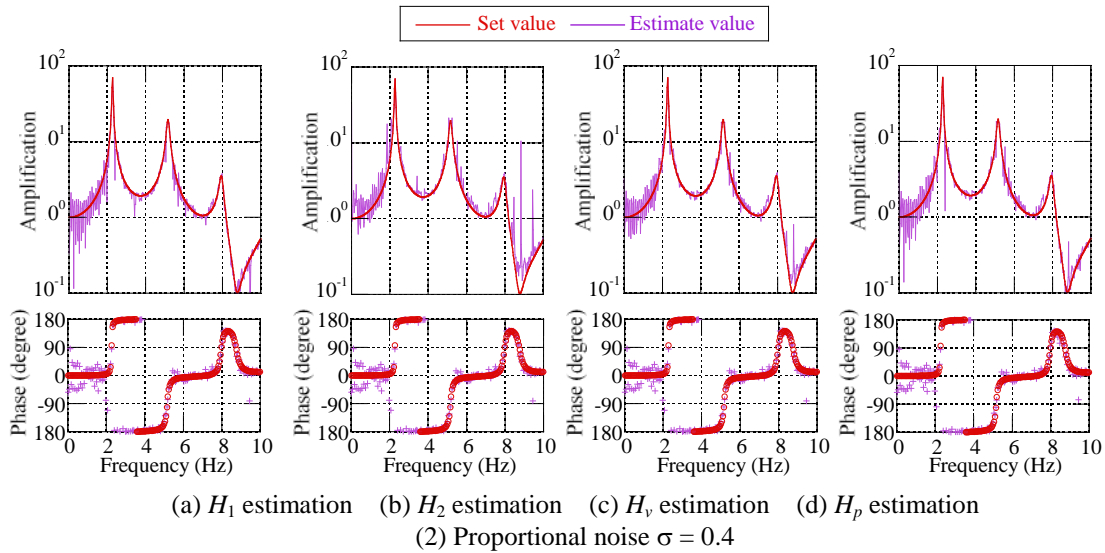
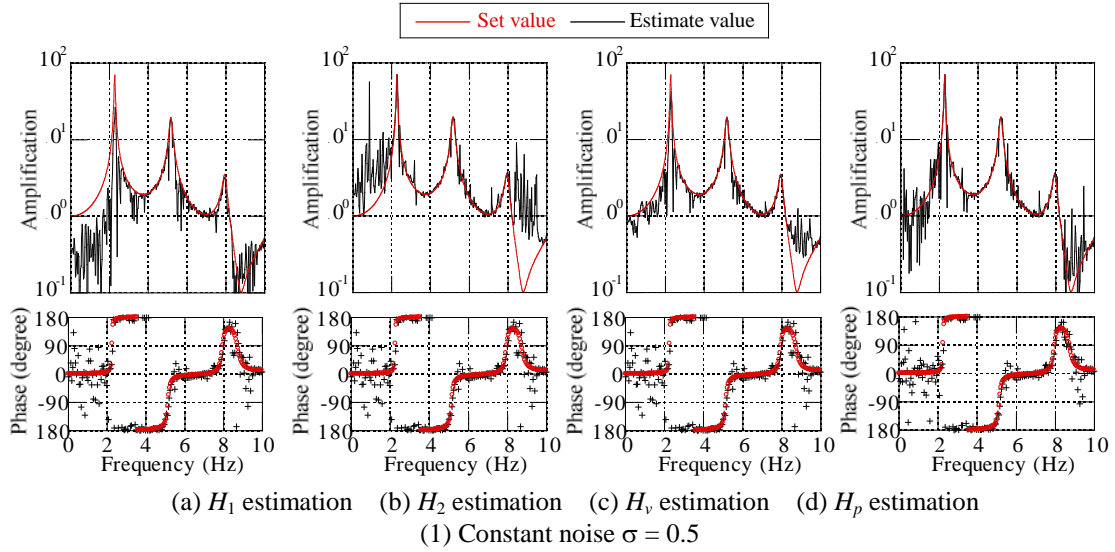


Figure 9 FRF of observation points 5 and 1

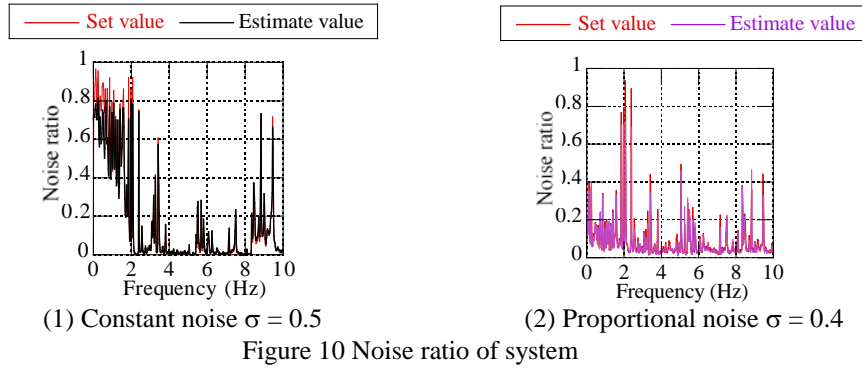


Figure 10 Noise ratio of system

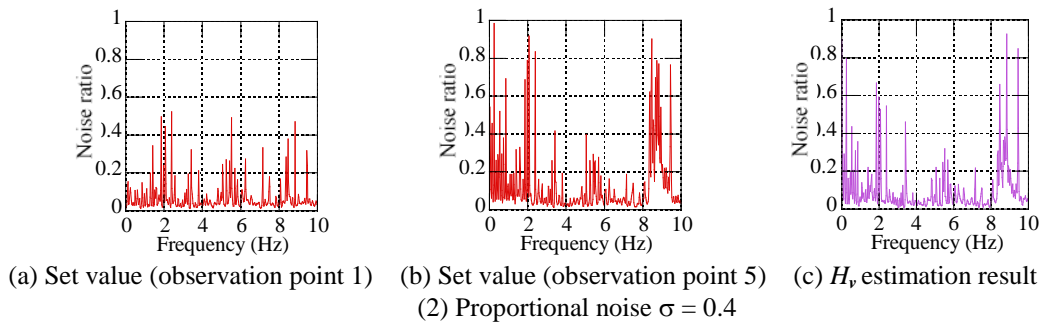
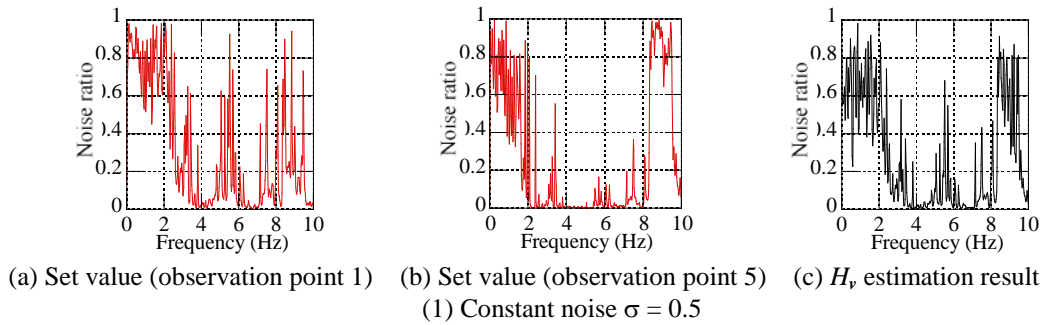


Figure 11 Noise ratio of observation points 1 and 5

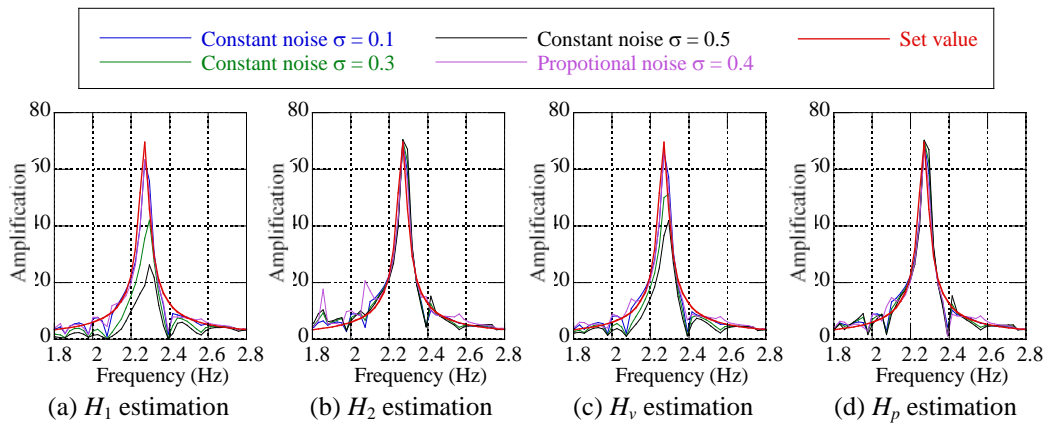


Figure 12 FRF of observation points 5 and 1 in the vicinity of the 1st resonant frequency (1.8-2.8 Hz)

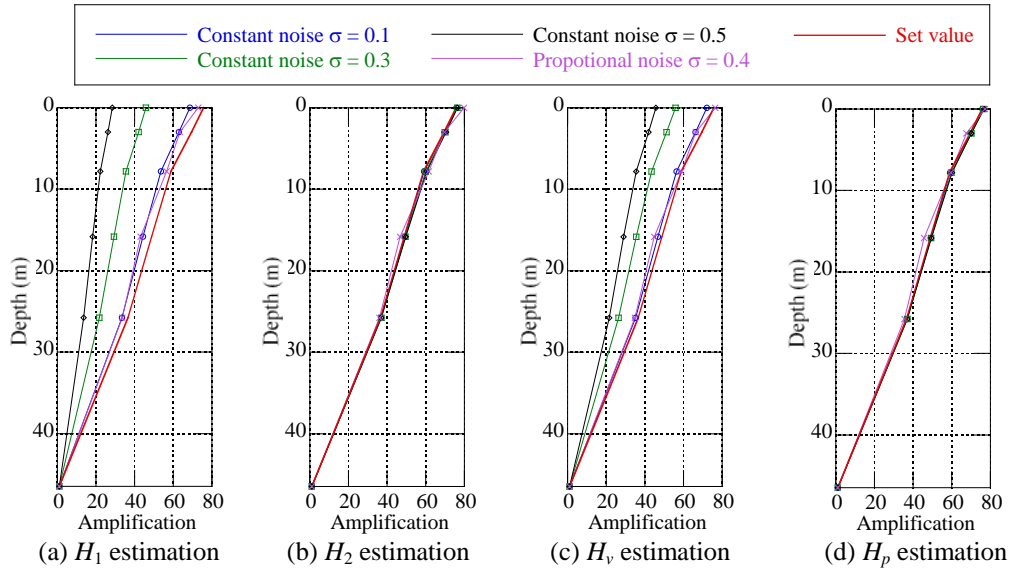


Figure 13 Depth distribution of amplification at the 1st resonant frequency (2.2Hz)

5 CONCLUSION

The authors have assumed the process of vertical array earthquake records, evaluated FRF estimate values by the proposed method by adding noises normally distributed to response signals calculated by a numerical model and summarized features of the existing methods. The knowledge obtained in this study is below.

- (1) All methods that were examined perform FRF estimation with high precision for noises in proportion to observed values.
- (2) Although noises in proportion to the sum of observed value power of all points are assumed for the proposed method (H_p estimation), in the case that constant noises that are not assumed by the H_p estimation are contained in observed values, appropriate FRF and all noises were estimated. This result revealed that influences of noise distributions on FRF estimate values are small in the H_p estimation and all the estimated noise are useful as an index to discuss on FRF estimate precision.
- (3) Estimate precision of the existing SISO system methods (H_1 , H_2 , H_v estimations) is governed by amplitudes of the mixture levels (noise ratio) of noises included in observed values and the magnitude relation of the noise ratios of two observation points referred. When the noise ratios of both two observation points are great, FRF amplitudes are underestimated by H_1 estimation and overestimated by H_2 estimation. When the noise ratio of the object point is greater, a good result is obtained by H_1 estimation and when the noise ratio of the reference point is greater, a good result is obtained by H_2 estimation. The H_v estimation gives an average FRF of both. When the noise ratios of the reference point and the object point are same, a good result is obtained. In the case that the noise that does not depend on frequency such as white noise is contained in all observation points with the same amplitude level, the magnitude relation of the noise ratios of the two observation points to be referred vary for each frequency. In such a case, it is difficult to estimate well FRF of all bands by the existing SISO methods. The H_p estimation have advantages of both existing SISO methods and can perform FRF estimation reasonably.

ACKNOWLEDGEMENT

The authors sincerely thank Kazufumi Hanada, a Former Professor in Nihon University, and Hiroo Shiojiri, a Professor in Nihon University for their helpful advices for the study.

REFERENCES

Sawada, T., Tsujihara, O., Hirao, K. & Yamamoto, H. 1992. Modification of SLP and its application to

- identification of shear wave velocity and quality factor of soil. *Proceedings of the Japan society of civil engineers*, No.446, I-19, 205-213. (in Japanese)
- Bendat, J.S. & Piersol, A.G. 2000. Random data analysis and measurement procedure. New York: *Wiley Interscience*.
- Izumi, M., Katukura, H. & Tobita, J. 1990. Properties of ambient vibration system of structures. *Journal of structural and construction engineering (Transaction of AIJ)*. 409. 83-93. (in Japanese)
- Yamazaki, F., Lu, L. & Katayama, T. 1991. Orientation error estimation of seismometers in array observation. *Proceedings of the Japan society of civil engineers*, No.432, I-16, 231-240. (in Japanese)
- Tsujihara, O. & Sawada T. 1999. A remark on accuracy in identification of shear wave velocity and quality factor of subsurface ground using vertical array records. *Journal of structural engineering*. Vol.45A. 801-808. (in Japanese)
- Nakamura, M., Suzumura, J. & Hanada, K. 2006. An evaluation method of frequency response function through observed motions with noise. *Journal of structural engineering*. Vol.52A. 801-808. (in Japanese)
- Hanada, K. 1988. The modal identification and system identification for the soil-structure system. *CRIEPI research report*. U05. (in Japanese)

Strong Ground Motion and Damage to Large Scale Buildings by September 30, 2009 Earthquake in Padang, Indonesia

Y. Goto

Earthquake Research Institute, The University of Tokyo, Japan

M. H. Pradono

Agency for the Assessment and Application of Technology, Indonesia

R. P. Rahmat

Graduate School of Kyoto University, Japan

A. Hayashi and K. Miyatake

Oriental Consultants Co. Ltd., Japan

ABSTRACT: On September 30, 2009, an earthquake of Mw 7.6 struck the west coast of Sumatra of Indonesia, affecting Padang and Pariaman, causing significant damage to about 150,000 houses and buildings as well as ruining more than 1,000 lives. One of the remarkable features of this disaster was damage to large-scale reinforced concrete buildings in Padang, the capital city of West Sumatra. In order to know the anti-seismic deficiencies of these buildings in this area, the authors surveyed and analyzed in detail some of the damaged buildings and the shaking intensity of the ground during the earthquake

1 INSTRUCTION

According to BMKG (Agency for Meteorology, Climatology and Geophysics of Indonesia), the epicenter was located about 80km west of Padang and at a depth 71km. The magnitude on the Richter scale was 7.6. The earthquake was supposed to be inner-plate type. No significant tsunami was generated.

The significant damage area extended over Padang city (Population about 840,000), Pariaman city (70,000), Padang Pariaman prefecture (380,000) and Agam prefecture (420,000). The damage features differed site-dependently. Padang, which is the capital of West Sumatra State, suffered significant damage to its many modern large-scale buildings. In the hilly area of Pariaman, the remarkable feature was severe damage to low-rise non-engineered residential houses.

In this paper, the authors discuss damage analysis of large scale reinforced concrete buildings. These buildings have important roles in supporting the backbone function of the capital city and the damage they suffered might indicate common deficiencies of the same kinds of buildings in many other cities.



Figure 1. Area Map, Epicenter
Attached to OCHA Indonesia Earthquake,
Situation Report No.16 (20 Oct. 2009)

2 GROUND SHAKING IN PADANGGETTING STARTED

Since the shaking during this earthquake was not recorded instrumentally in the downtown area of Padang, the authors estimated its intensity and predominant frequency through several approaches, namely, a questionnaire survey on the intensity of the shaking, a micro-tremor observation, a wave synthesis using a recorded wave on a rock site near Padang, and a monitoring video recorded at a building in Padang.

2.1 Questionnaire survey

The questionnaire survey, applied to residents in the area, comprised 34 questions, and was developed to estimate the JMA Intensity by Ota et al (1979). This method has been widely applied to many areas of many earthquakes since the 1970s and has been useful for estimating seismic intensities in area where no seismometer was located. The original questionnaire sheet had, of course, been written in Japanese, but Honda et al (2005) had translated it to Bahasa Indonesia and used it for the residents of Banda Aceh in 2005. We modified it a little to make it more relevant to the life style of Padang.

About 720 residents in the downtown area of Padang were interviewed by ten local students and the answers were analyzed following the method improved by Ota et al (1998) to fit high-intensity areas. The extracted JMA intensity as the average of all the answers was "5 upper" and the deviation from the average is shown in Figure 2. The students explained each item of the questionnaire to residents, discussed the answers with them, and marked one of the answers listed on the sheet. Thus, the intensities were slanted according to the students who conducted the interviews. However, the areal deviation is still helpful in interpreting the damage distribution in Padang.

2.2 Micro-tremor observation

We observed micro-tremors at typical sites in the downtown area of Padang as one way to estimate the seismic response feature of the ground, and analyzed the observed data by the H/V spectrum method (Nakamura method). Figure 3 shows the spectra. The rather long-period components of around one to two seconds are clearly predominant, and they seem to lengthen from south to north. There is a hilly area on the left bank of the river mouth of Mata Air Timur (Jiraku river), so the surface soil layer is assumed to be shallow in the southern area and to become thick in the north. This assumption is supported by the variation of the predominant period of micro-tremors from south to north.

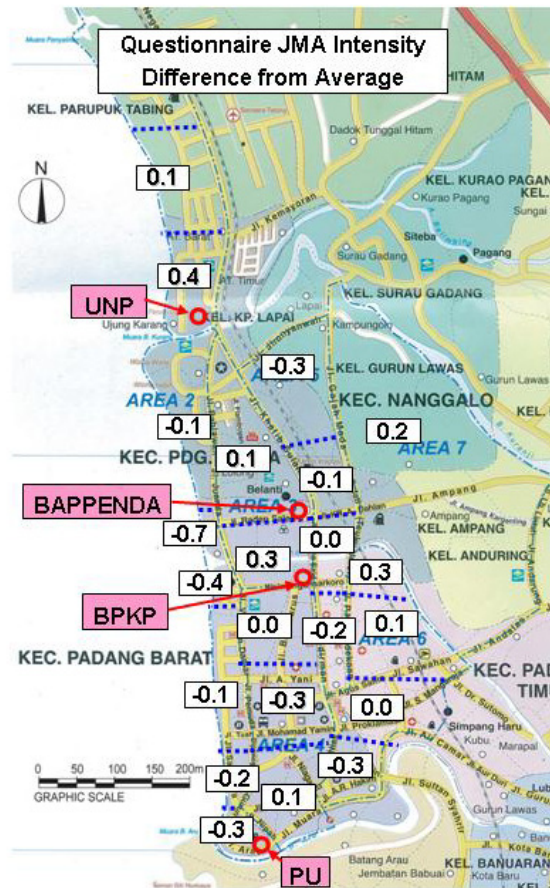


Figure 2. JMA Intensity difference from average (Red box denotes typical building.)

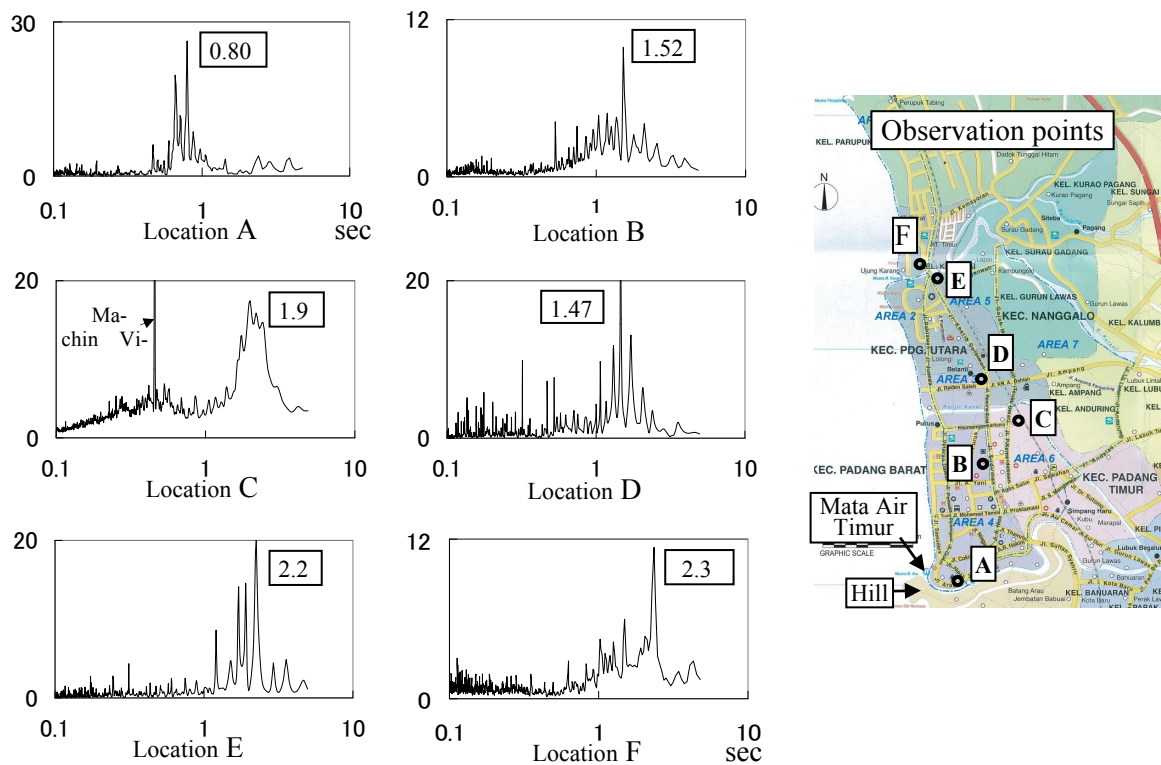


Figure 3. H/V spectra of micro-tremor in Padang city

2.3 Wave synthesizing

There was no instrumentally observed record of the shaking in the downtown area of Padang during the earthquake. However, BMKG recorded the shaking by a strong-motion seismograph placed on a rocky site in Andalas University, which is about 11km east of the downtown area of Padang. Additionally, an array observation using three seismographs located at the Andalas University site, a stiff soil site and a soft soil site of the downtown area was being operated by EWBJ (Engineers Without Borders, Japan) and Andalas University. Although it did not record the September 30 earthquake, it did record several other rather small earthquakes. We used these earthquake records to synthesize a provisional shaking in the downtown area during the 2009 September 30, 2009 earthquake.

Figure 4 shows a conceptual diagram of the synthesizing process.

- 1) Extract a Fourier transfer function averaging 4 earthquake records which were recorded from April to December 2009, which were 0.25-1.25 kine at maximum (Figure 5).
- 2) Compose an assumed soil column model fitting the transfer function. The depth and V_s of the soil layer were assumed using the data presented by Kiyono and Kubo of Kyoto Univ. The other profiles were determined by a trial and error method (Figure 6).
- 3) Calculate a non-linear (equivalent linear) response of the soil column model using the BMKG record as the incident wave. An improved SHAKE code with a frequency dependent damping was used. The synthesized wave and the response spectrum are shown in Figure 7.

Due to the effect of the soft soil layer, the short-period component of the incident wave is cut off and the peak acceleration is decreased. However, the long-period component is amplified and the relative response velocity at 1.8 seconds reaches 150 kine. JMA instrumental seismic intensity is **5.3** and MMI is about **8**.

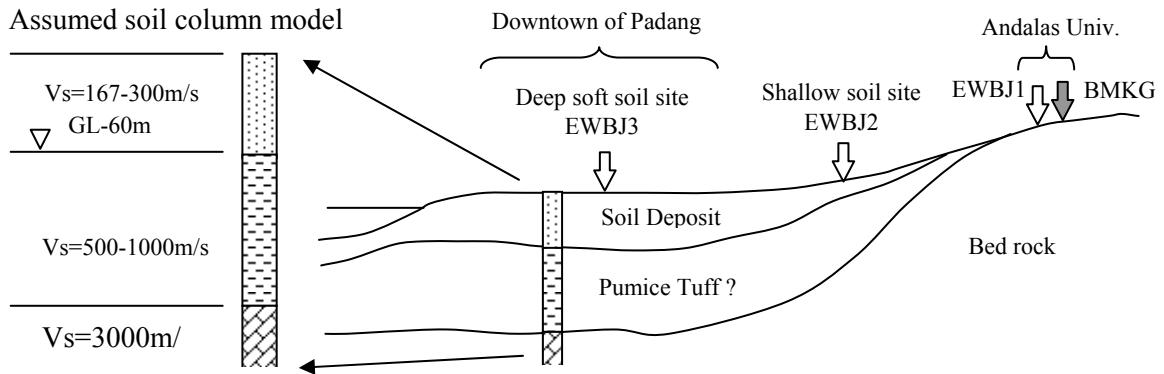


Figure 4. Conceptual diagram of the synthesizing process

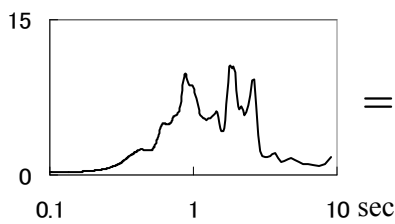


Figure 5. Averaged Fourier transfer function

$$= \frac{\sum (\text{Fourier spectrum}_{\text{EWBJ-3}})}{\sum (\text{Fourier spectrum}_{\text{EWBJ-1}})}$$

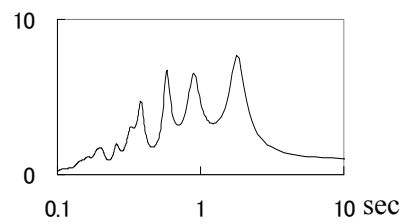


Figure 6. Synthesized Fourier transfer function

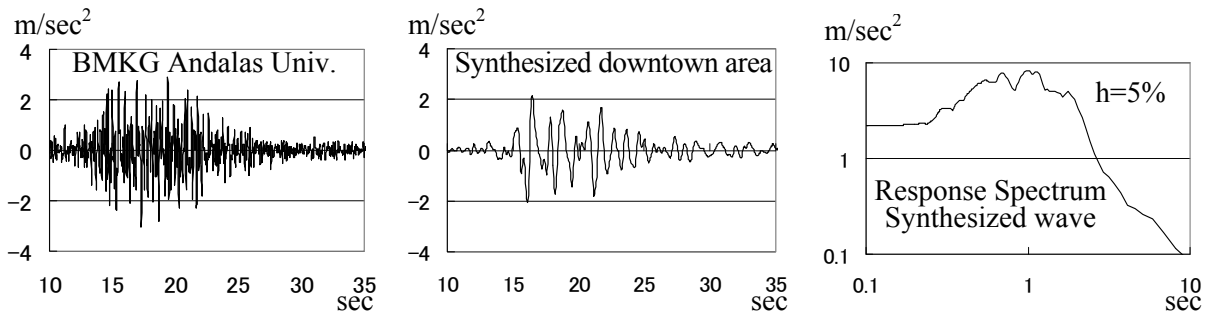


Figure 7. Incident wave, Synthesized wave and Response spectrum of the synthesized wave

2.4 Period of shaking recorded by a monitoring video camera

The Emergency Operation Center of West Sumatra State is located in the downtown area of Padang. A monitoring video camera was located on the ceiling of the operation room and



Figure 8. Clips of the video records

recorded the responses of chairs on casters and an unlocked door during the initial stage of the strong shaking. By tracking the movement of the chairs and the door in frames (Figure 8), we could draw time histories of the movements, as shown in Figure 9. The chairs and the door moved at one- to two-second period, which is consistent with the predominant period of the synthesized wave.

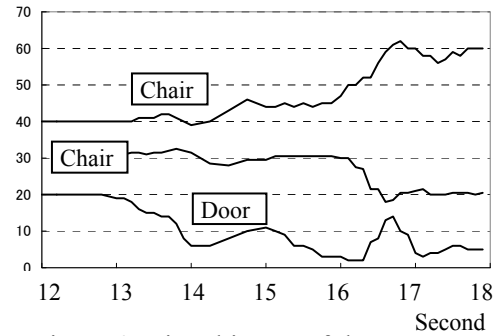


Figure 9. Time history of the movements

3 STUDY ON THE DAMAGE TO LARGE SCALE BUILDING

3.1 Detail field survey on a typically damaged building

The BPKP (Financial and Development Supervisory Board) building was located at the center of the downtown area. It was severely damaged but remained almost upright. Construction of this building started in 2003. After the first construction stage, the first and the second floors were completed and ready for use. In 2006, all five floors were completed. In the September 2007 Sumatra earthquake (offing Bengkulu) the terracotta roof collapsed. That roof was then replaced by a lightweight thin-steel roof (photo 2). During the on-site survey, we removed the cover materials near the top and bottom of all columns and evaluated the damage degree of each one using the seismic damage evaluation method developed by the Japan Building Disaster Prevention Association (1991). Table 1 shows the damage degree frequencies for each floor. Photos 3-5 show typical damaged columns according to damage degree. The third-floor columns were severely damaged. This damage obviously resulted from the reduction of column cross-section on this floor.



Photo 1. BPKP building



Photo 2. Lightweight roof

Table 1. Damage degree frequencies by floors

	1F	2F	3F	4F	5F
0	34	15	2	35	35
I	0	0	3	0	0
II	0	6	3	0	0
III	1	11	10	0	0
IV	0	2	10	0	0
V	0	1	7	0	0



Photo 3. Damage degree V



Photo 4. Damage degree IV



Photo 5. Damage degree III

We measured all the major building components, namely, the columns, the floor heights, the beams, the plate thicknesses and the reinforcing bars. The main bars were from $\phi 19 \times 16$ to $\phi 17 \times 12$ and the hoop bars were $\phi 10$ spaced at 120mm to 150mm. The concrete strength of representative portions was measured with a Schmidt Hammer, and the steel bar strength was measured with a Vickers Hardness Tester. The micro-tremor on the building was also measured. The Fourier spectra of the tremor are shown in Figure 11. The sway and the torsion vibration periods of the building are clearly observed.

3.2 Response analysis

Using these measured dimensions, a lumped mass frame model was developed. The weights of inner and perimeter walls of the building were included in the floor plate lumped mass. The stiffnesses of the columns and beams were assumed to be 100% of the original elastic-range value. The frame model was analyzed by a versatile software system for structural analyses (SAP2000). Figure 12 shows the analyzed modes and the natural periods. The periods in the horizontal X direction and in torsion coincided with those of the micro-tremor. However, the period in the horizontal Y direction was different. The model did not take into account the remaining stiffness of the brick walls and the decreasing stiffness of the damaged columns. These two factors must have compensated in the horizontal X direction and in torsion. The damage was considerably smaller in the horizontal Y direction than in the horizontal X direction, thus suggesting that the wall stiffnesses in the Y direction might not have decreased much.

The moment capacity diagrams of the columns were also calculated at all floors and the typical results are shown in Figure 13. To compare these capacities with the actual stress levels in the columns, the equivalent static seismic loading method was applied based on SNI-03-1726-2002 (recent seismic code used in Indonesia). The dead weight was assumed to include the weights of the structural members (columns, beams, and plates) and perimeter walls, and live load (20N/mm² for office).

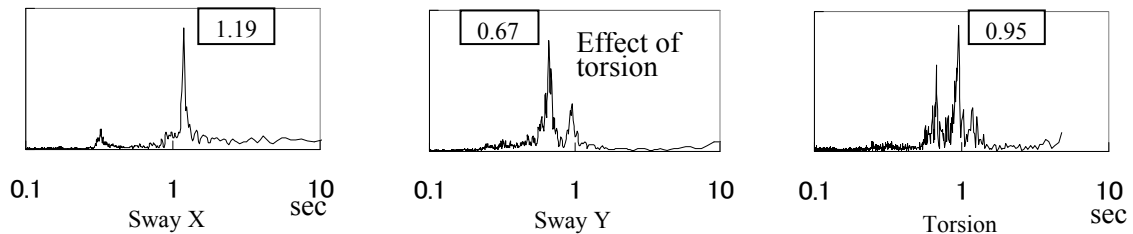


Figure 11. Fourier spectra of micro-tremor at 5th floor

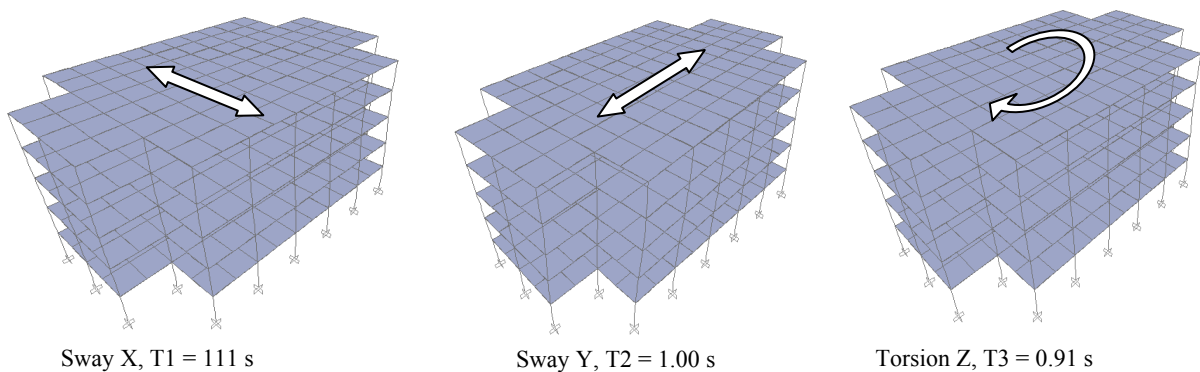


Figure 12. Frame model and analyzed natural vibration

The equivalent static seismic coefficient was also assumed based on the SNI-03-1726-2002. Thus, the nominal static equivalent base shear V is;

$$V = \frac{C_1 I}{R} W_t \quad (1)$$

where C_1 is obtained from Figure 14 using first natural period T_1 , and W_t is total building weight, including an appropriate live load.

In the BPKP case, T_1 is 1.11 seconds. Therefore, based on the figure and soft soil (Tanah Lunak) condition, C_1 is $0.9/T_1 = 0.9/1.11 = 0.811$. I is importance factor, taken as 1.0 for office buildings. R is seismic reduction factor. For a normal moment resisting frame, R is taken as 3.5. Therefore, V becomes 0.232. The weight is quantified as $W_t = 39,005$ kN following the assumption mentioned above. Thus the base shear force is $V = 0.232 \times 39,005 = 9,036$ kN. The base shear V must be distributed along the height of the structure, i.e.,

$$F_i = \frac{W_i z_i}{\sum_{i=1}^n W_i z_i} V \quad (2)$$

where F_i is the load acting on the mass center at floor- i , W_i is weight of floor- i , Z_i is height of floor- i , and n is the total number of stories. Based on three-dimensional frame analyses, the axial force and the demand moment at a typical column of the 1st and 3rd floor are shown together with the moment capacity in Table 3.

The demand moment exceeds the capacity, so the column could collapse if the actual seismic force reached the level of the design seismic load denoted by SNI-03-1726-2002.

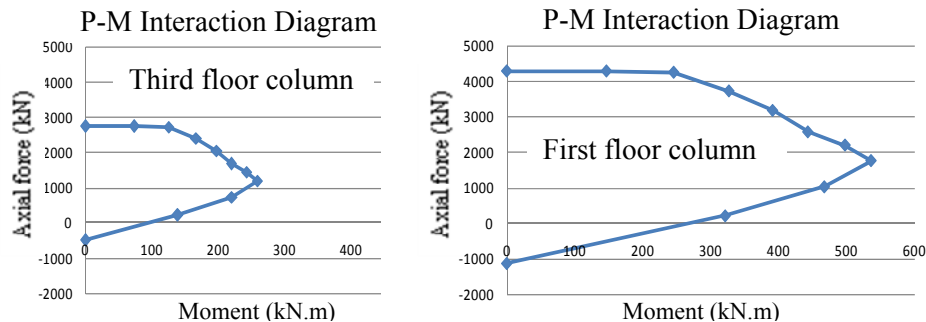


Figure13. Axial force and Moment capacity interaction curves at typical columns

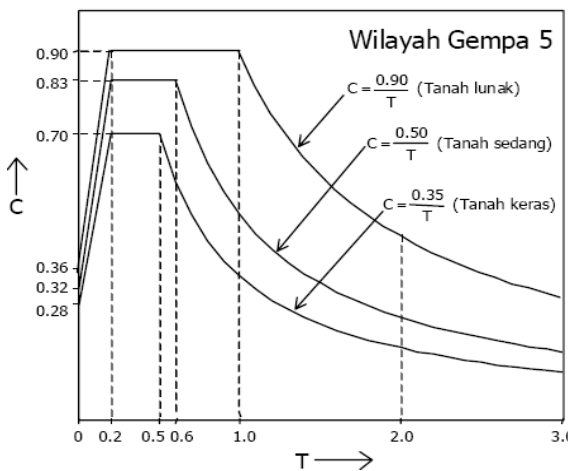


Figure 14. C_1 curves by SNI-03-1726-2002

Table 2. Seismic force distribution

Floor Name	Height (m)	Weight (kN)	Force per floor (kN)
Floor-4	20	4847	3012
Floor-3	16	8540	2410
Floor-2	12	8540	1807
Floor-1	8	8540	1205
Floor-G	4	8540	602

Table 3. Demand moment vs. Capacity moment

Floor Name	Axial force (kN)	Demand moment (kNm)	Capacity moment (kNm)
Floor-3	865	504	230
Floor-1	1525	792	515

Figure 15 compares the C1 curve to the synthesized wave response spectrum. The C1 curve shifted to the capacity moment level of the third floor column is also shown. It is clear that the seismic force acting on the BPKP building during the September 30, 2009 earthquake far exceeded its capacity and reached the level of the design seismic load denoted by SNI-03-1726-2002. According to the design document of the BPKP building, it was designed based on the previous design code of the SNI-03-1726-2002. The design calculation was based on the seismic coefficient method and the design seismic coefficient was 0.07. In spite of the very small design load, the advantage of a moment frame structure might have contributed to avoiding collapse. If the reinforcing bar arrangement, especially the hoop bars, had been adequate, the columns might not have been so severely damaged. Unfortunately, this was not so.

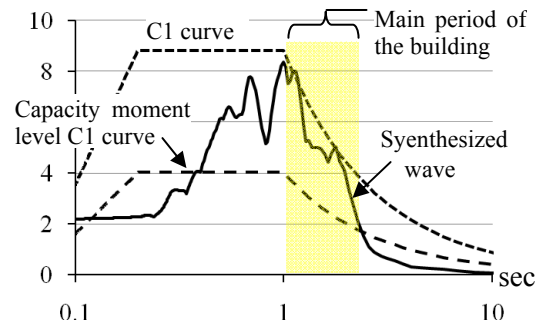


Figure 15. Comparison of C1 curve to the synthetic response spectrum

4 CONCLUSIONS

- (1) From the questionnaire survey, the JMA intensity in the downtown area of Padang was estimated to be 5-upper on average.
- (2) The micro-tremor H/V spectra predominated at the rather long periods of 1.0-2.0 seconds in the downtown area of Padang.
- (3) The synthesized wave using the EWBJ array observation and the BMKG record was also 5-upper level of the intensity and had a predominant period in 0.5-2.0 seconds. Its response spectrum nearly reached the design spectrum level denoted by SNI-03-1726-2002.
- (4) One of the damaged large scale buildings was designed by the seismic coefficient method using a design seismic coefficient 0.07. Although the demand moment at the columns exceeded the capacity moment and the columns were heavily damaged, they did not collapse. If the reinforcing, especially the hoop bars, had been arranged adequately, the columns might not have been so severely damaged.

ACKNOWLEDGEMENTS

The data used in this paper was obtained during field surveys by the authors under "The Preparatory Study on Disaster Management Program for Indonesia" implemented by JICA, 2009. The authors would like to express their sincere gratitude to JICA. They also express their sincere gratitude to Professor Yoshiaki NAKANO of the University of Tokyo, and to Professor Junji KIYONO of Kyoto University for their kind discussions and advices. Finally, the authors would like to acknowledge the contributions of EWBJ and BMKG for their efforts in operating the strong earthquake motion recording system.

REFERENCES

- Ohta Y., Goto N. & Ohashi H. (1979). "Estimation of seismic intensity during earthquake by questionnaire method." *Research report of engineering department of Hokkaido University*, No. 92, 117-128
- Ohta Y., Koyama M. & Nakagawa K. (1998). "Revision of algorithm for seismic intensity determination by questionnaire survey -in high intensity range-" *J. JSNDS 16-4*, 304-323
- Honda R., Takahashi Y., Pradono M. H. & Kurniawan R. (2005) "2004 Off Sumatra Earthquake -Questionnaire Seismic Intensity Survey in Banda Aceh" *Proc. 28th JSCE Earthquake Engineering Symposium*, 2005

Seismic vulnerability of shallow tunnels. Application to the metro of Thessaloniki, Greece

S. Argyroudis, K. Pitilakis

Department of Civil Engineering, Aristotle University of Thessaloniki, Greece

ABSTRACT:

A numerical approach is proposed for the construction of fragility curves and the vulnerability assessment of shallow metro tunnels in alluvial deposits, when subjected to seismic loading. The transversal response of the tunnel is calculated under quasi static conditions applying the induced seismic ground deformations which are calculated through 1D equivalent linear analysis for an increasing level of seismic intensity. The proposed approach allows the evaluation of new fragility curves considering the distinctive features of the tunnel geometries and strength characteristics, the input motion and the site specific soil properties as well as the associated uncertainties. The comparison between the new fragility curves and the existing empirical ones highlights the important role of the local soil conditions, which is not adequately taken into account in the empirical curves. The effect of the soil conditions is also highlighted through an application to the metro line of Thessaloniki.

1 INTRODUCTION

Underground structures have been proven in most strong earthquakes less vulnerable than aboveground structures, however they may still be susceptible to seismic damage, especially the shallow ones in poor geological conditions (Hashash et al. 2001; Power et al. 1998). The damage of a metro underground line may produce important indirect effects to human lives and to the operation of the global transportation system of an urban area. The Kobe's metropolitan line failure is a typical example (Shinozuka 1995). Hence, it is of high importance for risk managers, city planners and authorities to know the expected degree of damage of each transportation component due to various earthquake scenarios. Fragility curves, which express the probability of a structure reaching a certain damage state for a given earthquake parameter, play an important role in the overall seismic risk assessment of a transportation network.

So far the vulnerability assessment of tunnels has been mainly based on expert judgment (ATC13 1985; NIBS 2004) or empirical fragility curves (ALA 2001), derived from actual damage in past earthquakes all over the world (Dowding and Rozen 1978; Owen and Scholl 1981; Wang 1985; Sharma and Judd 1991). ALA (2001) produced empirical fragility curves for peak ground acceleration for bored and cut and cover tunnels with poor-to-average and good construction, based on regression analysis of a worldwide damage database. Recently, fragility curve methodologies using numerical approaches have become widely adopted as they are more readily applied to different structure types and geographical regions where seismic damage records are insufficient. Although such approaches are commonly used in case of bridges (Moschonas et al. 2009; Choi et al. 2004; Karim and Yamazaki 2001), buildings (Kappos et al. 2006) and other elements, their use for the fragility analysis of tunnels is still limited.

The main objective of this paper is to develop, check and apply a comprehensive numerical approach for the construction of fragility curves for shallow metro tunnels in alluvial deposits, considering structural parameters, local soil conditions and the input ground motion characteristics. The comparison between the new fragility curves and the existing empirical ones highlights the important role of the local soil conditions, which is not adequately taken into account in the empirical curves.

The response of tunnels to seismic shaking may be described in terms of two principal types of deformations; the first including both axial and curvature deformations, occur along the longitudinal axis of the tunnel; the second one, perpendicular to the longitudinal axis of the tunnel cross section, is resulting in “ovaling” deformations of a circular tunnel cross section and “racking” deformations of a rectangular cross section (Wang 1993; Hashash et al. 2001). This paper considers the seismic response of tunnels along the transversal direction, and thus the ovalisation and racking of the lining are the only mechanisms taken into account for the circular and rectangular tunnel sections respectively.

In particular, the transversal seismic response of the tunnel due to upward travelling SH or SV waves is evaluated under quasi-static conditions, applying the induced on the tunnel cross section and the surrounding soil free field seismic ground deformations, which are calculated independently through a 1D equivalent linear analysis (EQL). Different tunnel cross sections, input motions and soil profiles are employed. Defining the damage levels according to the exceedance of strength capacity of the most critical sections of the tunnel, the fragility curves could be constructed, as a function of the level and the type of the seismic excitation, considering the related uncertainties. The proposed fragility curves are finally used for vulnerability assessment and the estimation of seismic risk in case of Thessaloniki Metro line.

2 PROCEDURE FOR DERIVING FRAGILITY CURVES

2.1 Overview

The proposed approach is based on the quasi static analysis of tunnels in the transversal direction, considering the soil-structure interaction through 2D coupled numerical analyses. The general flowchart of the procedure is illustrated in Figure 1 (Argyroudis 2010). In general, the transversal seismic analysis of underground structures based on imposed seismic ground displacements is quite common in practice (e.g. Hashash et al 2001; Ptilakis and Tsiniadis 2010). Being essentially a static analysis, this approach is cost effective compared to more elaborate full dynamic time-history analysis. Especially for the needs of a comprehensive parametric fragility study like the present one, where different soil profiles, input motions and tunnel geometries are used, the aforementioned approach is adequate.

The effect of soil conditions and ground motion characteristics in the global soil and tunnel response is taken into account by using different typical soil profiles and seismic input motions. The response of the free field soil profiles and the induced seismic ground deformations are calculated through an 1D numerical analysis, for an increasing level of seismic intensity. The nonlinear soil behavior is considered through the variation of shear modulus and damping ratio with shear strain in the framework of a 1D EQL ground response analysis; the Mohr-Coulomb criterion is used to model the 2D soil-tunnel behavior. The results of the 1D free field soil response analyses are also employed to define the appropriate stiffness parameters in the finite element analyses, varying along the tunnel sides and compatible to the strains developed during the ground shaking. On the other hand the closed form solutions usually assume elastic soil behavior compatible, at the best, to a single average value of soil deformation (i.e. at the tunnels mid-depth) estimated through empirical or semi-empirical expressions.

The level of tunnel damage is described by a damage index expressing the exceedance of the lining strength capacity and the fragility curves are estimated based on the evolution of damage index with the increasing earthquake intensity, considering associated uncertainties. The proposed approach allows the evaluation of new fragility curves considering the distinctive features of the tunnel geometries and strength characteristics, the input motion characteristics and the soil properties. In contrast, the available empirical fragility curves do not consider adequately soil characteristics and they rather describe an average behavior of the tunnel in seismic action.

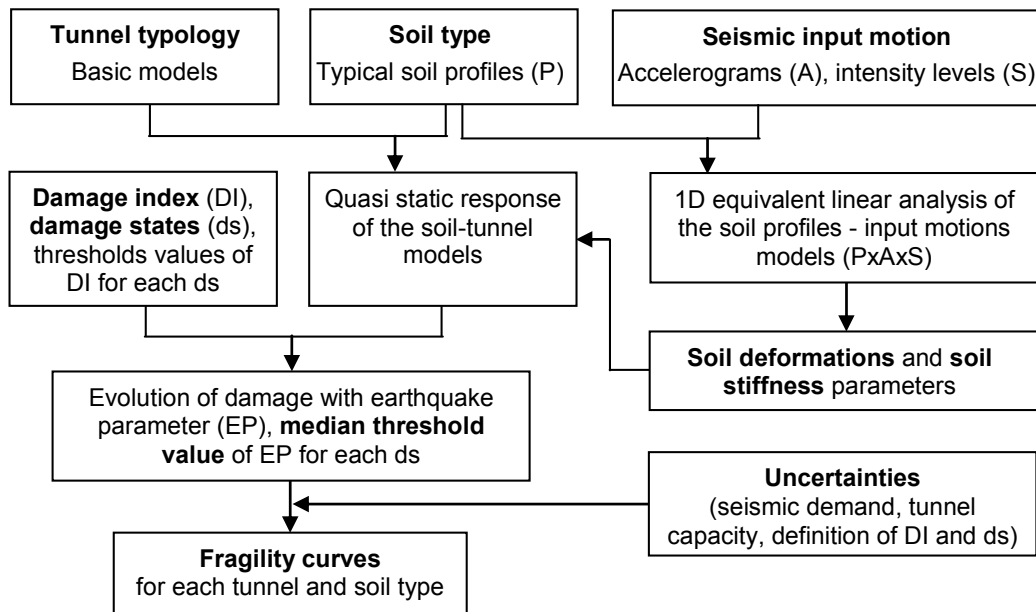


Figure 1. General flowchart of the procedure for deriving numerical fragility curves for tunnels in alluvial deposits

2.2 Definition of damage states

The damage states of already existing empirical fragility curves for tunnels are based on a qualitative damage description from past earthquakes. Although various damage indexes and related parameters have been proposed for the fragility analysis of buildings and bridges, no such information is available for tunnels. Considering this serious lack of references, in the present approach the damage index (DI) is defined as the ratio between the actual (M) and capacity (M_{Rd}) bending moment of the tunnel cross section. A definition based on moments is compatible with the use of displacements, according to the equal displacement approximation. In line with other approaches, it is assumed that the tunnel's behavior is approximated to that of an elastic beam subjected to deformations imposed by the oscillating surrounding ground due to seismic waves propagating perpendicular to the tunnel axis (Hashash et al 2001). The actual bending moment (M) is calculated as the combination of static and seismic loads. The capacity of the tunnel is estimated based on material and geometry properties of the beam considering the induced static and seismic axial forces (N) and bending moments (M).

According to previous experience of damages in tunnels and applying engineering judgment, four different damage states are considered due to ground shaking. They refer to minor, moderate, extensive and complete damage of the tunnel lining and they are described in Table 1. Although the proposed limits of damage index are not yet fully documented, they give a realistic description for the expected damage.

Table 1. Definition of damages states for tunnel lining.

Damage state (ds_i)	Range of damage index (DI)	Central value of DI
ds0. None	$M/M_{Rd} \leq 1.0$	-
ds1. Minor/slight	$1.0 < M/M_{Rd} \leq 1.5$	1.25
ds2. Moderate	$1.5 < M/M_{Rd} \leq 2.5$	2.00
ds3. Extensive	$2.5 < M/M_{Rd} \leq 3.5$	3.00
ds4. Collapse	$M/M_{Rd} > 3.5$	-

2.3 Estimation of fragility curve parameters

In line with similar procedures (Shinozuka et al. 2000; NIBS 2004; Moschonas et al 2009) the proposed fragility curves are described by the lognormal probability distribution function (Eq.1):

$$P_f(ds \geq ds_i | S) = \Phi \left[\frac{1}{\beta_{tot}} \cdot \ln \left(\frac{S}{S_{mi}} \right) \right] \quad (\text{Eq. 1})$$

where $P_f(\bullet)$ is the probability of being at or exceeding a particular damage state, ds_i , (Table 1), for a given seismic intensity level defined by the earthquake parameter, S (given here as Peak Ground Acceleration-PGA), Φ is the standard cumulative probability function, S_{mi} is the median threshold value of the earthquake parameter S required to cause the i_{th} damage state, and β_{tot} is the total lognormal standard deviation. The development of fragility curves according to Eq.1 requires the definition of two parameters, S_{mi} and β_{tot} .

Using the results of the coupled numerical analysis, the damage versus the selected earthquake intensity parameter (PGA in this case) diagram can be plotted, which represents the evolution of damage index with increasing earthquake intensity. The median threshold value of the earthquake parameter, S_{mi} , can be obtained for each damage state based on the aforementioned diagram and the damage index definitions given in Table 1. A lognormal standard deviation (β_{tot}) that describes the total variability associated with each fragility curve has to be estimated. Three primary sources of uncertainty are considered (NIBS 2004), namely the definition of damage states (β_{ds}), the response and resistance (capacity) of the tunnel (β_C) and the earthquake input motion (demand) (β_D). The total variability is modeled by the combination of the three contributors, assuming that they are statistically independent and lognormally distributed random variables (Eq.2):

$$\beta_{tot} = \sqrt{\beta_{DS}^2 + \beta_C^2 + \beta_D^2} \quad (\text{Eq. 2})$$

Due to the lack of a more rigorous estimation, for the parameter β_{ds} we assigned a value equal to 0.4 following the approach of HAZUS (NIBS 2004) for buildings; β_C is assigned equal to 0.3 according to analyses for bored tunnels of BART system (Salmon et al. 2003). The last source of uncertainty, associated with seismic demand, is described by the average standard deviation of the damage indices that have been calculated for the different input motions at each level of PGA.

3 APPLICATION FOR TYPICAL SHALLOW TUNNELS AND SOIL PROFILES

3.1 Tunnel sections

Two typical shallow tunnel sections are considered, a circular (bored) tunnel with a 10m diameter and a rectangular (cut and cover) one-barrel frame with dimensions 16x10m. The lining of the circular tunnel is composed of 0.50m thick precast concrete segments, while that of the rectangular tunnel is composed by 0.9m thick side concrete walls, 1.2m thick roof slab and 1.4m thick base slab. The upper points of the circular and rectangular section are in a depth of 10m and 3.5m respectively. The concrete material is characterized by the following linear elastic parameters: Young's modulus $E=30.5\text{GPa}$, Poisson ratio $\nu = 0.2$.

3.2 Input motions

Records from different earthquakes, in soil conditions similar to soil class A of Eurocode 8, were selected as input motion in outcrop conditions for the 1D ground response analyses (Table 2). The mean acceleration spectrum of the selected input signals is plotted together with the EC8 spectra for soil class A in Figure 2.

The time histories are scaled from 0.1 to 0.7g in order to calculate the induced stresses in the tunnel for gradually increasing level of seismic intensity. In particular, for amplitudes equal or lower to 0.3g, the first four records were used, while for amplitudes greater of 0.3g the next six records were applied. This distinction was made in order to scale the real records to amplitudes as much as possible consistent with their frequency characteristics.

Table 2. Selected records applied to the bedrock of the soil profiles.

Record station		Earthquake	Magnitude M_w	Epical distance (km)	PGA (g)	Predominant period (sec)
1	OTE	Kozani, 1995	6.5	17.0	0.142	0.50
2	Kypseli	Parnitha, 1999	6.0	10.0	0.120	0.43
3	Gebze	Kocaeli, 1999	7.4	41.8	0.218	1.06
4	Cubbio-Piene	Umbria-Marche, 1998	4.8	18.0	0.235	1.08
5	Hercegnovi Novi	Montenegro, 1979	6.9	65.0	0.256	0.74
6	Sturno	Campano Lucano, 1980	7.0	32.0	0.323	2.30
7	Gilroy1	Loma Prieta, 1989	6.9	28.6	0.440	0.37
8	Griffith Park Observ.	Northridge, 1994	6.7	25.4	0.289	0.10
9	Whitewater Trout Farm	Palm Springs, 1986	6.2	7.3	0.517	0.52

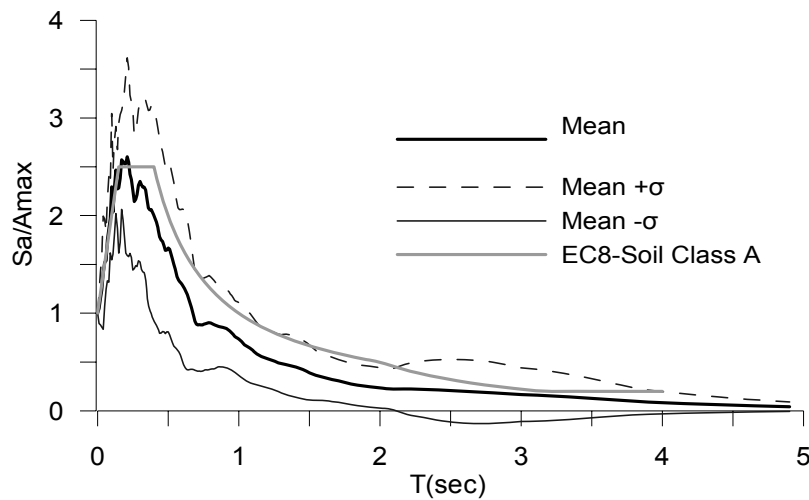


Figure 2. Mean acceleration spectra ± 1 standard deviation of the input time histories for the 1D ground response analyses and comparison with the spectrum provided by EC8 (soil type A).

3.3 Soil profiles

Fourteen ideal soil deposits were considered, corresponding to soil types B, C and D of Eurocode 8 (EC8 2004), ranged according to the shear wave velocity (V_{s30}) values (Figure 3). Three different thicknesses were assumed, equal to 30m (profiles: B30sand, B30clay, C30sand, C30clay, D30sand, D30clay), 60m (profiles: B60a, C60a, D60a, B60, C60, D60) and 120m (profiles: B120, C120). Typical values of the different soil properties were selected for each soil layer. The 60m and 120m profiles constitute of a surface 5m thick sand layer overlaying clay layers, while the 30m profiles consist solely of sand or clay.

3.4 Estimation of the imposed seismic ground displacements

The imposed quasi-static seismic ground displacements have been computed using a 1D EQL approach with the code EERA (Bardet et al 2000), assuming an equivalent linear elastic soil behavior. The variations of shear modulus G/G_0 and damping ratio D with the shear strain level γ were defined according to the available data in the literature as a function of plasticity index and effective stress (Darendeli 2001). Curves with $PI=30\%$ for clay and $PI=0\%$ for sand materials were selected in this study (Figure 4). For the seismic bedrock, the curves proposed by Schnabel et al. (1972) were applied.

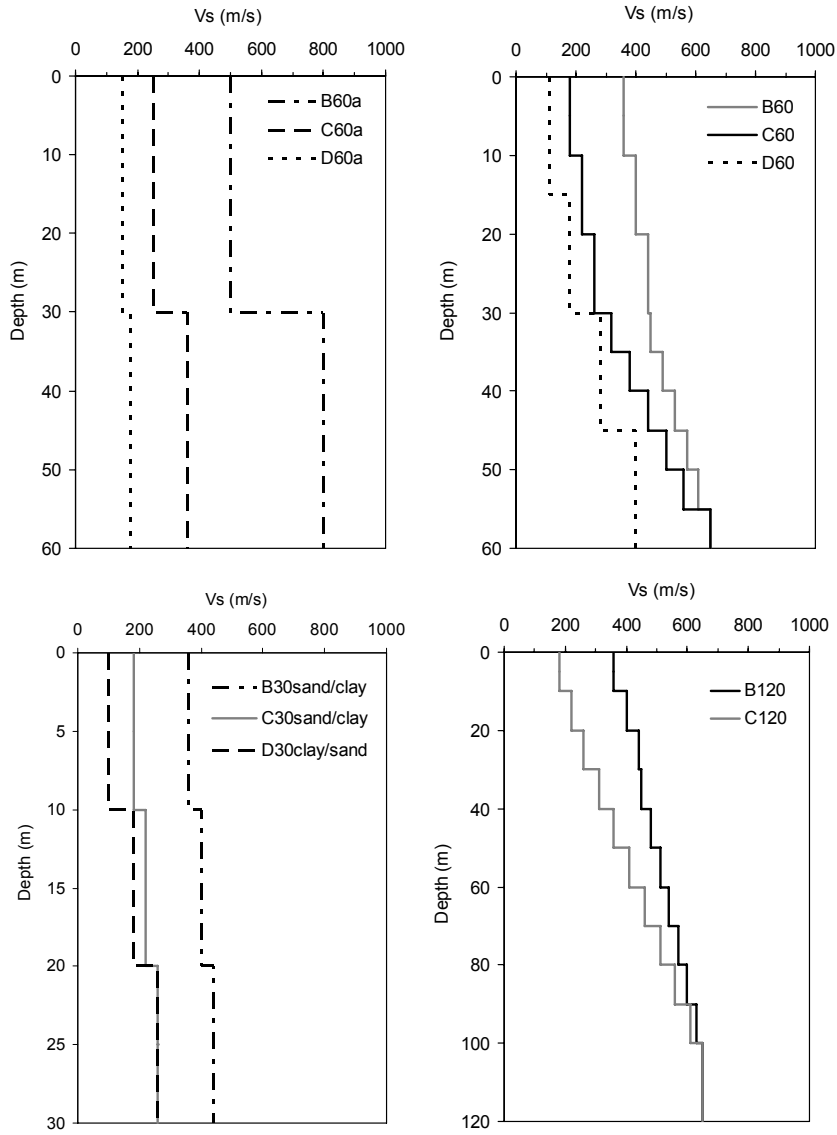


Figure 3. Variation of shear wave velocities of the examined soil profiles.

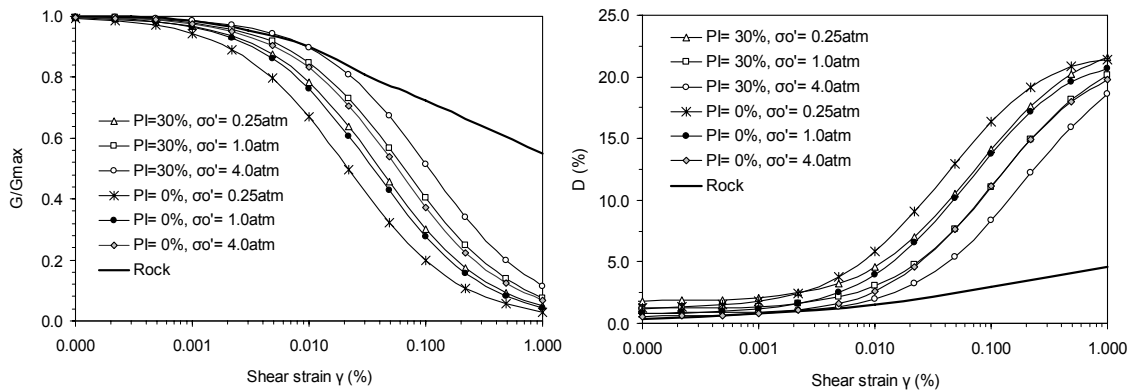


Figure 4. Shear modulus reduction (G/G_{max}) and variation of damping ratio (D) with shear strain (γ).

Each soil profile is discretised by appropriate number of layers varying from 2.5 to 10m thickness. In the iterative procedure, the ratio of effective and maximum shear strain is assumed equal to 0.65. The cumulative displacements in each soil layer and depth were estimated for each soil profile and input motion, based on the computed peak shear strain versus depth. These peak displacements' profiles are imposed on the lateral boundaries of the plain strain soil model in order to estimate the response of the tunnel lining under quasi-static conditions. We avoided to apply the computed displacements' pattern directly on the tunnel lining through springs and dashpots because recent studies (Pitilakis and Tsinidis, 2010) have proved that the epistemic uncertainties associated to the selection of these parameters may be very important, affecting the final results. Moreover, it was found that the displacements that are estimated from the displacement time histories in each layer for the time instance where the shear strain takes the maximum value at the tunnel's depth, are similar or even lower than the aforementioned ones based on the peak values. Therefore, the displacements' patterns used herein, which are based on the peak shear strains, constitute a more conservative and easier to apply approach.

The computed variation of G versus depth was also used to evaluate the corresponding modulus of elasticity (E) of each soil layer, which is used in the quasi static analysis of tunnel. In particular, an average value of E is calculated for each soil layer based on the average values computed for the different input motions. Figure 5 shows a typical example of the computed ground response in terms of maximum acceleration a_{max} (PHGA), normalized shear stiffness G/G_{max} , peak shear strain γ_{max} , and cumulative displacement D_n . The computed PGA value at the surface of each soil profile is selected as the representative parameter of the seismic intensity in the fragility curves.

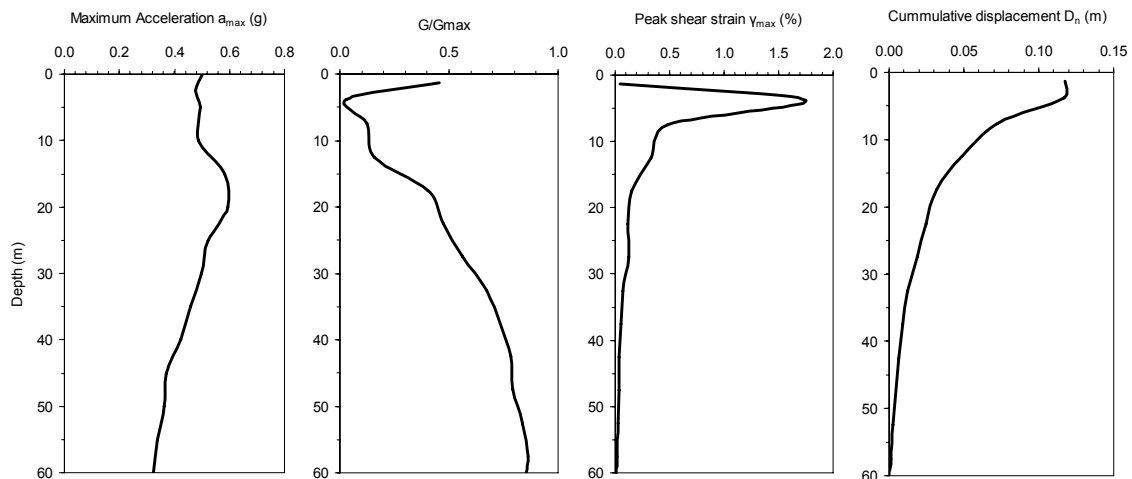


Figure 5. Example of 1D ground response analysis results with EERA and estimation of displacements versus depth (Soil profile: C60, Input motion: Montenegro, 0.5g for outcrop conditions).

The relative stiffness of the structure and the surrounding soil is an important parameter describing the soil-structure interaction identity of underground structures (Hashash et al. 2001). It may be quantified by the flexibility ratio (F), which is a measure of the flexural stiffness (resistance to ovaling for circular tunnel or racking for rectangular frame) of the medium relative to the lining. The flexibility ratio an important factor that contributes to the soil-structure interaction. It depends on the characteristics of the medium (modulus of elasticity E_m or shear modulus G_m) and the geometrical and material properties of the tunnel. The flexibility ratios that correspond to the different soil profiles and the two tunnels of the present study are given in Figure 6. The shear depended modulus of elasticity of the surrounding soil has been estimated through the 1D ground response analyses for the different input motions, as described above. They vary from 0.2 to 55 covering a wide range of soil-structure interaction cases.

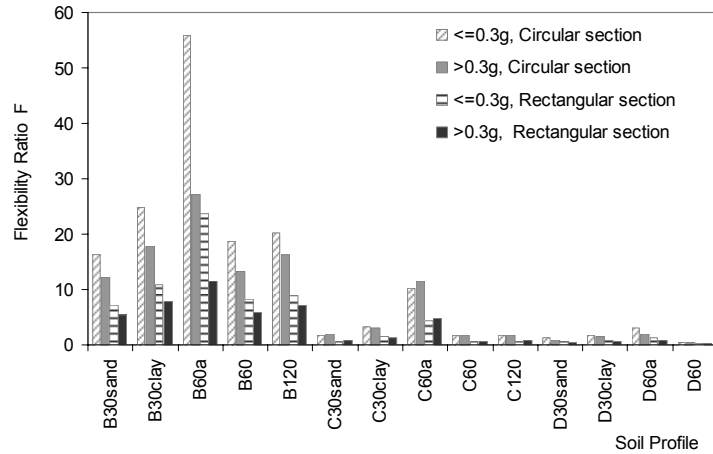


Figure 6. Flexibility ratios F for the different soil profiles and the two tunnel sections.

3.5 Numerical analyses

The response of the tunnel is calculated under quasi-static conditions applying the induced free field cumulative displacements, which were calculated through the 1D EQL analysis. A plane strain ground model with the tunnel cross section is simulated using the finite element code PLAXIS 2D (Plaxis 2002). The lateral extent of the model is properly selected in order to simulate the soil structure interaction and to avoid boundary effects. Based on sensitivity analysis it was found that a distance equal to three times the diameter of the circular section (i.e. 30m) from both sides of the tunnel axis is adequate for the analysis.

The side boundary conditions were fixed in the vertical direction and free to move in the horizontal direction, while the nodes at the bottom of the mesh were fixed in both directions. Prior to the application of the imposed displacement, a set of initial static analyses was performed to properly model the initial static conditions, the excavation of the tunnel and the construction of the lining. The circular tunnel excavation was simulated through the volumetric contraction of the tunnel section corresponding to volume loss equal to 0.2-0.5% for soil type B and 1% and 2% for the soil types C and D respectively.

The behaviour of the tunnel lining was assumed to be linear elastic, while the soil was characterized by a Mohr-Coulomb yield criterion for all the stages of the analysis. Strain compatible soil shear stiffness moduli, are used for the quasi-static analysis. Figure 7 shows a representative example of the tunnel response after imposing the shear ground displacements.

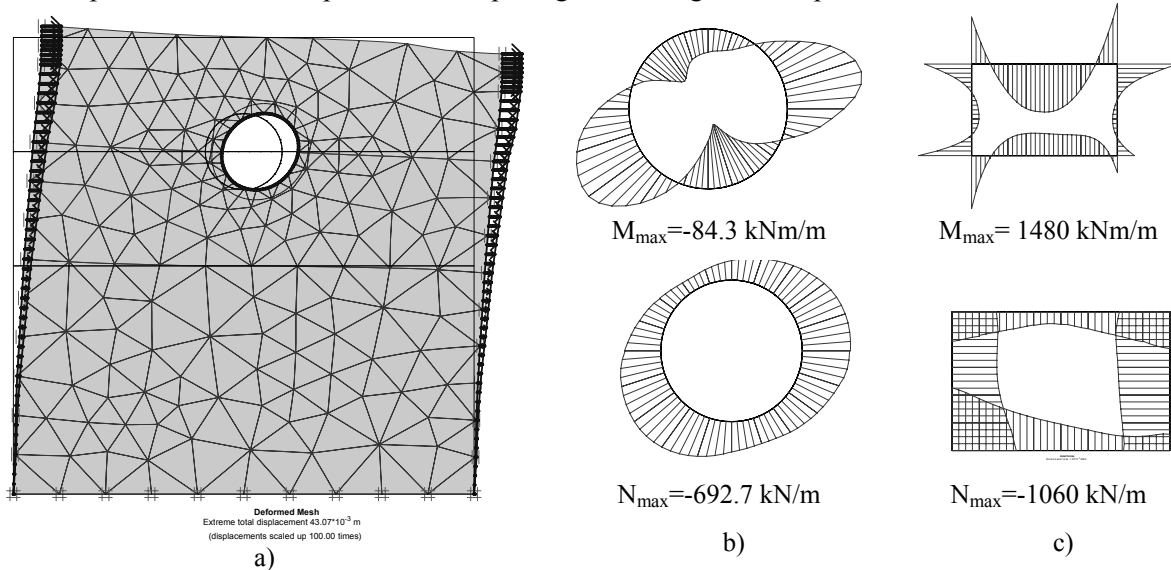


Figure 7. Example of 2D analysis results: deformed mesh (a), total moment and axial forces of the circular (b) and rectangular (c) tunnel lining (Soil profile: B60a, Input motion: Kypseli, 0.3g).

4 FRAGILITY CURVES

The derivation of fragility curves (i.e. the definition of the median threshold value of PGA for each damage state) is based on the construction of diagram of the computed damage indices versus PGA at the ground surface according to the definitions of Table 1. The diagram is estimated by linear regression analysis, considering the natural logarithm of the damage index (LnDI) as the dependent variable and PGA as the independent variable. Similar approaches are used for the derivation of fragility analysis for bridges (e.g. Karim and Yamazaki 2003, Choi et al. 2004, Nielson and DesRoches 2007, Pinto 2007). Examples of the evolution of damage with PGA are given in Figure 8 for the two tunnel sections, where an average linear regression is fitted to the data set, bounded by the corresponding standard deviation.

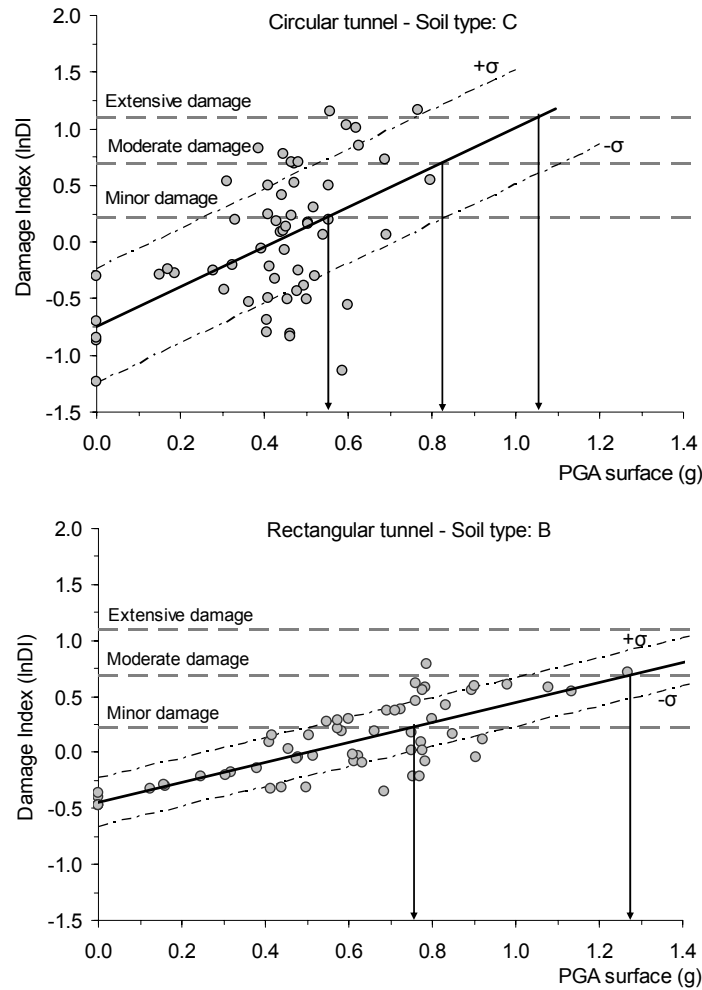


Figure 8. Examples of the evolution of damages with PGA at the ground surface for circular and rectangular tunnel cross-sections. Estimation of the median threshold values of PGA for each damage state.

The sets of fragility curves derived for each soil type (B, C and D) following the procedure that is described in this paper, are given in Figures 9 and 10 for the circular and rectangular tunnel section respectively. In the same figures the parameters of the lognormal distribution in terms of median and standard deviation are presented. Comparing the fragility curves derived for the three soil types, it is noted that for the same PGA in both tunnel types the vulnerability is gradually decreasing from soil type D to C and from soil C to B. The fragility curves for extensive damages for soil type B in both tunnel sections, and for soil type D in case of rectangular tunnel, (dashed lines), are derived based on extrapolation of the available computation results. The extrapolated values of damage index for the extensive damages could be attributed to several reasons, i.e. higher stiffness in case of soil class B and predominance of non-linear soil behavior and internal damping expected in the case of soil class D.

A practical consequence of these observations is that the probability of extensive damages is very low for circular tunnels in stiff soils, even for very important ground accelerations. The same is expected for rectangular tunnels in soft soils. These remarks are consistent with the few available observations from recent strong earthquakes as it is further discussed in the next section.

Comparing the fragility curves derived for the two tunnel types, it is observed that the rectangular shallow tunnel, constructed with cut and cover, is more vulnerable than the circular, normally bored, tunnels, for all soil types. The higher standard deviation values are estimated in the case of the circular section in soil type C and D, which reflects the variability in the results in terms of PGA at the surface and damages indices values.

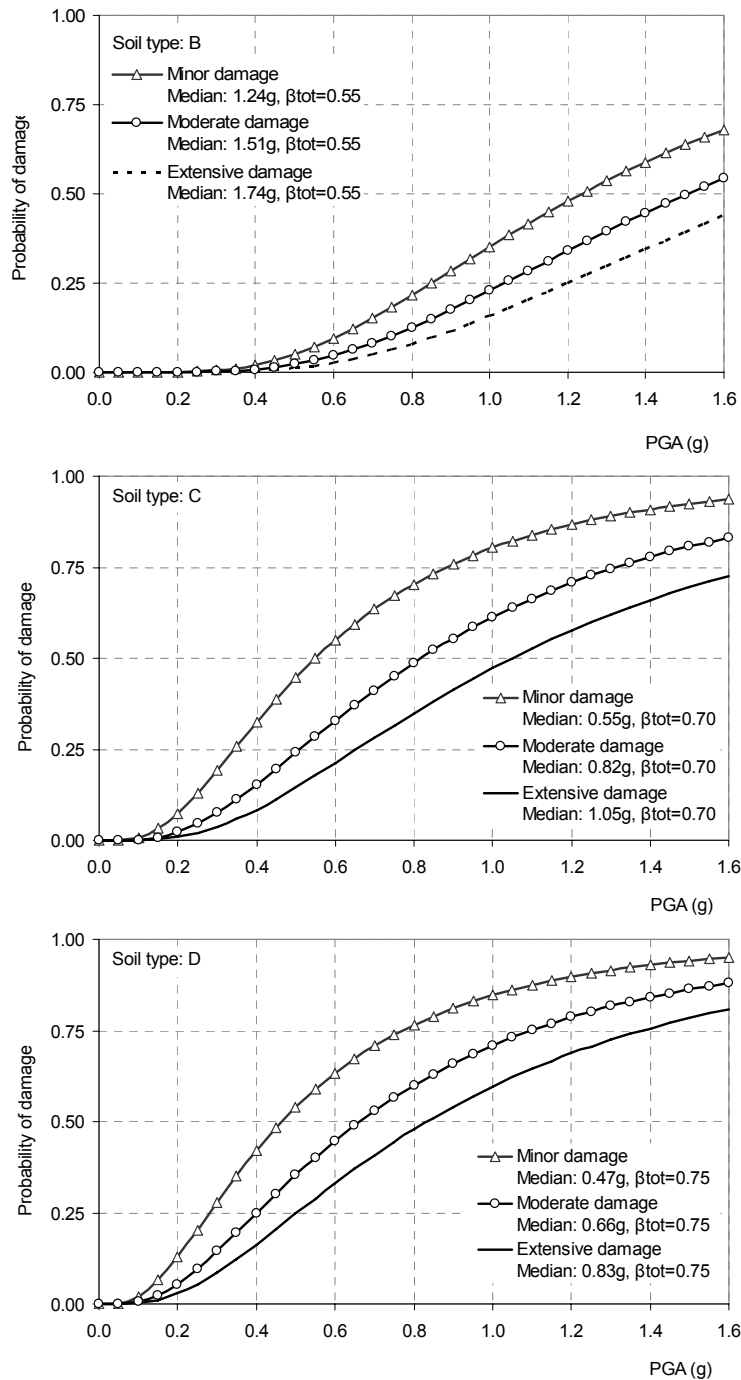


Figure 9. Fragility curves for circular (bored) tunnel section (dashed curve derived by extrapolation of numerical results).

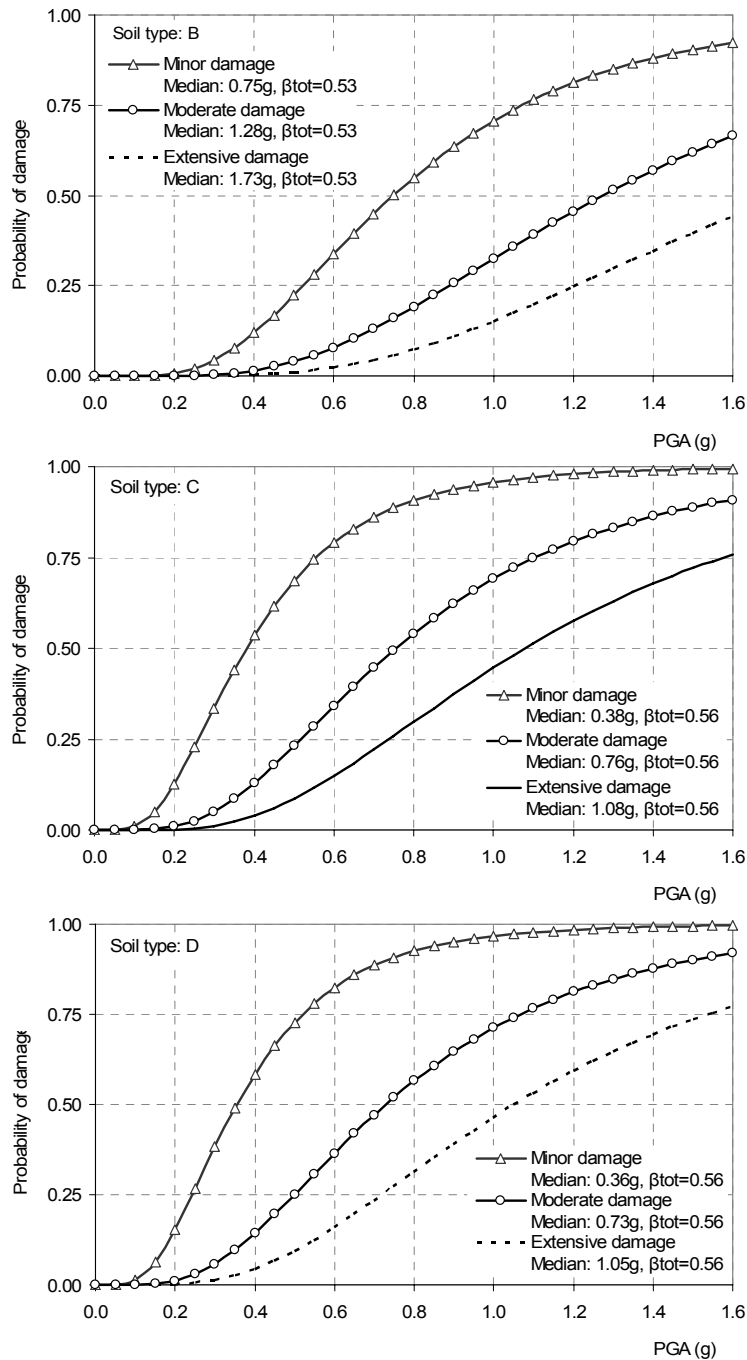


Figure 10. Fragility curves for rectangular (cut and cover) tunnel section (dashed curves derived by extrapolation of numerical results).

5 COMPARISON BETWEEN NUMERICAL AND EMPIRICAL DAMAGE DATA

The numerically derived fragility curves are compared with the empirical ones that are proposed by ALA (2001) based on observed damage data in tunnels from past earthquakes (Figure 11). In these empirical curves PGA values have been estimated using available ground motion prediction equations, with all the uncertainties associated to these models. Moreover, the database includes tunnels of various functions (i.e. highway, transit, railroad, water supply and communications). They are classified as tunnels in rock and tunnels in soil, and for poor-to-average and good construction practices and maintenance conditions. Finally, the definition of the damage states is strictly qualitative, based mainly on the extent of the observed cracking of the tunnel liner, and independently of the type of damage producing these cracking; for example cracking

due to transversal stressing is not differentiated from cracking in the longitudinal axis. In the present comparison, we selected to compare our resulting fragility curves with the empirical fragility curves for alluvial (soil) and cut and cover tunnels with good quality construction. For this type of tunnels no empirical curves are provided for extensive damages, which is consistent with the numerical results. In particular, the threshold PGA values for extensive damages are very high or they are estimated based on extrapolation of the numerical results since the computed damage indexes are low, as it is described in the previous section.

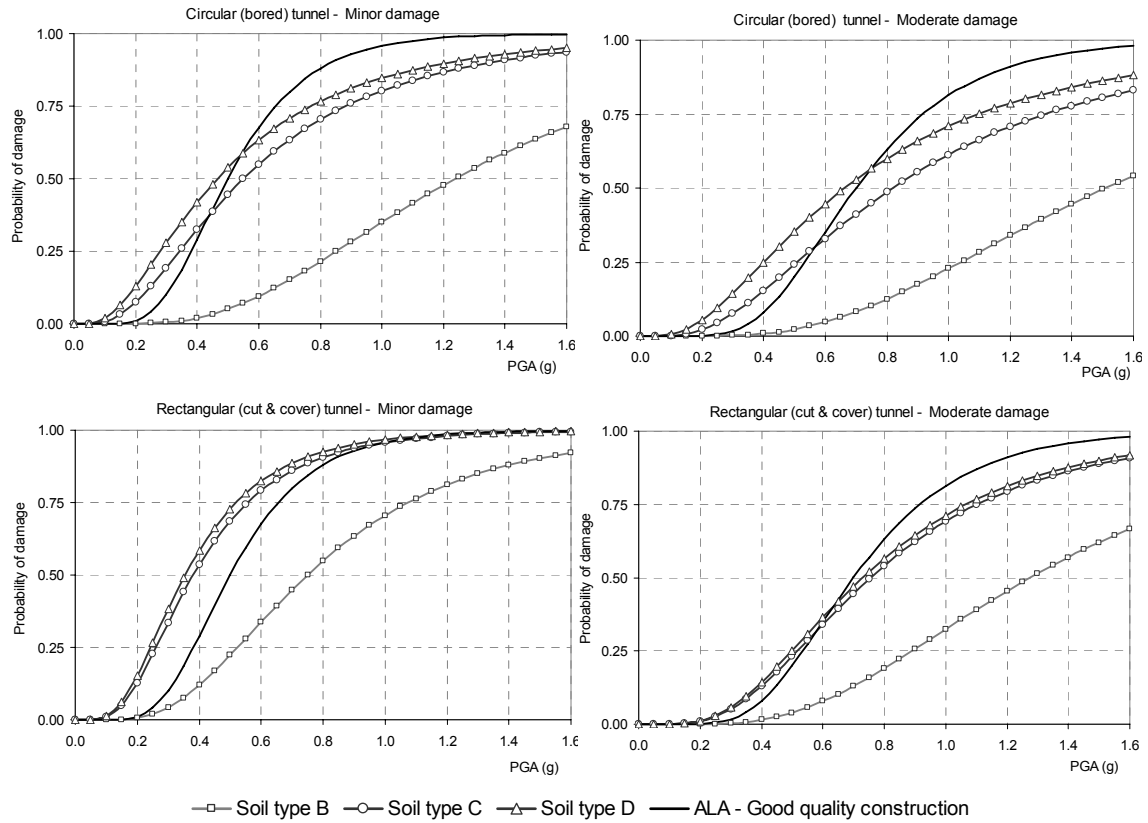


Figure 11. Comparison between numerical and empirical (ALA, 2001) fragility curves for circular (up) and rectangular (down) tunnel cross section.

The role of the soil conditions is very important to be neglected. The numerical fragility curves are seriously modified with the soil conditions, contrary to the empirical curves, which are rather describing an average response of the tunnels independently of soil conditions. Therefore, the empirical curves may over or underestimate the probability of damage. It is also interesting to remark that the empirical curves are well compared with the numerical ones for soil types C or D. This is due to the fact that the majority of damages have been reported in “moderate” and “poor” soil conditions that correspond to soil type C and D.

The proposed fragility curves are applied to estimate the damage probabilities of cut and cover tunnels that were subjected to strong ground motion in recent earthquakes (Table 3). Two rectangular stations in Athens (Monastiraki, Sepolia) and one in Kobe (Dakai) are examined. The details about the structure geometry and response, site soil conditions and recorded ground motions are given by Gazetas et al. (2005). The observations are well predicted by the fragility curves in case of Athens metro. The prediction is less satisfactory in case of Dakai station. This divergence may be attributed to the fact that the present fragility curves are referring to modern structures designed and constructed according to recent improved seismic code prescriptions, while Dakai station was not designed according to modern codes. Moreover, the curves were developed for one-barrel rectangular section, without the presence of the vulnerable central columns as it is the case of Dakai station.

Table 3. Comparison between observations and estimations from fragility curves for cut and cover tunnels.

Earthquake	Tunnel type and location	PGA on site (free field)	Soil type	Observed damage	Probability of damage
Parnitha, 1999	Monastiraki station	0.34g	Stiff sandy clays and highly weathered rock formations down to at least 60 m depth, $V_{s30}=400\text{m/s}$	None	None: 0.93 Min.: 0.06 Mod.: 0.01 Ext.: 0.00
Parnitha, 1999	Sepolia station	0.31g	0-7m: sandy to silty clay, 7-15m: stiff sandy clay with gravels, 15-25m: fractured conglomerate, 'Athenian Schist', $V_{s30}=390\text{m/s}$	None	None: 0.95 Min.: 0.04 Mod.: 0.00 Ext.: 0.00
Kobe, 1995	Dakai station	~0.70g	alternations of mostly saturated loose sandy and soft clayey, $V_{s30}=300\text{m/s}$	Extensive	None: 0.14 Min.: 0.42 Mod.: 0.23 Ext.: 0.22

6 APPLICATION TO THESSALONIKI METRO (GREECE)

The Thessaloniki metro is under construction and includes a 9.5 km of line (with two independent single track tunnels) and 13 center platform stations. The major part of the line will be constructed by means of two Tunnel Boring Machines. The remaining section of the line will be constructed by the Cut and Cover method. The depth of the tunnels starts from -14m at the New Railway Station, continues to -18m at the longer part of the project, reaches its maximum level at -31m in University area and finishes at -13m at the terminal station of N. Helvetia.

The proposed fragility curves for the bored tunnel (circular section) are used for the seismic risk estimation of Thessaloniki metro. The line is divided in 13 segments between the stations and each one is classified in a soil class, in order to select the corresponding fragility curves (Table 4). The maximum value of PGA at the free surface is defined along the segments, based on the maps with the spatial distribution of PGA for each scenario (Figure 12). The expected level of damage is estimated for two seismic scenarios with mean return periods equal to 475 and 950 years, which are derived from the detailed Microzonation study of the city (Pitilakis and Kakderi 2011). The distribution of the expected damage probabilities is presented in Figure 13 for each segment and seismic scenario. The damage probabilities are low in all cases; however the higher values are estimated for the segments that pass through soil type C. Therefore, the effect of soil conditions is very important both for the seismic response of soil deposits and nearby soil-structure systems.

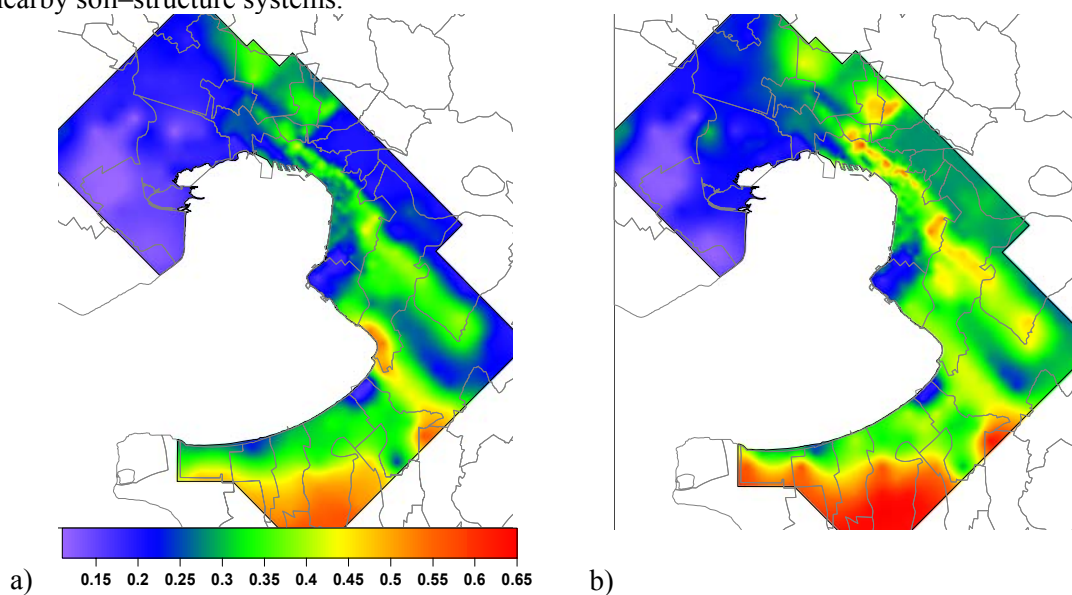


Figure 12. Distribution of mean peak ground acceleration (PGA in g) for the 475 (a) and 950 (b) years seismic scenario.

Table 4. Soil classification and PGA values along each segment of Thessaloniki metroline.

Metro line segment		Soil class	PGA (g)	
			Tm=475 years	Tm=950 years
1	NRS - Dimokratias Sq.	C	0.378	0.441
2	Dimokratias Sq. - Venizelou	B	0.356	0.386
3	Venizelou - Ag. Sophia	B	0.382	0.361
4	Ag. Sophia - Sintrivani	B	0.342	0.350
5	Sintrivani - Panepistimio	B	0.300	0.325
6	Panepistimio - Papaphi	B	0.294	0.315
7	Papaphi - Efkliidi	B	0.300	0.305
8	Eflikidi - Fleming	B	0.308	0.255
9	Fleming - Analipseos	C	0.280	0.400
10	Analipseos - Patrikiou	C	0.286	0.440
11	Patrikiou - Voulgari	C	0.227	0.441
12	Voulgari - N. Helvetia	B	0.260	0.386
13	N. Helvetia - Terminal Pylaias	B	0.310	0.361

7 CONCLUSIONS

A simple yet comprehensive numerical methodology is proposed to construct fragility curves for shallow metro tunnels in alluvial deposits, when subjected to transversal seismic loading. Tunnel response is calculated under quasi static conditions, applying at a certain distance from the tunnel the induced seismic ground deformations, which are calculated through a 1D equivalent linear analysis. Seismic inputs with different frequency content are used, scaled in different levels of seismic loading. Typical tunnel cross sections (circular and rectangular) and soil profiles, classified as B, C and D according to EC8, are employed. Defining different damage states, the fragility curves could be derived as a function of the level of peak ground acceleration at the ground surface, considering the related uncertainties in the definition of damage states, the demand and the capacity of the tunnel.

So far the vulnerability assessment of tunnels is based on simple empirical fragility curves, without properly considering soil and tunnel characteristics. With the proposed fragility curves we consider in a more systematic way the distinctive features of the tunnel geometric and strength properties, as well the input motion characteristic and soil properties. The proposed fragility curves should be used for shallow tunnels, circular or rectangular, in shallow alluvial deposits classified according to EC8 soil categories. The important role of the soil conditions is also highlighted through an application to the under construction metro line of Thessaloniki.

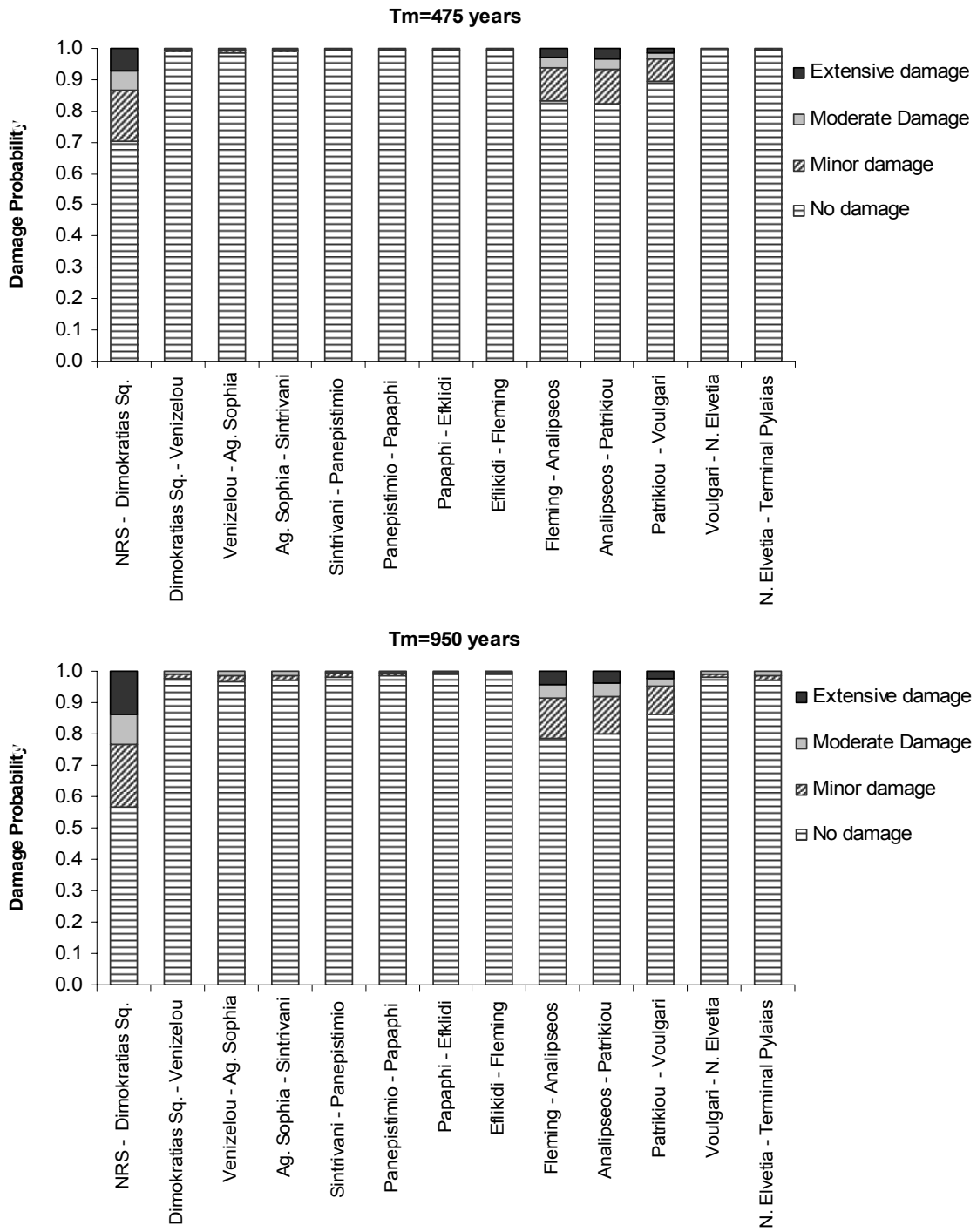


Figure 13. Estimated damage probabilities for Thessaloniki metro segments

8 REFERENCES

- American Lifelines Alliance (ALA) (2001), Seismic fragility formulations for water systems, part 1-Guideline, ASCE-FEMA, 104 p.
- ATC-13 m(1985), Earthquake damage evaluation data for California, Applied Technology Council, Redwood City.
- Argyroudis S. (2010), Contribution to seismic vulnerability and risk of transportation networks in urban environment, PhD thesis, Department of Civil Engineering, Aristotle University of Thessaloniki, Greece.
- Bardet J.P., Ichii K. and Lin C.H. (2000), EERA: a computer program for equivalent-linear earthquake site response analyses of layered soil deposits, University of Southern California, Department of Civil Engineering 40 p.
- Choi E., DesRoches R., Nielson B. (2004), Seismic fragility of typical bridges in moderate seismic zones, *Engineering Structures* 26: 187-199.
- Darendeli M.B. (2001), Development of new family of normalized modulus reduction and material damping curves, PhD thesis, University of Texas, Austin.
- Dowding C.H., Rozen A. (1978), Damage to rock tunnels from earthquake shaking, *Journal of the Geotechnical Engineering Division* 104: 175-191.
- EC8 (2004). Eurocode 8: Design of structures for earthquake resistance. European Committee for Standardisation: Brussels, Belgium, The European Standard EN 1998-1.
- Gazetas G., Gerolymos N., Anastasopoulos I. (2005), Response of three Athens metro underground structures in the 1999 Parnitha earthquake, *Soil Dynamics and Earthquake Engineering* 25: 617-633.
- Hashash Y.A., Hook J., Schmidt B., Chiangyao J. (2001), Seismic design and analysis of underground structures, *Tunnelling and Underground Space Technology* 16: 247-293.
- Kappos A., Panagopoulos G., Panagiotopoulos Ch., Penelis G. (2006), A hybrid method for the vulnerability assessment of R/C and URM buildings, *Bulletin of Earthquake Engineering* 4: 391-413.
- Karim K.R., Yamazaki F. (2001), Effect of earthquake ground motions on fragility curves of highway bridge piers based on numerical simulation. *Earthquake Engineering and Structural Dynamics* 30: 1839-1856.
- Moschonas I., Kappos A., Panetsos P., Papadopoulos V., Makarios T., Thanopoulos P. (2009), Seismic fragility curves for Greek bridges: methodology and case studies, *Bulletin of Earthquake Engineering* 7: 439-468.
- NIBS (2004), HAZUS-MH: technical manuals, Federal Emergency Management Agency and National Institute of Building Science, Washington, DC.
- Nielson B.G., DesRoches R. (2007), Seismic fragility methodology for highway bridges using a component level approach, *Earthquake Engineering and Structural Dynamics* 36: 823-839.
- Owen G. N., Scholl R.E. (1981), Earthquake engineering of large underground structures, in report No. FHWA/RD-80/195, Federal Highway Administration and National Science Foundation, 279p.
- Pinto P.E. (Ed.) (2007), Probabilistic methods for seismic assessment of existing structures, LESSLOSS Report No. 2007/06, Istituto Universitario di Studi Superiori di Pavia, IUSS Press.
- Pitilakis K., Tsinidis G. (2010), Seismic design of large, long underground structures: metro and parking stations, highway tunnels, in: *Proceedings of International Geotechnical Conference: Geotechnical Challenges in Megacities (GEOMOS2010)*, Moscow.
- Pitilakis K., Kakderi K. (2011). Seismic risk assessment and management of lifelines, utilities and infrastructures, 4th Japan-Greece Workshop on Seismic Design of Foundations and Innovations in Seismic Protection, October 6-7, Kobe, Japan.
- Plaxis 2D (1998), Reference Manual, version 7.
- Power M., Rosidi D., Kaneshiro J., Gilstrap S., Chiou S.J. (1998). Summary and Evaluation of Procedures for the Seismic Design of Tunnels, Final Report for Task 112-D-5.3(c), MCEER Highway Project, Sponsored by US Department of Transportation, Federal Highway Administration, FHWA Contract Number DTFH61-92-C-00112.

- Salmon M., Wang J., Jones D., Wu Ch. (2003), Fragility formulations for the BART system, in: Proceedings of the 6th U.S. Conference on Lifeline Earthquake Engineering, TCLEE, Long Beach.
- Schnabel P.B., Lysmer J., Seed H.B. (1972), SHAKE: a computer program for earthquake response analysis of horizontally layered sites, Report No. UCB/EERC-72/12, Earthquake Engineering Research Center, University of California, Berkeley, December, 102p.
- Sharma S., Judd W.R. (1991), Underground opening damage from earthquakes, *Engineering Geology* 30: 263-276.
- Shinozuka M. (1995). The Hanshin-Awaji earthquake of January 17, 1995: performance of lifelines, Technical Report NCEER-95-0015.
- Shinozuka M., Feng M.Q., Kim H.-K., Kim S.-H (2000), Nonlinear static procedure for fragility curve development, *Journal of Engineering Mechanics* 126: 1287-1296.
- Wang J.M. (1985), The distribution of earthquake damage to underground facilities during the 1976 Tang-Shan earthquake, *Earthquake Spectra* 1: 741-757.
- Wang J.N. (1993), Seismic design of tunnels. A simple state-of-the-art design approach, Monograph 7. Parsons, Brinckerhoff: Quade & Douglas Inc., New York.

Towards an analytical tool for quantifying vulnerability of simple RC buildings to permanent co-seismic slope deformation

S.D. Fotopoulou, K.D. Pitilakis

Department of Civil Engineering, Aristotle University of Thessaloniki, Greece

ABSTRACT: The present study focuses on the development of an analytical methodology for the evaluation of the vulnerability of low-rise RC structures to earthquake induced landslide displacements. The vulnerability is quantified through specific probabilistic fragility functions for predefined limit states. The fragility curves express the probability of exceeding each limit state as a function of the Peak Horizontal Ground Acceleration (PHGA) at the seismic bedrock, given by the seismic hazard analysis, for all the building typologies considered. The numerical computations are conducted in two separate phases. In the first phase, the differential displacement potential at the building's foundation level is estimated using an adequate non-linear finite difference dynamic slope model. Properly selected and corrected ground motions are applied as dynamic excitation at the base of the model to assess the foundation response and the associated ground displacements are computed accordingly. In order to check the validity of the results of the dynamic analysis, they are compared, in terms of horizontal slope displacements, with Newmark-type displacement approaches. In the second phase, a non-linear fibre-based FEM analysis is performed to assess the building's response for different ground landslide displacements induced by the earthquake. To this end, the calculated differential displacement demand is directly applied as static time history to the building model at the foundation level. Structural limit states are defined in terms of a threshold value of building's material strain. The developed methodology is applied to single bay–single story RC buildings with varying strength and stiffness characteristics of the foundation system (isolated footings, continuous foundation), standing near the crest of a relative slow moving earth slide. Various sources of uncertainty concerning the capacity of the building, the deformation demand and the definition of limit states are considered in the analysis. The derived fragility curves reflect the important differences that may be observed on the performance of the structures to the landslide deformation demand depending on the stiffness of the foundation system.

1 INTRODUCTION

Moderate and strong earthquakes can potentially trigger landslides in mountainous areas that can be devastating for the population and the built environment (Keefer 2002). The impact of earthquakes on the stability of slopes has been investigated by many researchers using methods of different complexity that may vary from the traditional limit-equilibrium (LEM) pseudostatic method and simplified displacement based procedures to advanced stress-strain numerical approaches. Despite the advances made on seismically induced landslide hazards, research on the physical vulnerability of different elements at risk subjected to landslides triggered by earthquakes has been limited and is still on progress. Even advanced frameworks such as HAZUS (NIBS, 2003) multi-hazard loss estimation methodology address the vulnerability estimation of buildings and infrastructures to earthquake induced ground failure due to landslides cautiously.

A major constraint to this appears to be the scarcity of accurate and reliable data on the degree of damage to various elements at risk impacted by different landslide hazards.

In the content of quantitative risk estimation, physical (structural) vulnerability of the exposed elements to landslides comprises a key component that is generally enclosed in the definition of risk [R] through the following formulation (Varnes, 1984):

$$[R] = [H] \times [V] \times [E] \quad (1)$$

Where [H]: hazard, [E]: exposure (global value or cost of elements at risk in a given territorial system).

From a natural-sciences perspective, physical vulnerability may be defined as the degree of loss (expressed on a scale from 0 to 1) to a given element at risk resulting from the occurrence of a specified landslide event of given type and intensity. There is no unique vulnerability value for the exposed elements. Depending on the potential consequences, it should be estimated with respect to the structural properties of exposed elements (e.g. typology, construction quality, foundation type, state of maintenance, use etc) and to the mechanism and magnitude of the landslide processes. The geographic location of the exposed building or infrastructure in relation to the unstable slope (e.g. crest, base etc) is also an additional important contributing factor. Due to the multi-dimensional and multi-parametric nature of the problem and the various uncertainties involved, the introduction of a probabilistic analysis framework is always given that sufficient data are made available.

The present paper aims at the proposition and quantification of an efficient analytical methodology to assess the vulnerability of simple RC buildings due to permanent seismically induced landslide displacements. The methodology results to the construction of fragility curves that describe the probability of exceeding each limit state versus the Peak Horizontal Ground Acceleration (PHGA) at the assumed seismic bedrock. In next sections, we first describe the methodology key components. Then, we provide a numerical application to an idealized case study where the deformation demand due to the earthquake induced landslide hazard and the building response are treated at separate stages. In addition, we assess the reliability of the results of the dynamic analysis through their comparison with Newmark-type displacement methods. Finally, we present the analytical procedure to develop fragility functions that can be used to quantitatively evaluate the structural vulnerability in seismic and landslide risk analysis.

2 METHODOLOGY

A schematic representation of the proposed framework is illustrated in Figure 1. Building classification (foundation and superstructure details) constitutes the capacity of the building. The earthquake demand, the landslide type and the relative location of the building to the potential unstable slope constitute the deformation demand of the building. It is noted that the difference in stiffness between the building's foundation and the surrounding soil can also be a critical factor in accurately determining the deformation demand for the building (e.g. for the case of stiff foundation resting on soft soil material). Structural response data obtained by analyzing the building capacity under the deformation demand is processed by the methodology for fragility curve generation to yield the results. Limit states, which are determined with respect to the building classification, properly selected empirical criteria and expert judgment, are required at this step. The final step of the methodology will result to the construction of the analytical fragility relationships.

The proposed methodology is applicable for the vulnerability assessment of low-rise frame RC buildings impacted by earthquake induced relative slow moving earth slides. It is principally based on a comprehensive set of numerical computations and statistical analysis. In terms of numerical simulation, a two-step uncoupled analysis is conducted. In the first step, we perform a nonlinear Soil-Foundation-Interaction analysis using FLAC2D (Itasca, 2008) finite difference code. A dynamic slope model is constructed and properly selected and corrected ground motions are applied at the base of the model to estimate the differential permanent displacements at the building's foundation level. Then, we assess the building's response for different differential ground landslide displacements induced by earthquake with progressively increased intensities.

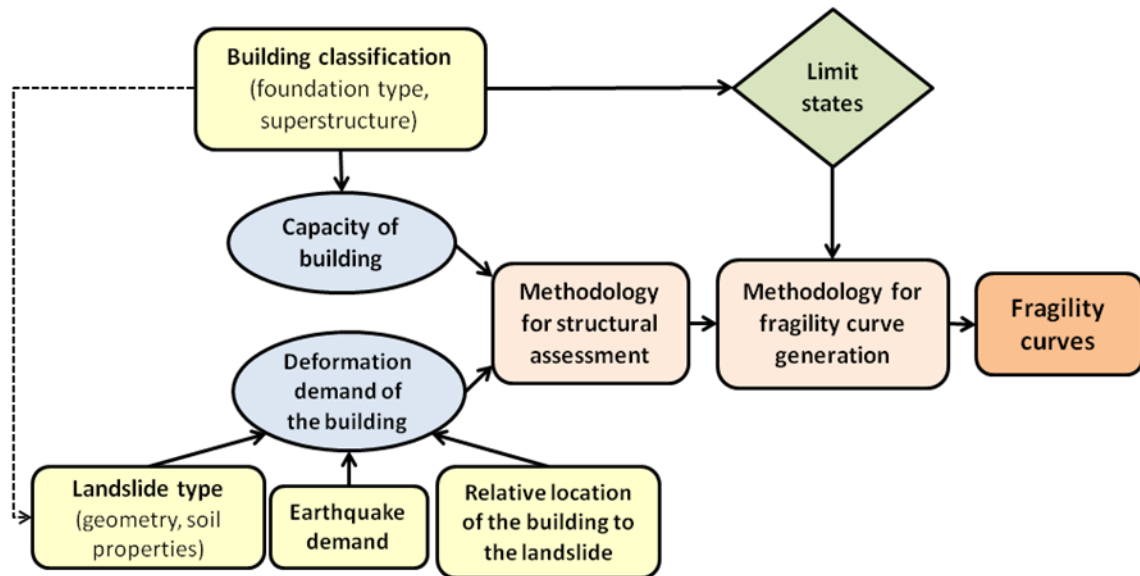


Figure 1 Flowchart for the proposed framework of fragility analysis of RC buildings

To fulfill this task, the previously computed differential displacements are directly applied as input static time histories to the building nonlinear model at the foundation level. The numerical non-linear static analysis of the building is performed through the fibre-based finite element code SEISMOSTRUCT (Seismosoft, Seismostruct, 2010). It 's worth noticing that the complex issue of combined damages on the building by ground shaking and ground failure due to landslide is not taken into account in the evaluation of the building's vulnerability, that is assessed only for the effect of the permanent co-seismic displacement. In other words, no initial damage to the building's structural members (e.g. in terms of stiffness and strength degradation) is assumed to occur due to ground shaking.

The landslide type (rock fall, debris flow, earth slide, etc) is a crucial parameter of the proposed methodology as landslides of different types and sizes usually require different and complementary methods to estimate vulnerability. The damage caused by a slow moving landslide on a building is mainly attributed to the cumulative permanent (absolute or differential) displacement and it is concentrated within the unstable area. A relative slow moving earth slide that will produce tension cracks due to differential displacement to a RC building, exposed to the landslide hazard, is considered in this study.

The characteristics (amplitude, frequency content and duration) of the earthquake ground motion in relation to the soil dynamic properties and stratigraphy can significantly influence the derived deformation demand for the building. Material damping, the impedance contrast between sediments and the underlying bedrock, and the characteristics of incident wavefield are considered to represent the governing factors for site amplification/attenuation (Kramer and Stewart, 2004; Pitilakis 2010). A fundamental period of the earthquake close to the natural period of the site can lead to resonance phenomena and, consequently, to an amplified energy content of the ground motion. Combining a low-frequency seismic input motion together with a resonance phenomenon in the low-frequency range, the slope failure potential assumes its highest values (Bourdeau et al., 2008).

The position of the building with respect to the landslide area is a very important contributing factor in estimating vulnerability. In large landslides, there are sensitive areas where damage in terms of total displacement or released energy will be more likely (or much higher). This occurs, for instance, in the landslide boundaries, such as the head or lateral sides, or at local scarps where tensile stresses develop with the result of cracks, surface ground depletion and local rotation (Fell et al., 2008). In contrast to landslides triggered by intense precipitation that are generally uniformly distributed along the slopes, landslides triggered by earthquakes tend to be clustered near ridge crests and hill slope toes. Peng et al. (2009) attributed this ridge-crest clustering

to topographic effects, and the clustering at hill slope toes to dynamic pore-pressure changes in the water-saturated material of lower hill slopes. Topographic effects may alter the amplitude and frequency content of the ground motions along slopes (Bouckovalas and Papadimitriou, 2005; Ktenidou 2010). Moreover, the effect of soil-structure interaction due to the presence of a structure at the cliff can further modify the seismic response at the topographic irregularity, depending on the soil-structure impedance contrast (Assimaki et al., 2007). In the current study, RC buildings of different stiffness characteristics standing near the slope's crest where the seismic ground motion due to topographic effects is generally amplified are considered.

For a landslide of given type, mechanism and intensity, the typology of the exposed structure is also a key factor in the vulnerability assessment methodology. Geometry, material properties, state of maintenance, code design level, soil conditions, foundation and structure details, number of floors etc. are among typical typological parameters which determine the capacity of the building to withstand the specified co-seismic landslide displacement. The response to permanent total and differential ground deformation depends primarily on the foundation type. A structure on a deep foundation (e.g. piles) compared to shallow foundations often experiences higher resistance ability and hence a lower vulnerability. For shallow foundations (figure 2), the distinction is between rigid or flexible/unrestrained foundation systems. It is important to notice that the stiffness of the foundation should be regarded in relation to the stiffness of the underlying soil. When the foundation system is rigid (e.g. continuous raft foundation), the building is expected rather to rotate as a rigid body and a failure mainly attributed to the loss of functionality of the structure is anticipated. In this case, the damage states are defined empirically, as there is limited structural demand to the members of the building (apart from possible P- Δ effects at larger rotations). On the contrary, when there is sufficient flexibility in the foundations allowing for the walls or columns to move independently with respect to each other (e.g. isolated footings), the various modes of differential deformation produce structural damage (e.g. cracks) to the building members (Bird et al. 2005, 2006). An analytical procedure analogous to that of the response due to seismic ground motion is possible in this case.

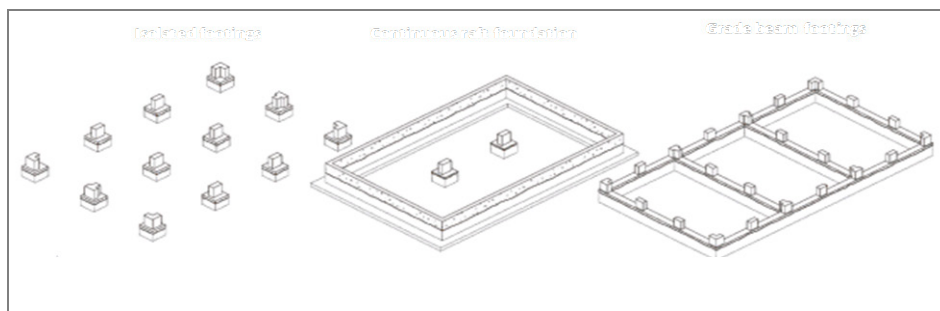


Figure 2. Typical shallow foundation systems - Types and layout

When building response to ground failure comprises structural damage, damage states can be classified using the same schemes used for structural damage caused by ground shaking. Limit states are defined in terms of limit value of a component's strain based, based on the work of Crowley et al. (2004), Bird et al. (2005), Negulescu and Foerster (2010) and engineering judgment. Different limit strains are adopted for "low" and "high" code designed structures.

The fragility curves are numerically estimated in terms of peak horizontal ground acceleration at the "seismic bedrock", (PHGA) versus the probability of exceedance of each limit state considering various sources of uncertainty. The selection of the PHGA against the differential displacements value is a key point of the present method and it is explicitly related to the main parameter of any seismic hazard assessment. In that way the soil and topographic amplification is directly included in the analysis.

In the probabilistic approach proposed herein, several uncertainties are involved concerning the capacity of the building, the definition of the limit states and the deformation demand (differential permanent displacement). The uncertainty in the displacement capacity is a function of the material properties, geometric properties, and the yield strain of steel and post-yield strain capacities of the steel and concrete. The uncertainty in the demand includes all of the variability

associated with the ground motion estimation plus additional uncertainties associated with the landslide type and size, the relative position of the building to the landslide area, the variability in soil parameters and stratigraphy and the uncertainty within the assessment of ground deformations.

3 APPLICATION

3.1 Deformation demand of the building

An application of the methodology described in the previous section to an idealized case study is presented herein. In order to establish correlation between the earthquake demand and the permanent differential displacements (deformation demand) for the building, dynamic non-linear analyses are performed using the explicit finite difference code FLAC 2D 6.0 (Itasca, 2008). The soil materials are modeled using an elastoplastic constitutive model with the Mohr-Coulomb failure criterion with tension cutoff, assuming a zero dilatancy non-associated flow rule for shear failure and an associated rule for tension failure. A small amount of mass and stiffness -proportional Rayleigh damping (1 to 3%) is also assigned to compensate for the energy dissipation during the elastic part of the response and during wave propagation through the site. The center frequency of the installed Rayleigh damping is selected to lie between the fundamental frequencies of the input acceleration time histories and the natural modes of the system. The soil type is selected to represent dry, medium dense sand corresponding to soil category C of EC8 (CEN-European Committee for Standardization, 2003); its material, physical and dynamic properties are provided in Table 1.

Table 1. Soil properties

Properties	Soil C
Constitutive model	Mohr Coulomb
Dry density (KN/m ³)	18
Vs (m/sec)	250
Poisson's ratio	0.3
Cohesion (KPa)	0
Friction angle (degrees)	36
N ₁₍₆₀₎	21
Dr(%)	60

Table 2. Foundation properties

Properties	Foundation system	
	Stiff foundation	Flexible foundation
Element	beam	
Length (m)	6	
Density (KN/m ³)	24	
Young's modulus (KPa)	2.90E+7	
Moment of inertia I (m ³)	0.0053	
Area (A) (m ²)	0.4	
Load (KN/m)	Uniform distributed q=25KN/m ²	Concentrated load P=50KN/m

The 2D dynamic slope model, schematically illustrated in Figure 3, has a total length of 300m and the elevations of ground surface vary from 80 to 100 m. The slope height and inclination are taken as 20m and 30° respectively. The model is discretized to allow for a maximum frequency of at least 10Hz to propagate through the grid without distortion. A finer discretization is adopted in the slope area, whereas towards the lateral boundaries of the model, where the accuracy requirements loosen, the mesh is coarser. Free field absorbing boundaries (Cundall et al. 1980) are applied along the lateral boundaries while quiet (viscous) boundaries (Lysmer and

Kuhlemeyer, 1969) are applied along the bottom of the dynamic model to minimize the affect of artificially reflected waves. In order to apply quiet boundary conditions along the same boundary as the dynamic input, the seismic motions must be input as stress loads combining with the quiet (absorbing) boundary condition.

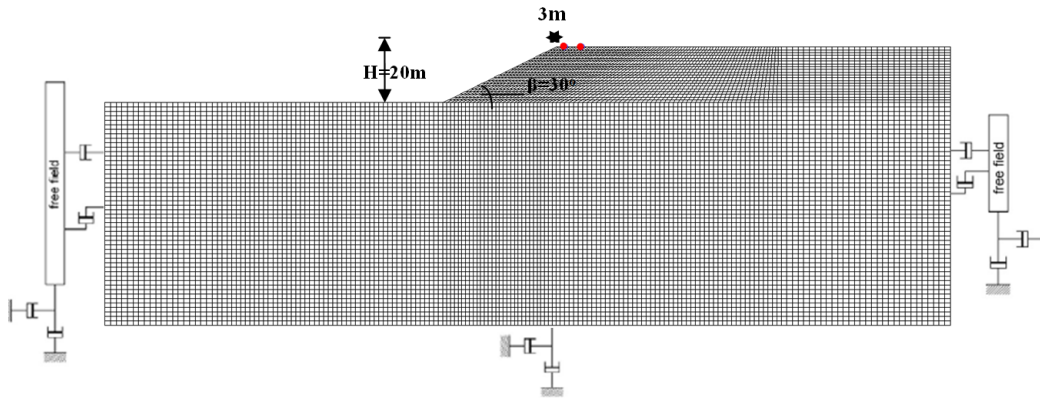


Figure 3. FLAC dynamic model

A building is assumed to be located 3m from the slope crest. At this stage, the building is modeled only by its foundation with a width of 6m (uncoupled approach). Two different shallow foundation systems are considered (Table 2): isolated footings and a uniform loaded continuous slab foundation. In the first case, the foundation is simulated with concentrated loads at the footings' links. As a consequence, no relative slip and/or separation between foundation and subsoil are permitted. In the second case, the foundation system is modeled as a deformable elastic beam connected to the grid through appropriate interface elements that can approximate the potential Coulomb sliding and/or tensile separation of the beam.

Prior to the dynamic simulations, a static analysis is carried out to establish the initial effective stress field throughout the model. The dynamic input motion consists of SV waves vertically propagating from the base. Six different earthquake records are used as excitation for the dynamic analysis: (i) Valnerina (Cascia-L), Italy, $M_s=5.8$, 1979, (ii) Athens (Kypseli-L), Greece, $M_w=5.9$, 1999, (iii) Montenegro-[TRA (EW)], former Yugoslavia, $M_w=6.9$, 1979 and (iv) Northridge (Pacoima Dam -L), USA, $M_s=6.7$, 1994, (v) Campano Lucano (Sturmo-L), Italy, $M_w=6.9$, 1980 and (vi) Duzce (L), Turkey, $M_w=7.2$, 1999. They all refer to outcrop conditions. The records are selected to cover a range of seismic motions in terms of the seismotectonic environment, amplitude, frequency content and significant duration. Before applied along the base of the model, they are subjected to appropriate correction (baseline correction and filtering) to assure an accurate representation of wave transmission through the model. Note that due the compliant base considered the appropriate input excitations to FLAC model correspond to the upward propagating wave train that is taken as one-half the outcrop motion (Mejia and Dawson, 2006). Figure 4 presents the normalized elastic response spectra of the input motions together with the proposed elastic design spectrum of EC8 (CEN-European Committee for Standardization, 2003) for soil type A (rock).

The input accelerograms are scaled to five levels of peak ground acceleration, namely $PHGA=0.1, 0.3, 0.5, 0.7$ and $0.9g$, so as to assess the building response for different displacement magnitudes. This procedure will allow resulting in different damage states for the building and finally to be able to construct the corresponding fragility curves. Figure 5 presents the maximum computed values of permanent ground displacement at the slope area in relation to the corresponding differential displacements at the foundation level for the different assumed building's foundation configurations. A strong, positive linear correlation between the two variables is detected. Thus, differential deformation can be easily determined by the residual maximum slope displacement using an appropriate linear relationship. Figure 6 depicts the maximum values of differential displacements for the building with flexible and stiff foundation system de

rived from the dynamic analysis by applying the different scaled accelerograms. It is observed that the specific characteristics (frequency content and duration) of the seismic ground motions can significantly influence the magnitude of the computed differential displacement at the foundation level. Moreover, it is worth pointing out that when the soil structure interaction is considered, the differential horizontal displacements at the beam foundation are practically zero and the total differential displacement vector for the building is generally decreased.

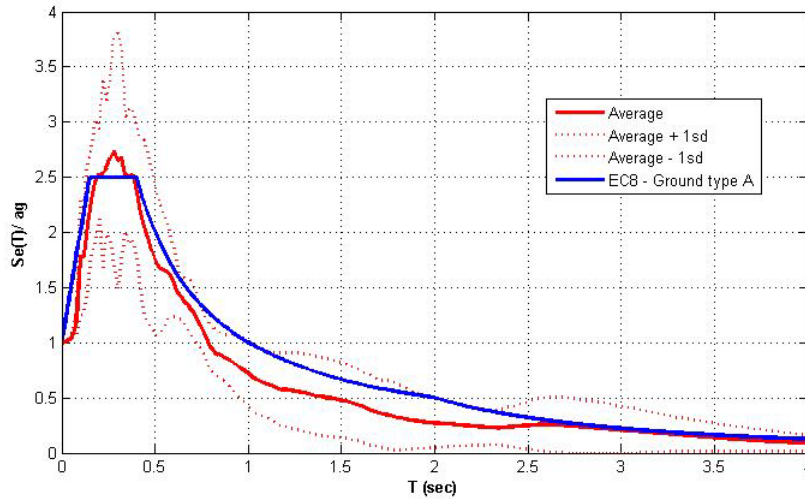


Figure 4. Normalized average elastic response spectrum of the input motions in comparison with the corresponding elastic design spectrum for soil type A (rock) according to EC8.

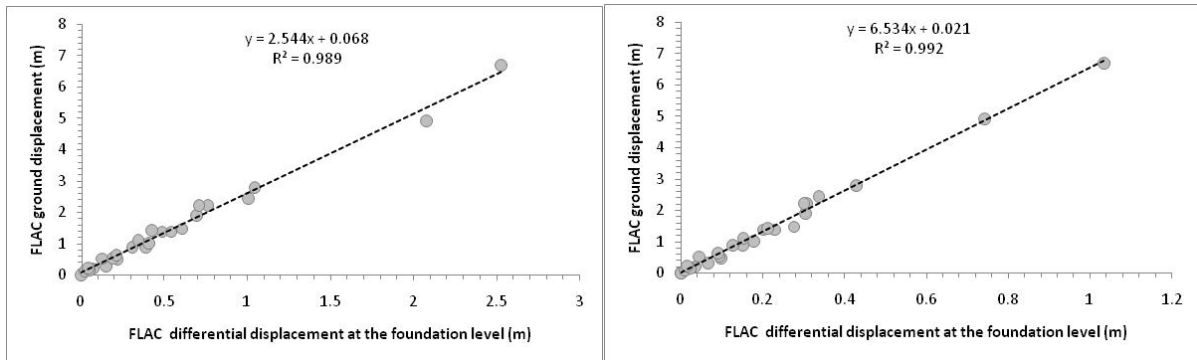


Figure 5. Regression of differential displacement vector for buildings with flexible (left) and stiff (right) foundation system on the maximum computed permanent ground displacement

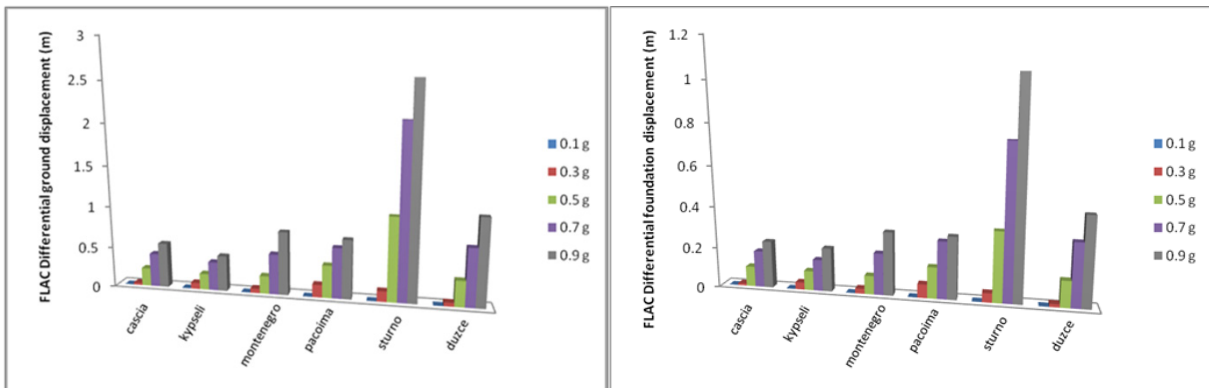


Figure 6. Maximum values of differential displacement vector for buildings with flexible (left) and stiff foundation system (right).

3.1.1 Comparison with Newmark-type displacement methods

To validate FLAC numerical results, they are compared, in terms of maximum permanent horizontal displacement, with the Newmark-type displacement methods. The conventional analytical Newmark rigid block model (Newmark, 1965) and a simplified coupled stick-slip deformable sliding block model (Bray and Travasarou, 2007), are used to calculate permanent displacements of the slide mass.

Newmark's method treats the potential landslide block as a rigid mass (no internal deformation) that slides in a perfectly plastic manner on an inclined plane. The block is assumed to have a known yield or critical acceleration, k_y , which comprises the threshold base acceleration required to overcome the shear resistance of the slope and initiate failure. The cumulative permanent slope displacement has been obtained by double integration of the surface outcropping accelerograms. The freeware software by Jibson and Jibson (2003) was used for that calculation.

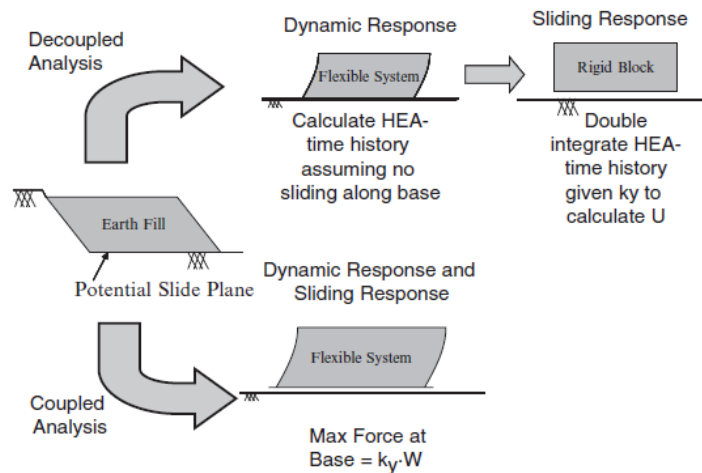


Figure 7. Decoupled dynamic response/rigid sliding block analysis and fully coupled analysis (Bray 2007).

The dynamic site response and the sliding block displacements are computed separately in the 'decoupled' approach or simultaneously in the 'coupled' stick-slip analysis (Figure 7). A 'coupled' stick-slip analysis offers a more 'realistic' representation of the physical mechanism of earthquake-induced deformation over the rigid-block and two-step decoupled approaches. Bray and Travasarou (2007) developed a simplified seismic displacement procedure based on a one-dimensional multi-degree of freedom non-linear coupled stick-slip model (Rathje and Bray 2000) to represent the behavior of an idealized sliding mass. The method captures the primary influence of the system's yield coefficient (k_y), its initial fundamental period (T_s), and the ground motion's spectral acceleration at a degraded period equal to $1.5T_s$. The initial fundamental period of the sliding mass (T_s) has been estimated using the simplified expression: $T_s = 4H/V_s$, where H is the average height and V_s is the average shear wave velocity of the potential sliding mass. For the purpose of this study, the parameter $S_a(1.5T_s)$ was obtained from the rock outcrop scaled response spectra.

The horizontal yield coefficient, k_y , has been computed for both methods via a pseudostatic slope stability analysis using Spencer method of slides (Spencer 1967) that satisfied full equilibrium.

The results of the above methods are summarized in Figures 8 and 9 in comparison with the co-seismic numerical displacements calculated herein. The direct application of Newmark rigid block approach is found to underestimate the computed displacements. This can be regarded as relevant considering that the method is based on the inherent assumption that the slide mass behaves as a non-compliant rigid block. The results of fully coupled stick-slip deformable sliding block model introduced by Bray and Travasarou (2007) are generally in good agreement with that of the dynamic analysis. However, in both methods a large scatter on the predicted residual

displacements is detected recognizing the need to adopt a fully probabilistic framework, as proposed in Bray and Travararou (2007).

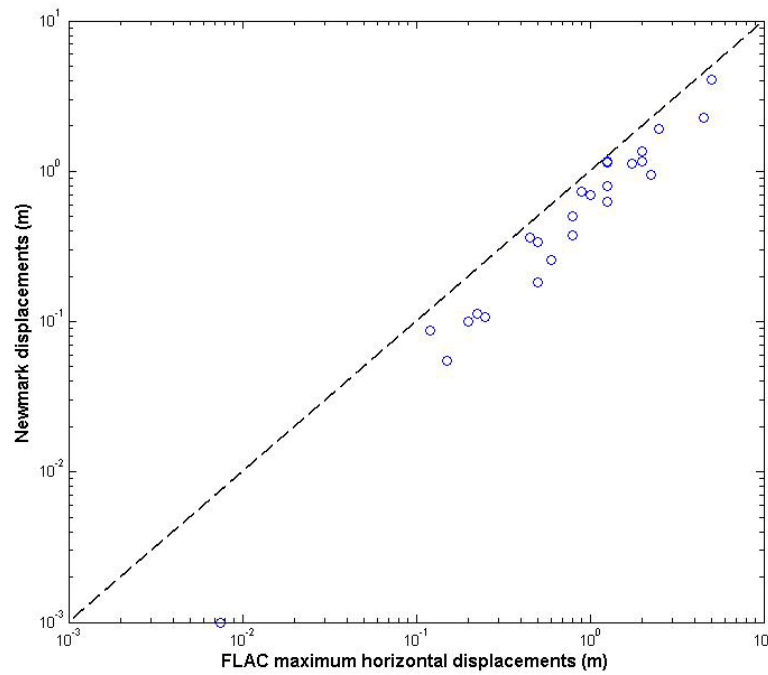


Figure 8. Comparison between Newmark with maximum horizontal displacement from 2D dynamic analyses.

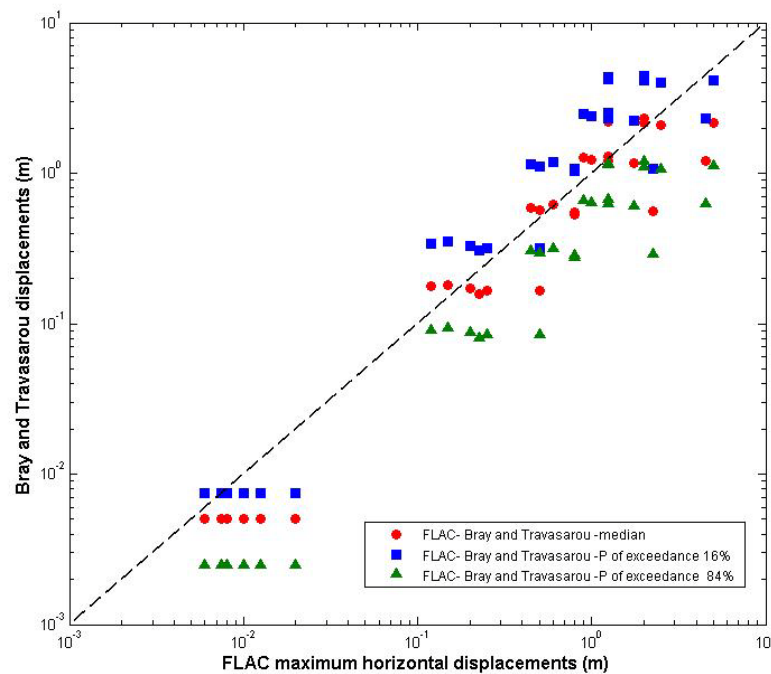


Figure 9. Comparison between Bray and Travararou (2007) displacements with maximum horizontal displacement from 2D dynamic analyses.

3.2 Analysis of the building's response

The analyses of the building is conducted using the finite element code SeismoStruct (Seismosoft, 2010), which is capable of calculating the large displacement behavior of space frames under static or dynamic loading, taking into account both geometric nonlinearities and material inelasticity. Both local (beam-column effect) and global (large displacements/rotations effects) sources of geometric nonlinearity are automatically taken into account. Distributed inelasticity elements are used based on the so-called fibre approach to represent the cross-section behaviour, where each fibre is associated with a uniaxial stress-strain relationship. The sectional stress-strain state of beam-column elements is then obtained through the numerical integration of the nonlinear uniaxial stress-strain response of the individual fibres (typically 300-400) in which the section has been subdivided. For an employment of a displacement-based (DB) finite element formulation with the use of nonlinear models, structural elements should be subdivided into a number of segments (typically 4 to 5) and the delimiting sections follow the Navier-Bernoulli approximation (plane sections remain plane). For the present analysis, the frame sections have been discretized into 300 fibres and the structural members, into 4 elements. Nonlinear static time-history analyses are performed for all numerical simulations. In particular, the differential permanent (ground or foundation) displacement (versus time) curves, directly extracted from the FLAC dynamic analysis, are statically imposed at one of the RC frame supports.

The studied buildings are single bay-single storey RC bare frame structures RC frame that vary in their foundation system: buildings with flexible foundation system (isolated footings) and buildings with stiff but not completely rigid foundation system (continuous uniform loaded foundation of finite stiffness characteristics). The beneficial contribution of masonry infill walls to the building capacity is not considered in this study. The building's height and length are 3m and 6m respectively. Columns and beams have rectangular cross sections (beam: 0.30x 0.50 m, column: 0.40x 0.40m). The structures have been designed according to the provisions of the Greek Seismic Code (EAK 2000), for a design acceleration $Ad = 0.36 g$, and a behavior factor $q = 3.5$. The adopted dead and live loads ($g = 1.3 \text{ kN/m}^2$ and $q = 2 \text{ kN/m}^2$) are typical values for residential buildings. The longitudinal section reinforcement degree used is 1% for the columns and 0.75% for the beams.

The use of single bay-single storey structures is justified from the observation that the number of storey and bays do not seem to comprise crucial parameters in the determination of the building's performance subjected to permanent ground displacements. The latter is also discussed in Bird et al. (2005) and Negulescu and Foerster (2010) for the vulnerability assessment of RC buildings due to differential settlements. Hence, one bay-one storey RC structures despite their simplicity are found to be adequately representative of the performance of real low-rise RC frame buildings.

The material properties assumed for the members of the reference RC buildings are described below. A uni-axial nonlinear constant confinement model (Fig. 10 (a)) is used for the concrete material ($f_c=20\text{MPa}$, $f_t=2.1\text{MPa}$, strain at peak stress 0.002mm/mm , confinement factor =1 for unconfined and 1.2 for confined concrete, specific weight= 24KN/m^3), assuming a constant confining pressure throughout the entire stress-strain range (Mander et al. 1988). For the reinforcement, a uni-axial bilinear stress-strain model with kinematic strain hardening (Fig. 10(b)) is utilized ($f_y=400\text{MPa}$, $E=200\text{GPa}$, strain hardening parameter $\mu = 0.005$, specific weight= 78KN/m^3). This simple model is characterized by easily identifiable calibrating parameters and by its computational efficiency.

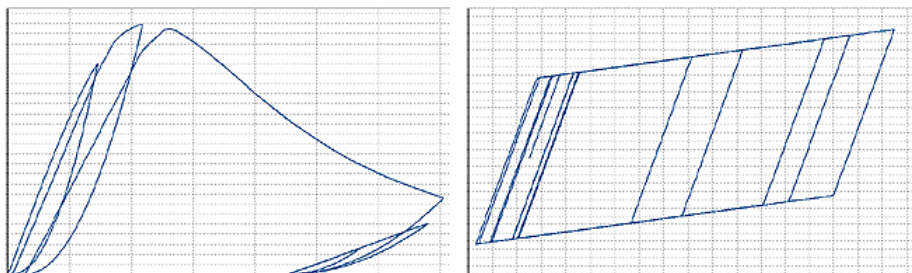


Figure 10. Stress-strain models for concrete (left) and steel (right) material

A sensitivity analysis is performed for the reference building cases which allows for identifying the influence of different parameters on the structural response and proposing a preliminary probabilistic framework of the damage estimation. The parameters selected to vary are: the yield strength of steel ($f_y=210, 400, 500$ MPa), the compressive ($f_c=16, 20, 30$ MPa) and tensile ($f_t=2.0, 2.1, 3.0$ MPa) strength of concrete, the reinforcement ratio ($\rho=0.8\%, 1\%, 1.2\%$ for columns and $\rho=0.55\%, 0.75\%, 0.95\%$ for beams) and the confinement factor (1.0, 1.2, 1.3) for progressively increasing levels of differential displacements extracted from the previous dynamic stress strain analysis for increasing level of input acceleration time histories. The yield strength of steel material (for $f_y=210$ MPa) is proved to be the most influential factor for both buildings with stiff and flexible foundations. Moreover, the deformed shapes of buildings with flexible foundation system are found to be essentially the same irrespective of the variability in the strength parameters and the level of demand, observation that is in accordance with that of Bird et al. (2005). The same trend is observed to the buildings with stiff foundation (Fig. 11). In both building typologies, a column failure mechanism is detected. The reason is that the axial stiffness of the beams is generally much higher compared to the flexural stiffness of the columns. Moreover, in the case of buildings with flexible foundations, the applied differential displacement vector is mainly governed by the horizontal component that determines the deformation mode (Fig. 11(a)). On the contrary, in buildings with stiff foundation system the applied displacements are practically vertical (Fig. 11(b)). Hence, it is concluded that the inclination of the applied differential permanent displacement constitutes a fundamental parameter in determining the deformed shape of the building when subjected to a permanent displacement at the foundation level.

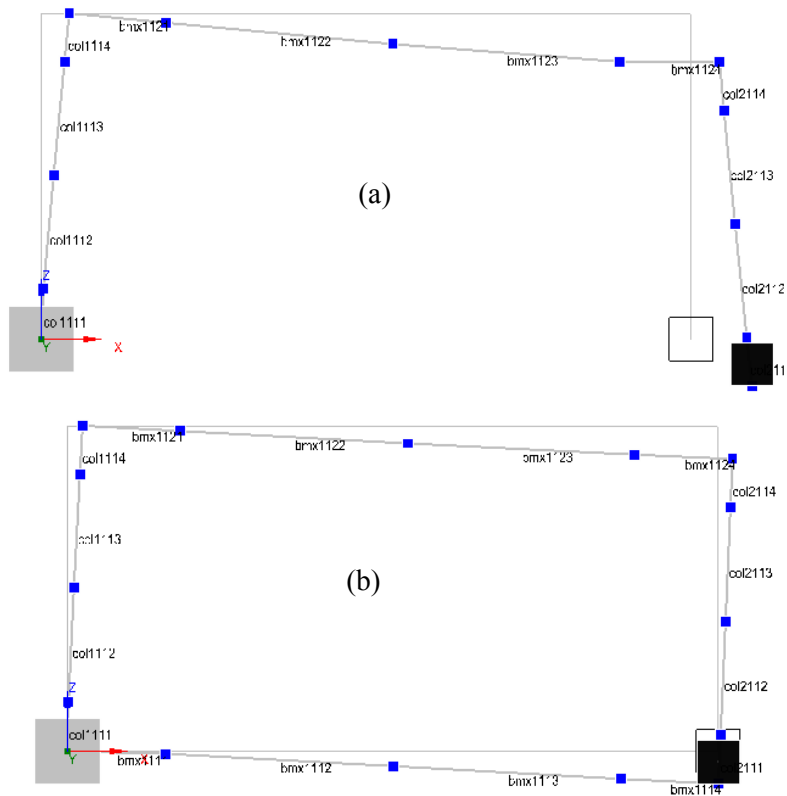


Figure 11. Deformed shapes for buildings with flexible (a) and stiff (b) foundations

3.3 Fragility analysis

We derived in this stage different sets of analytical fragility curves for low-rise (single bay-single storey) RC buildings with varying stiffness of the foundation system. Each curve provides the conditional probability of exceeding a certain limit or damage state under a range of seismic induced landslide events of given type and intensity. The landslide intensity is expressed in this work in terms of peak horizontal ground acceleration (PHGA) at the seismic bedrock that is the initial trigger of the slow moving slide. This will result to permanent differential displacements at the foundation level.

In order to identify the building performance (damage) state and to construct the corresponding fragility curves, a damage index (DI) is introduced describing the steel and concrete material strains. Within the context of a fibre-based modelling approach, such as that implemented in SeismoStruct, material strains do usually constitute the best parameter for identification of the performance state of a given structure (Seismosoft, 2010). In all cases analyzed (600 in total), the steel material strain (ϵ_s) yields more critical results. Thus, it was decided to adopt only this parameter as a damage index hereafter for simplicity reasons. In this way, it is possible to establish a relationship between the damage index (ϵ_s) and the input motion intensity in terms of the PHGA values at the assumed seismic bedrock, for the different building typologies and consequently to assign a median value of PHGA to each limit state. Figure 12 presents PHGA - damage index relationships for low-rise, “high code” designed RC frame buildings with stiff and flexible foundation system.

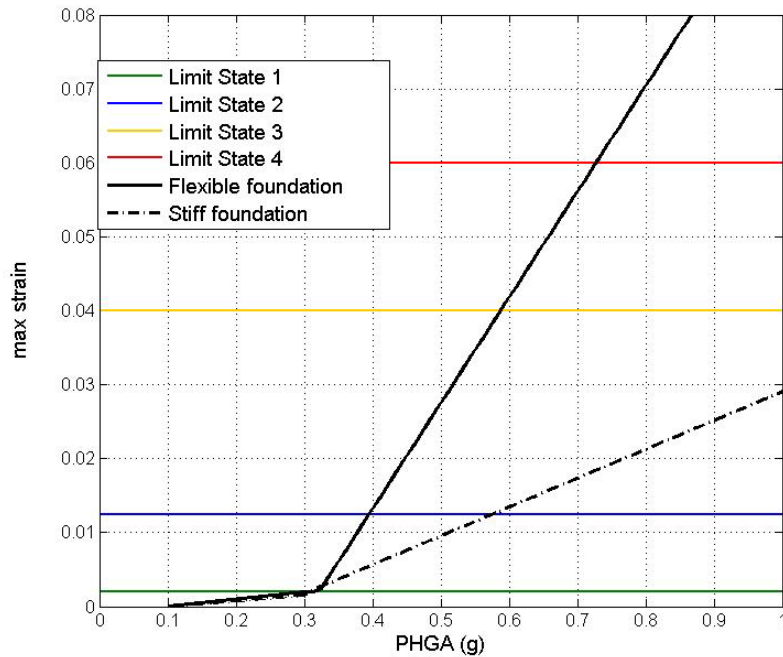


Figure 12. PHGA–damage index relationships for 1story-1story RC frame buildings with stiff and flexible foundation system

The next step is the definition of the damage or limit states. Based on the work of Crowley et al. (2004), Bird et al. (2005, 2006) and engineering judgment, 4 limit states (LS₁, LS₂, LS₃, LS₄) are employed. Considering that low code RC buildings are poorly constructed structures characterized by a low level of confinement, the limit steel strains needed to exceed post yield limit states should have lower values compared to high code, properly constructed RC buildings. As a consequence, we decided to adopt different limit state values for exceedance of extensive and complete damage for low and high code frame RC buildings. A qualitative description of each damage band for reinforced concrete frames is given in Table 3 while the limit state values finally adopted in quantitative terms are presented in Table 4. These concern exceedance of mi-

nor, moderate, extensive and complete damage of the building. The first limit state is specified as steel bar yielding that is the ratio between yield strength and modulus of elasticity of the steel material.

Table 3. Structural damage state descriptions for RC frame buildings (Crowley et al. 2004)

Structural damage band	Description
None to slight	Linear elastic response, flexural or shear type hairline cracks (<1.0 mm) in some members, no yielding in any critical section
Moderate	Member flexural strengths achieved, limited ductility developed, crack widths reach 1.0 mm, initiation of concrete spalling
Extensive	Significant repair required to building, wide flexural or shear cracks, buckling of longitudinal reinforcement may occur
Complete	Repair of building not feasible either physically or economically, demolition after earthquake required, could be due to shear failure of vertical elements or excessive displacement

Table 4. Definition of Limit states for “low” and “high” code design RC buildings

Limit state	Steel strain (ϵ_s) –low code	Steel strain (ϵ_s) –high code
Limit State 1	Steel bar yielding	Steel bar yielding
Limit State 2	0.0125	0.0125
Limit State 3	0.025	0.04
Limit State 4	0.045	0.06

In order to construct the fragility relationships, appropriate cumulative distribution functions, as the ones proposed in HAZUS (NIBS, 2004), that describe the fragility relationships have been generated. For structural damage, given peak horizontal ground acceleration PHGA, the probability of exceeding a given limit state, SL_i, is modeled as:

$$f(PHGA) = \Phi \left[\frac{1}{\beta_i} \ln \left(\frac{PHGA}{PHGA_i} \right) \right] \quad (1)$$

Where:

$\Phi[\cdot]$ is the standard normal cumulative distribution function,

$PHGA_i$ is the median value of peak ground acceleration at which the building reaches the limit state, i,

β_i is the standard deviation of the natural logarithm of peak ground acceleration for limit state, i.

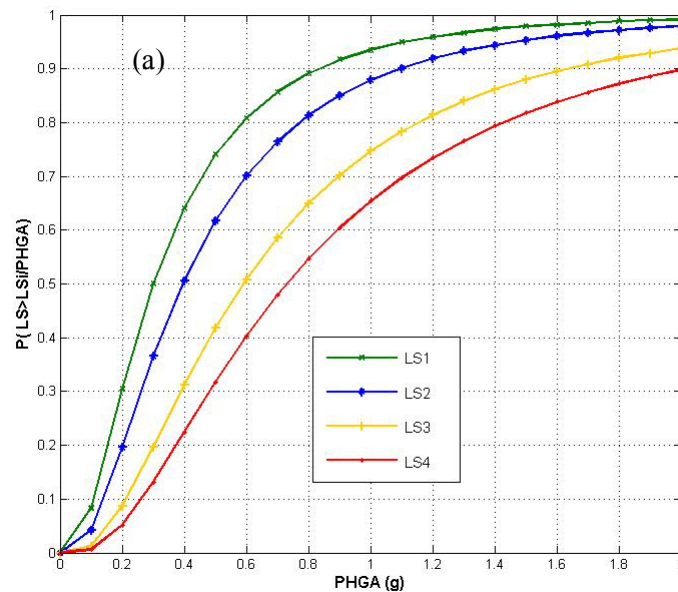
The median values of peak horizontal ground acceleration that correspond to each limit state can be defined for the threshold values of the aforementioned damage indexes as the values that corresponds to the 50% probability of exceeding each limit state. The standard deviation values (β) describe the total variability associated with each fragility curve. Three primary sources contribute to the total variability for any given damage state (NIBS, 2004), namely the variability

associated with the definition of the limit state threshold values, the capacity of each structural type and the landslide demand. Based on the work of Crowley et al (2004), Bird et al (2006) and HAZUS (NIBS, 2004) prescriptions, the uncertainty in the definition of limit state threshold values, for all building types and limit states, is assumed to be equal to 0.4 while the variability of the capacity is assumed to be $\beta = 0.3$ for “low code” and $\beta = 0.25$ for “high code” buildings. The last source of uncertainty associated with the demand, is taken into consideration through a convolution procedure, i.e., by calculating the variability in the results of numerical simulation (in terms of maximum steel strain) carried out in Seismostruct for the computed differential displacement time histories. It should be mentioned that this variability is different for the two different building types. In particular, it is higher in the case of the buildings with flexible foundation system. The total uncertainty is estimated as the root of the sum of the squares of the component dispersions. The median (expressed in terms of peak horizontal ground acceleration PHGA) and beta values of each limit state for buildings with flexible and stiff foundation system are shown in Table 5.

Table 5. Parameters of fragility functions

Foundation type	Median PHGA (g)				Dispersion β_i
	LS ₁ (g)	LS ₂ (g)	LS ₃ (g)	LS ₄ (g)	
Flexible	0.30	0.395	0.59	0.73	0.80
Stiff	0.31	0.575	>0.9	>0.9	0.74

Figure 13 illustrates the derived sets of fragility curves for the two building typologies. High code designed RC structures are considered in this study. Similar fragility relationships that are generally associated with a more rapid transition from low levels of damage to collapse could also be constructed for low code structures. As expected, the building with stiff foundation system would sustain less damage due to earthquake induced slow moving slides compared to the building with the flexible foundation system. More specifically, only minor and moderate damages are possible for the former for the specified levels of deformation.



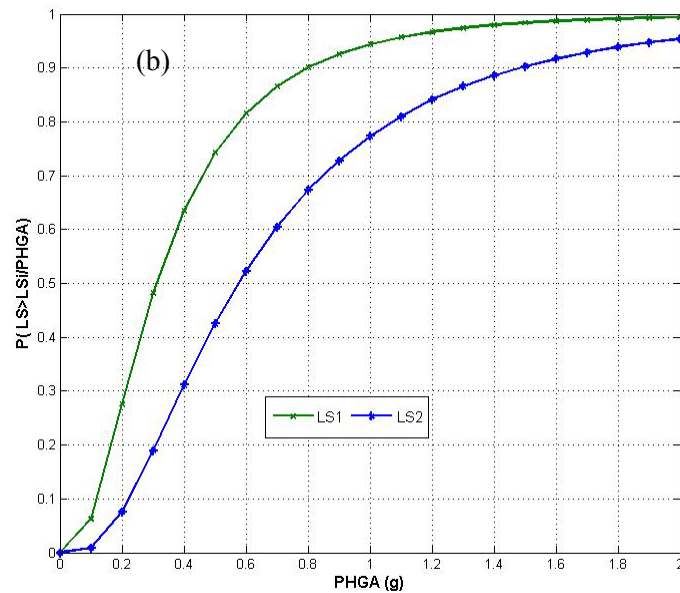


Figure 13. Fragility curves for one bay- one storey RC buildings with flexible (a) and stiff (b) foundation system

It should be noticed that only the structural damage of the building members is considered in this research. The total damage (structural and non-structural) will be quite different (certainly larger) in case of the building with the stiff foundation as a considerable amount of damage may be attributed to the rotation of the whole building as a rigid body. In the latter, the damage can only be defined using empirical criteria and expert opinion (Bird et al, 2005). Furthermore, it is worth pointing out that the complex issue of combined ground shaking and ground failure due to landslide is not taken into account in the evaluation of the building's vulnerability. Thus, no strength or stiffness degradation to the building's structural members due to the effect of ground shaking is assumed to occur.

The reliability and accuracy of the proposed methodology has been assessed by its application to a reference RC building located near the crown of the Kato Achaia slope where most of the structural damage was concentrated in consequence of the Iliia-Achaia, Greece 2008 (Mw=6.4) earthquake (Fotopoulou et al. 2011). Both the structure and slope configuration were realistically reproduced using non-linear constitutive models to prove the validity of the developed methodological framework. The proposed curves were found to adequately capture the performance of the representative RC building affected by the slope co-seismic landslide differential displacement.

4 CONCLUSIONS

An analytical methodology to assess physical vulnerability of RC buildings subjected to earthquake induced slow moving earth slides has been presented. The procedure results to the construction of fragility relationships for RC buildings via numerical simulations and statistical analysis concerning different soil types, slopes geometries, the relative location to the landslide mass and the specific characteristics of the structure (including both foundation and superstructure details). In the present study, the proposed approach has been implemented to low-rise RC frame buildings that differ in the foundation system (isolated footing and continuous foundation). Various uncertainties, related to the capacity of the building, the deformation demand and the definition of limit states have been incorporated in the analysis in a cost effective manner. It is observed that RC buildings with stiff foundation system would sustain less structural damage compared to buildings with flexible foundations.

It is noteworthy that the derived fragility curves pertain to a reference structure with a specific combination of geometry, material properties and limit states. An extensive parametric study considering various building typologies, slope configurations and soil properties should be car-

ried out in order to derive generic fragility functions to be included in the evaluation of the seismic risk and the design of appropriate mitigation measures at building or aggregate scale. Such analysis is currently underway. Further validation of the fragility curves with well documented case histories is desirable to enhance their effective implementation within a probabilistic risk assessment study.

5 ACKNOWLEDGEMENTS

The work described in this paper was supported by the project SafeLand “Living with landslide risk in Europe: Assessment, effects of global change, and risk management strategies” under Grant Agreement No. 226479 in the 7th Framework Program of the European Commission. This support is gratefully acknowledged.

6 REFERENCES

- Assimaki, D. and Kausel, E. (2007). “Modified Topographic Amplification Factors for a Single-Faced Slope due to Kinematic Soil-Structure Interaction”, *Journal of Geotechnical and Geoenvironmental Engineering*, 133, 1414–1431.
- Bird, J. F., Crowley, H., Pinho, R., and Bommer, J. J. (2005). “Assessment of building response to liquefaction induced differential ground deformation”. *Bulletin of the New Zealand Society for Earthquake Engineering*, 38(4), 215-234, 2005.
- Bird, J. F., Bommer, J. J., Crowley, H., and Pinho, R. (2006). “Modelling liquefaction-induced building damage in earthquake loss estimation”, *Soil Dynamics and Earthquake Engineering* 26(1), 15-30.
- Bouckovalas, G.D. and Papadimitriou, A.G. (2005). “Numerical evaluation of slope topography effects on seismic ground motion”. *Soil Dynamics and Earthquake Engineering*, 25, 547-558.
- Bourdeau, C., Havenith, H. B., Fleurisson, J. A., and Grandjean, A. G. (2004). “Numerical Modelling of Seismic Slope Stability”, *Engineering Geology for Infrastructure Planning in Europe*, Springer Berlin / Heidelberg, 104, 671-684, 2004.
- Bray, J. D. and Travasarou, T. (2007). “Simplified Procedure for Estimating Earthquake-Induced Deviatoric Slope Displacements”. *Journal of Geotechnical and Geoenvironmental Engineering*, 133(4), 381-392, 2007.
- Bray, J.D., (2007). “Simplified seismic slope displacement procedures”. *Earthquake Geotechnical Engineering*. Ed. K. D. Pitilakis, 2007 Springer.
- CEN-European Committee for Standardization: prENV 1998-1 – Eurocode 8: Design of structures for earthquake resistance. Part 1: General rules, seismic actions and rules for buildings, Draft No. 4, Brussels, Belgium, 2003.
- Crowley, H., Pinho, R., and Bommer, J. J. (2004). “A probabilistic displacement-based vulnerability assessment procedure for earthquake loss estimation”. *Bulletin of Earthquake Engineering*, 2(2), 173-219.
- Cundall, P. A., Hansteen, H., Lacasse S., and Selnes, P. B. (2000). NESSI – soil structure interaction programme for dynamic and static problems. Report 51508-9, December, Norwegian Geotechnical Institute.
- EAK (2000). Greek Seismic Code, Organization of Seismic Planning and Protection.
- Fell, R., Corominas, J., Bonnard, C., Cascini, L., Leroi, E. and Savage, W.Z. (2008). “Guidelines for landslide susceptibility, hazard and risk zoning for land-use planning”. *Engineering Geology*, Vol. 102, pp. 99–111.
- Fotopoulou, S., Anastasiadis, A., and Pitilakis, K. (2011). “Building vulnerability to the 2008 Ilia- Achaia earthquake triggered slides”. *2nd World Landslide Forum*, Rome, 2011 (accepted for publication).
- Itasca Consulting Group, Inc. FLAC (Fast Lagrangian Analysis of Continua), ver. 6.0. Itasca Consulting Group, Inc., Minneapolis, 2008.
- Jibson, R. W. and Jibson, M. W. (2003). “Java programs for using Newmark’s method and simplified decoupled analysis to model slope performance during earthquakes”. US Geological Survey Open File Report: 03-005.
- Keefer (2002). “Investigating landslides caused by earthquakes – A historical review”, *Surveys in Geophysics* 23: 473–510, 2002.
- Kramer, S. L. and Stewart, J. P. (2004). “Geotechnical Aspects of Seismic Hazards”. In: *Earthquake Engineering: from Engineering Seismology to Performance-Based Engineering*, Y. Bozorgnia, V. Bertero (Eds.), CRC Press, 4, 85 pp.

- Ktenidou, O.-J. (2010). Theoretical and instrumental study of site and topographic effects on strong ground motion in Aegion, Ph.D. thesis, Aristotle University Thessaloniki, Greece, 2010.
- Lysmer, J. and Kuhlemeyer, R. L. (1969). Finite dynamic model for infinite media, *Journal of Engineering Mechanics*, No. 95, pp. 859–877.
- Mander, J. B., Priestley, M. J. N., and Park, R. (1988). “Theoretical stress-strain model for confined concrete”, *Journal of Structural Engineering*, 114(8), 1804-1826.
- Mejia, L. H. and Dawson, E. M. (2006). “Earthquake Deconvolution for FLAC”, *Proc. 4th International FLAC Symposium*, Madrid, Spain, pp. 211-219, 2006.
- National Institute of Building Sciences (2003), Direct Physical Damage - General Building Stock. HAZUS-MH Technical manual, Chapter 5, Federal Emergency Management Agency, Washington, D.C.
- Negulescu, C. and Foerster, E. (2010). Parametric studies and quantitative assessment of the vulnerability of a RC frame building exposed to differential settlements, *Natural Hazards and Earth System Sciences*, 10, 1781-1792.
- Newmark, N. M. (1965). “Effects of earthquakes on dams and embankments”, *Geotechnique*, 15, 139–160, 1965.
- Peng, W. F., Wang, C. L., Chen, S. T., and Lee, S. T. (2009). “Incorporating the effects of topographic amplification and sliding areas in the modeling of earthquake-induced landslide hazards, using the cumulative displacement method”. *Computers and Geosciences*, 35(5), 946-966.
- Pitilakis, K. D. (2010). Geotechnical Earthquake Engineering. Ziti Publications. (in Greek)
- Rathje, E. M. and Bray, J. D. (2000). “Nonlinear coupled seismic sliding analysis of earth structures”, *J. Geotech. Geoenviron. Eng.*, 126(11), 1002–1014.
- SeismoSoft, SeismoStruct – A computer program for static and dynamic nonlinear analysis of framed structures, 2010, (online): Available from URL: www.seismosoft.com
- Spencer, E. (1967). “A method of analysis of the stability of embankments assuming parallel inter-slice forces”, *Geotechnique*, 17(1), 11-26.
- Varnes, D.J., (1984). “Landslides hazard zonation: A review of principles and practice”. UNESCO, Paris.

ESTIMATION OF EARTHQUAKE INDUCED DRY SETTLEMENTS OF CFR DAMS

D. Egglezos

Dr Civil Engineer NTUA, Geotechnical Engineering Office

ABSTRACT: The estimation of dry settlement, arising from seismic action, is a significant factor for the proper design of rockfill dams. This applies particularly to Concrete Face Rockfill (CFR) Dams, where the deformed (due to the settlement) dam geometry imposes increased stress upon the concrete slab of the upstream face. In this work, a simple method for calculating dynamic dry settlement in CFR dams is presented, based on simple empirical relations for a) estimating settlement on sand from earthquake (Egglezos 2008), and b) calculating a notional value of void ratio for gravel (instead of the actual value) in order to simulate dynamic behavior of gravel to that of an imaginary sand material referring hitherto as “equivalent sand” (Egglezos, 2010). The application of these empirical relations allows the estimation of rockfill settlement, through relevant equations for sand (Egglezos 2007, 2010). The results from the empirical relations apply directly to a 2-D ordinary static FE analysis, in order to obtain the post earthquake stress-strain field and the permanent deformation (vertical settlement and lateral spreading) induced from the seismic shock. The deformed geometry of the CFRD may be exploited for determining the concrete slab stress state, aiming to an effective design.

1 INTRODUCTION

1.1 *General*

The estimation of dry settlement, arising from seismic action, is a significant factor for the proper design of rockfill dams. This applies particularly to Concrete Face Rockfill (CFR) dams, where the deformed dam geometry (due to the settlement) imposes increased stress upon the concrete slab of the upstream face.

In this work, a simple method for calculating dynamic dry settlement in CFR dams is presented, based on simple empirical relations for a) estimating settlement on sand from earthquake (Egglezos 2008) and b) calculating a notional value of void ratio for gravel (instead of the actual value). This notional value refers to “equivalent sand” and allows the estimation of rockfill settlement, through relevant equations for sand (Egglezos 2007, 2010).

2 METHODOLOGY

2.1 *Outline of the concept*

The basic idea is the exploitation of empirical relations that predict quite accurately the dry settlement of granular soils. This prediction is applied strictly to free-field conditions (horizontal layering of soil), which is not the case of a dam layering. The difference between free-field and dam layering is located to the difference in lateral boundary conditions (earth at rest in the first case and

unrestrained slopes in the latter). Having this in mind the proposed methodology utilizes the vertical strains as resulted from the above mentioned empirical relations, and transforms them to the relevant vertical stress required to induce equal strain. The application of this extra loading, properly distributed all over the dam body, within terms of an ordinary 2-D static FE analysis, with accurate boundary conditions (comprising the foundation bedrock and the upstream concrete slab) is assumed to reproduce efficiently the deformed dam geometry and, consequently, to serve for the proper dam design. This assumption is examined thoroughly in next paragraphs, through application in characteristic case studies. It is worth-noting that the main advantage of this procedure is that it utilizes simple calculational tools (at least for preliminary estimations) instead of time-consuming rigorous dynamic elastoplastic analyses.

2.2 Free field dry settlement of gravel

In brief, the estimation of settlement is based on simple empirical relations (Egglezos, 2007, 2008) for the calculation of volumetric strain $\varepsilon(N)$ at the end of N cycles, at characteristic points, with parameters that correspond to: the initial stress (p'_o, τ_{xy}) and density (equivalent void ratio e_{es}) state of soil, the peak horizontal acceleration at the point examined (a_{max}) imposing cyclic stress CSR, and the number of (equivalent) loading cycles N , in relation to the earthquake magnitude M :

The main equations applying are the following:

$$\varepsilon(N) = \varepsilon_1 N^{c(e_{eq})} \leq \varepsilon_{VOL,max}, \varepsilon_1 = \varepsilon(N=1) \quad (1)$$

$$\varepsilon_{VOL,max} = \frac{e_o - e_{min}}{1 + e_o} \quad (2)$$

$$\varepsilon_1 = 0.77 CSR_{TX}^{1.55} (p'_o / p_a)^{0.77} e_{es}^{5.70} \frac{1-P}{1-(0.8P)^{0.58}} \leq \varepsilon_{VOL,max} \quad (3)$$

$$CSR_{TX} = \frac{1}{0.90} \frac{1}{c_r} CSR_{ff} \quad (4)$$

where, c_r ($0.40 \leq c_r \leq 0.70$) is adequate correction factor for the stress state (e.g. Kastro, 1975) and CSR_{ff} refers to free field conditions

$$CSR_{ff} = 0.65 a_{max} \frac{p'_o}{p_o} \quad (5)$$

The above equations (1-5) apply to clean sand. In order to be used for gravel (rockfill material) a notional void ratio e_{es} must be calculated (“equivalent sand ratio”), instead of the nominal void ratio e_o of the gravel. This transformation allows the prediction of gravel behavior with the application of empirical relations for sand (Egglezos 2007, 2010). The equations (6-11) for the determination of the “equivalent sand” ratio are the following.

$$e_{es} = \left(\frac{0.52}{3.92 CRR^{1.58} (0.54 N_L)^{c(e_{eq})}} \right)^{(1/4.70)} \quad (6)$$

$$c(e_{eq}) = 1.07 CRR^{0.202} e_{eq}^{1.584} \quad (7)$$

$$e_{eq} = 1.0 - 0.5 DR(\%) / 100 \quad (8)$$

$$e_{\max} = 1.71(GC - 0.54)^2 + 0.56 \quad (9)$$

$$e_{\min} = 1.11(GC - 0.50)^2 + 0.36 \quad (10)$$

$$CRR(GC > 0.60) = 0.14e_o^{-1.24} N_L^{-0.27} \exp(0.77GC) \quad (11)$$

The symbols in equations (1-11) represent the following magnitudes: p_o' =initial vertical effective stress and p_a =atmospheric pressure, $CSR=q_c/p_o'$ =cyclic stress ratio, q_c =simple amplitude cyclic shear stress, $P=\tau_{xy}/\tau_{CT}$ =static shear stress ratio (τ_{xy} =initial static shear stress, τ_{CT} =static shear stress on CT-line), e =void ratio (density parameter), $CRR=CSR$, GC =gravel content (weight of material (not percent) for nominal diameter $d>2$ mm) and N_L the number of cycles (for $CSR=CRR$) to cause initial liquefaction (generally $N \neq N_L$), e_{\max} and e_{\min} correspond to the extremes of the gravel void ratio (as calculated from empirical relations proposed by the author, Egglezos, 2010).

The constants' values in the above expressions resulted from multi-variable regression of the empirical equations upon numerous data from drained cyclic triaxial tests (Egglezos 2004, 2007, 2008, 2010).

The total (free-field) settlement Δh_{ff} is calculated with the integration of volumetric strain along the soil column of interest: $\Delta h_{ff} = \sum \varepsilon(N)_i \Delta h_i$

The calculated values of permanent deformations $\varepsilon(N)_i$ may serve for the estimation of notional gravity loading Δp_i that produce equal deformation: $\Delta p_i = E_i \varepsilon(N)_i$,

where E_i refers to the Young Modulus of the rockfill.

The settlement Δh_{ff} is likely to underestimate the dam settlement since the dam slopes are not constrained. However, a reasonable value of dam settlement can be attained if a correction factor is applied to Δh_{ff} : $\Delta h_{dam} = c_f \Delta h_{ff}$ ($c_f = 1.40-1.70$)

As a practical rule c_f can be calculated with the following formula: $c_f = (k_o/k_a)$, where k_o and k_a correspond to the earth at rest and the active state coefficient, respectively.

The whole procedure for the estimation of free-field settlement is very easily programmable in a simple computational environment of general use.

2.3 CFRD dry settlement and lateral spreading

The equations 1-11 apply strictly to free field state (horizontal soil layering and constraint of lateral movement). The direct application to the dam geometry is likely to underestimate the expected settlement, attributed to different boundary conditions, that is free up and downstream slopes.

However, a reasonable application for dams may be attained with ordinary 2-D static stress-strain FE analyses, according to the following steps.

- 2-D FE analyses for the calculation of the initial stress-strain field (p_o' , τ_{xy}) of the dam at characteristic points (Fig.1)
- determination of the seismic motion (acceleration time-history, normative value etc)
- estimation of horizontal acceleration response at the previously mentioned points (e.g. through 2-D dynamic response analyses)
- calculation of free field settlement, utilizing the results from the two previous steps, according to the empirical relations (eqns. 1-11)
- evaluation of the (assumed gravity) vertical load, which is required in order to produce the above (free field) settlement Δp_i
- repetition of the 2-D (static) analyses of the dam with application of the extra gravity load (calculated in the previous step) at the dam body, for the estimation of vertical settlement and horizontal spreading, of the actual geometry.

For the 2-D analyses the basic mechanical properties of rockfill (E , ν , c and ϕ) are utilized. The rockfill material is simulated as an elastoplastic M-C material with dilatancy ψ . Any (usual)

software code able to manage 2-D stress-strain response, for elastoplastic M-C material, is considered proper for the analyses (eg. PLAXIS, Phase, SIGMA/W etc.).

As far as the points are concerned, it seems that for typical dams of height about 80-150m, a number of 10 points lying in equal distances from top to bottom, along three lines (upstream, central and downstream section) are enough for an efficient calculation (Fig.1). The application of the extra gravity forces Δp_i may be reduced to three areas per vertical zone (totally 9 areas) as a mean of 4 successive values (Fig.1).

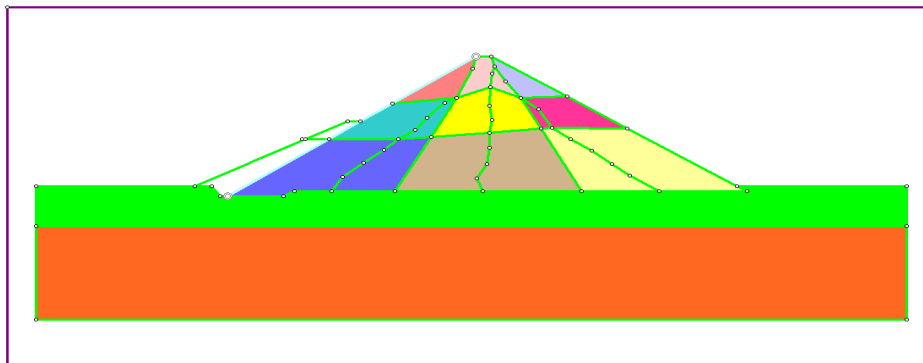


Figure 1. Characteristic points and areas for the calculation of dry settlements

3 A PRACTICAL EXAMPLE – APPLICATION TO IASMOS CFRD

3.1 Dam characteristics – Input data for the analyses

The proposed methodology for dry dynamic settlement calculation, applies to the Iasmos dam (a 100m height CFR dam at Thrace, Northern Greece), assuming conservatively (since it concerns the design stage) a rather low density of the rockfill material (DR = 80%), corresponding to the level of attained compaction (moderate constructional performance). The main dam features (e.g. geometry, materials) are presented in Table 1 and Figure 2 respectively. The earthquake motions (5 acceleration time histories) at the ground surface of the dam area are obtained from the relevant seismic hazard analysis (Papazachos et al. 2010) and correspond to reasonable seismic scenarios for the design of the dam. All the acceleration time-histories were scaled to 0.343g according to the requirements of the designer (application of importance factor). The basic data of the seismic motions are presented in Table 2. The strongest design seismic motions (KGS-ew, HKD-ew accelerographs) are shown indicatively in Figure 3.

Table 1. IASMOS Dam Features - Data for the analyses

Dam	Material properties		Geometry		
	DR(%)	GC	upstream slope	downstream slope	height (m)
Iasmos	80	90	1:1.5	1:1.6	100

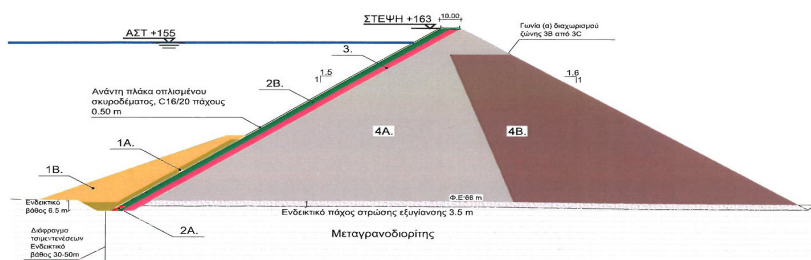


Figure 2. IASMOS dam features (EDAFOMICHANIKI 2011)

Table 2. Seismic motions of IASMOS dam used for the analyses.

DESIGN EARTHQUAKE S	MAGNITUDE E M	DISTANCE R (km)	PGA (cm/s ²)	PGA (g)	SCALING FACTOR PGA _d =0.343	PGA _d (g)
KGS	6.3±0.2	19±3				
ew			224.3	0.229	1.50	0.343
ns			210.8	0.215	1.60	0.343
MIE	5.6±0.2	19±3				
ew			232.4	0.237	1.45	0.343
MYG	7±0.1	65±5				
ew			252.6	0.257	1.33	0.343
HKD	7±0.1	65±5				
ew			253.4	0.258	1.33	0.343

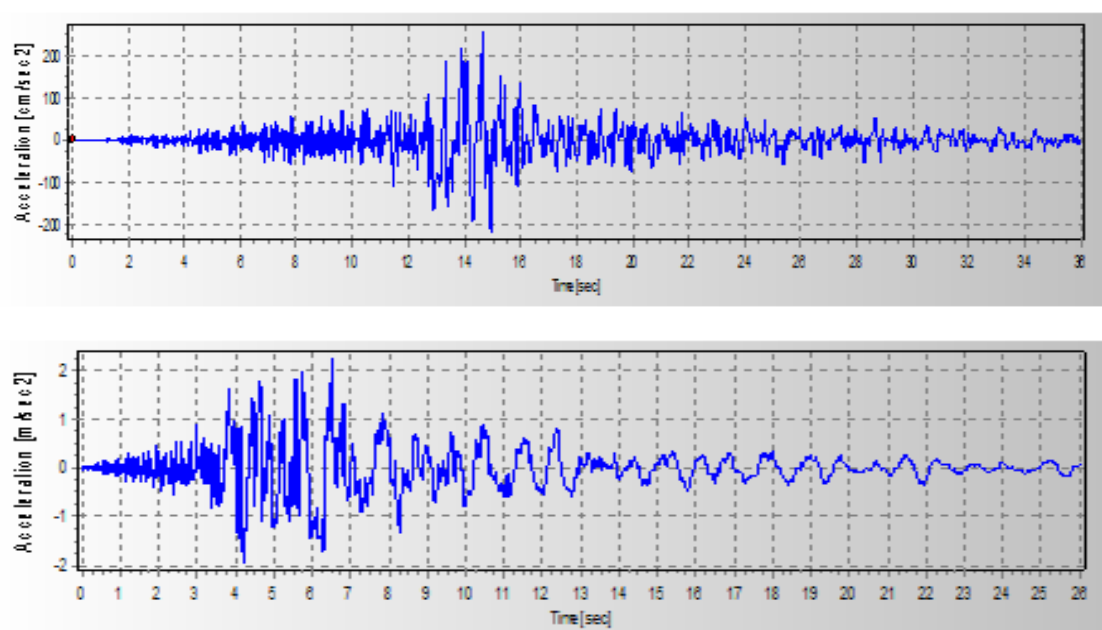


Figure 3. Acceleration time histories from a) HKD-ew and b) KGS-ew

3.2 Dynamic response of the dam

The dynamic response of the dam (EDAFOMICHANIKI, 2011) resulted from 2-D “equivalent” linear analyses at the central section of the dam, for the 5 design acceleration time-histories/accelerographs. The main results of the dynamic analysis are shown tabulated in Table 3.

In addition, the strongest response at the dam crest (maximum acceleration from acceleration time-history KGS-ew) is shown indicatively in Figure 4. The variation of maximum acceleration from the KGS-ew time-history, along the central section of the dam, is shown in Figure 5.

Table 3. Results of the dynamic analysis of IASMOS dam

EARTHQUAKE		a_{max}	v_{max}	d_{max}	T_{DAM}
		g	m/s	m	s
KGS-ew	EMPTY	0.95	1.30	0.20	0.90
	HALF	0.92	1.25	0.19	0.90
	FULL	0.88	1.20	0.17	0.90
HKD-ew	EMPTY	0.80	0.75	0.08	0.69
	HALF	0.80	0.72	0.08	0.69
	FULL	0.78	0.70	0.09	0.69
MYG-ew	EMPTY	0.65	0.90	0.13	0.80
	HALF	0.61	0.85	0.12	0.80
	FULL	0.60	0.81	0.12	0.80
KGS-ns	EMPTY	0.70	0.83	0.12	0.80
	HALF	0.70	0.83	0.12	0.80
	FULL	0.67	0.80	0.12	0.80
MIE-ew	EMPTY	0.38	0.10	0.006	0.44
	HALF	0.37	0.09	0.006	0.45
	FULL	0.28	0.20	0.025	0.46

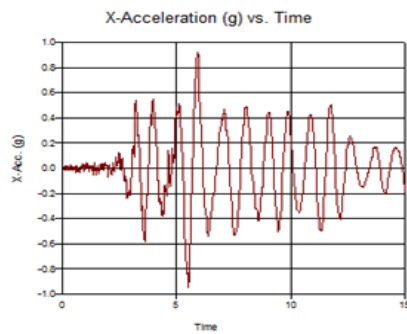


Figure 4. Crest response from KGS-ew

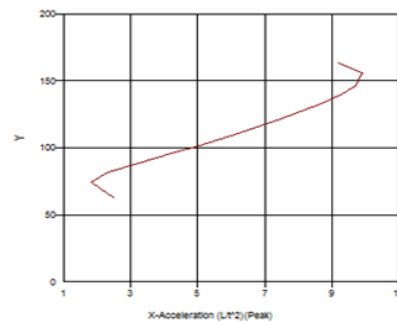


Figure 5. Acceleration variation from KGS-ew (dam's central section)

3.3 Calculation of permanent dam deformation

The calculation of dry settlement and lateral spreading of the dam is performed through 2-D static FE staged analyses, as stated in the previous paragraph. For the analyses, a proper number of stages were used in order to simulate the successive constructional stages and characteristic operational states of the dam (empty, half-filled reservoir, full reservoir). From these analyses, the initial vertical stress and shear stress at characteristic points of the dam was obtained. Indicatively, the stress-field for the “full-reservoir” state is shown in Figure 6. At characteristic points, the maximum horizontal acceleration was obtained according to the results of the 2-D dynamic analyses.

The above data (initial stress field and horizontal acceleration) with the data referring to dam material properties (E , $DR\%$) were used as input for the application of the empirical relations, in order to determine the “free-field” settlement and the equivalent notional body forces Δp_i .

The results from the application of the empirical relations (extra gravity forces Δp_i) were applied at the last computational stage, in order to produce the deformed dam geometry. The dry settlement and the lateral spreading of the dam are presented in Figures 7 and 8 respectively, for the “full” reservoir state.

The calculated dry settlement and the lateral spreading of the 3 characteristic dam states are shown concisely, for the 5 design time-histories, in Table 4.

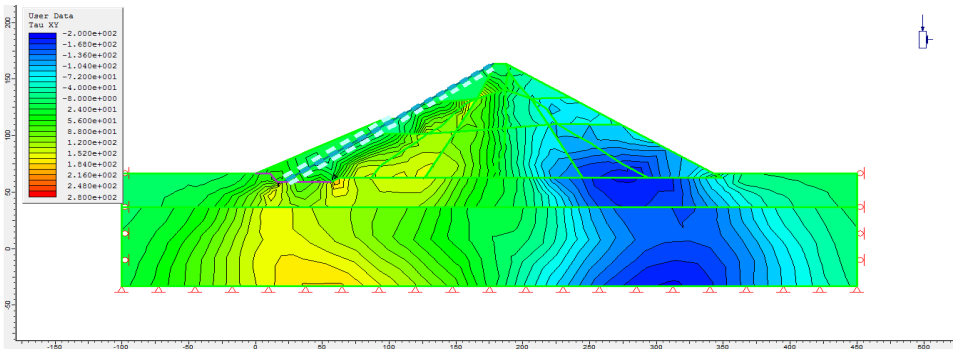
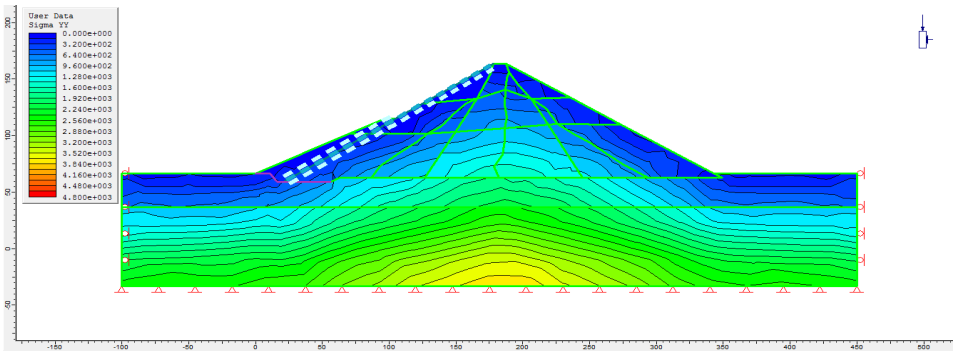


Figure 6. Stress-field for the “full-reservoir” a) vertical stress b) shear stress IASMOS dam

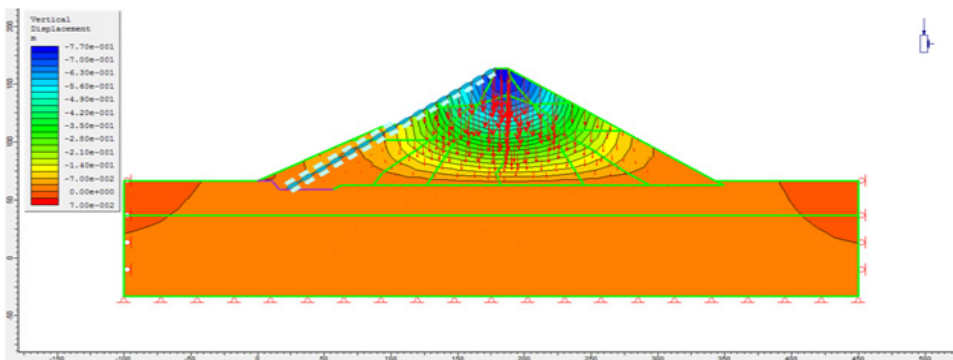


Figure 7. Dry Settlement of IASMOS dam (KGS-ew, full reservoir)

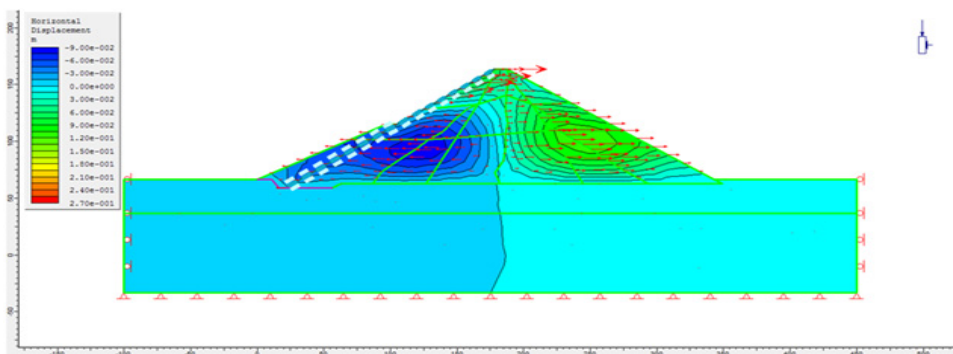


Figure 8. Lateral spreading of IASMOS dam (KGS-ew, full reservoir)

Table 4. Dry settlement of central section (m)- IASMOS dam

Earthquake	No of cycles	M	Δ_{ff}			Δ_{dam}		
			Empty	Half	Full	Empty	Half	Full
HKD-ew	11	7+0.1	0.43	0.41	0.44	0.71	0.68	0.73
MYG-ew	11	7+0.1	0.33	0.32	0.37	0.54	0.53	0.61
KGS-ew	7	6.3+0.2	0.39	0.46	0.44	0.64	0.76	0.73
KGS-ns	7	6.3+0.2	0.26	-	-	0.43	-	-
MIE-ew	4	5.6+0.2	0.12	-	-	0.20	-	-

4 EVALUATION OF THE RESULTS

4.1 Data for the evaluation

For evaluation purposes, the proposed method for dry settlement calculation is applied to other CFR dams (Mesohora Dam at central Greece and Zipingpu Dam at Sichuan of China), utilizing published data (Dakoulas 2008 and Xu Zeping 2008, respectively).

In the case of Mesohora dam the dry settlement is not a measured value but a reasonable assumption of the author (Dakoulas 2008) for the dynamic analysis of the dam, according to reported measurements in analogous cases. In addition the applied seismic motion is also a – reliable- hypothetical scenario, with application of Koyna acceleration time-history (India, 1967, M=6.5).

On the other hand, for the Zipingpu dam there are published data (Xu Zeping 2008) concerning the actual dynamic response of the dam from the strong earthquake of Sichuan (May 12, 2008, M=7.8). These data comprise the acceleration at the crest (1.6g) and the bottom of the dam (0.45g), the maximum vertical settlement at the crest (0.82m) and the lateral spreading (0.28m, downstream).

The above cases are examined through application of the proposed methodology (verification of assumptions in the case of Mesohora dam and comparison to measured data in the case of Zipingpu dam) in the following paragraphs.

4.2 Application of the proposed method

4.2.1 Dam features

The seismic response of the two dams is obtained from a simplified approach and not from a rigorous 2-D dynamic response analysis.

The dam characteristics (geometry and materials) are presented in Table 5 and Figures 9 and 10 for Mesohora and Zipingpu dam respectively. Both CFR dams have about the same height (~150m) and slope geometry (~1:1.4 upstream and 1:1.5 downstream). As far as the materials of the body dam are concerned, 3 cases are examined relating to three different relative densities of the rockfill material (DR = 80, 90, 100%), corresponding to the attained compaction (constructional performance). For simplicity reasons the dam body is considered to consist of a unique homogeneous rockfill material (that is no account is taken for the dam zonification).

Table 5. Dam Features - Data for the analyses

Dam	Material properties		Geometry			Seismic data			
	DR(%)	GC	upstream slope	downstream slope	height (m)	time-history	a_{max} at crest (g)	M	N_{eq}
Mesohora	80/90/100	90	1:1.4	1:1.5, 1:1.6	156	Koyna	1.1	6.5	8
Zipingpu	80/90/100	90	1:1.4	1:1.5, 1:1.6	156	Sichuan	1.6	7.8	15

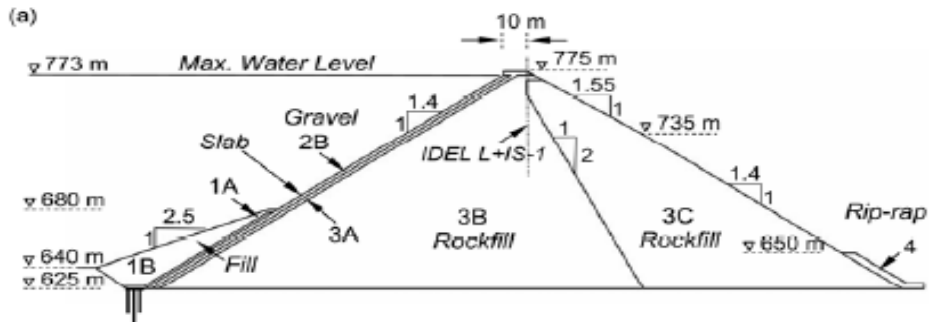


Figure 9. Mesochora dam features. (Dakoulas 2008)

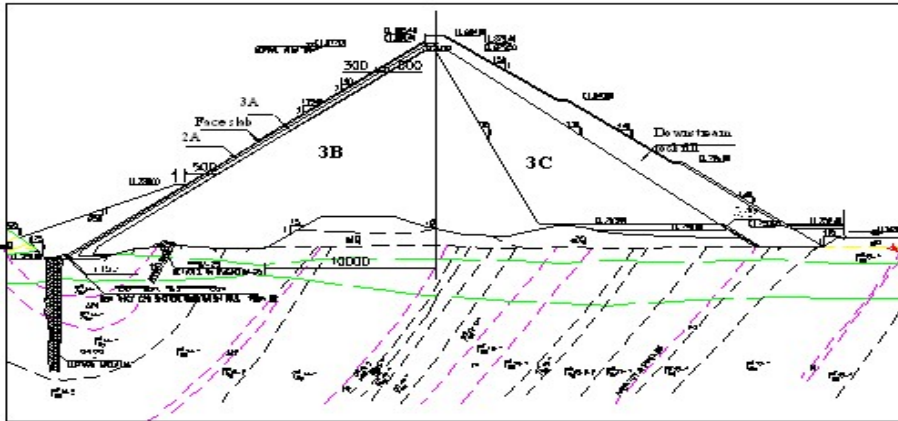


Figure 10. Zipingpu dam features (Xu Zeping 2008)

4.2.2 Seismic data:

The seismic response of the two dams is taken after a simplified approach and not as rigorous 2-D dynamic response analysis through acceleration time-histories. The selected seismic motions for evaluation of the seismic performance are the Koyna (India, 1967, $M=6.5$) and the Sichuan earthquake, (Sichuan, May 12, 2008 $M=7.8$), for the Mesohora and the Zipingpu dam respectively. The basic data concerning the seismic motion are shown in Table 5. For simplicity reasons, the distribution of acceleration from crest to bottom is taken in accordance to published charts for idealized geometry of dam and canyon (Dakoulas & Gazetas 1986). This distribution is presented in Figure 11.

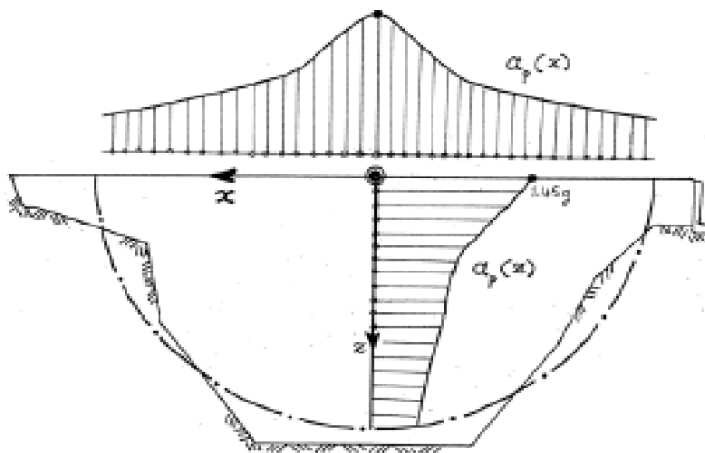


Figure 11. Distribution of acceleration for idealized geometry of dam and canyon (Dakoulas & Gazetas 1986)

4.2.3 Analytical Procedure:

The procedure for the calculation of dry settlement in Mesohora and Zipingpu dams is described previously in paragraph 2.3 and comprises the following steps:

- 2-D FE stress-strain static analysis for the determination of stress field at 10 characteristic points of the central section
- Estimation of the maximum horizontal acceleration along the vertical axis of the central section of the dams (according to the distribution shown in Fig.11)
- Application of the empirical relations (eqns. 1-11) for the calculation of “free-field” dry settlement
- Correction of the results for the calculation of the dam dry settlement, through the correction factor c_f

4.2.4 Evaluation results

The resulting settlement values are well compared to those reported in the relevant literature. According to recent research (e.g. Dakoulas 2008, Wieland 2007), the typical expected values of dry settlement on 100-150m height CFR dams, (recordings from case history CFR dam settlements, due to severe earthquakes), range from 0.50 to 1.00m. Indeed, dry settlements resulting from the analyses, are in good agreement with the aforementioned range, at least for the seismic shocks that cause the most intense amplification at the dam crest. In brief the results from the analysis and the available published data are presented in Table 6.

Table 6. Dry settlement of central section (m)

Dam	DR(%)	Earthquake	No of cycles	M	Δ_{ff}			Δ_{dam}		
					Empty	Half	Full	Empty	Half	Full
Mesohora	80				0.73	0.73	0.88	1.10	1.10	1.32
	90	Konya	8	6.5	0.47	0.46	0.58	0.71	0.69	0.87
	100				0.31	0.30	0.39	0.47	0.45	0.59
Zipingpu	80				1.78	1.76	2.02	2.67	2.64	3.03
	90	Sichuan	15	7.8	0.98	0.97	1.15	1.47	1.46	1.73
	100				0.56	0.55	0.67	0.84	0.83	1.01

5 SYNOPSIS -CONCLUSIONS

The application of the proposed methodology for calculation of dry settlements of CFR Dams requires as initial data a) the stress field of the dam in static condition, b) the distribution of horizontal acceleration in the dam body, for the examined seismic action and c) the choice of a relative density to account for the compaction of the rockfill material.

In case there is lack of data from dynamic analyses, a proper simplified distribution of acceleration from the crest to the bottom of the dam from published charts (e.g. Gazetas and Dakoulas 1995) can be used for the dry settlement calculations (at least for preliminary studies), with significant accuracy.

The above data can be used as input to the following step by step procedure: a) application of the empirical relations for the estimation of the earthquake induced free-field settlements of the rockfill, b) estimation of a notional extra gravity loading consistent to the calculated settlements and c) conduction of 2-D FE geostatic analysis under the extra gravity loading with output the permanent displacement of the dam body (vertical settlements and lateral spreading). Alternatively, at step (c) a simplified “correction” of the free-field output may be applied, to account for the sloppy boundary conditions of a dam (in this latter case only vertical settlement can be calculated).

As a practical rule, arising from parametrical application of the proposed method and comparison to measured data, a relative density with a value of DR=100% seems to reflect well in the in-situ conditions of the rockfill. This is consistent to the high compaction requirements as it is described regularly in the studies of rockfill dams and the typically expected relevant constructional performance as a result of systematic supervision and high quality control of these earth-structures. However, at the stage of the design of a new CFR dam a rather more conservative

approach is recommended (DR=80-90%) to account for occasional lower constructional performance.

The proposed methodology for dry settlement calculations applied for a) the design of a new CFR Dam (Iasmos Dam), b) the estimation of dry settlement, of already existing CFR dams (Mesohora, Central Greece and Zipingpu (China)), for strong earthquake motions. The results of these analyses are consistent to: a) the range of dry settlements reported from numerous case studies (e.g. Wieland, 2007) of CFR dams as a consequence of strong seismic motion (0.50 – 1.00m) –all three cases examined in this paper b) the assumption of other researchers (0.25-0.50m) in terms of calculating the stresses to be developed in the concrete face slab (Mesohora dam – Dakoulas, 2008) and c) the measured values of settlement in the case of Zipingpu dam from the 12 May 2008, M=7.8, Sichuan earthquake (0.83-1.01m predicted vs 0.82m measured settlement). Although a simplified approach relating to the dynamic response and the dam geomaterial properties was applied, the results are quite encouraging. It is obvious that the results may benefit from improvement of the accuracy of the data input (geomaterial properties, dam zonation and rigorous dynamic analysis for the horizontal acceleration distribution in the dam body).

As a final conclusion, it can be stated that the proposed methodology can offer a simple yet effective tool, for estimating dry settlement of CFR dams arising from strong seismic motions and contributes to the study of complex interaction between concrete slab – rockfill dam body – impounded water mass – bedrock foundation.

6 REFERENCES

- Dakoulas, P. 1993. Response of Earth Dams in Semi-Cylindrical Valleys Subjected to Oblique SH Waves. *Journal of Engineering Mechanics, ASCE* 119(1): 74-90.
- Dakoulas, P. 1993. Earth Dam - Canyon Interaction Effects For Obliquely Incident SH Waves. *Journal of Geotechnical Engineering, ASCE* 119(11): 1696-1716.
- Gazetas, G. and Dakoulas, P. 1992. Seismic Analysis and Design of Rockfill Dams: State of the Art. *Journal of Soil Dynamics and Earthquake Engineering* 11(1): 27-61.
- Rollins, K., Evans, M., Diehl, N.B., Daily, W.D. 1998. Shear modulus and damping relations for gravel. *J. Geotechn. and Geoenvironm. Engineering, ASCE* 124(5): 396-405
- Dakoulas, P., Evangelou V. 2008. Nonlinear 3D analysis of a concrete face rockfill dam 1st PanHellenic Conference of large dams. Larisa, Greece:TEE (in greek)
- Dakoulas, P. and Gazetas G., 1986. Seismic Lateral Vibration of Embankment Dams in Semi-Cylindrical Valleys. *Earthquake Engineering and Structural Dynamics* 14: 19-40.
- EDAFOMICHIANI ATE. 2010. *Study for the dynamic response of Iasmos dam*. Athens. Greece. (in greek)
- Egglezos D. 2007. Empirical relations for earthquake pore pressure build-up in gravel. 4ICEGE, Thessaloniki, Greece.
- Egglezos D. 2010. Updated Empirical relations for earthquake pore pressure build-up in gravel. Proc. 6th PanHellenic Conference on Geotechnical and Geoenvironmental Engineering. Volos. Greece (in greek) 2010.
- Egglezos D. 2004. Theoretical and experimental investigation of soil under cyclic loading. *Doctoral Thesis*. Athens:NTUA
- Egglezos D.N. 2007. Estimating earthquake induced settlements on granular soils – Application to shallow foundations. Proc. 2nd Japan-Greece Workshop on seismic design, observation and retrofit of foundations. Tokyo, Japan.
- Egglezos D.N. 2007. Prediction of earthquake induced settlements on granular soils, Proc. 4th ICEGE. Thessaloniki. Greece.
- Makdisi F.I. & Seed H.B. 1978. Simplified procedure for estimating dam and embankment earthquake induced deformations. *Journal of the Geotechnical Engineering Division, ASCE* 104 (GT7): 849-867
- Papazachos K.V., Papaioannou Ch. *Seismic Hazard Analysis of Iasmos Dam*. Thessaloniki. Greece: AUTH
- Wieland, M. 2007. Seismic Performance of CFRDs. *Water Power and Dam Construction*. March
- Xu Zeping. 2008. Performance of Zipingpu CFRD during the strong earthquake. www.chincold.org.cn/chincold/zt/dwj/zjbg/webinfo/2009/9/1280908328342316.htm

Effect of Soil and Interface Nonlinearities on the Response of Caisson-Supported Bridge Piers

A. Zafeirakos, N. Gerolymos

Soil Mechanics Laboratory, National Technical University, Athens, Greece

ABSTRACT: The seismic response of caisson supported bridge piers is numerically investigated with due consideration to soil and interface nonlinearities. Evaluation of system performance is carried out under the prism of a new capacity design *paradigm* where soil "failure" mechanisms are mobilized to protect the superstructure. To investigate the effectiveness of such an approach, a caisson-column supported bridge structure is used as an example. Two alternatives are compared: one complying with conventional capacity design, with over-designed foundation so that the soil is marginally plastified; the other following the new design philosophy, with under-designed foundation, "inviting" the plastic "hinge" into the soil (Anastasopoulos et al. 2010). The two alternatives are then subjected to an artificial accelerogram appropriately calibrated so that both systems would exhibit the same spectral response in a linear elastic regime, allowing thus the seismic performance of the two systems to be achieved on a "fair" basis. Key performance measures of the systems are then compared, such as: accelerations, spectral response, displacements, pier base rotations and settlements. It is shown that separation of the caisson from the supporting soil and extensive soil plastification contribute beneficially to the seismic performance of both the foundation and the superstructure.

Keywords: Caisson foundations; Dynamic soil-structure interaction; Soil capacity mobilization; Seismic performance measures

INTRODUCTION

Caisson foundations deeply embedded in soft soil have been widely used to support major structures, especially bridges. Despite their large dimensions, caissons have been shown not to be immune to seismic loading as it was believed for many years, as was confirmed in the Kobe (1995).

Interestingly, although the lateral and seismic response of deep foundations has been of considerable interest for many years leading to the development of a number of methods of varying degrees of accuracy, efficiency and sophistication, only few of them are devoted to caissons. Instead, the methods of solution developed for (rigid) embedded foundation and for (flexible) piles have been frequently adopted.

This paper aims to shed some light in the seismic design of caisson foundations under the prism of performance based design, which in geotechnical earthquake engineering has, until recently, received little attention. More specifically, a new seismic design philosophy is applied, in which yielding of the soil-foundation system is "utilised" to protect the superstructure—exactly the

opposite of conventional capacity design (in which plastic "hinging" is restricted to the superstructure, thus underestimating the effect of soil and foundation).

To unravel the effectiveness of the new design philosophy (compared to conventional capacity design), a simple but realistic bridge structure founded on caisson foundation is used as an example. Two configurations are analysed and compared: (a) the first comprises a 8 m pier founded on a rigid cubic caisson, and (b) the second consists of a 33 m pier founded on a similar caisson, corresponding to a conventionally and an un-conventionally designed system respectively. Both systems are subjected to an artificial acceleration time history imposed at the base. This artificial seismic excitation is appropriately calibrated in a way that the spectral acceleration of a 1-DOF oscillator placed at the surface remains constant for a wide range of frequencies, practically unaffected by the dynamic characteristics of the soil-structure system (e.g. effective fundamental period). The analysis methodology will be explained thoroughly in the sequel.

Evidently, it is shown that allowing plastic hinging at the foundation restricts the loading transmitted to the superstructure, but without avoiding the increase of earthquake-induced foundation settlements and rotations. Overall, however, the new design approach provides substantially larger safety margins.

PROBLEM DEFINITION AND ANALYSIS METHODOLOGY

Problem definition and model description

The studied problem is portrayed in Figure 1: A bridge pier is founded through a rigid cubic caisson of side $h = 10$ m in a 20 m thick 2-layer cohesive soil stratum. The soils are saturated with $S_u = 65$ kPa at the upper 6 m and $S_u = 130$ kPa at the lower 14 m. The two alternative design approaches, conventional and un-conventional, are represented by two different column heights. In both cases the concentrated mass of the deck, m , is 2700 Mg, corresponds to a static factor of safety in both systems $FS_V = 5$. The design spectral acceleration is chosen $S_a = 0.6$ g.

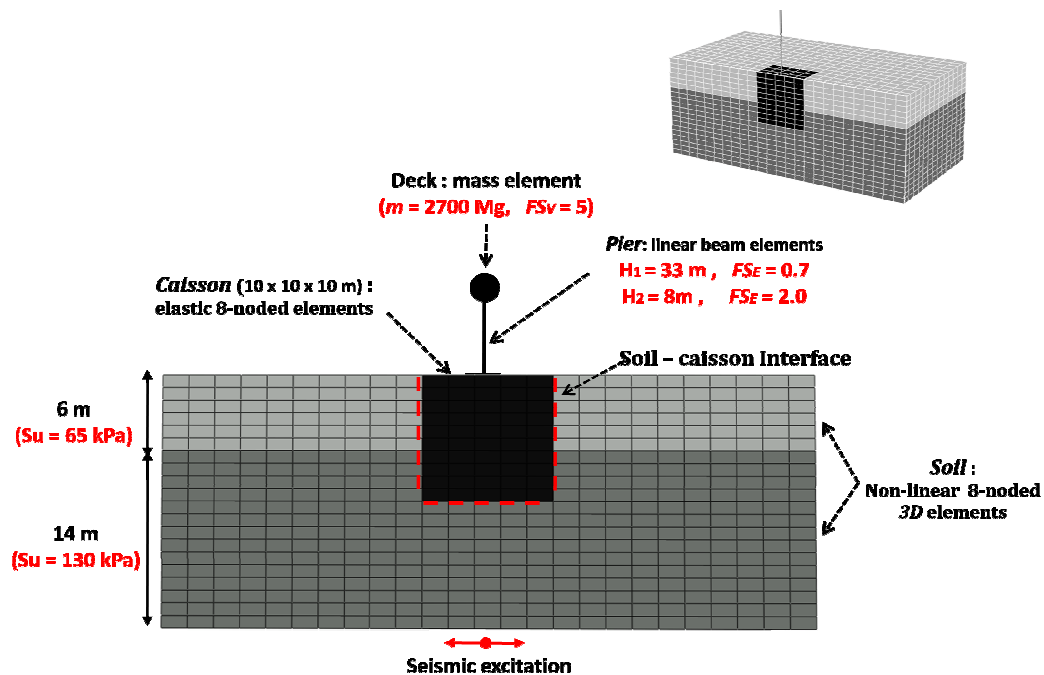


Fig 1. Overview of the finite element modeling: 3D conditions are assumed, taking account of soil inelasticity and soil-caisson interface.

The problem is analysed with the use of the advanced Finite Element code ABAQUS. Both caisson and soil are modeled with 3-D elements, elastic for the former and nonlinear for the latter. The mass-and-column superstructures are modeled as single degree of freedom oscillators. The caisson is connected to the soil with special contact surfaces, allowing for realistic simulation of possible detachment and sliding at the soil-caisson interfaces. To achieve a reasonable stable time increment without jeopardizing the accuracy of the analysis, we modified the default hard contact pressure-overclosure relationship with a suitable exponential relationship. The soil stratum reaches 10 m deeper than the caisson base, thus having a negligible influence on the response. To ensure uniform stress distribution at the head of the caisson, the nodes of the associated elements are properly kinematically constrained. Inelastic soil behaviour is described through the Von-Mises yield surface with nonlinear kinematic hardening and an associative plastic flow rule. The model of ABAQUS is calibrated using the methodology proposed by Gerolymos et al. (2005), Gerolymos (2006). Rayleigh damping, representing material damping, is taken equal to 5% between the eigenfrequency of the soil deposit and the dominant frequency of the earthquake ground motion. Appropriate kinematic constraints are imposed to the lateral edges of the model, allowing it to move as the free field (Giannakou et al. 2010).

The column heights associated with the two alternative design approaches, are calculated as illustrated in Figure 2:

- For a specific vertical force at the head of the caisson, the moment (M)–horizontal load (Q) interaction diagram is produced, corresponding to the failure envelope (in M – Q space). Since $M = Q \cdot H$, the interaction between M and Q may also be interpreted as the lever arm height above the pier base (H) that leads to failure for a given Q . Furthermore, each point on the failure envelope corresponds to a safety factor for seismic loading $FS_E = 1.0$. In Fig.3 the results are presented normalized with respect to the pure moment capacity M_u (with no horizontal loading) and the pure horizontal capacity Q_u (with no moment loading) of the caisson–soil system.
- Given the mass of deck, $m = 2700$ Mg, and the design spectral acceleration, $Sa = 0.6$ g, the pseudo-static pier base shear force, $Q = m \cdot Sa$, is calculated, leading, in our case, to a ratio of $Q / Q_u = 0.4$.
- Having calculated Q / Q_u , the respective moment, M , at failure is extracted, $M / M_u = 0.65$, resulting further in a pier height $H = 16$ m (for a $FS_E = 1.0$).
- Given the pier height for $FS_E = 1.0$, a shorter pier, $H = 8$ m, is designed in compliance with conventional capacity design, resulting from a $FS_E = 2.0$ and a taller pier, $H = 33$ m, is considered in the spirit of the new philosophy, designed with a $FS_E = 0.7$ (lower than 1.0 – *under-designed* pier). In fact, as it will be shown below, the under-designed system will not allow the design seismic action to develop. Hence, FS_E does not really have a physical meaning in this case; it is just an *apparent* temporary factor of safety.

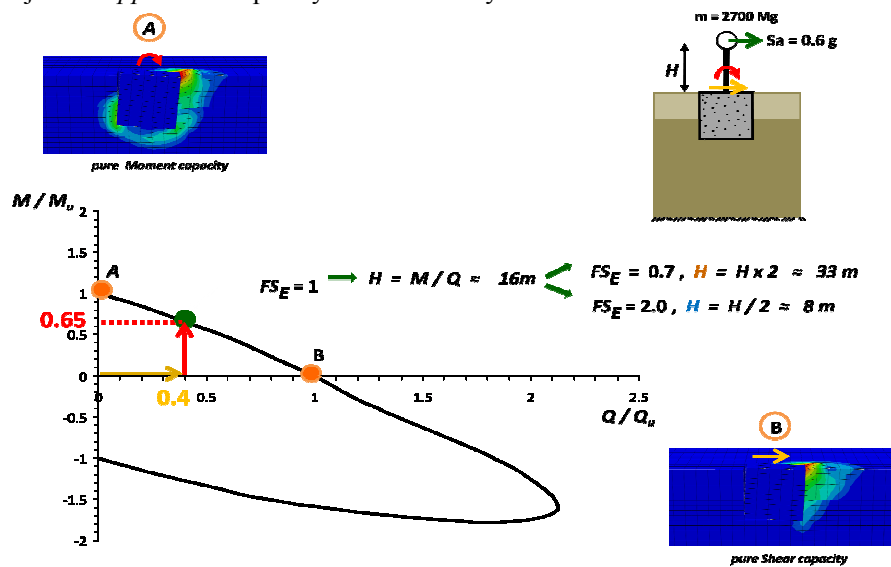


Fig 2. Failure envelope of the soil–caisson configuration and calculation process of the alternatives' column heights.

The pier is modeled with 3-D linear elastic beam elements having properties of concrete. The cross-section of the pier is calculated so that the elastic (fixed-base) vibration period $T_{st} = 0.6$ sec, for both cases, deliberately larger than the first natural period, $T = 0.41$ sec, of the soil profile used in the analysis. In this way spurious oscillations at the boundaries of the model are limited as a result of a destructive interference (existence of a cut-off period for radiation damping equal to the first natural period of the soil profile) of the outward spreading waves (Gerolymos and Gazetas 2006, Gerolymos et al. 2008). This results in a solid cylindrical section with a diameter of $d = 3$ m for the conventionally designed pier ($H = 8$ m) and a hollow section of $d = 8.5$ m and thickness $t = 1.5$ m for the un-conventionally designed pier ($H = 33$ m).

Methodology

The seismic performance of the two alternatives is investigated through nonlinear time-history analysis. It should be highlighted that in most published earthquake response analyses the examined systems are subjected to a variety of seismic motions to capture the interplay between the exciting dynamic characteristics (e.g. dominant periods, frequency content, PGAs, sequence of pulses) and the vibrational characteristics (natural, T_{st} , and effective fundamental period, T_s) of the structures. This paper, however, follows a methodology in which both systems are subjected to an appropriately calibrated seismic motion, so that their effective fundamental periods T_s fall within a plateau of constant spectral accelerations, thus eliminating the aforementioned interactions. Having, in this way, removed any bias of the response mechanisms on the dynamic properties, we may focus on the main question posed in this study, whether plastic mobilization of soil is beneficial or detrimental, and compare the two alternatives on a "fair" basis. The procedure, also schematically illustrated in Figure 3, consists of the following steps:

- 1) A real accelerogram (also denoted as "natural" record) is selected as seismic excitation for both systems. In this paper the one recorded at Sakarya during 1999 Turkey earthquake is used. (Fig. 3a).
- 2) The "natural" record is then used as base excitation in a one-dimensional wave propagation analysis of the 2-layer soil profile and the free-field (top of soil profile) acceleration time-history (Fig. 3c) along with the respective response spectrum are derived. This spectrum is then compared with an artificial *target response spectrum* (Fig. 3d), which, in our case, resembles a typical code design spectrum, having a plateau in $Sa = 0.6$ g for a wide range of periods (0.2 to 1.6 sec; it will be shown that the effective periods T_s of both over and *under-designed* systems fall into this specific range).
- 3) Within a heuristic optimization procedure (trial and error technique), the base excitation is back-calculated by deconvoluting the calculated free-field motion, until the response spectrum matches the *target*. Upon matching, the new modified motion is used as the base seismic motion for the 3-D analyses of both systems (Fig.3b).

The process remains independent of the selected "natural" accelerogram.

ANALYSIS : RESULTS AND DISCUSSION

The comparison of the performance of the two design alternatives subjected to the artificial accelerogram is presented in Figures 4–7, in terms of acceleration and displacement time-histories, deck "floor" response spectra, pier base moment–rotation and settlement–rotation.

The acceleration time–histories calculated at the deck are presented in Fig. 4a. Even though both systems were subjected to a design spectral acceleration of $Sa = 0.6$ g (Fig. 4c), the response of the *under-designed* ($H = 33$ m) system is significantly smaller, reaching a maximum of $a = 0.3$ g, in accord with the design seismic factor of safety $FS_E = 0.7$, than for the *over-designed* ($H = 8$ m, $FS_E = 2.0$) where the full seismic action is developed ($a = 0.6$ g). This is the first evidence that mobilization of soil capacity hinders the development of the design seismic action, which is further demonstrated in the substantial decrease in the "floor" spectral accelerations at the mass of the superstructure (i.e., the spectral accelerations of the computed motion of the superstructure mass) in the *under-designed* case, as depicted in Fig. 4b.

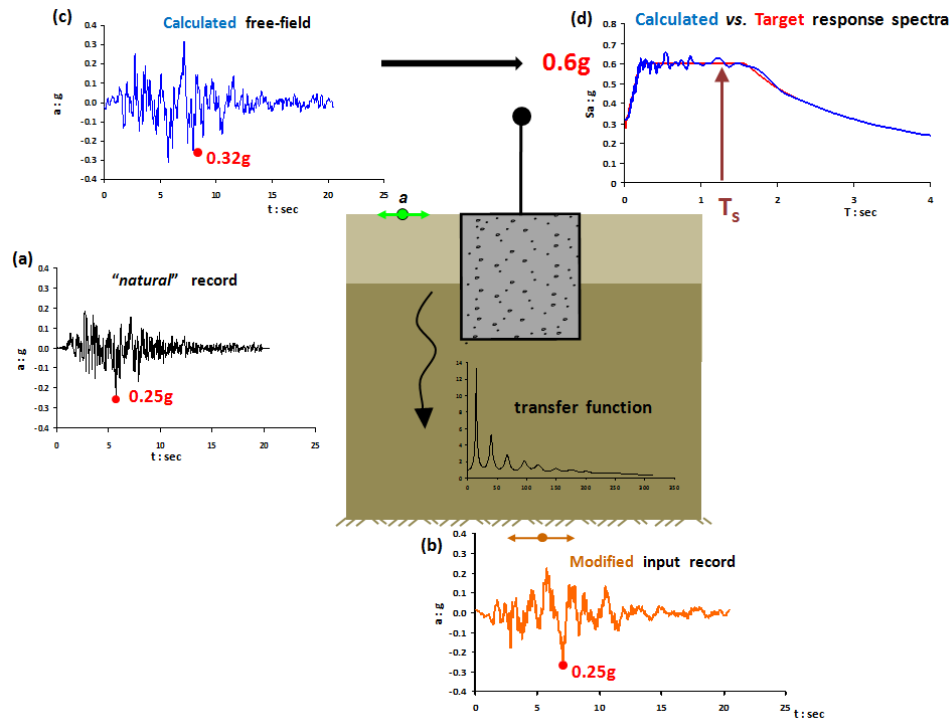


Fig 3. Schematic illustration of the methodology for calculating the artificial accelerogram used in the dynamic analysis of both alternatives.

The effective periods due to soil–structure–interaction effects, T_s , of the alternatives were derived from the free oscillations at the end of each shaking, resulting in $T_s = 0.8$ sec for the *over-designed* and $T_s = 1.5$ sec for the *under-designed* system (Fig. 4a), both falling within the range of the target spectrum plateau, $S_a = 0.6$ g. The main prerequisite for the validity of our methodology is thus met.

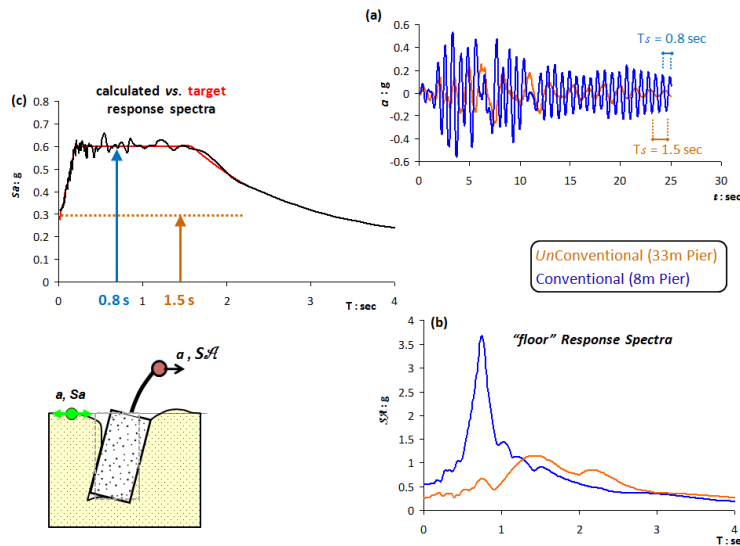


Fig 4. Comparison of the response of the two alternatives subjected to the artificial accelerogram. (a) Acceleration time–histories at the deck mass, with the respective effective periods T_s . (b) Response spectra of the motion of the mass. (c) Computed free-field and target response spectra used for the dynamic analyses.

The time histories of deck horizontal displacement, i.e. the *drift*, for the two alternatives are compared in Figure 5. As graphically illustrated in the adjacent sketch notation, the *drift* has two components (see also Priestley et al. 1996): (i) the "rigid drift" $U_{rigid} = \theta H$, i.e. the displacement due to motion of the caisson as a rigid body, and (ii) the "flexural drift", i.e. the structural displacement due to flexural distortion of the pier column. Both U_{rigid} and U_{flex} are presented normalized with the respective maximum total displacement, U_{total_max} . This way, the contribution of pier flexural distortion and caisson rotation to the final result of interest (i.e. the total drift) can be inferred. As might have been expected, for the conventional design (*over-designed foundation*) the drift is mainly due to pier distortion U_{flex} , and thus increased structural distress. Exactly the opposite is observed for the *under-designed* foundation of the new design philosophy: the *drift* is mainly due to foundation rotation U_{rigid} , causing less seismic loading on the pier but increased total displacements due to soil yielding. Nevertheless, the total residual displacement for the new concept might be slightly larger, but quite tolerable: $U_{residual} \approx 5$ cm (compared to ≈ 0.5 cm for the conventional). In a nutshell, choosing to design a bridge pier *unconventionally* could substantially reduce the cost but would also demand appropriate provisions to accommodate for the increased seismic displacements

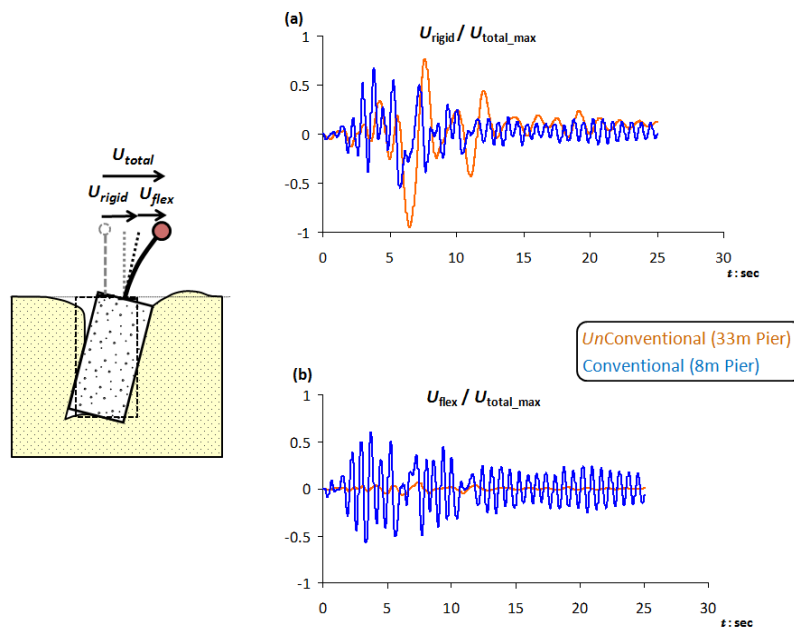


Fig 5. Comparison of the response of the two alternatives. (a) Time-histories of the "rigid-body" drifts normalized with the respective maximum total drift. (b) Time-histories of the flexural drifts normalized with the respective maximum total drift.

In Figure 6a the comparison is portrayed in terms of the foundation experienced moment-rotation ($M-\theta$). As expected, while the conventionally designed foundation experiences limited inelasticity (Fig. 6a2), the *under-designed* foundation (new design philosophy) behaves strongly inelastic (Fig. 6a1). Since both piers were modeled for elastic behavior, the main difference between the two alternatives lies in the mechanism of energy dissipation due to soil yielding. However, energy dissipation is not attainable at zero cost: in our case the cost is the increase of foundation settlement. Fig. 7b compares the settlement-rotation ($w-\theta$) response for the two alternatives. The conventionally designed system is subjected to a practically elastic settlement $w \approx 3$ cm (Fig. 6b2). In marked contrast, the *under-designed* system of the new philosophy experiences larger but quite tolerable dynamic settlement: $w \approx 10$ cm (Fig. 6b1). Moreover, despite the excessive soil plastification, not only the structure does not collapse, but the residual (permanent) rotation is rather limited (as already attested by the residual deck drift), providing further evidence that mobilisation of soil capacity failure acts as a "safety valve" for the superstructure.

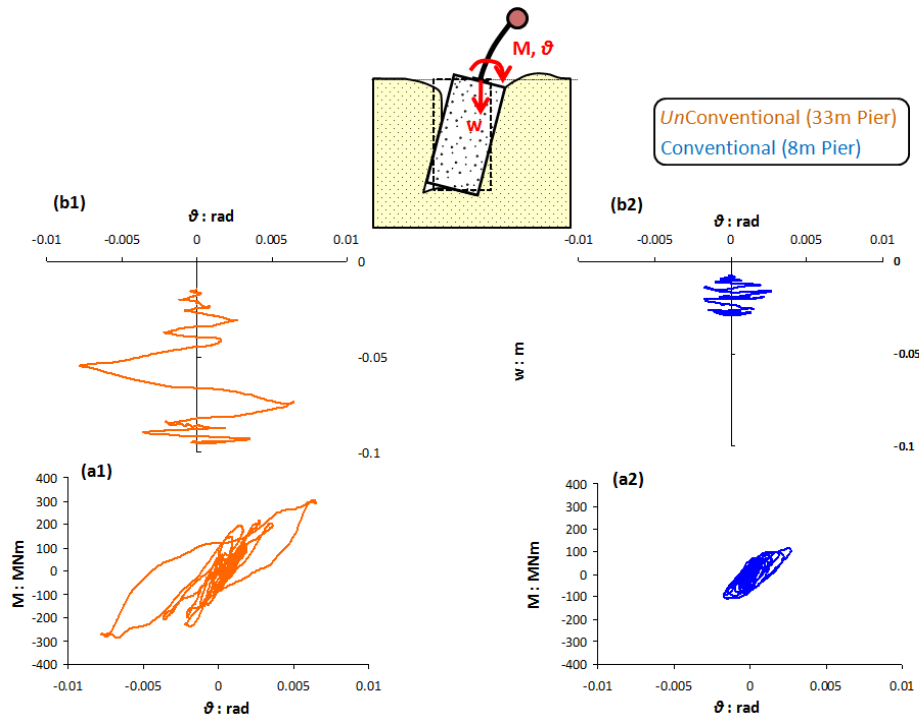


Fig 6. Comparison of the response of the two alternatives. (a1), (a2) Overturning moment–rotation (M – θ) response. (b1), (b2) Caisson settlement–rotation (w – θ) response.

Figure 7 compares the response of the two alternatives in terms of plastic shear strain contours at the end of the shaking. In the conventionally designed system (Fig. 7b) there is very little inelastic action in the soil, concentrated mainly at the top and bottom of the caisson. In contrast, the new design scheme (Fig. 7a) experiences rather extended “plastic hinging” in the form of mobilization of passive-type soil failure in front and back of the caisson accompanied by gap formation and sliding in the sides (deformation scale factor = 20).

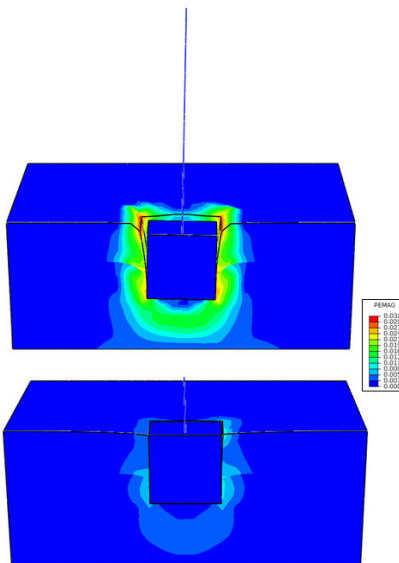


Fig 7. Contours of plastic shear strain at the end of shaking for both alternatives (deformation scale factor = 20).

ACKNOWLEDGEMENTS

The authors would like to acknowledge financial support from the EU 7th Framework research project funded through the European Research Council's Programme "Ideas", Support for Frontier Research – Advanced Grant, under Contract number ERC-2008-AdG 228254-DARE.

REFERENCES

- Anastasopoulos, I., Gazetas, G., Loli, M., Apostolou, M., Gerolymos, N. 2010. Soil failure can be used for seismic protection of structures. *Bull Earthq Eng* 6(4):705–722, pp. 309-326.
- Gerolymos, N., Gazetas, G. 2006. Winkler model for lateral response of rigid caisson foundations in linear soil. *Soil Dyn Earthquake Eng* 26(5): 347–361.
- Gerolymos, N., Gazetas, G. 2006. Static and dynamic response of massive caisson foundations with soil and interface nonlinearities- Validation and results. *Soil Dyn Earthquake Eng* 26 (5), pp. 377-394.
- Gerolymos, N., Gazetas, G., Tazoh, T. 2005. Seismic response of yielding pile in non-linear soil. In: *Proc. 1st Greece–Japanworkshop*, seismic design, observation, and retrofit of foundations, Athens, 11–12 October, pp 25–36.
- Gerolymos, N., Giannakou, A., Anastasopoulos, I., Gazetas, G. 2008. Evidence of beneficial role of inclined piles: observations and numerical results. *Bull Earthq Eng* 6(4): 705–722
Special Issue: Integrated approach to fault rupture- and soil-foundation interaction.
- Giannakou, A., Gerolymos, N., Gazetas, G., Tazoh, T., Anastasopoulos, I. 2010. Seismic Behavior of Batter Piles: Elastic Response. *Journal of Geotechnical and Geoenvironmental Engineering*, ASCE, 136, No.9, 1187-1199.
- Priestley, M.J.N., Seible, F., Calvi, G.M. 1996. Seismic design and retrofit of bridges. Wiley, New York

Single Pile vs. Pile Group Lateral Response under Asymmetric Cyclic Loading

S. Giannakos, N. Gerolymos, G. Gazetas

Soil Mechanics Laboratory, National Technical University, Athens, Greece

ABSTRACT: To gain insight into the inelastic behavior of piles, the response of a vertical pile embedded in a dry dense sand and subjected to cyclic lateral loading was studied experimentally in centrifuge tests conducted in Laboratoire Central des Ponts et Chaussées. A three-dimensional finite element analysis with the use of a new constitutive model for the cyclic behavior of sand was performed in order to capture the cyclic response of the single pile. Performance measure parameters were introduced to evaluate the overall response of the pile-soil system indicating that the proposed model is suitable for the prediction of the lateral response of a pile under cyclic loading and the domination of the mechanism of “system densification” upon soil densification in cyclic loading. The response of an 1x2 pile group under cyclic lateral loading is also investigated showing that the model is capable of representing the shadow effect of the pile group.

1 CENTRIFUGE LATERAL CYCLIC LOAD PILE EXPERIMENTS

Three centrifuge tests on a single pile subjected to cyclic horizontal loading were performed by Rosquoët et al (2004) at Laboratoire Central des Ponts et Chaussées (LCPC). The centrifuge models were 1/40 in scale and involved pile head loading with three different force time histories. The loading time histories were: i) 12 cycles from 960 kN to 480 kN (test P32) ii) 12 cycles from 960 kN to 0 kN (test P344) iii) 6 cycles from 960 kN to -960 kN (test P330). The experimental set up and the loading time histories (in prototype scale) are portrayed in Figure 1.

The cyclic lateral load tests were conducted on vertical friction pile placed in a sand mass of uniform density. The Fontainebleau sand centrifuge specimens were prepared by the air sand-raining process into a rectangular container (80 cm wide by 120 cm long by 36 cm deep), with the use of a special automatic hopper developed at LCPC (Garnier, 2002). The desired density of the dry sand was obtained by varying three parameters: a) the flow of sand (opening of the hopper), b) the automatically maintained drop height, and c) the scanning rate. Laboratory results from drained and undrained torsional and direct shear tests on Fontainebleau sand reconstituted specimens indicated mean values of peak and critical-state angles of $\phi_p = 41.8^\circ$ and $\phi_{cv} = 33^\circ$, respectively. Figure 1 depicts the idealized small strain shear modulus G_o used. Evidently, in this dense sand the pile used may be considered as flexible. The model pile at scale 1/40 is a hollow aluminum cylinder of 18 mm external diameter, 3 mm wall thickness, and 365 mm length. The flexural stiffness of the pile is 0.197 kN m^2 and the elastic limit stress of the aluminum is 245 MPa. The centrifuge tests were carried out at 40 g.

The instrumentation included two displacement sensors, located at the section of the pile above the ground surface, and 20 pairs of strain gauges, positioned along the length of the pile so that the bending moment profile $M(z)$ could be measured during the tests. The resultant earth

pressure $p = p(z)$, per unit length along the pile, was obtained by double differentiation of $M(z)$ as established by Matlock and Reese (Reese and Van Impe, 2001). The strain gauges were spaced at 0.6 m in prototype scale starting from the ground level to the pile tip. This single pile was driven into the sand at 1 g before rotating of the centrifuge. In flight, the single pile was subjected quasi-statically to horizontal cyclic loading through a servo-jack connected to the pile with a cable. With such a configuration the pile head is not submitted to any parasitic bending moment. The test results were obtained in the form of horizontal force-displacement time histories at the head of the pile, as well as of bending moment along the pile.

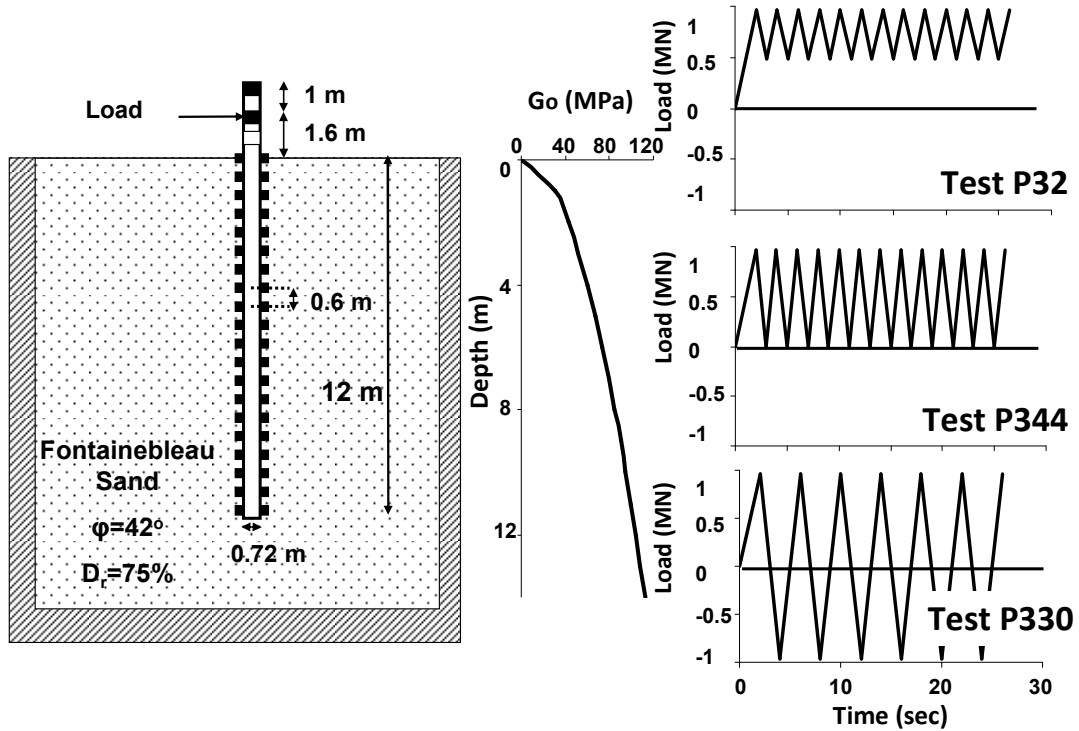


Figure 1. Experimental setup of the centrifuge tests conducted in LCPC and load time histories of the three tests (P32, P344 and P330). All dimensions refer to the modeled prototype

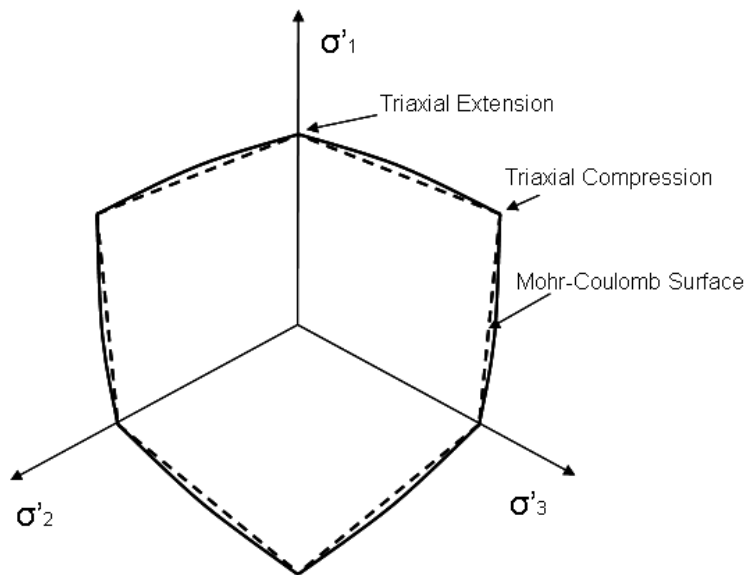


Figure 2. Shape of yield criterion of the proposed constitutive model

2 FINITE ELEMENT MODELING

The above mentioned centrifuge tests were modeled numerically in 3D using the finite element code ABAQUS. The pile is assumed to be linear elastic while the cyclic soil behavior is described via a nonlinear constitutive law with kinematic hardening law and associated plastic flow rule. Approximately 43000 elements were used for each analysis. The soil is modeled with 8-node brick elements while the pile is modeled with 3D beam elements placed at its center and connected with appropriate kinematic restraints with the nodes at the perimeter of the pile in order to model the complete geometry of the pile. The solid elements inside the perimeter of the pile have no stiffness. In this way, each pile section behaves as a rigid disc: rotation is allowed on the condition that the disc remains always perpendicular to the beam axis, but stretching cannot occur.

3 CONSTITUTIVE SOIL MODEL

Soil behavior is modeled through a constitutive model with nonlinear kinematic hardening and associated plastic flow rule. The evolution law of the model consists of two components: a nonlinear kinematic hardening component, which describes the translation of the yield surface in the stress space (defined through the back-stress α), and an isotropic hardening component, which defines the size of the yield surface σ_0 at zero plastic deformation. The kinematic hardening component is defined as an additive combination of a purely kinematic term (linear Ziegler hardening law) and a relaxation term (the recall term), which introduces the nonlinearity. The model incorporates two hardening parameters C and γ that define the maximum transition of the yield surface, and the rate of transition, respectively. A user subroutine is imported in ABAQUS, which relates the model parameters to the principal stresses and the Lode angle at every loading step. Incorporating the Lode angle effect allows for significant accuracy in three-dimensional shear response environments. The yield surface of the proposed constitutive model is determined to fit the Mohr-Coulomb failure response in a triaxial loading test for both compression and extension conditions assuming linear interpolation for the intermediate stress states. For this reason, the parameter k is introduced which is a function of Lode angle and takes values from 0 to 1. $k=0$ corresponds to pure triaxial extension conditions and $k=1$ to pure triaxial compression conditions. In summary, the constitutive model parameters are calibrated to match the Coulomb failure criterion on the principal stresses plane for every apex of the hexagon with the smooth envelope of Figure 2.

The distribution of Young's Modulus varies parabolically with depth according to:

$$C = E = E_0 \left(\frac{\sigma_v}{100} \right)^m \quad (1)$$

where E_0 is the reference Young's Modulus, σ_v the vertical stress and m a parameter that defines the distribution of E with depth. E_0 is equal to 192000 kPa and m is equal to 0.5 according to the calibration performed by Gerolymos et al (2009). The hardening parameter γ , which is a function of the internal friction angle, was calibrated to correspond to a critical-state friction angle $\phi_{cv} = 33^\circ$. The constitutive model parameters E_0 , m and γ were calibrated only to predict the recorded "force – displacement" curve at the head of the pile from the strain gauges for the 12 cycles of loading of test P32.

4 NUMERICAL SIMULATION

The model is then used to simulate test P344 where the single pile is subjected to one-way cyclic load with maximum horizontal force 960 kN and minimum horizontal force 0 kN. Subsequently it is applied to predict the response of an 1x2 pile group subjected to the same average

horizontal cyclic loading. It should be noted that the applied loads always stay in the domain of service loads. Bending moment, shear force and soil reaction profiles were compared, but due to lack of space, only the results for the bending moments are presented herein.

4.1 Simulation of single pile

The computed force-displacement curve at the pile head is compared to the experimental data in Figure 3 for the 12 cycles of loading. In one way cyclic loading, the pile displacement increases as the number of cycles increases. In this figure it is observed that the model is capable of predicting the plastic shakedown response of the pile. This plastic shakedown response is the resultant of the following two mechanisms: (a) Soil densification due to the reduction of voids, and (b) “System densification” due to the gradual extension of the resisting soil mass, towards greater depths with cyclic loading. Only the second mechanism is captured by the proposed model. Despite the small discrepancy in the residual displacement at the pivot point of each unloading phase, the comparison is quite satisfactory.

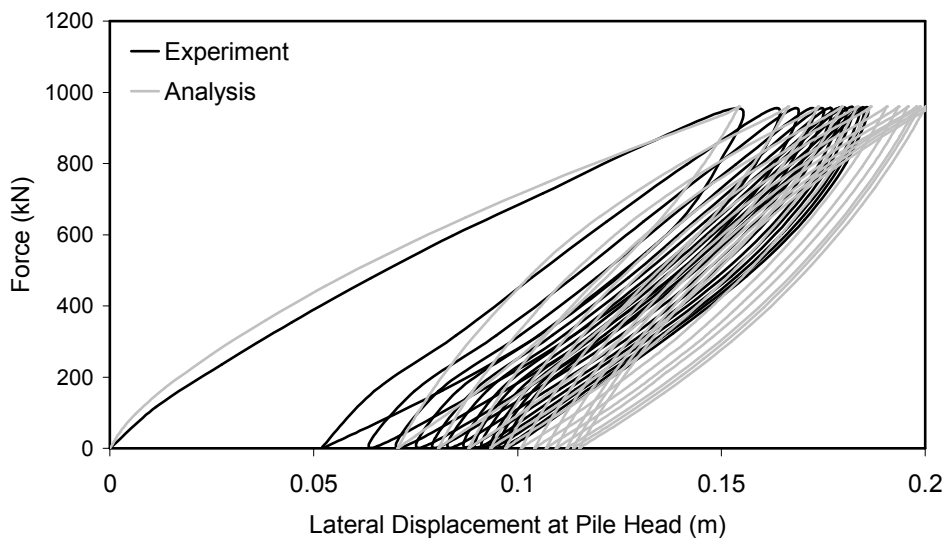


Figure 3. Experimental and Computed Force – Displacement curve at pile head for single pile

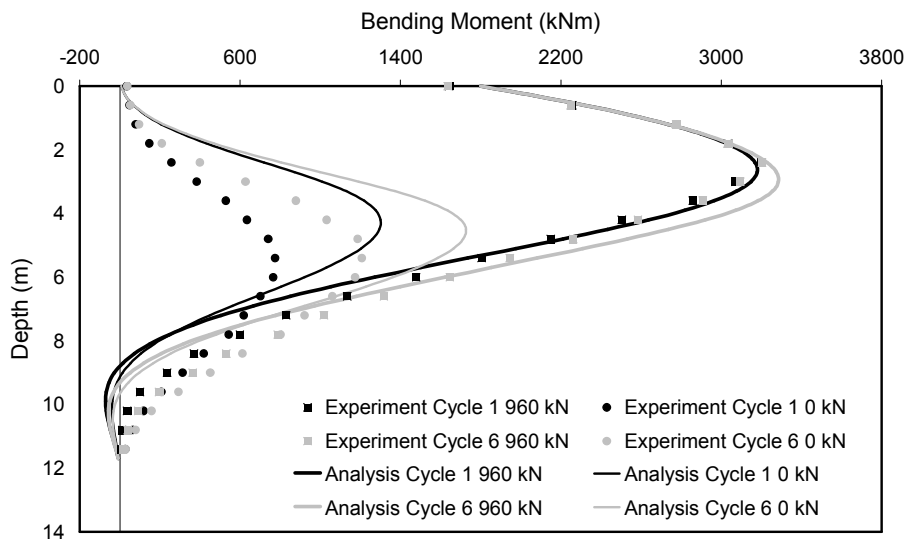


Figure 4. Comparison of computed and recorded bending moment distributions for test P344 at two different stages of loading : a) at the 1st cycle, and b) at the 6th cycle. The maximum applied load is 960 kN and the minimum load is 0 kN.

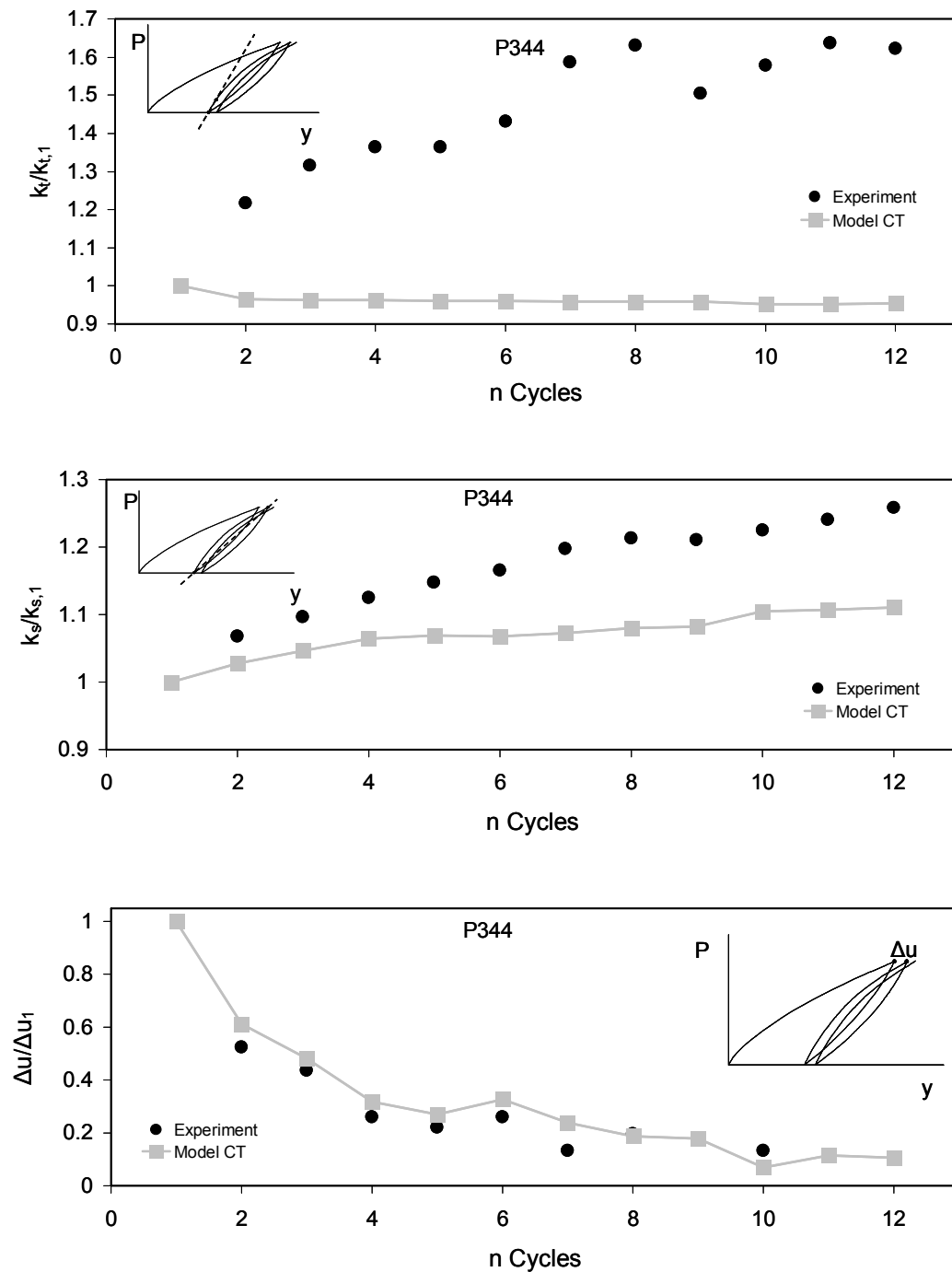


Figure 5. a) Normalized tangent stiffness with respect to the first cycle of loading, b) Normalized secant horizontal pile stiffness with respect to the first cycle of loading, c) Relative pile-head displacement between two consecutive re-loading-unloading reversal points normalized with the one between the loading-unloading and the first re-loading - unloading reversal points

Figure 4 compares the bending moment profiles at the first and sixth cycle of loading. In general, the agreement between the measured and the computed curves is quite satisfactory. The model predicts well the shape of the moment distribution and the increase of the bending moments with the increase of the number of cycles both for loading and unloading of the pile. The model is also capable of simulating the depth of the maximum bending moment both for loading and unloading conditions as well as the shift of the maximum bending moment at a higher depth as the number of cycles increases. The discrepancy in the unloading phase is attributed to that the developed soil constitutive model cannot reproduce soil densification.

Three performance measure parameters were introduced to evaluate the overall response of the pile-soil system. Figure 5a depicts the tangent stiffness at each unloading-reloading reversal point divided by the tangent stiffness at unloading-reloading reversal point of the first cycle, which is indicative of the elastic response of the pile. It is interesting to observe that the computed tangent stiffness remains constant for the proposed model described above, unaffected by cyclic loading, while the measured tangent stiffness increases in test P344. This increase in the measured tangent stiffness is attributed to soil (material) densification during cyclic loading, an effect that is not simulated by the utilized soil constitutive model and which prevails in the elastic response of the pile.

Figure 5b presents the secant stiffness between two sequential reversal points normalized by the secant stiffness of the first cycle, which is indicative of the overall response of the pile during cyclic loading. It is worthy of note that both the computed and the measured secant stiffnesses increase with the number of cycles. Given that the system densification is captured numerically, the difference between measured and computed response is only attributed to soil densification.

Figure 5c presents the relative pile head displacement between two consecutive re-loading-unloading reversal points normalized with the one between the loading-unloading and the first re-loading-unloading reversal points. The pile displacement at pivot points increases in the asymmetric cyclic loading with a decreasing rate and the pile finally reaches a zero-plastic strain rate equilibrium. It is observed that the computed versus measured response is in well agreement, implying that the mechanism of “system densification” dominates upon that of soil densification.

4.2 *Simulation of 1x2 pile group*

Having compared and validated the proposed constitutive model with the analysis of a single free-head pile under lateral cyclic loading in nonhomogeneous sand, the effects of lateral cycling loading on a 1x2 pile free-standing free-head pile group are investigated. The piles, located at a distance of three diameters, are parallel to the load direction. The pile heads are hinged (zero bending moment) to the pile cap via appropriate kinematic constraints which ensure the diaphragmatic action towards the loading direction.

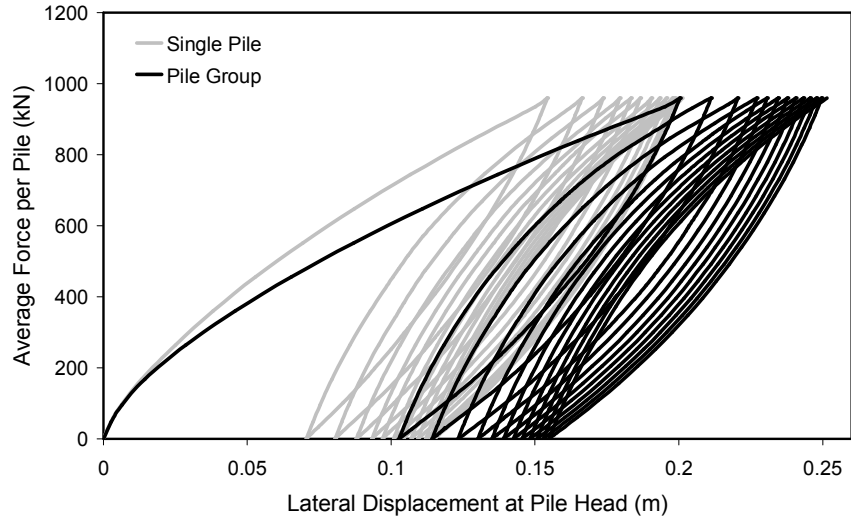
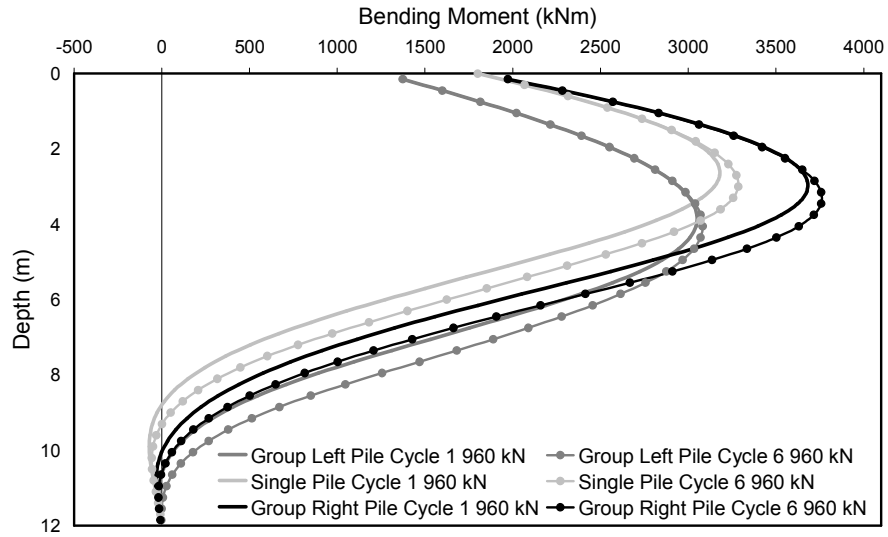


Figure 6. Force – Displacement curve of the single pile and the pile group for the loading of test P344



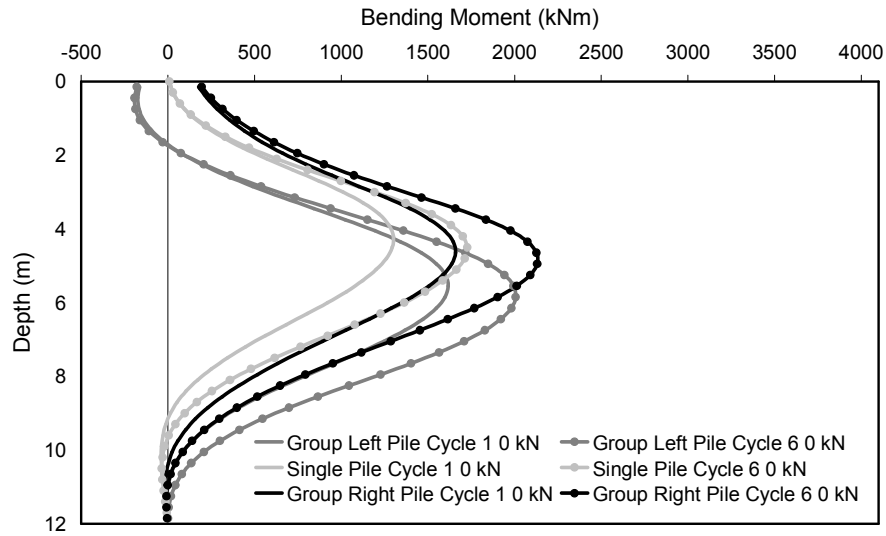


Figure 7. Comparison of computed bending moment distributions of the pile group and the single pile for test P344 at two different stages of loading : a) at the 1st cycle, and b) at the 6th cycle. The maximum applied load is 960 kN and the minimum load is 0 kN.

The pile group is subjected to an asymmetric cyclic lateral loading similar to that of test P344 but with double amplitude (1920 kN). Figure 6 plots the average force per pile versus group displacement and compares it with the corresponding force-displacement loop of the single isolated pile. For the same average load, the group displacement is greater than that of the solitary pile. This behavior is attributed to that the passive failure zones of the piles in the group tend to overlap (shadow effect) as the lateral load increases, thus reducing the average soil resistance on the piles in the group. The shadow effect becomes more dominant with decreasing pile-to-pile distance. As in the case of the free-head single pile, the group displacement increases at a decreasing rate with the number of cycles finally reaching a plastic shakedown equilibrium. Interestingly, the force-displacement loop of the pile group is wider than the corresponding of the single isolated pile, implying greater soil plastification.

Figure 7 depicts the detailed distribution of bending moments with depth along each pile in the group computed for different stages of loading. Comparison is given with the respective results from the analysis of the single isolated pile. As in the case of the single pile, it is observed that the maximum bending moment increases with the number of cycles and shifts to greater depths following the progressive extension of soil yielding for both piles of the group. Furthermore, the leading pile develops the largest bending moment in comparison to both the trailing and the single pile which shows an intermediate response. The discrepancy in the bending moment distribution between the trailing and the leading pile is attributed to the shadow effect. Finally, upon unloading, and for zero applied lateral force, the bending moments are not zero, instead they retain large values comparable to those for the maximum applied load. This reduction in the maximum values is about 40% for the bending moments. It should be noted, that in the case of a linear soil all the aforementioned quantities would vanish to zero, as soil elasticity would act as a restoring force for the pile.

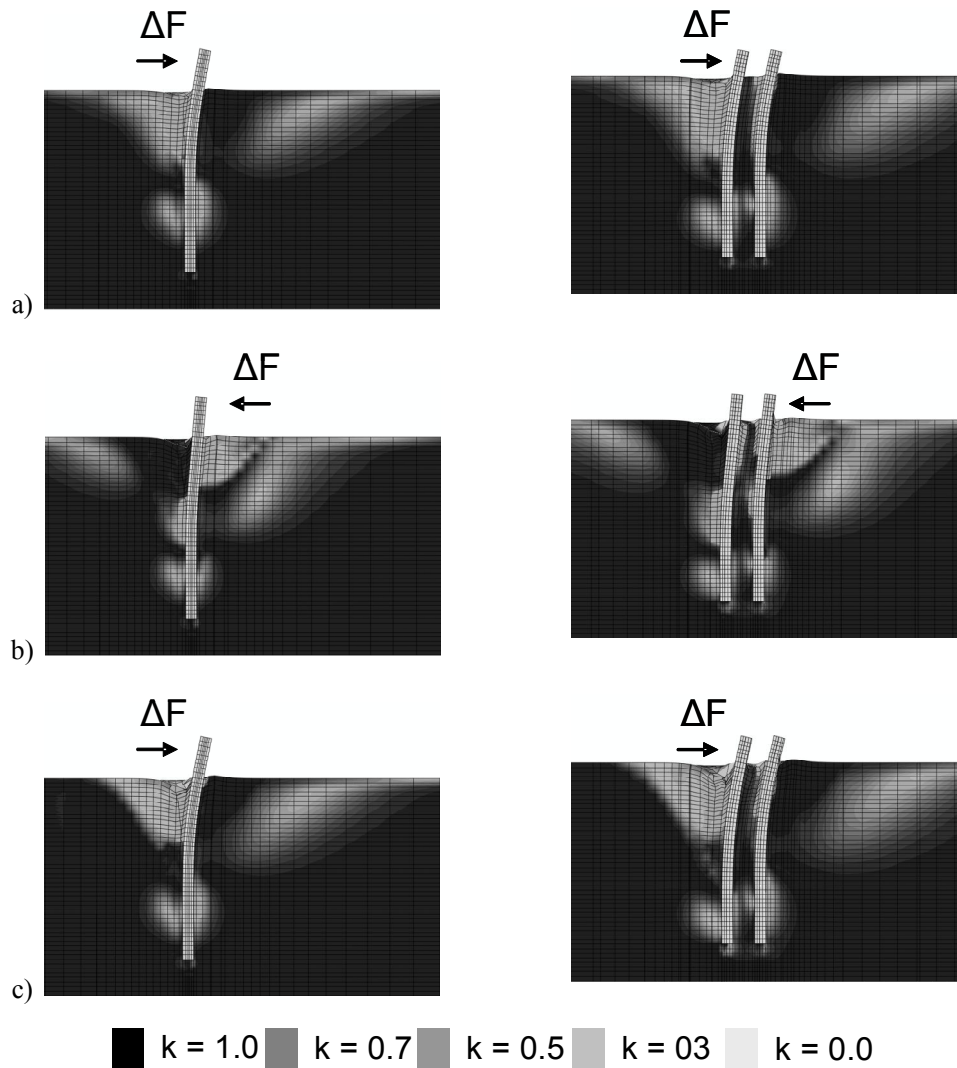


Figure 8. Cross-section of the model with the contours of the active and passive stress states in terms of the state parameter k at three different stages of loading of the single pile and the pile group: a) at the 1st cycle at 960 kN, b) at the 12th cycle at 0 kN, and c) at the 12th cycle at 960 kN. $k = 1$ corresponds to pure triaxial compression loading condition (passive state), and $k = 0$ to pure triaxial extension loading condition (active state) while $k \approx 0.5$ sets the boundaries between the active and the passive state. (Deformation Scale Factor = 5)

Figure 8 depicts the contours of the active and passive stress states in terms of the state parameter k at three different stages of : a) at the 1st cycle at 960 kN, b) at the 12th cycle at 0 kN, and c) at the 12th cycle at 960 kN for the single pile and the pile group. $k = 1$ corresponds to pure triaxial compression loading condition (passive state), and $k = 0$ to pure triaxial extension loading condition (active state) while $k \approx 0.5$ sets the boundaries between the active and the passive state. It is interesting to observe that the plastic shakedown effect on the single pile is reflected by the gradually developing fan-shaped stress bulb, the frontal part of which represents the mobilized soil mass that is in a passive state and expands with increasing cycles of loading, while the trailing part corresponds to the mobilized soil zone that is in an active state and shrinks with increasing number of cycles. The larger the bulb of “passive” stresses the greater the lateral soil reactions that resist the applied load, and finally, the pile reaches a steady state equilibrium of constant plastic strain (plastic shakedown). For the case of the pile group, the gradual expansion of the compression stress bulb with number of cycles signals the plastic

shakedown process until the pile group reaches a steady state equilibrium of constant plastic strain. The shadow effect is manifested by the formation of a relaxation zone ($k = 0$) at the back of the leading pile which softens the response of the trailing one.

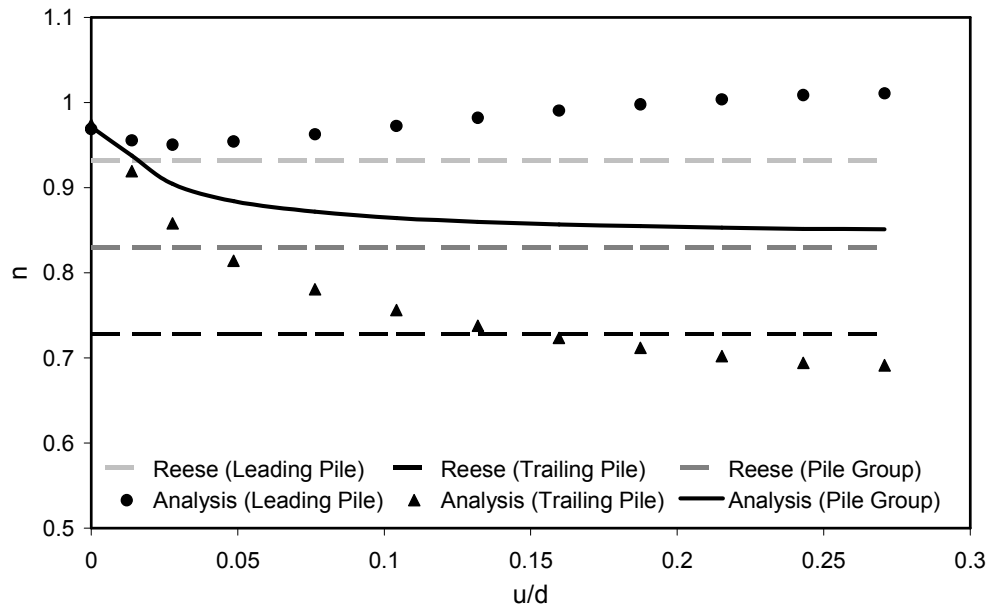


Figure 9. Comparison of efficiency factors of the numerical analysis with the efficiency factors proposed by Reese and Van Impe.

Finally, Figure 9 compares the efficiency factors of the piles (should not be confused with pile-to-pile interaction factors) calculated with the constitutive model and proposed by Reese and Van Impe (2001). It is interesting to observe, that the calculated efficiency factors converge to those of Reese and Van Impe (2001) at very large pile head displacements, with a small discrepancy for the leading pile which shows to recover its initial stiffness ($\eta_l \approx 1$), a hardening response which may be attributed to the plastic shakedown effect. On the contrary, the computed efficiency factor for the trailing pile decreases with increasing horizontal displacement, as a result of the shadow effect, but at decreasing rate due the plastic shakedown induced hardening response of the pile group (reaching a minimum value of $\eta_t \approx 0.7$).

Of equal, if not more, interest is that at zero and/or very small pile displacements (elastic response), all the three computed efficiency factors (for the leading pile, the trailing pile and the pile group) are very close to 1 (≈ 0.97), implying that pile-to-pile interaction has an insignificant effect on the elastic response of the pile group. This could possibly suggest a “destructive” interference in pile-to-pile interaction rather than that pile-to-pile interaction factors are zero (which are certainly not, according to valid published results, e.g. Mylonakis and Gazetas 1998). The negligible pile-to-pile interaction effect is also evident in Figure 6 which compares the computed force-displacement response of the single pile and the pile group.

5 CONCLUSIONS

A simplified constitutive soil model for the static and cyclic response of piles embedded in cohesionless soil was materialized into a three-dimensional finite element code. The model predictions were compared with experimental results of a single pile in dry sand, and subsequently it was applied at a pile group of two piles with similar geometric characteristics and soil conditions to those of the experimental tests. The main conclusions are:

- The plastic shakedown response of both the single pile and the pile group is mostly attributed to the so-called “system” densification rather than to cyclically-induced soil densification.
- During cyclic loading, the mechanism of “system” densification dominates upon soil densification with the contribution of the latter to the macroscopic response of the piles (or pile group) being rather insignificant.
- The formation of a relaxation zone at the back of a leading pile (in the pile group) significantly reduces the lateral soil resistance on the trailing pile. This behavior, well-known in the literature as “shadow effect” is more prominent at large pile deformations.
- The efficiency factor of the leading pile decreases with increasing pile displacement but at extremely large deformations recovers if not overpasses its initial (zero-amplitude) strain value. On the contrary, the efficiency factor of the trailing pile decreases monotonically with loading, but at a decreasing rate, finally reaching an asymptotic value.
- The asymptotic values of all three efficiency factors (for the leading pile, the trailing pile and the pile group) compare well with those by Reese and Van Impe, 2001.

6 ACKNOWLEDGEMENTS

The financial support for this paper has been provided under the research project “DARE”, which is funded through the European Research Council’s (ERC) “IDEAS” Programme, in Support of Frontier Research–Advanced Grant, under contract/number ERC–2–9–AdG228254–DARE.

REFERENCES

- Garnier J., 2002, “Properties of soil samples used in centrifuge models”, *Invited Keynote Lecture, International Conference on Physical Modelling in Geotechnics – ICPMG ’02*, R. Phillips et al. (Eds), published by A.A. Balkema, Rotterdam, 1, pp 5-19.
- Gerolymos N., Escoffier S., Gazetas G., Garnier J., 2009, “Numerical Modeling of centrifuge cyclic lateral pile load experiments”, *Earthquake Engineering and Engineering Vibration*, 8, pp 61-76
- Mylonakis, G. and Gazetas, G. 1998, “Vertical Vibration and Distress of Piles and Pile Groups in Layered Soil”, *Soils and Foundations*, Vol. 38, No 1, pp. 1-14
- Reese L.C., Van Impe W.F., 2001, *Single Piles and Pile Groups under Lateral Loading*, A.A.Balkema. Rotterdam
- Rosquoët F., Garnier J., Thorel L., Canepa Y., 2004, “Horizontal cyclic loading of piles installed in sand : Study of the pile head displacement and maximum bending moment”, *Proceedings of the International Conference on Cyclic Behaviour of Soils and Liquefaction Phenomena*, Bochum, T. Triantafyllidis (Ed.), Taylor & Francis, pp 363-368.

Seismic Analysis of Reinforced–Earth Wall on Precarious Soil Improved with Stone Columns

P. Tasiopoulou, G. Gazetas

Soil Mechanics Laboratory, National Technical University, Athens, Greece

ABSTRACT: The seismic response of a 15 m high reinforced-earth retaining wall on top of a soil deposit containing liquefiable soil layers is explored with effective-stress dynamic time history analyses. The simultaneous generation and dissipation of seismic excess pore-water pressures (EPWP) is reproduced in the analysis. The need for, and effectiveness of, soil improvement with 60 cm stone columns placed in a triangular configuration is demonstrated with a series of graphs. Improvement results from both the increased rate of EPWP dissipation and, mainly, the increased stiffness/strength of the system.

1 INTRODUCTION: THE MAJOR PROJECT

A significant project is heading to the final stage of planning — architectural, static, geotechnical, hydraulic and electromechanical: the Cultural Center of Stavros Niarchos Foundation located in the Athens coastal, covering approximately 200,000 square meters. The cultural center will include two interconnected buildings, the "National Opera" and the "National Library", and a theme park of grand expanse. The park will be developed on a manmade hill (landfill) of mild slope which culminated in an almost vertical edge 15m high, a small distance from the Library. Figure 1 shows a section of the hill, its vertical edge and the Library. Being the conception of the famous architect RENZO PIANO (the architect of the Kansai airport terminal), the entire center and its facilities is planned to be in excellent harmony with the upgraded environmental surroundings and will consist a model of energy efficiency and economy in the use of water resources. The seismic design of the structural components of the project, including seismic isolation systems, is of equal importance from an engineer's point of view.

The stability of the practically vertical slope was one of the most interesting and challenging geotechnical issues, not only due to its significant height (15m), but also due to the precarious foundation soil, which comprises silty sand layers loose enough to be considered liquefiable. Moreover, because of the close proximity of the retaining wall to the library through an exit zone only 10m wide, the seismic motion for the design of the wall was chosen to be sufficiently high corresponding to a return period of 1000 - 2000 years — as in the case of the two buildings (Library and Opera).

The lack of space also led to the solution of an reinforced - earth retaining wall for the support of the vertical verge of the park hill. The current paper sheds light to the major findings regarding the seismic stability and the deformation of landfill – retaining wall – soil system, through dynamic effective stress analyses.

2 NUMERICAL MODELING

2.1 Two-dimensional modelling of stone columns

In the framework of the present study, the numerical simulation of the stone columns was performed assuming plane strain conditions. Several methods have been developed in the literature to convert the axisymmetric unit cell to the equivalent plane strain model in terms of drainage (permeability) and bearing capacity (column stiffness). The method that was followed in this study has been proposed by Indraratna and Redana (1997) and validated by Tan, Tjahyon and Oo (2008).

According to this method, the total cross-sectional area of one column and its surrounding soil are preserved in both conditions (Figure 2). The plane-strain column width is given by the following relationship based on the equivalence of area replacement ratio:

$$b_c = B \frac{r_c^2}{R^2} \quad (1)$$

The relationship between R and B may be given by the following equation based on the equivalence of total area for a square pattern of columns (Barron 1948):

$$R = 1.13B \quad (2)$$

Given that the replacement ratios and the Young's moduli of the soil are equal for axisymmetric and plane strain conditions ($a_{s,plane} = a_{s,axis}$ and $E_{s,plane} = E_{s,axis}$), the plane strain column stiffness is the same with the axisymmetric one ($E_{c,plane} = E_{c,axis}$). The plane strain soil permeability is taken equal to its axisymmetric counterpart, i.e., $k_{h,plane} = k_{h,axis}$ and $k_{v,plane} = k_{v,axis}$. This method thus retains the axisymmetric material properties for the plane strain geometry.

The validity of these approximations has been tested in two stages by Tan, Tjahyon and Oo (2008): comparison of unit-cell simulations and comparison with the field data from an embankment case history. It was shown that they reproduce well the 3D behaviour of stone columns.

In this study, the two-dimensional modeling of the stone columns has been based on the above method. The actual stone column configuration in the field close to the Library consists of a triangular grid of stone columns with diameter 0.60m and spacing 2m, covering a width of 16m under and slightly beyond the wall (Figure 2). The spacing of 2m was preserved in the numerical simulation.

2.2 Dynamic numerical analysis

The goal of this study is to investigate the behavior of the earth retaining wall under seismic conditions *with* and *without* stone columns. The actual stone column configuration in the field close to the Library consists of a triangular grid of stone columns with diameter 0.60m and spacing 2m, covering a width of 16m under and slightly beyond the wall (Figure 3). The spacing of 2m was preserved in the numerical simulation. Thus, for $B = 2$ m and $r_c = 0.30$ m, the equivalent width of the stone columns in the plane strain model becomes 0.14m ($b_c = 0.07$ m) using Equation (1).

In total, two categories of dynamic analyses in terms of effective stresses were conducted, using the finite difference code FLAC (Itasca, 2005):

- with stone columns (Figure 4)
- without stone columns.

In particular, Figure 4 illustrates the soil profile with stone columns and the points of recording the excess pore pressure time histories in the dynamic analyses. These points were kept the same for the analyses without the stone columns to directly compare the results from the two categories of analyses. Figures 5 and 6 present the permeability values of the soil layers assigned to the numerical models with and without stone columns. The seismic input motion at the base of the models is shown in Figure 7. The simulation involves the constitutive law of Byrne (1991) for pore pressure generation which is incorporated in the standard Mohr-Coulomb plasticity model.

3 BEHAVIOUR OF EARTH WALL *WITH* AND *WITHOUT* STONE COLUMNS

In both cases (with and without stone columns), the deformation pattern of the soil – wall system is similar, by the displacements are considerably larger if no stone columns are installed. The displacement vectors in Figure 8 indicate the outward rigid-body movement and rotation around the toe of the wall of the reinforced part of the fill (which was modeled to behave elastically). This is accompanied by large displacements deep in the soil under the wall, tending to form an almost circular failure mode. In particular, the maximum horizontal wall displacement at the top is 23 cm with stone columns and 37 cm without stone columns (Figure 9).

The distribution in space and time of excess pore water pressures (EPWP) is portrayed in Figures 10 - 14. It is evident that both the dense and the medium sand exhibit similar response in the two cases. The excess pore pressures are dissipated at the same rate within the "critical" zone (below the earth wall), thanks to seepage of pore water towards the toe of the wall, which occurs regardless of the presence or not of stone columns (Figures 10 and 11). This flow path towards the toe of the wall stems from the difference of the overburden stress and consequently of the excess pore pressure developing in the free field (no fill on top) as opposed to the soil below the fill. Thus the water pressures developing below the landfill are much higher than those in the free field. This difference which is very profound at the boundary of the wall, results in the above described water flow (from high pressures to lower ones).

Away from the "critical" area, the silty sand experiences more or less the same response in terms of EPWP generation. However, the dissipation of EPWP is understandably more profound with stone columns (Figures 13 and 14). This offers a rather clear evidence of a beneficial role of the stone columns. In addition, the increased stiffness of the foundation soil due to the presence of stone columns reduces significantly the outward movement of the earth retaining wall.

4. CONCLUSIONS

Improvement of the ground underneath the reinforced-earth walls which form the terminal boundary of the hill, was necessitated from the large height of the wall (up to 15 m) and the presence of soft and / or liquefiable soils in the supporting ground. "Stone-columns" have emerged as the likely choice to provide increased stiffness/strength in the foundation and help in rapidly dissipating "deleterious" seismic excess pore-water pressures. The scope of the numerical study is to assess the effectiveness of a particular stone column configuration in achieving these two objectives.

To this end, a numerical 2-dimensional (2D) seismic response analysis is performed in terms of effective stresses. To overcome the serious limitation of plane-strain modeling for the truly 3D geometry of the stone columns, an approximate equivalence of the axisymmetric flow of a single *circular* stone column with the 2D lateral flow of a single *row* stone column was enforced, along with stiffness compatibility.

The main conclusion of our study is that thanks to the relatively high permeability of the dense sand, medium sand and silty sand layers, dissipation of excess pore-water pressures developing during shaking is substantial. The presence of stone columns under the wall increases somewhat the rate of dissipation; but, moreover, it leads to increased robustness and thereby significant improvement of computed wall performance.

5. REFERENCES

- Byrne, P. M. (1991) "A Cyclic Shear-Volume Coupling and Pore-Pressure Model for Sand," in Proceedings: Second International Conference on Recent Advances in Geotechnical Earthquake Engineering and Soil Dynamics (St. Louis, Missouri, March 1991), Paper No. 1.24, 47-55.
- Indraratna, B., and Redana, I. W. (1997) "Plane-strain modeling of smear effects associated with vertical drains." *Journal of Geotechnical and Geoenvironmental Engineering*, 123(5), pp. 474-478.
- Itasca. *Fast Lagrangian Analysis of Continua*. Itasca Consulting Group Inc., Minneapolis, Minnesota, 2005.
- Tan, S. A., Tjahyong, S. and Oo, K. K. (2008) "Simplified Plane-Strain Modeling of Stone-Column Reinforced Ground", *Journal of Geotechnical and Geoenvironmental Engineering*, ASCE, February 2008, pp. 185-194.

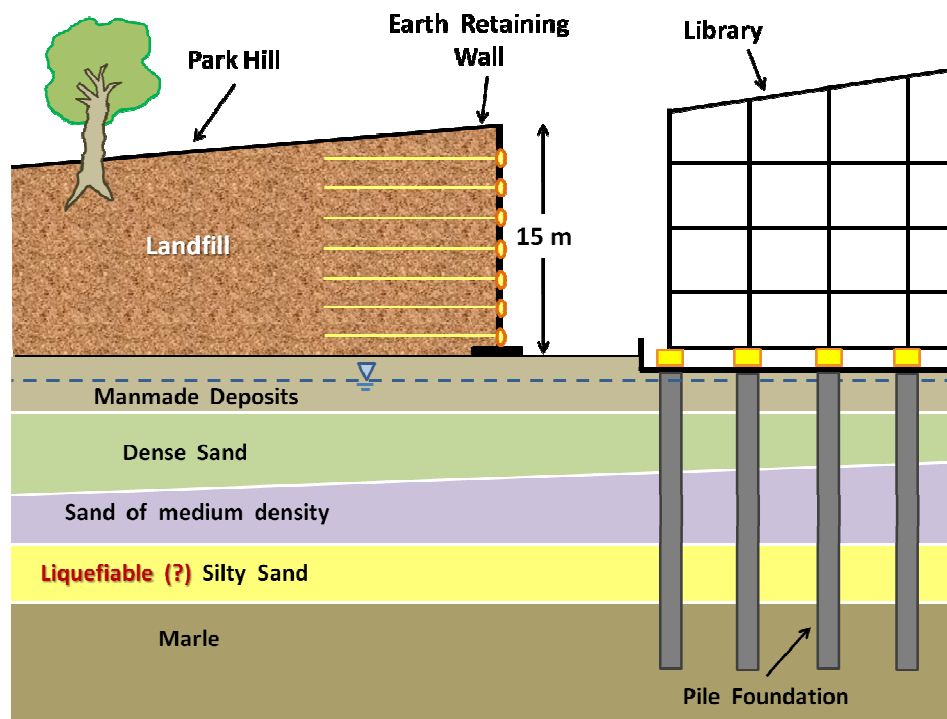


Figure 1. Sketch of the section of the retaining wall at the proximity with the Library.

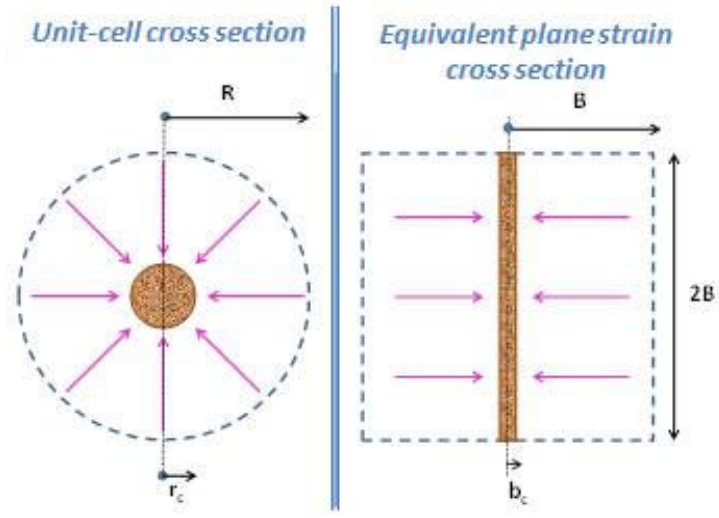


Figure 2. Equivalence of axisymmetric and two-dimensional unit cell of a stone column.

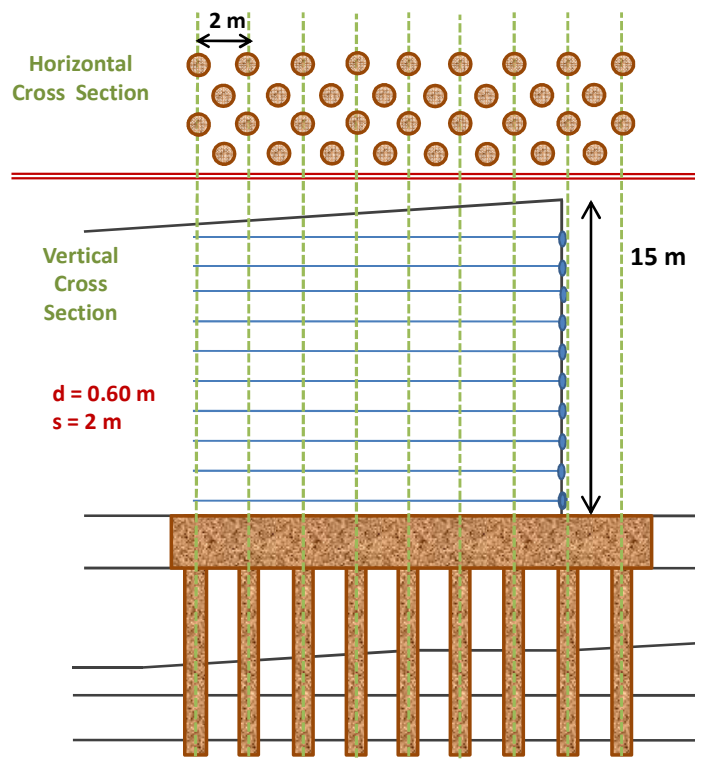


Figure 3. Stone column configuration below the reinforced earth-wall.

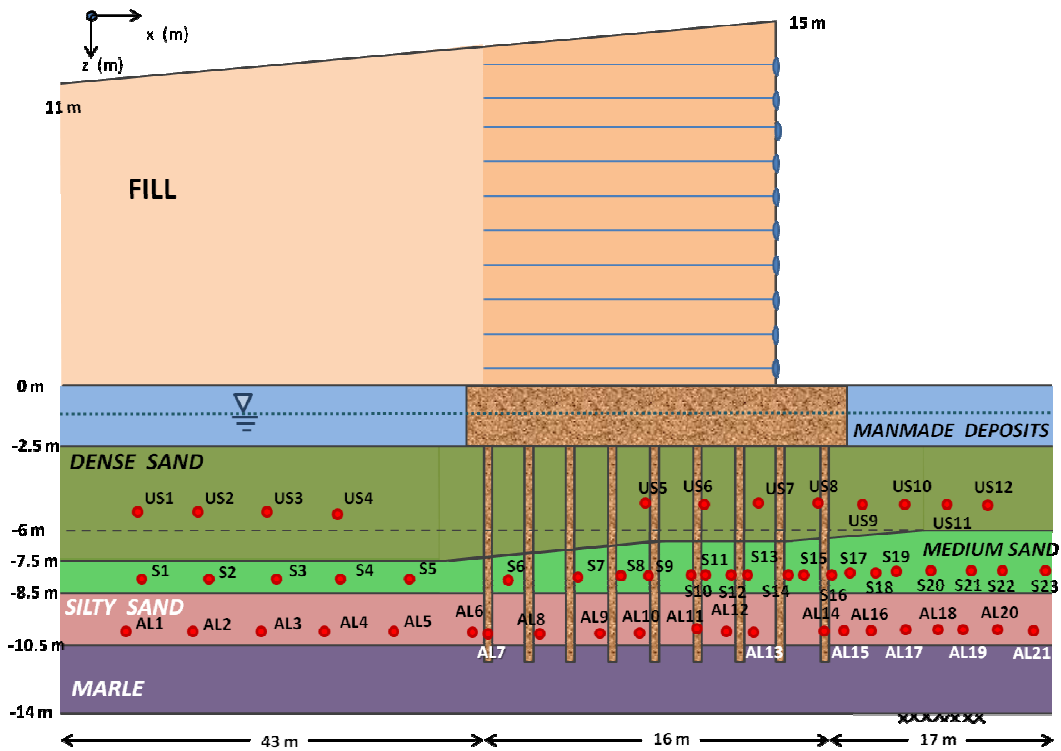


Figure 4. Sketch of the soil profile *with* stone columns and illustration of the points of recording of excess pore pressures.

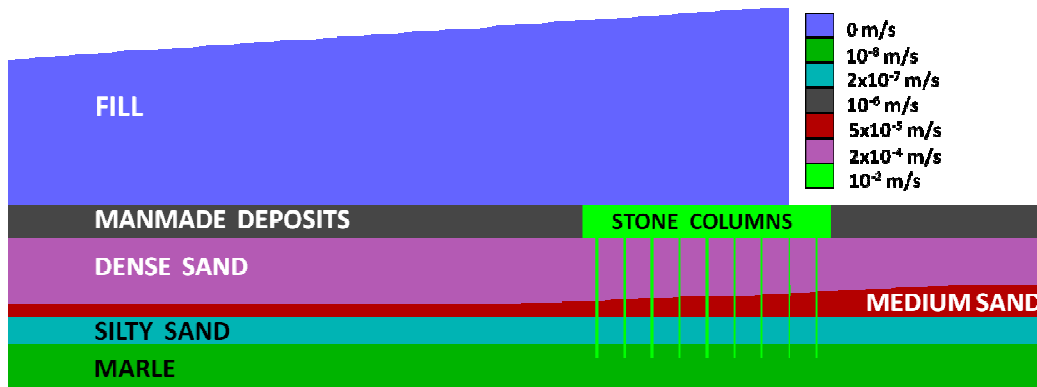


Figure 5. Illustration of the permeabilities of the soils of the numerical model *with* stone columns.

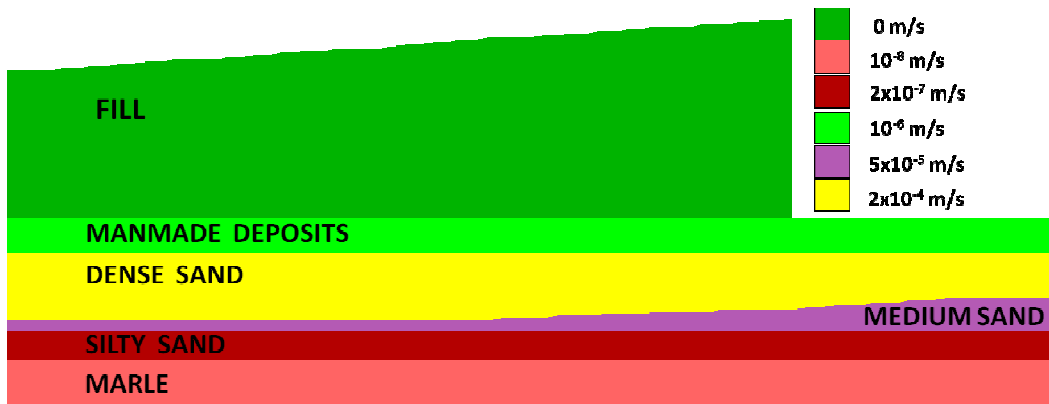


Figure 6. Illustration of the permeabilities of the soils of the numerical model *without* stone columns.

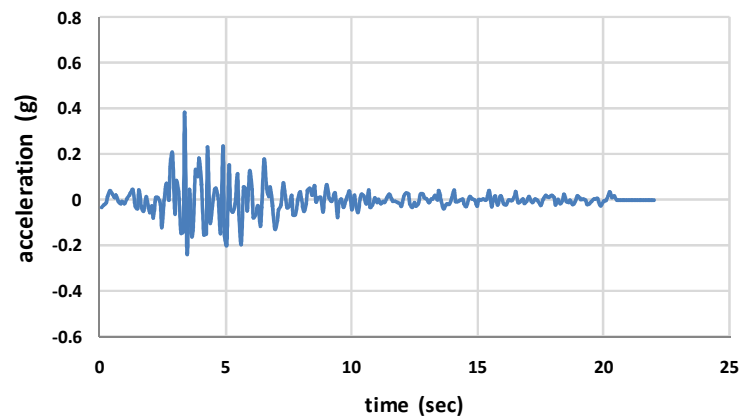


Figure 7. Input ground motion at the base of the numerical models.

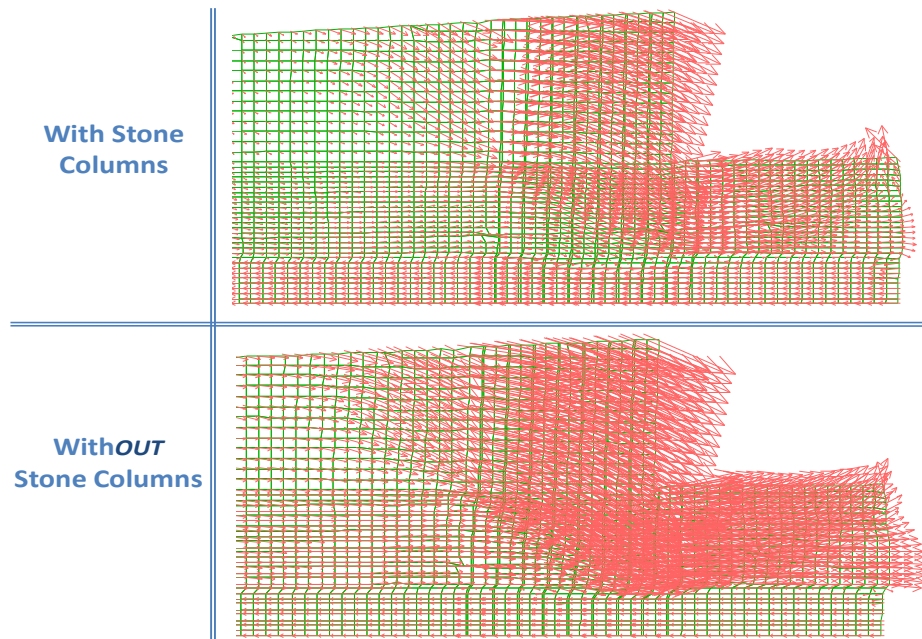


Figure 8. Displacement vectors at the end of shaking *with* and *without* stone columns.

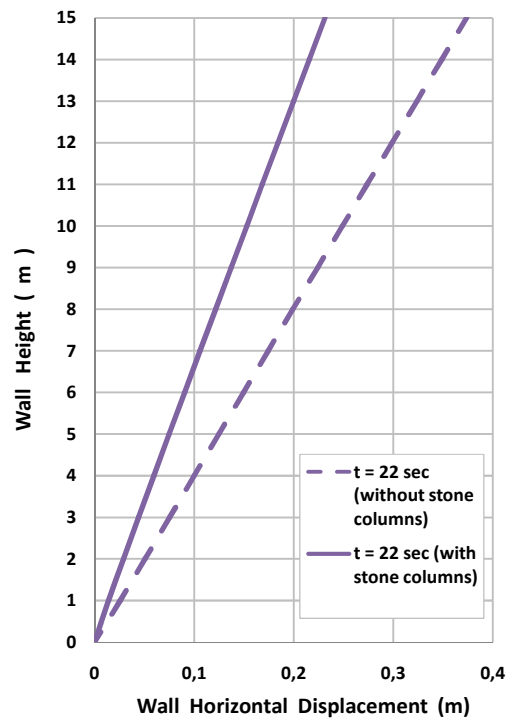


Figure 9. Distribution of horizontal displacements of the wall at the end of shaking *with* and *without* stone columns.

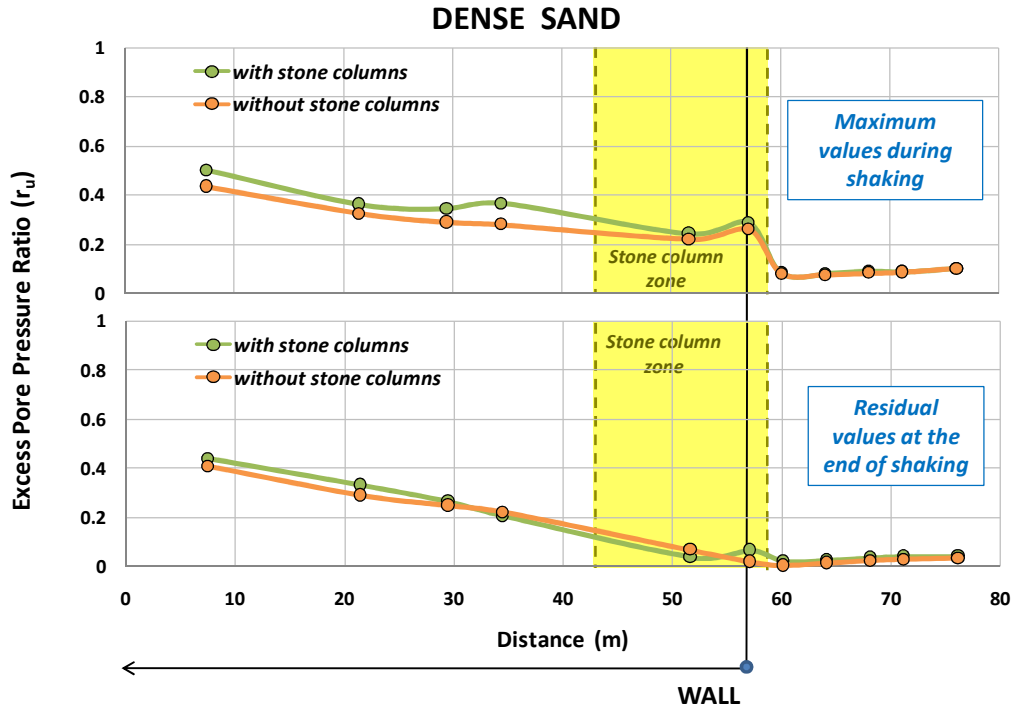


Figure 10. Distribution of maximum and residual excess pore pressure ratios along the dense sand layer (Figure 4) *with* and *without* stone columns.

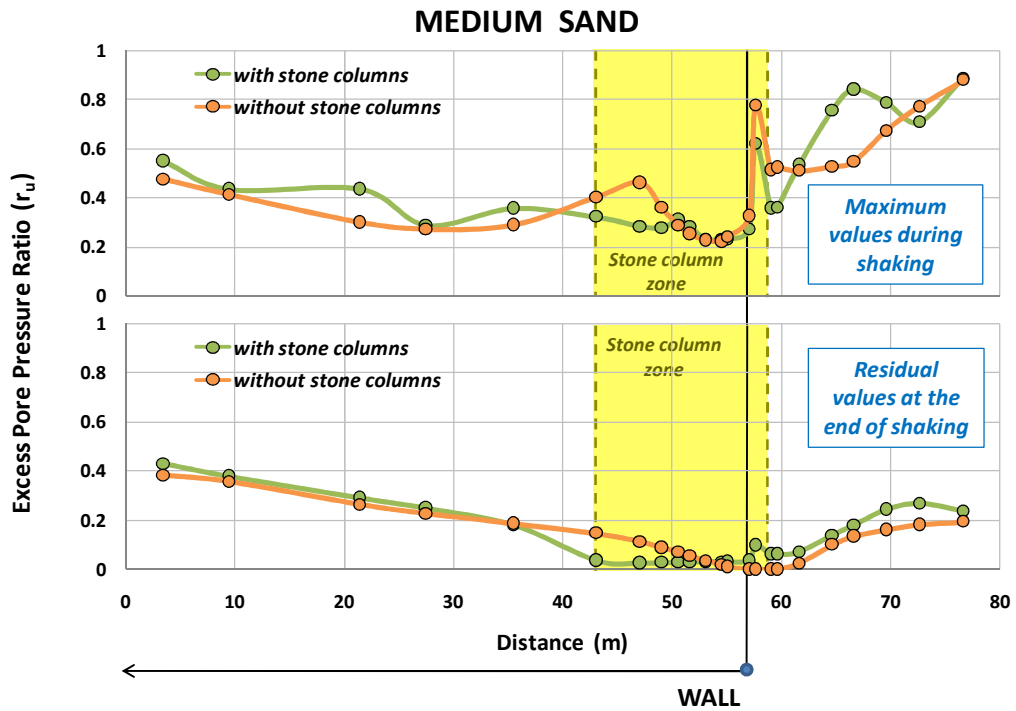


Figure 11. Distribution of maximum and residual excess pore pressure ratios along the medium sand layer (Figure 4) *with* and *without* stone columns.

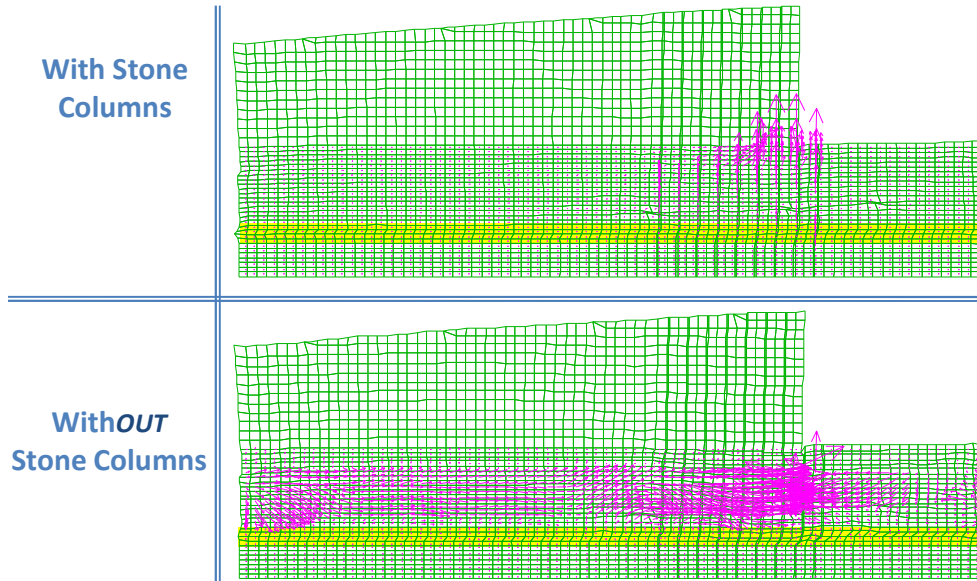


Figure 12. Flow vectors during shaking *with* (above) and *without* (below) stone columns. The silty sand layer has been colored yellow.

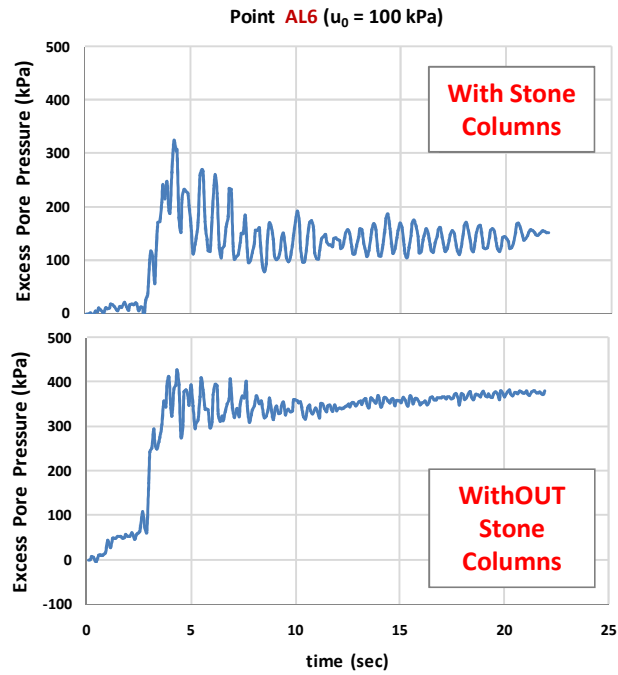


Figure 13. Time histories of excess pore-water pressures at a selected point within the silty sand layer (Figure 4) *with* stone columns (above) and *without* stone columns (below).

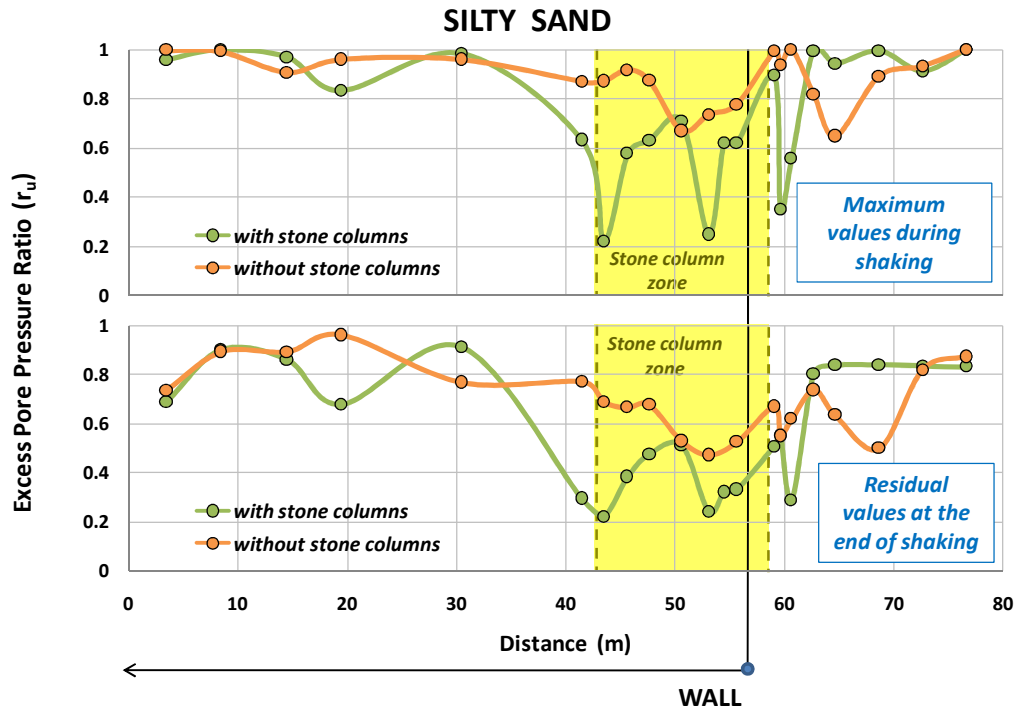


Figure 14. Distribution of maximum and residual excess pore pressure ratios along the silty sand layer (Figure 4) *with* and *without* stone columns.

Correlation of Ground Motion Characteristics with Liquefaction in the Christchurch February 2011 earthquake

P. Tasiopoulou, E.Smyrou, G. Gazetas

Soil Mechanics Laboratory, National Technical University, Athens, Greece

I.E. Bal

Fyfe Europe S.A., Athens, Greece

ABSTRACT: Hit by two severe earthquakes in September 2010 and February 2011, the city of Christchurch and its environs have suffered extensive damage that has been augmented by phenomena of widespread soil liquefaction and associated ground deformations. This paper has been aimed to find out the quantifiable parameters that could provide a better insight to seismologists and engineers who try to systematically investigate the reasons behind soil failures that occurred in the February shaking correlating the soil behavior to the particular features of the recorded ground motions.

1 INTRODUCTION

The $M_w = 6.3$ earthquake of February 22 was the strongest seismic event in a series of damaging aftershocks in and around Christchurch after the Darfield earthquake on 4th of September in 2010. The source of the Darfield earthquake was in a sparsely populated area and thus it caused no life losses. Serious damage was mainly due to extensive liquefaction. By contrast, the Christchurch earthquake was generated on a fault in close proximity to the city, culminating in a death toll of 181 people.

The Canterbury Plains are covered with river gravels hiding any evidence of past fault activity in this region. The newly revealed Greendale fault was therefore completely unknown. Only a portion of it was revealed in the ground surface during the Darfield earthquake. Clearly the second fault (of February 2011) appears as a continuation of the first, although no fault structure directly connecting the faults has been recognized.

Thanks to a dense network of strong ground motion stations a large number of records have been obtained, providing valuable information on the event, and offering the possibility to relate damage versus ground shaking. Due to its magnitude, shallow depth and proximity the February earthquake proved particularly destructive for the Central Business District (CBD) of Christchurch, the buildings of which suffered extensive damage. In addition to structural damage due to high spectral accelerations, important soil-related failures have directly affected houses and bridges. Apart from the southern part of the city on the hills and the Lyttelton port area, the city is built on deep estuarine soil, which has been shaped in the last thousands of years with the ever changing riverbed. Fine sands that are the dominant soil type and the high ground water level have contributed to widespread liquefaction in each one or both events. Often accompanied by 'lateral spreading', liquefaction amplified the level of damage, resulting in failure of structures in CBD and surrounding areas.

2 STRONG MOTION RECORDS

Thanks to a dense network of seismographs covering the broader area of Christchurch (Figure 1) a large number of ground motions were recorded during the Christchurch February 2011 earthquake. The CBD area includes four seismic stations, i.e. CBGS, CCCC, REHS and CHHC. The first three records are truly free-field motions. CHHC was located near the base of a 2-story building and its motion may bear to some degree the effect of the structure. These ground motions may not have been the strongest ones recorded in terms of PGA values; however, due

to certain features, their effect on structures or soils was detrimental.

There is a certain variation in the recorded acceleration time histories (Figure 1). For instance, the range of PGA values varies within a factor of 2, from 0.34g (CHHC-NS) to 0.72g (REHS-EW). A dominant common feature in all records is the sign of liquefaction: long period cycles with reduced acceleration amplitudes, occurring after a threshold acceleration has been reached. Soil softening due to excess pore water pressures in combination with sufficient acceleration values has led to amplification of large periods affecting a broad category of structures, as indicated by the acceleration spectra. Especially, the spectral amplification at periods exceeding 2 sec is attributed to the fact that once liquefaction has occurred, the overlying soil 'crust' oscillates with very low frequencies, causing the bulges observed in the acceleration spectra for periods of about 3 sec (see Youd & Carter (2005) for similar observations from the then available liquefaction-affected acceleration spectra).

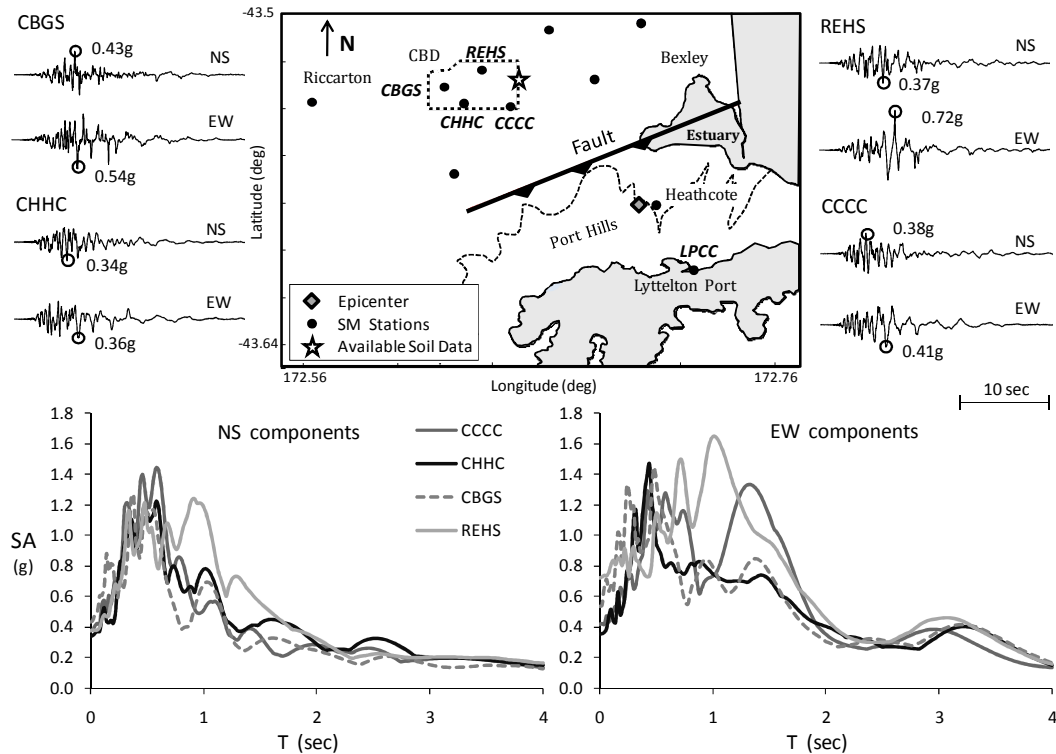


Figure 1. Map of the Christchurch broader area showing the intersection of the fault plane with the ground surface (from GNS Science), the location of the accelerograph stations, the epicenter, and the location with available soil data. Acceleration time histories and spectra of four CBD (Central Business District) seismic stations for NS and EW directions.

3 POLARITY OF THE RECORDED MOTIONS

The two orthogonal components of a record are usually aligned with North-South and East-West (Figure 1), or, ideally, if the faults were known, with Fault-Parallel and Fault-Normal, directions. Mathematically there is at least one specific angle at which a certain ground motion parameter, such as PGA, PGV or PGD, reaches a maximum, indicating the governing direction for that ground motion parameter and revealing a certain polarity of the recorded motion. Polarity plots can be useful in determining the dominant shaking direction of an earthquake and in unveiling any directivity effects (Shabestari & Yamazaki, 2003).

A first index of intensity is the value of peak ground acceleration (PGA), the spatial distribution of which is depicted on the map of Figure 2. Additionally, for the records from the four CBD

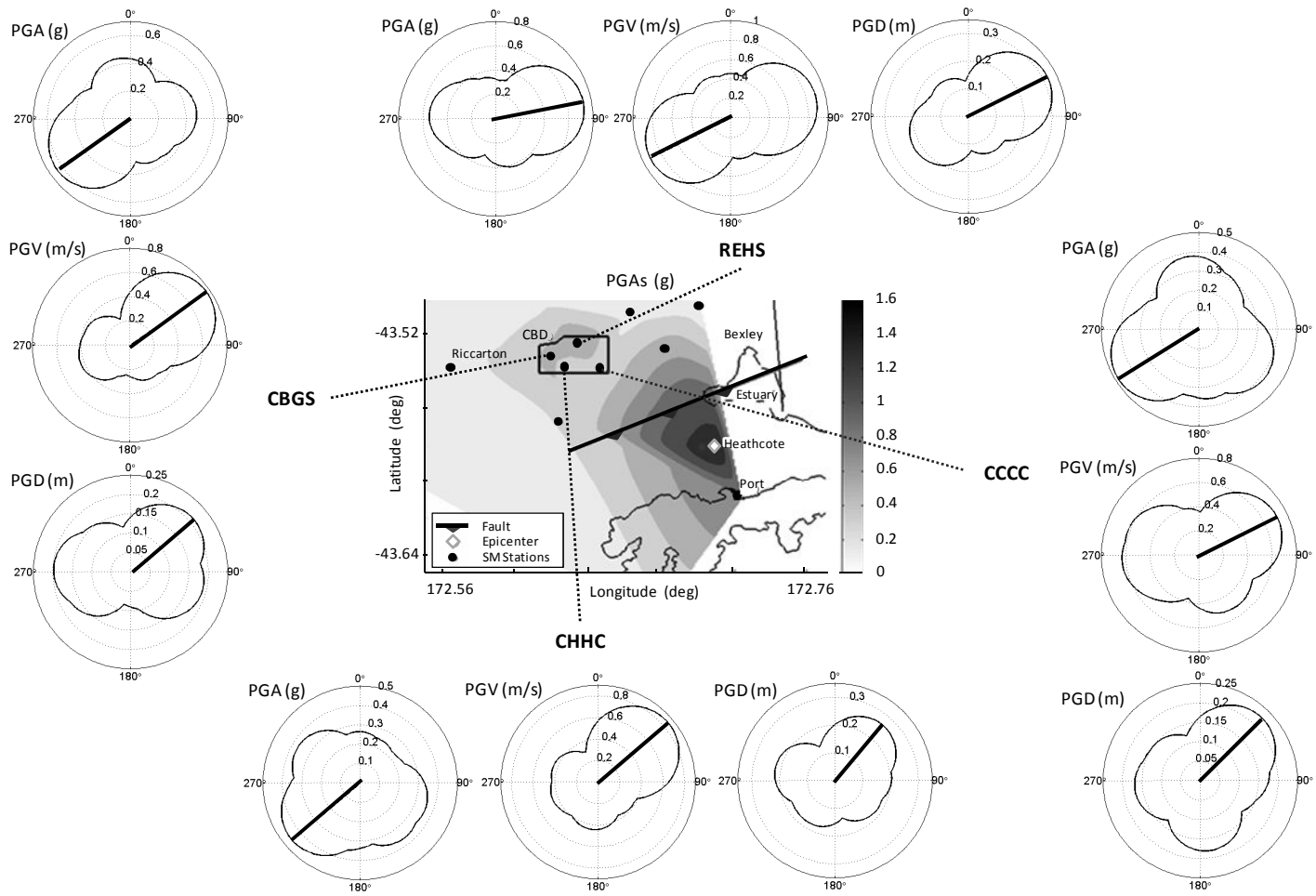


Figure 2. Observed polarity for the records in CBD in terms of peak ground acceleration, velocity, displacement. The contours of PGA on the map were computed by interpolation using all records in Christchurch.

stations (i.e. CCCC, REHS, CBGS and CHHC) the maximum peak values of ground acceleration, velocity and displacement are calculated trigonometrically, by varying the angle by 1° between 0° and 180° , resulting in asymmetric plots of positive and negative maxima (in absolute terms). The graphs consistently exhibit distinct polarity in a direction that practically coincides with that of the fault line. Knowing the polarity of shaking may offer information on the rupture mechanism and insight into the dominant damage observed in the area of CBD.

4 LIQUEFACTION

The Christchurch urban area, extending from Riccarton in the west to Bexley in the east and reaching Heathcote valley and the Port Hills in the south, is located on Canterbury Plains and its dominant geomorphic feature is the river floodplains. In particular, the rivers of Avon primarily and Heathcote (secondarily), originating from various springs in western Christchurch, form endless meanders through the city and the eastern suburbs, as they head to the estuary near the sea. As depicted in Figure 3a, the subsoil in CBD systematically comprises profiles with random variations in layering in the upper 15-25 m (Cubrinovsky et al., 2010; Toshinawa et al., 1997). The volcanic bedrock is located at an approximate depth of 400 m and emerges on the surface at the southern border of Canterbury Plains, forming the Port Hills of Banks Peninsula. Thick layers of gravel formations overlay the bedrock (Brown and Webber, 1992). The surficial sediments have an average thickness of about 25 m and consist of alternating layers of alluvial sand, silt and gravel. They have been deposited by overbank flooding (Eidinger et al., 2010) — hence, their loose disposition. In CBD, in particular, sand and non-plastic silt with low content of fines are the dominant soil types (Rees, 2010). The latter feature combined with the high ground water level (from 0 to 3 m) below the center of the city, explains the sensitivity to liquefaction.

There is significant variability of soil deposits within short distances that can differentiate the ground motion characteristics. For example, Toshinawa et al. (1997) describe the soil profiles of two characteristic sites 1.2 km distant, one consisting of only sandy gravels and sand close to CBGS seismic station (Figure 1), and the other comprising silt and peat deposits to a depth of 7 m close to REHS seismic station. According to the aforementioned paper, during a 1994 distant earthquake greater amplification was observed at the second site, close to REHS, in agreement with the records of February 2011 (Figure 1). However, both sites belong to the same broader classification of soft soils (class D) for structural design purposes in the New Zealand design standards (NZS 1170.5, 2004). This seems quite reasonable in cases of strong earthquakes, where the response of such type of soft mostly sandy soils is expected to be dominated by the effects of severe liquefaction.

To investigate the soil response in the CBD urban area during accounting for liquefaction effects, a typical “generic” soil profile was chosen (Figure 3a). Soil properties have been obtained from boreholes conducted close to the Fitzgerald Bridge, situated at the eastern part of CBD (see the star sign on the map in Figure 1). Standard Penetration Tests (SPT) values were obtained from Bradley et al. (2009) and Rees (2010). Shear wave velocity, V_s , values were based on empirical correlations with SPT (Dikmen, 2009).

With the “generic” soil profile defined, dynamic effective-stress analyses were conducted in order to capture the excess pore water pressure rise and dissipation, using the finite difference code FLAC (Itasca, 2005). The LPCC ground motion recorded on the volcanic outcrop at Lyttelton Port was selected as the (outcrop) input motion referred to the base of the gravel formations (Figure 3b). The presumption that this rock motion (the only one on [soft] rock in the area) is a suitable candidate for the base of CBD is only a crude approximation. Because, although, the LPCC and CBD stations have the same distance from the about 65° -dipping fault, LPCC lies on the hanging-wall and CBD on the foot-wall of this partly-thrust and partly-strike-slip fault. The NS and EW components of the LPCC record excited the soil column in two different one-dimensional wave propagation analyses. The numerical simulation involves the constitutive law of Byrne (1991) for pore pressure generation which is incorporated in the standard Mohr-Coulomb plasticity model.

In general, as one would expect, the results of the analysis in terms of acceleration time histories and acceleration spectra for the two components (Figure 3b) demonstrate that, as the

shear waves propagate from the base of volcanic rock, the soil de-amplifies the low-period components of motion and amplifies those of high period. Moreover, the computed response on top of the dense gravel formation indicates that there is no substantial influence of the gravel layer in altering the input motion, other than de-amplifying the values in the high frequency range (above 5 Hz) and slightly amplifying lower frequencies. In addition, the peak ground acceleration values do not change.

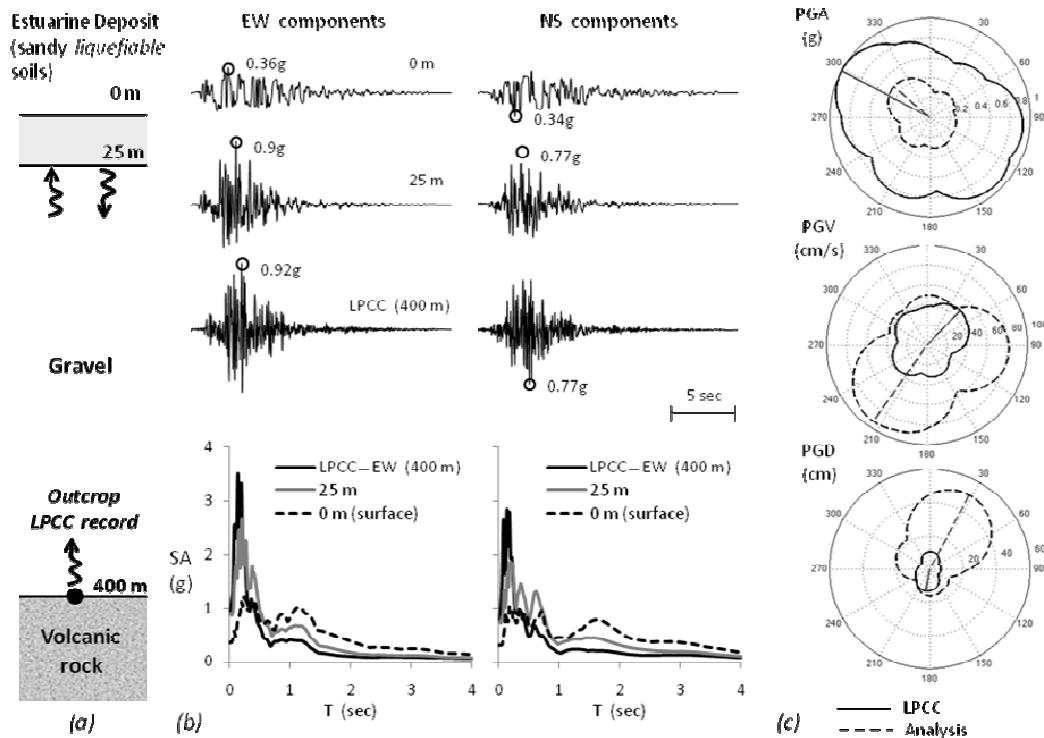


Figure 3. (a) Typical in-depth soil profile on CBD; (b) Accelerograms and response spectra of the LPCC record used as excitation (applied in outcrop), and at two different depths obtained from the analyses; (c) Polarity plots of LPCC record and output of analysis on the ground surface.

In contrast to the minor effect of gravel on the soil response, the surficial soil layers play a dominant role in defining the ground motion characteristics — hardly a surprise: these layers behave as a filter cutting-off the high frequency spikes, while the duration of motion cycles is lengthened. As a result, the peak accelerations have diminished to 0.35 g approximately in both directions. Moreover, in terms of spectral acceleration values, there is considerable spectral amplification to 1 g in the higher period range of up to 1.8 sec. Overall, both components show similar response, with certain disparities in the frequency content, e.g. NS output is richer in higher periods.

Polarity plots have also been constructed for LPCC motion and the computed ground surface motion. They are portrayed in Figure 3c. Evidently, there is no single (common) dominant direction for all PGA, PGV and PGD values, contrary to the consistency in polarity of the CBD records (Figure 2). Especially the PGA principal direction is normal (rather than parallel) to the fault. This discrepancy with CBD polarity might be attributed to the fact that Lyttelton is on the hanging wall side, whilst CBD lies on the foot-wall. For the ‘thrust’ component of faulting this difference may indeed have an effect, but this is an issue that needs further investigation and is beyond the scope of this paper. The polarity of the output diverges only slightly from the polarity of LPCC. The comparison of polarity plots demonstrates clearly the cut-off of PGA values in all directions and increase of PGV and PGD values. Evidently, the liquefied layers play the role of a seismic isolator reducing the acceleration amplitude of the wave components propagating through them.

To validate the analysis, a comparison between real records and numerical results is attempted. The record selected for the comparison, CBGS, is depicted on the map of Figure 1. The CBGS station is located in the Botanic Gardens and the recorder is housed in a really light kiosk (Figure 4a). Visible are the signs of liquefaction sandboils, although they had been cleaned following the earthquake (the picture was taken by our research team in April 2011 (Tasiopoulou et al., 2011)). No other facilities exist in the surroundings ensuring free field conditions. Moreover, the soil profile described by Toshinawa et al. (1997) is appropriate for this location.

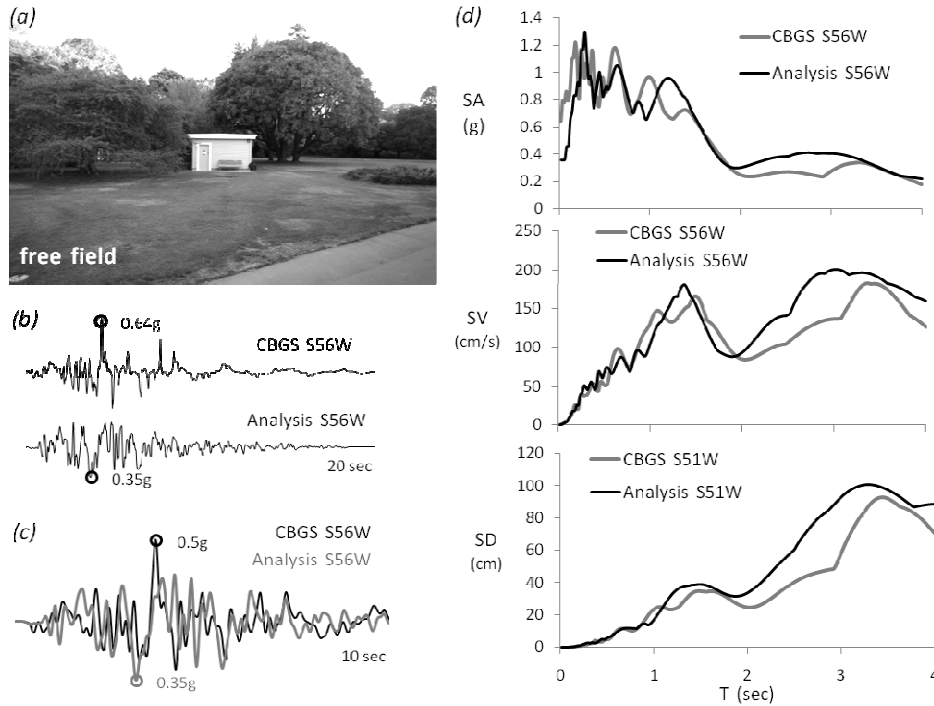


Figure 4. (a) The CBGS seismic station, with the remnants of liquefaction sandboils seen as scars on the grass; (b) acceleration time histories of CBGS: record and analysis; (c) Comparison of (the about) acceleration time histories after filtering them at 4 Hz; (d) Comparison of acceleration 5%-damped spectra between CBGS record and analysis.

As already discussed, LPCC and the four CBD records have different polarity. However, LPCC was the only option in search for a rock outcrop motion to be used as excitation in our analysis. That is why the comparison of spectra has been conducted in the direction of polarity of the CBGS record. For example, the strong PGA and PGV direction (polarity) for CBGS is approximately S56W and its PGD polarity is S51W. The acceleration time histories of the CBGS recorded and computed motions in the direction of S56W are depicted in Figure 4b. Although these time histories seem to differ, especially in terms of PGA values, a closer look reveals that they have certain common features, better depicted in Figure 4c after filtering-out components with frequency above 4 Hz. Notice in particular that the main pulse at 4 sec exists in both time histories. The response spectral SA, SV, and SD are compared in Figure 4d. The agreement of analysis with reality confirms that a realistic insight of the mechanisms of soil response during Christchurch earthquake have been gained from the analysis.

5 CONCLUSIONS

The $M_w = 6.3$ Earthquake of Christchurch was a surprising and unusual event which occurred in an unknown fault that had already been awakened from the September 2010 stronger earth-

quake, and it had a strong thrust component and a steeply dipping plane. The study focuses on the basic features of the recorded strong motions connecting the findings to the nonlinear behavior of the soil layers. Liquefaction, a phenomenon that has played a major and devastating role, has been examined through a "generic" downtown soil profile and dynamic effective stress analysis. The LPCC record was applied as the base excitation, being the only one available rock outcrop motion. Despite several uncertainties, the output spectra obtained from the liquefaction analyses and the one recorded in the free field in the Botanic Gardens have shown quite a satisfactory match provided that the compared spectra are aligned with the strong direction of the recorded motion. The dominant direction of the CBGS record is consistently almost parallel to the fault plane whilst the Lyttelton record exhibits more inconsistencies, something that may be related to the effects of the hanging-wall and the steep thrust–fault plane. The governing direction of each record has been found by simply turning the record in every possible direction with one-degree intervals and re-recording the strong motion parameters sought.

6 ACKNOWLEDGEMENTS

The financial support for this paper has been provided under the research project “DARE”, which is funded through the European Research Council’s (ERC) “IDEAS” Programme, in Support of Frontier Research-Advanced Grant, under contact/number ERC-2-9-AdG228254-DARE.

REFERENCES

- Bradley, B.A, Cubrinovski, M., Dhakal, R.P. & MacRae, G.A. 2009. Probabilistic seismic performance assessment of a bridge-foundation-soil system. *Proceedings of the NZSEE Conference*, Christchurch, N. Zealand, 3-5 April.
- Brown L.J., & Weeber, J.H. 1992. Geology of the Christchurch urban area: Scale 1:25,000. Institute of Geological & Nuclear Sciences, Geological Map 1, New Zealand.
- Byrne, P. 1991. A cyclic shear-volume coupling and pore-pressure model for sand. *Proceedings of Second International Conference on Recent Advances in Geotechnical Earthquake Engineering and Soil Dynamics*, St. Louis, Missouri.
- Cubrinovski, M., Green, R., Allen, J., Ashford, S., Bowman, E., Bradley, B., Cox, B., Hutchinson, T., Kazavanjian, E., Orense, R., Pender, M., Quigley, M., Wilson, T. & Wotherspoon, L. 2010. Geotechnical reconnaissance of the 2010 Darfield (New Zealand) earthquake. *Bulletin of the New Zealand Society for Earthquake Engineering*, 43:243-320.
- Dikmen, Ü. 2009. Statistical correlations of shear wave velocity and penetration resistance for soils. *Journal of Geophysics and Engineering* 6:61-72.
- Eidinger, J., Tang, A. & O'Rourke, T. 2010. Technical Council on Lifeline Earthquake Engineering (TCLEE), Report of the 4 September 2010 Mw 7.1 Canterbury (Darfield), New Zealand Earthquake, American Society of Civil Engineers.
- Itasca, (2005). Fast Lagrangian Analysis of Continua, Itasca Consulting Group Inc., Minneapolis, Minnesota.
- NZS 1170.5 2004. Structural design actions, Standards New Zealand, Wellington, NZ.
- Rees, S. D. 2010. Effects of fines on the un-drained behavior of Christchurch sandy soils. *PhD Thesis*, Civil and Natural Resources Engineering, University of Canterbury, Christchurch, New Zealand.
- Shabestari, K.T. & Yamazaki, F. 2003. Near-fault spatial variation in strong ground motion due to rupture directivity and hanging wall effects from the Chi-Chi, Taiwan earthquake. *Earthquake Engineering and Structural Dynamics* 32:2197-2219.
- Tasiopoulou P., Smyrou, E., Bal, I. E., Gazetas, G. & Vintzileou, E. 2011. Geotechnical and Structural Field Observations from Canterbury, New Zealand Earthquakes. *Research Report*, National Technical University of Athens, Greece.
- Toshinawa, T., Taber, J. J. & Berrill, J. B. 1997. Distribution of ground-motion intensity inferred from questionnaire survey, earthquake recordings, and microtremor measurements: a case study in Christchurch, New Zealand, during the 1994 Arthurs Pass Earthquake. *Bulletin of the Seismological Society of America*, 87:356-369.
- Youd, T.L. & Carter, B.L. 2005. Influence on soil softening and liquefaction on spectral acceleration. *Journal of Geotechnical and Geoenvironmental Engineering ASCE*. 131(7):811–825.

Parametric Dimensional Analysis on Rocking of 1-dof Systems

R. Kourkoulis, P. Kokkali

Soil Mechanics Laboratory, National Technical University, Athens, Greece

ABSTRACT: This paper investigates the metaplastic rocking response of single degree of freedom oscillators that are founded through surface square footings on inelastic soil. Dimensional analysis has been performed in an attempt to produce results pertaining to a group of cases that exhibit common characteristics which are hereafter termed as equivalent systems. The system response has been found to be depending on non-dimensional parameters such as: the factor of safety against vertical load, the imposed acceleration amplitude, the frequency ratio between the soil and the rocking oscillator, the dimensionless flexibility of the oscillator, the ratio of the available shear strength over the earthquake-induced stress, and the “rigidity ratio” which is the ratio of the soil shear modulus (at small strains) over the undrained shear strength. Systems exhibiting equality between their respective non-dimensional terms are shown to respond equivalently for the same type of imposed shaking. A parametric analysis has been performed to reveal the impact of each dimensionless term on the overall system response. It was shown that dimensionless toppling rotation θ_{ult}/θ_c (where θ_c is the toppling rotation of the equivalent rigid block) is a function of the factor of safety against vertical loads FS_v and the slenderness ratio h/B : the toppling rotation decreases with FS_v , while the role of the h/B becomes increasingly important for low values of FS_v . A simplified “empirical” equation that approximately captures these phenomena is proposed.

1. INTRODUCTION

The understanding of the profound role of soil-structure interaction (SSI) phenomena on the design of earthquake resistant structures has been substantially aided by the research work of Jennings & Bielak (1973), Veletsos & Nair (1975), Kausel & Roesset (1975), Gazetas (1983), Wong & Luco (1985), Gazetas (1991). In these studies the soil-structure system is considered to behave elastically by idealizing soil as a linear visco-elastic material, while the structure is assumed elastic and in full contact with the supporting soil. Yet, such an assumption can be hardly met when considering the intensity of some of the recently recorded ground accelerations (e.g. the recorded accelerations in the latest 2011 earthquake event in New Zealand exceeded 1.0 g).

Recent research however suggests that the inevitable non-linear foundation response can well be surprisingly beneficial for the structure. Inelastic foundation behavior may materialize either in the form of sliding or uplifting *of the foundation* from the supporting ground when the seismic inertia exceeds the footing’s capacity, or may involve mobilization of soil strength. In all three cases it is expected that the finite foundation capacity will “isolate” the superstructure by limiting the inertia forces transmitted to the above ground system, hence reducing its dynamic distress [Pecker, 1998; Pender; 2007].

Among those who aimed to elucidate the interplay between foundation uplifting and soil failure, Gazetas and Apostolou (2004) studied the rocking response of a simple rigid structure lying on yielding soil under monotonic and dynamic conditions. Anastasopoulos et al., 2010, investigated the positive effect of foundation rocking for 1-dof systems under seismic action, while Gelagoti et al. (2011) were among the first to demonstrate its decisive role in the seismic protection of simple low rise frame structures.

The present study aims to shed light on the effect of key factors governing the rocking behavior of 1-dof foundations, such as the slenderness (i.e. geometrical characteristics) of the system and the factor of safety against vertical load controls. The former has been proven to determine the uplifting potential of the system while the latter defines the form of inelastic foundation behavior (i.e. uplifting *or* soil yielding). Dimensional analysis has been performed in an attempt to produce results pertaining to a group of cases that exhibit common characteristics which are hereafter termed as equivalent systems.

2. DIMENSIONAL ANALYSIS

Dimensional analysis is a mathematical tool that emerges from the existence of physical similarity and reveals the relationships that govern natural phenomena (Langhaar; 1951). By using dimensional analysis, it becomes feasible to derive broadly applicable results and give a better understanding of the significant parameters of the problem examined. In this case, dimensional analysis is employed in order to describe the response of 1-dof systems on surface square foundations subjected to rocking due to static or dynamic loading. A typical example of such system (representative of a single bridge pier) is portrayed in Figure 1a. The system has height h and foundation width B , while the structural flexibility is expressed through the eigenperiod T_{str} . The system carries a total mass m . The depth of the soil deposit is z and the density ρ , while the undrained shear strength is S_u and the shear wave velocity V_s .

The full formulation of the dimensionless problem under consideration is initially attempted for the simplest case of a rigid block rocking on rigid base, while the additional parameters (i.e. those controlling the degree of soil plastification, or the flexibility of the rocking superstructure) are gradually introduced upon it.

Identification of Dimensionless Terms

For the simplest case of a rigid block on rigid base depicted in Fig. 1b, its rocking behavior depends on its geometric characteristics and the characteristics of shaking which, for idealized pulses, are solely its amplitude a_E and characteristic frequency f_E . As such, the body rotation may be expressed as:

$$\theta = f(B, h, g, a_E, f_E) \quad (1)$$

According to the Vaschy-Buckingham Π -theorem, a dimensionally homogeneous equation involving k variables may be transformed to a function of $k - r$ dimensionless Π -products, where r is the minimum number of reference dimensions necessary for the description of the physical variables.

Applying the Π -theorem in (1) which contains $k=6$ independent variables involving $r=2$ reference dimensions obviously results in 4 dimensionless Π -products. In this context, (1) may be re-written in dimensionless terms as:

$$\theta = f(B/h, f_E/p, a_E/g) \quad (2)$$

where

$$p = \sqrt{\frac{3g}{4R}} \quad (3)$$

is a frequency parameter (initially introduced by Housner, 1964) indicative of the dynamic properties of the rigid body. In Eq. (3) R is half the diagonal of the rigid body defined as:

$$R = \sqrt{(B/2)^2 + h^2} \quad (4)$$

In order to render Eq. (1) applicable to more realistic systems, the soil and structure specific characteristics should be taken into account; this is accomplished by introducing in the equation the soil and structure's eigenperiods T_{soil} and T_{str} respectively, and the soil strength, which –for the system under consideration– is defined as S_u .

Lastly, in order to capture kinematic soil response while realistically accounting for wave propagation effects, (1) should include parameters z , ρ and V_s . Incorporating all of the above parameters in (1) yields:

$$\theta = f(B, h, g, a_E, f_p, T_{str}, m, S_u, z, \rho, V_s) \quad (5)$$

which apparently contains $k=12$ independent variables involving $r=3$ reference dimensions (i.e. length, mass and time). Following the same procedure as before, (5) is re-written in non-dimensional terms as

$$\vartheta = f\left(\frac{h}{B}, \frac{a_E}{g}, \frac{f_E}{\rho}, \rho T_{str}, \frac{V_s}{\rho z}, \frac{mg}{S_u B^2}, \frac{\rho V_s^2}{S_u}, \frac{S_u}{\rho z a_E}\right) \quad (6)$$

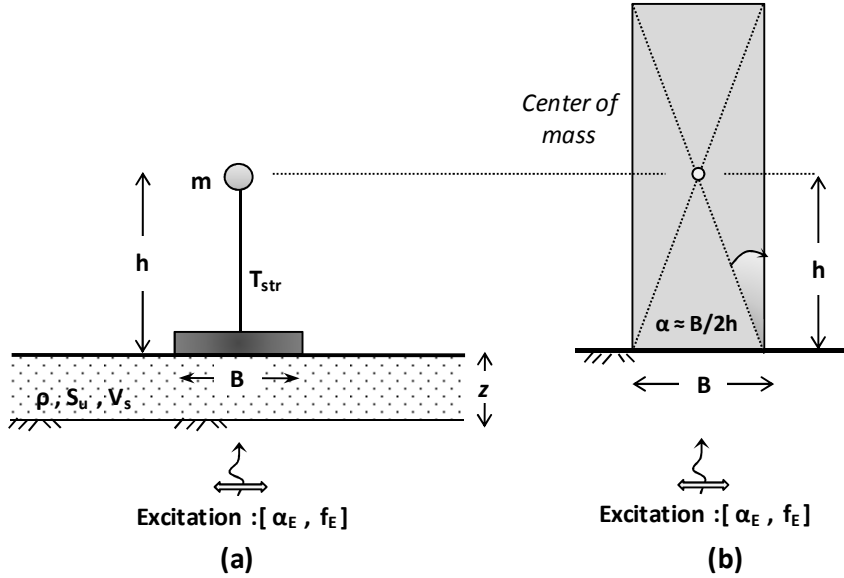


Figure 1. Schematic illustration of the Problem analysed: (a) complete formulation; (b) an approximation replacing the rocking oscillator by an equivalent rigid block on rigid base.

The parameter $\frac{mg}{S_u B^2}$ understandably represents the factor of safety against vertical load for 1-dof systems on square surface footings and will be referred to in the ensuing as FS_v . The flexibility of the oscillator is expressed through the oscillator flexibility parameter ρT_{str} .

Soil nonlinearity is expressed through the term $r = S_u / \rho z a_E$ in which S_u represents the available shear strength and $\rho z a_E$, is an index of the earthquake-induced stress at depth z . Alternatively, r may be considered as an index of the mobilization of soil shear strength due to the imposed acceleration a_E . The last factor, $v = \rho V_s^2 / S_u$, termed “rigidity ratio” in soil mechanics literature, is the ratio of the soil shear modulus (at small strains) over the undrained shear strength.

Presumably, in its present form, this analysis is not capable of capturing the effect of excitation type (i.e. number of strong motion cycles etc) as it only integrates the peak amplitude and characteristic frequency of shaking. Hence, its validity is limited to excitations which can be amplitude or frequency –scaled.

In accord with the manipulation defined so far, the dimensionless settlement and moment of the foundation may be expressed as follows:

$$\frac{w}{B} = f\left(\rho t, \frac{h}{B}, FS_v, \rho T_{str}, \frac{\rho V_s^2}{S_u}, \frac{S_u}{\rho z a_E}, \frac{V_s}{\rho z}, \frac{a_E}{g}, \frac{f_E}{\rho}\right) \quad (7)$$

$$\frac{M}{S_u B^3} = f\left(\frac{\vartheta}{\vartheta_c}, \frac{h}{B}, FS_v, \rho T_{str}, \frac{\rho V_s^2}{S_u}, \frac{S_u}{\rho z a_E}, \frac{V_s}{\rho z}, \frac{a_E}{g}, \frac{f_E}{\rho}\right) \quad (8)$$

Table 1 summarizes the independent variables and the dimensionless products of the dimensional analysis for dynamic and static loading.

Table 1. 1-dof systems on surface square foundations subjected to rocking due to static or dynamic loading: Identification of dimensionless Π -products.

Independent Variables									
h	B	m	T_{str}	ρ	S_u	V_s	z	a_E	f_E
Dimensionless Products									
Aspect ratio	$\frac{h}{B}$	Rigidity ratio	$\frac{\rho V_s^2}{S_u}$						
Factor of safety	FS_v	Relative frequency ratio	$\frac{V_s}{\rho z}$						
Oscillator flexibility parameter	ρT_{str}	Acceleration amplitude parameter	$\frac{a_E}{g}$						
Soil strength mobilization index	$\frac{S_u}{\rho z a_E}$	Frequency parameter	$\frac{f_E}{\rho}$						

3. ANALYSIS METHODOLOGY

The finite element method (*Abaqus FE code*) is employed in the ensuing in order to confirm the adequacy of the dimensionless terms defined above and perform parametric analyses of the effect of each term in the rocking behavior of 1-dof systems. Figure 2 depicts the finite element model used. A “characteristic” slice of the soil–structure system is studied considering plane-strain conditions accounting of both material (*soil*) and geometric (*uplifting* and *P- δ effects*) nonlinearities. Soil and footing are modeled with quadrilateral continuum elements. An elastic beam element is used for the superstructure and a mass element is located at height h above the footing base. The foundation is connected to the soil with special contact elements permitting detachment from the supporting soil. A large coefficient of friction at the soil–footing interface ensures that any detachment from the supporting soil is in the form of uplifting.

1-dof oscillators have been subjected to both monotonic and cyclic loading applying displacement–controlled vertical and horizontal loading at their top, while both recorded ground motions and idealized wavelets have been applied as excitation at the base of the model during nonlinear dynamic time history analyses.

Soil Modeling

Soil behavior is modeled through a nonlinear kinematic hardening model, with Von Mises failure criterion and associated flow rule [Anastasopoulos et. al., 2011b]. The constitutive model has been validated against experimental data and is appropriate for clay under undrained conditions which is the case for the problem studied here.

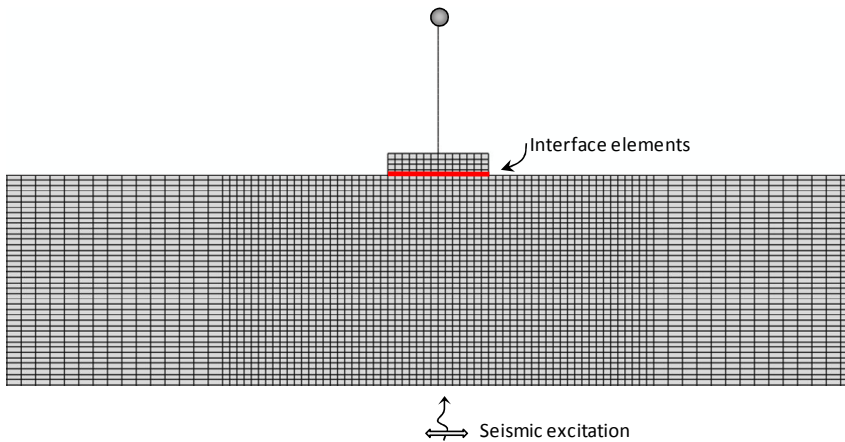


Figure 2. Finite element model assuming plane-strain conditions and taking account of material inelasticity (soil), geometric nonlinearities (footing detachment from the supporting ground) and second order phenomena ($P-\delta$ effects).

4. METHOD VERIFICATION

Prediction of Moment Capacity

In the course of validating our numerical methodology, the calculated ultimate moment is herein compared with published solutions. Several interaction diagrams can be found in literature (i.e. Batterfield & Gottardi, 1994; Gourvenec, 2007) correlating a footing's ultimate capacity with the amplitude of external loading. Among them, Gourvenec (2007) has derived interaction curves for footings of varying shape on an isotropic linear elastic – perfectly plastic clayey soil, of undrained shear strength S_u subjected to combined vertical and horizontal load and moment. This interaction curve is the result of three dimensional finite element analyses in the F.E code Abaqus; loading is directly applied at the footing, therefore second order ($P-\delta$) effects are not taken into account. Figure 3 plots the normalized ultimate moment with respect to the normalized vertical load : x stands for the inverse of the factor of safety ($x = 1/FS_V$), m is the dimensionless ultimate moment for each value of x examined and is calculated as $m = M_{ult} / S_u B^3$, where m_u is the maximum dimensionless ultimate moment. The two failure envelopes portrayed in Fig. 3 manifest an evidently satisfactory comparison: an indirect indication of the capacity of the adopted methodology. Both curves agree that ultimate moment tends to increase as x increases up to a certain value. In this case, (where $P-\delta$ effects are not accounted for) the critical value of x is 0.5 which corresponds to a factor of safety equal to 2. The ultimate moment decreases with decreasing safety factor thereafter until it is ultimately zeroed for extremely heavily loaded systems ($x = 0.95$).

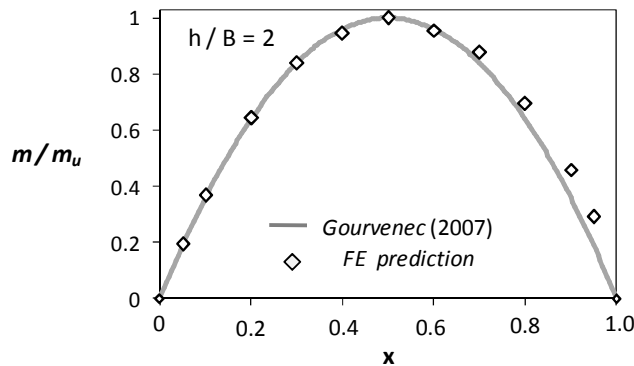


Figure 3. Evolution of Normalized dimensionless ultimate moment with normalized vertical load (x) when an 1-dof system of $h/B = 2$ is subjected to combined (M, Q, N) loading . The solid grey line corresponds to the Gourvenec (2007) solution and the discrete markers stands for the 2D F.E. solution.

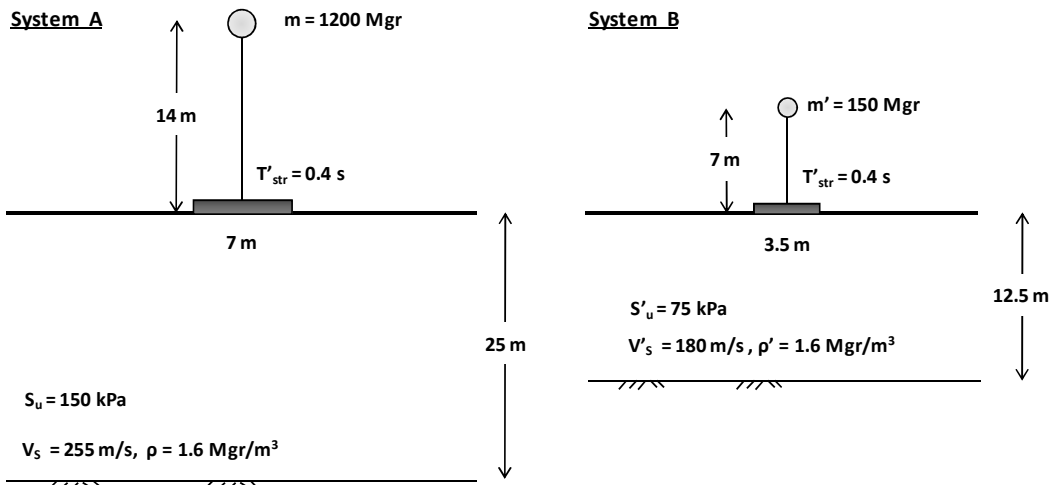


Figure 4. Numerical Example :Two unique systems may display a self-similar response as long as they share common dimensionless properties: $h / B = 2$, $FS_V = 2.5$, $pT_{str} = 0.4$, $\rho V_s^2 / S_u = 690$, $V_s / p z = 14.3$)

Dimensional Analysis Example

In an attempt to demonstrate the competence of the dimensional analysis described above, this section compares the response of two completely different systems portrayed in Figure 4 first to monotonically imposed loading on their top and then to dynamic excitation applied on the base of each model. The dimensionless terms generated earlier are common for both systems: for the cases presented herein, equivalent systems of varying geometry lie on clay strata of undrained shear strength $S_u = 75$ and 150 kPa, respectively. The two systems display the same factor of safety FS_V , and slenderness ratio h/B . Soil stiffness ratio $\rho V_s^2 / S_u$ is equal to 690 . The flexibility of the oscillators is equal to $pT_{str} = 0.34$, while the relative frequency of the soil-superstructure system $V_s / p z$, is equal to 14.3 .

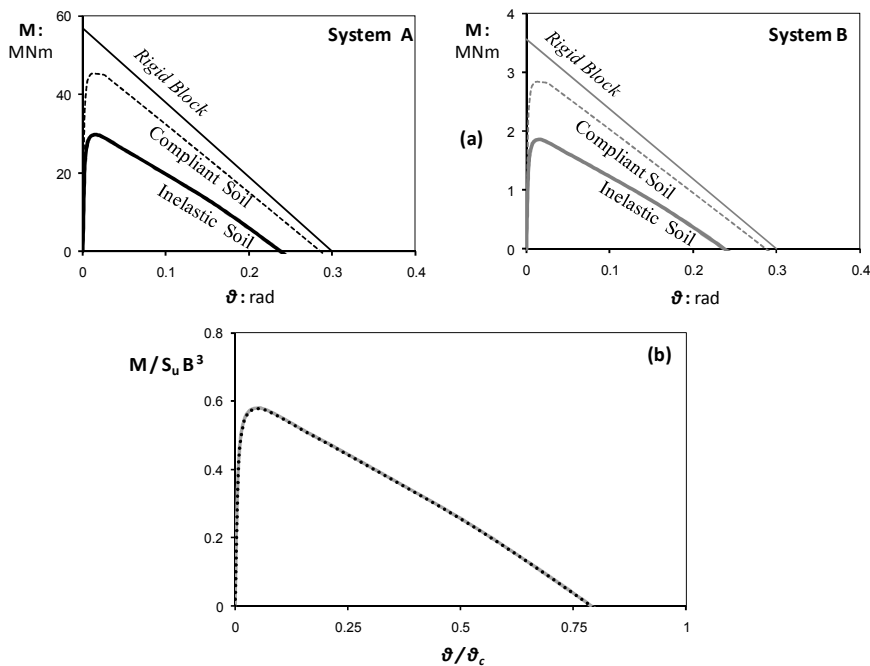


Figure 5. Moment–rotation curves of the two example systems : (a) in absolute and (b) in dimensional terms.

The response is plotted in terms of moment-rotation curves for the two systems subjected to monotonic loading in Figure 5. Evidently, for both systems the equivalent rigid block represents the upper-bound of response both in terms of moment capacity and overturning angle. Soil compliance is shown to reduce the moment capacity but has a minimal effect on the overturning angle. However, both the maximum moment attained and the overturning angles of the systems are drastically affected when soil inelasticity is accounted for. Note that although the developed moment drastically differs between the two systems (reflecting the difference in their mass and geometry), their overturning angles are exactly the same since both systems exhibit equal h/B ratios. Remarkably, all the discrepancies discussed so far fade away once results are plotted in non-dimensional terms (Figure 5c), when apparently both curves coincide.

Even more remarkable is the equivalence of the two systems when subjected dynamic loading (Figure 6). The systems have been excited by Takatori 000 record (Kobe, 1995). This time history is a very intense excitation with peak acceleration of $0.61g$ and long duration. Hence, nonlinearity prevails in terms of soil response. The comparison between the two curves is excellent both in terms of time histories of dimensionless acceleration and settlement and of loops of dimensionless moment vs dimensionless rotation. Acceleration time histories at the top of the oscillator (Figure 6a) are identical for the compared systems, both in terms of frequency content and details of the time history. The fact that the maximum acceleration at the top of the oscillator is significantly lower than the peak acceleration of the excitation mirrors that the foundation has reached its moment capacity: extensive soil yielding underneath the footing takes place in both cases, thus resulting in limiting the inertia transmitted to the superstructure. This behavior should be attributed to the low FS_v value. Note that the response of the two systems is equivalent also during the free-oscillation phase occurring at $pt > 12$.

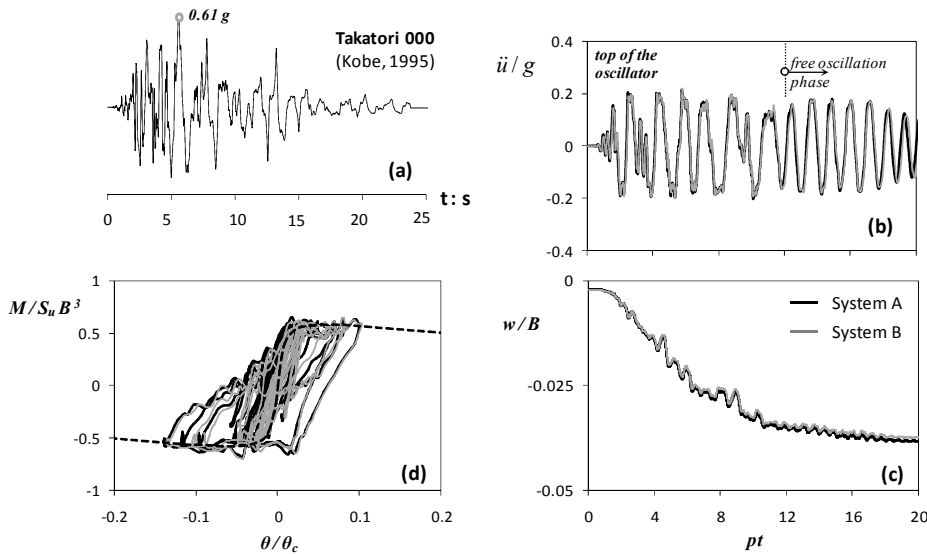


Figure 6. The two example systems display self similar behavior when excited by the (a) Takatori 000 record. Evolution of the dimensionless (b) acceleration at the top of the oscillator and (c) settlement (w/B). (d) Dimensionless moment-rotation loops at the foundation level.

5. PARAMETRIC ANALYSIS

5.1. The effect of Safety Factor FS_v

Two sets of equivalent systems have been examined (Table 2), both of aspect ratios $h/B = 2$. The first system exhibits a safety factor of $FS_v = 2$ thus representing heavily loaded systems, whereas the second pair has a $FS_v = 5$ and, as such, represents relatively lightly loaded systems. Expectedly, the response of the heavily and the lightly

loaded systems manifest substantial disparities: heavier systems develop greater dimensionless moment capacity, but overturn at smaller rotation (Figure 7).

A direct explanation of this behavior is offered by the examination of the contours of developed plastic strains for the two systems (Figure 7a). As the imposed displacement increases soil yielding prevails underneath the heavily loaded footing; a bearing capacity failure mechanism (under eccentrically applied vertical load) is developed, and an extended plastification bulge builds up. On the other hand, the lightly loaded system immediately detaches from the foundation soil under a minimum amount of imposed horizontal displacement, while plastic deformations solely accumulate at the footing edge where localization of stresses is unavoidable. To further demonstrate the aforementioned differences, the two systems are tested under monotonic and cyclic horizontal loading and their response is plotted in terms of moment-rotation and settlement-rotation curves.

Table 2. Effect of FS_v ; two pairs of equivalent systems where all the dimensionless terms but the FS_v are kept constant

	Low FS_v systems				High FS_v systems			
Independent Variables	System A		System B		System A		System B	
h	14		7		14		7	
b	3.5		1.75		3.5		1.75	
m	281	562	38	76	112.5	225	15	30
E	90000	180000	45000	90000	90000	180000	45000	90000
S_u	75	150	37.5	75	75	150	37.5	75
Dimensionless Products								
h/b	4				4			
FS_v	2				5			
E/ S_u	1200				1200			

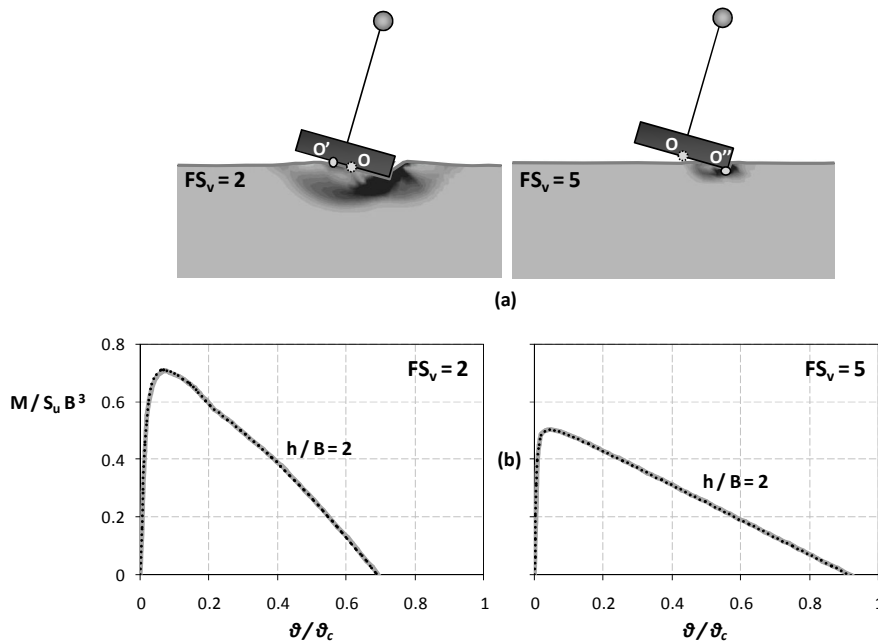


Figure 7. Effect of FS_v : Two sets of equivalent systems with $FS_v = 2$ (left column) and $FS_v = 5$ (right column) are subjected to monotonic horizontal pushover test : (a) Contours of soil deformations and plastic strains, (b) Dimensionless moment-rotation curves.

Monotonic Loading

As stated earlier, the dimensionless foundation overturning moment is $M/S_u B^3$, while the rotation of the foundation is normalized with the overturning angle of the corresponding rigid block rocking on a rigid base. In complete agreement with other experimental and analytical findings, systems with $FS_V = 2$ exhibit greater dimensionless moment capacity than those with $FS_V = 5$. Moreover, the inclination of the initial branch of the two curves (i.e. an indication of the elastic rotational stiffness K_R) for $0 < \theta < \theta_{max}$ is quite different: the heavily loaded system has a lower initial stiffness as a result of the significant soil plastification, which in turn provokes degradation of soil stiffness.

Finally, toppling of the lighter system occurs at a much higher rotation compared to the heavier system, a behavior that conspicuously reflects the detrimental effect of P- δ phenomena especially in case of low FS_V systems as explained in the ensuing. Indeed, recall that the rocking response of the high FS_V system is reminiscent of that of a rigid block rocking on a rigid base under the action of a horizontal load. In this latter case, ever since the system detaches from the ground, the pole of rotation lies exactly at the edge of the foundation and thus, P- δ phenomena tend to reduce the balancing moment due to the block's self weight.

On the other hand, low FS_V systems under the action of the same external load tend to procure extensive soil yielding underneath them which, in turn, brings about shifting of the pole of rotation away from the footing's center towards O' (Fig. 7a). In effect, the moment produced by the superstructure self-weight immediately tends to disturb the system's equilibrium under even low-amplitude rotation angles. As the rotation continues to accumulate, the P- δ induced moment ($M_{weight} = mg\delta'$) is augmented therefore accelerating the degradation of the footing moment capacity.

Cyclic Loading

Cyclic horizontal loading has been applied on the two sets of equivalent oscillators by gradually increasing displacement at their top

. Dimensionless results are presented for the case of slender oscillators with aspect ratio $h/B = 4$ (Table 2).

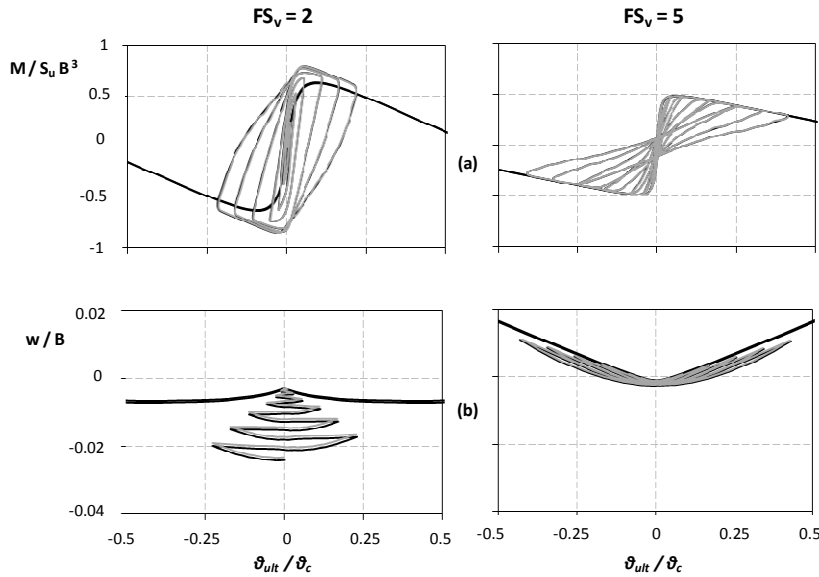


Figure 8. *Effect of FS_V* : the two pairs of equivalent systems are subjected to cyclic push over tests and the comparison of their response is illustrated in terms of (a) dimensionless moment–rotation curves and (b) dimensionless settlement–rotation curves.

In Figure 8 the response of the heavily and the lightly loaded systems is compared in terms of dimensionless moment–rotation and settlement–rotation curves. In all cases the static backbone curve is plotted for ease of reference. The shapes of the two loops reveal a quite pronounced difference: for low FS_V values the produced M- θ

loops are rounded, contrary to the high FS_V case where at least for θ values close to θ_{max} a S-shaped loop is developed (indication of footing uplifting). Interestingly though, in this latter case the cyclic response is successfully enveloped by the monotonic backbone curve, while for heavily loaded foundations a significant overstrength is apparent. This remarkable feature that is directly associated with the kinematic hardening property of soil materials (Bauschinger effect), has also found experimental justification in recent studies (e.g. Anastasopoulos et al., 2011). Accordingly, for high FS_V , where the soil is almost “underexploited” and the maximum moment capacity of the foundation is rather a geometric property (almost equals $mgB/2$) such hardening phenomena are not evident.

The qualitatively different response of heavily and lightly loaded systems is once more evident in terms of vertical displacements (w): heavily loaded systems react to imposed cyclic displacement by accumulating settlement whereas the lightly loaded uplift, thus developing minor residual settlement. Noticeably, although the imposed displacement at the top is equal for both systems, the developed rotation for the uplifting-dominated system with $FS_V = 5$ is obviously higher than that of the system with $FS_V = 2$. In the former case, the entire imposed displacement is acquired through rotation which, in the latter case is limited due to soil yielding. Yet, due to the symmetric nature of the imposed loading, both systems demonstrate zero residual rotation.

5.2. Foundation Metaplastic Ductility

In this paragraph, it is attempted to quantify the rotational ductility that may be offered by a foundation-structure system as a function of the h/B ratio and the normalized vertical load (x). In the ensuing, the foundation rotational ductility is defined as the ratio of the ultimate rotation that a foundation can sustain before overturning (θ_{ult}) to the maximum rotation (θ_c) of an equivalent rigid block lying on a rigid base. Recognizing that, θ_{ult}/θ_c ratios close to unity demonstrate a quite favorable foundation response with increased ductility levels, while θ_{ult}/θ_c close to zero indicates poor post-yielding behavior.

Figure 9(a) portrays the evolution of θ_{ult}/θ_c ratio with increasing normalized vertical load (x) for 1-dof systems with h/B ranging from 1 to 10. Apparently, four different curves can be identified (one for each aspect ratio) with their differences being most pronounced as x tends to 1.0. Interestingly though, all curves may be enveloped by two limit states: (a) a lower bound where $h/B = \infty$ (i.e foundation is subjected to pure moment) and an upper bound ($h/B = 0$) case (i.e. the foundation is subjected to pure shear).

In an attempt to integrate these phenomena in a simplified analytical solution that may be readily applied to roughly estimate the rotational ductility of any foundation structure system, the following formula is proposed:

$$\frac{\vartheta_{ult}}{\vartheta_c} = (1-x) + \frac{1}{3} \left[1 - \log \left(\frac{h}{B} \right) \right] \sqrt{x} \quad (11)$$

which is graphically depicted in Figure 9(b). Note that this formulation yields conservative results for the whole range of x and h/B values, while its accuracy is reduced for $x < 0.1$ (extremely lightly loaded systems) and $x > 0.9$ (extremely heavily loaded systems). Two distinct mechanisms may be identified:

- (a) *Foundation ductility decreases with increasing x for a given h/B ratio.* Lightly loaded systems present superior metaplastic response compared to their heavily loaded counterparts. As explained previously this difference may be attributed to the detrimental role of $P-\delta$ effects: naturally, large x values imply larger $P-\delta$ moments and hence reduced system ductility.
- (b) *Foundation ductility decreases with increasing slenderness ratio for a given x value.* To clarify this, two snapshots of the deformed mesh along with the corresponding displacement vectors at the instant of maximum moment are presented for two systems that exhibit common $x=0.4$ but completely different h/B ratios; a short structure and a very slender one. As evidenced, for low h/B ratios, the foundation is subjected to increased shear loading, which justifies the development of a rather translational failure mechanism. This “hybrid” mechanism indicates mobilization of passive failure at the front side of the foundation, which results increased safety margins against overturning (i.e., higher θ_{ult}/θ_c ratios).

6. SYNOPSIS AND CONCLUSIONS

In this study, dimensional analysis was performed to recognize the key parameters that control the rocking response of 1-dof systems on nonlinear soil. The finite element method was next employed to confirm the

adequacy of the dimensionless terms and perform parametric analyses of the effect of each term. It was concluded that the factor of safety FS_v not only defines the maximum moment that a foundation can sustain and its overturning angle, but also indicates the failure mechanism of the system. Lightly loaded oscillators tend to uplift from the supporting ground and soil yielding is limited. On the other hand, heavily loaded systems tend to accumulate settlement and soil yielding is intense. Moreover, when subjected to cyclic loading, heavily loaded systems tend to reach higher moment capacity compared to monotonic loading. The overturning angle of a system may directly correlated with the normalized vertical load (inverse of the factor of safety), and the aspect ratio h/B and a simplified formula is provided.

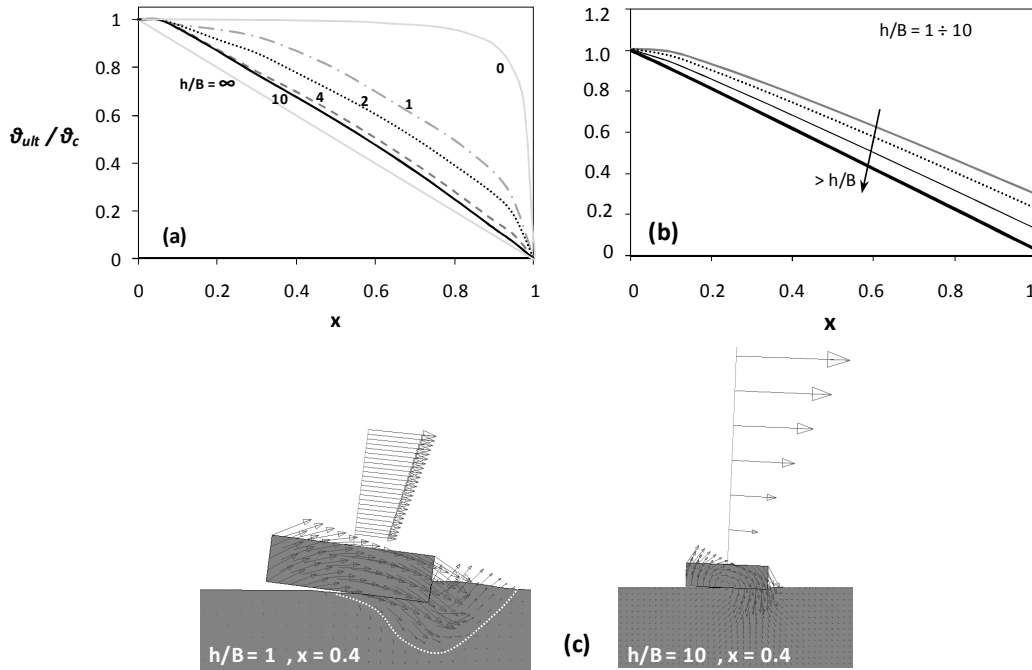


Figure 9. Effect of normalized vertical load (x) and h/B ratio on the normalized overturning angle of the foundation: (a) rigorous F.E. solution and (b) proposed simplified solution. (c) Snapshot of the deformed mesh superimposed with displacement vectors for two 1-dof systems that have the same x but different h/b ratios.

7. ACKNOWLEDGEMENT

The financial support for this paper has been provided under the research project “DARE”, which is funded through the European Research Council’s (ERC) “IDEAS” Programme, in Support of Frontier Research–Advanced Grant, under contract/number ERC–2–9–AdG228254–DARE.

8. REFERENCES

- ABAQUS, Inc. (2009), ABAQUS user’s manual, Providence, R.I.
- Anastasopoulos I., Gazetas G., Loli M., Apostolou M, N. Gerolymos, (2010a), “Soil Failure can be used for Seismic Protection of Structures”, *Bulletin of Earthquake Engineering*, Vol. 8, pp. 309–326.
- Anastasopoulos I., Gelagoti F., Kourkoulis R., G. Gazetas, (2010b) “Simplified Constitutive Model for Simulation of Cyclic Response of Shallow Foundations : Validation against Laboratory Tests”, *Journal of Geotechnical and Geoenvironmental Engineering*, ASCE doi:10.1061/(ASCE)GT.1943-5606.0000534.
- Butterfield R., Gottardi G.[1994] “A complete three - dimensional failure envelope for shallow footings on sand” *Géotechnique* 44(1), 181-184.

- Gazetas G., (1991) "Formulas and charts for impedances of surface and embedded foundations"., *J Geotech Eng ASCE*; 117(9), pp. 1363–81.
- Gazetas G., Apostolou M., Anastasopoulos I. (2003), "Seismic Uplifting of Foundations on Soft Soil, with examples from Adapazari (Izmit 1999, Earthquake)", *BGA Int. Conf. on Found. Innov., Observations, Design & Practice*, Univ. of Dundee, Scotland, September 25, pp.37-50.
- Gazetas, G. (1983) "Analysis of machine foundation vibrations: state of the art", *Int. J. Soil Dyn Earthq Eng*; 2, pp. 2–42.
- Gelagoti F., Kourkoulis R., Anastasopoulos I., and Gazetas G. (2011), "Rocking Isolation of Frames Founded on Isolated Footings", *Journal of Earthquake Engineering and Structural Dynamics (accepted for publication)*
- Gourvenec S. (2007) "Shape effects on the capacity of rectangular footings under general loading." *Géotechnique* 57(8), 637-646.
- Housner G.W., (1963), "The Behaviour of Inverted Pendulum Structures during Earthquake", *Bulletin of Seismological Society of America*, 53(2), pp. 403-417.
- Jennings P.C., & Bielak J. (1973) "Dynamics of building-soil interaction", *Bulletin of the Seismological Society of America*, 63(1), pp. 9-48
- Kausel E., & Roesset J.M. (1975) "Dynamic stiffness of circular foundations", *J Eng Mech Div, ASCE*; 101, pp. 771–85.
- Langhaar, H. L. (1951). "Dimensional analysis and theory of models", *Wiley*, New York.
- Pecker A., (1998), "Capacity Design Principles for Shallow Foundations in Seismic Areas", *Proc. 11th European Conference on Earthquake Engineering*, A.A. Balkema Publishing.
- Pender M. (2007) "Seismic design and performance of surface foundations", *4th International Conference on Earthquake Geotechnical Engineering*, Thessaloniki, Greece (available in CD-ROM).
- Veletsos A.S., & Nair V.V. (1975) "Seismic interaction of structures on hysteretic foundations", *J Struct Eng ASCE*, 101(1), pp. 109–29.
- Wong H.L., & Luco J.E., (1985) "Tables of impedance functions for square foundations on layered media", *Soil Dyn Earthq Eng*; 4, pp. 64–81.

Nonlinear Soil–Foundation Interaction: Numerical Analysis

I. Anastasopoulos, M. Loli, F. Gelagoti, R. Kourkoulis, and G. Gazetas

Soil Mechanics Laboratory, National Technical University, Athens, Greece

ABSTRACT: Modern theoretical studies and experimental investigations of the dynamic response of soil–footing–structure systems have revealed the fallacy behind the prohibition of non-linear foundation response, which is currently one of the cornerstones of aseismic design. Shallow foundations have been found to unavoidably respond non-linearly, experiencing uplifting and/or bearing capacity failure mechanisms when subjected to seismic episodes of significant magnitude. What is more, such non-linear behavior appears to have a beneficial role in the performance of the supported structure. Yet, before allowing foundation non-linearity in engineering practice, it is essential to develop valid and comprehensible tools for modeling the non-linear rocking behavior and predicting the associated foundation permanent displacements with sufficient accuracy. To this end, a numerical methodology has been formulated — which makes use of a simplified but fairly comprehensive constitutive soil model — and implemented within the ABAQUS FE code. The methodology is rigorously validated through the reproduction of a variety of physical model tests conducted on different soils (sand and clay) and at different modeling scales (making use of both large scale and reduced scale experiments). The paper presents the results of this validation procedure, showing that the numerical method is capable of reliably reproducing the details (ultimate capacity, stiffness degradation with increasing rotation, hysteretic response, settlement–uplifting behavior in relation to the rotation amplitude and the number of loading cycles) of non-linear cyclic foundation response.

1 INTRODUCTION

Figure 1a illustrates the problem under consideration: a shallow foundation carries the combined N – Q – M loading arising from the gravitational and inertial distress of the superstructure when submitted to dynamic excitation. If the load transmitted to the foundation is significant, strongly non-linear response may take place at the soil–foundation interface, expressed through loss of contact between the foundation and the supporting soil (uplift) and/or transient mobilization of bearing capacity failure mechanisms (soil yielding).

Figure 1b gives a schematic outline of the different modes of possible foundation response in connection with the foundation design perspective (i.e. in association with the design FS values for vertical and combined–seismic loading, FS_V and FS_E respectively). Two main modes of response are envisaged: the first is in accord with the currently prevalent design practice, which "protects" the foundation against the supported column by demanding the first to be relatively overdesigned ($FS_V \gg 3$, $FS_E > 1$); a less conservative — and certainly unconventional under the present design prism — treatment of the foundation would allow it to bear a significant part of the seismic distress by accepting a reduced FS_E value ($FS_E \approx 0.5$) and hence be subjected to a transient interplay of uplifting and soil yielding mechanisms. The latter approach has been identified as a valid method for the seismic isolation of structures by a number of modern studies [e.g. Martin & Lam, 2000; Gajan et al., 2005; Harden et al., 2006; Gazetas et al., 2007; Anasta-

sopoulos et al., 2010]. Yet, there is still quite a long way before such a major change in seismic design philosophy could be applicable in practice. Aside from reliability issues, a key prerequisite to render such concepts more attractive to engineers is the capability to realistically model the inelastic response of foundations.

Although several advanced and sophisticated constitutive models have appeared in the literature [e.g., Prevost, 1981; Dafalias & Manzari, 2004; Houlsby & Puzrin, 2006], the current state-of-the-art in non-linear analysis of foundations emphasizes the development of macro-element models [Paolucci et al., 2008; Chatzigogos et al., 2009; Gazan & Kutter, 2009]. This is not only because sophisticated constitutive models typically require extensive calibration of their numerous parameters. Being usually implemented in highly specialized finite element (FE) or finite differences (FD) codes, their use is also restricted to simple superstructures. Additionally, in most cases, such models can only be applied by numerical analysis specialists, prohibiting their use in practice. On the other hand, macro-elements constitute a valid solution, but are also usually restricted to simple superstructures.

In an attempt to overcome some of the above difficulties, this paper presents a simplified constitutive model for analysis of the cyclic response of shallow foundations. The model is based on a simple kinematic hardening constitutive model with Von Mises failure criterion, available in commercial FE codes. As it will be discussed in the sequel, the model is modified to be applicable for sand, following a simplified procedure, and is encoded in the FE code ABAQUS through a simple user subroutine. The model is rigorously validated with respect to large scale experiments studying the non-linear response of shallow foundations supported on clay and sand (performed at the UC Davis Centrifuge and the ELSA large scale facility in Italy respectively). Furthermore, after being appropriately modified in order to account for scale effects, the numerical method is employed in the simulation of a series of small-scale experiments performed at the Laboratory of Soil Mechanics in NTUA, where the non-linear foundation response under monotonic and cyclic loading was studied with regard to the design safety factors (FS_V and FS_E). Successful comparisons between analytical and experimental results manifest the effectiveness of the presented methodology in capturing the main attributes of non-linear shallow foundation response irrespective of the supporting soil material and the physical modeling scale. Moreover, requiring calibration of two parameters only, and being (relatively) easy to implement in a commercial FE code, the developed model is believed to provide a practically applicable engineering solution.

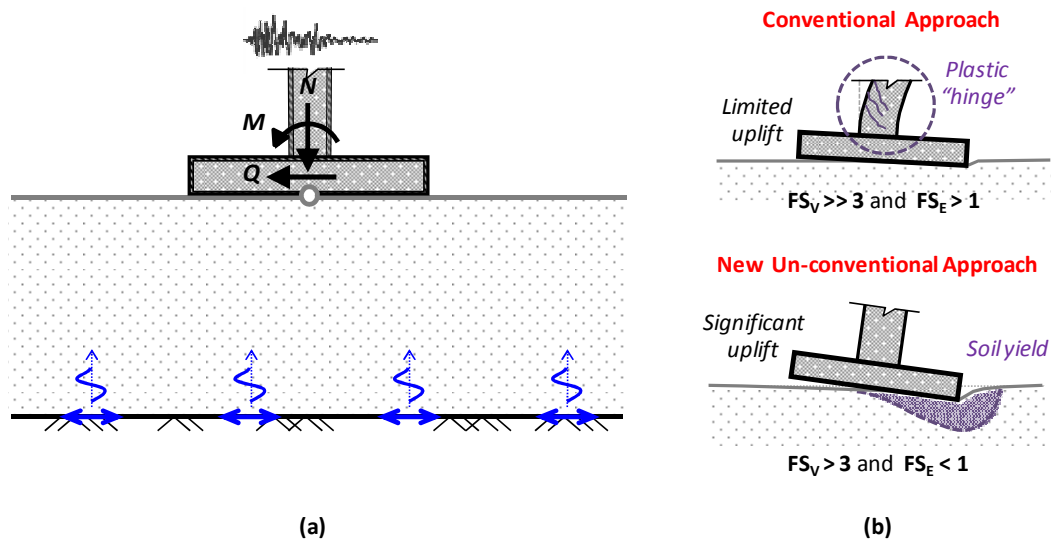


Figure 1. Problem definition: (a) shallow foundation subjected to seismic (combined N-Q-M) loading; (b) two foundation design alternatives: the conventional design approach and a new un-conventional design philosophy where the response is dominated by foundation uplifting.

2 CONSTITUTIVE RELATIONS

Anastasopoulos et al. [2011] have developed a simplified constitutive model which is based on the Von Mises failure criterion, modified however appropriately so as to model the pressure-dependent behavior of sands as well as that of clays.

The Von Mises failure criterion is combined with non-linear kinematic hardening, as illustrated in the graphs of Figure 2, and associated plastic flow rule. The evolution of stresses is defined as:

$$\sigma = \sigma_0 + \alpha \quad (1)$$

where σ_0 corresponds to the stress at zero plastic strain, and α is the "backstress", which determines the kinematic evolution of the yield surface in the stress space according to the relationship:

$$F = f(\sigma - \alpha) - \quad (2)$$

where $f(\sigma - \alpha)$ is the equivalent Mises stress with respect to the backstress α .

An associated flow rule is assumed and the plastic flow rate is:

$$\dot{\epsilon}^p = \dot{\epsilon}^p \quad (3)$$

where $\dot{\epsilon}^p$ is the equivalent plastic strain rate.

The evolution law of the model consists of two components: a non-linear kinematic hardening component and an isotropic hardening component. The kinematic hardening component is defined as an additive combination of a purely kinematic term and a relaxation term, which introduces the non-linearity. The evolution of the kinematic component of the yield stress is described as follows:

$$\dot{\alpha} = C \frac{1}{\sigma - \alpha} \dot{\epsilon}^p - \gamma \alpha \quad (4)$$

where C the initial kinematic hardening modulus ($C = \sigma_y / \epsilon_y = E$) and γ a parameter that determines the rate at which the kinematic hardening decreases with increasing plastic deformation. According to the evolution law governing the kinematic hardening component the backstress is contained within a cylinder of radius $\sqrt{2/3}C$. Given the bounded yield surface, all stress points lie within a cylinder of $\sqrt{2/3}\sigma_y$, where σ_y is the ultimate stress.

At large plastic strains, when σ approaches σ_y , the magnitude of α becomes equal to $\alpha_s = C/\gamma$ (see Figure 2c) and $(\sigma - \alpha)$ tends to σ_0 . Hence, the maximum yield stress can be defined as:

$$\sigma_y = \sigma_0 + C \quad (5)$$

For the case of clays, the undrained strength of which is pressure independent, the ultimate stress can be defined as $\sqrt{3}S_u$ and hence parameter γ can be calculated as:

$$\gamma = \frac{C}{\alpha_s} \quad (6)$$

In the case of sands however, shear strength depends also on confining pressure apart from the soil strength characteristics (i.e. the friction angle ϕ). This pressure-dependency is incorporated in the model by defining the yield stress at saturation as a function of octahedral stress and the friction angle, as follows :

$$\sigma_y = \sqrt{3} \left(\frac{\sigma_1 + \sigma_2 + \sigma_3}{3} \right) \sin \phi \quad (7)$$

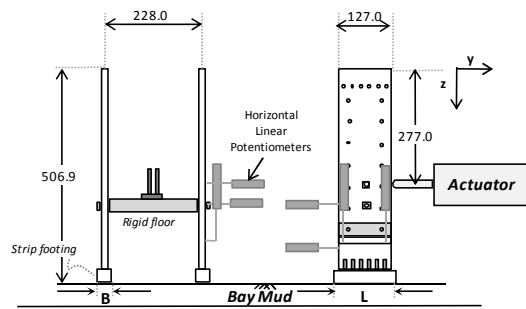
Accordingly, parameter γ may be calculated as:

$$\gamma = \frac{C}{\alpha_s} \quad (8)$$

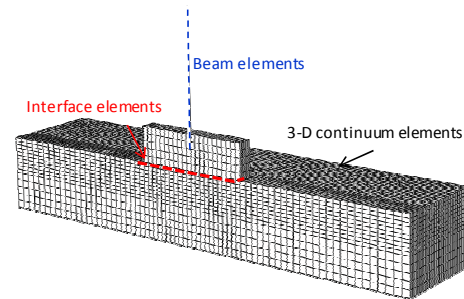
Regarding the other two parameters of the model, σ_0 may be defined as a fraction of σ_y ($\sigma_0 = \lambda \sigma_y$, with λ typically ranging from 0.1 to 0.3) whilst C may be determined with reference to empirical relationships or direct measurements of the small strain Young's modulus.

something which is not observed to the same extent in the experiment. The latter is indicative of increased plastic straining of the soil underneath the footing, hence resulting to higher dissipation of energy as elucidated by the area included within the experimental hysteresis loops. Increasing the input displacement magnitude (larger amplitude loading cycles) results in excessive soil plastification which is evident from both the experimental and the numerically computed moment–rotation loops. These hysteresis loops reveal a highly non-linear response of the soil–foundation system. Furthermore, the moment–rotation curve now conspicuously manifests the mobilization of the ultimate capacity ($M_{ult} \approx 300$ kNm) : increase of rotation for constant moment. It should be noted that the experimental hysteresis loops systematically reveal a non-symmetric behavior, which is attributed to some localized plastification underneath the footing edges possibly occurring due to earlier cycles of shearing or inhomogeneities in the construction of the physical model, which of course may not be reproduced in the analysis.

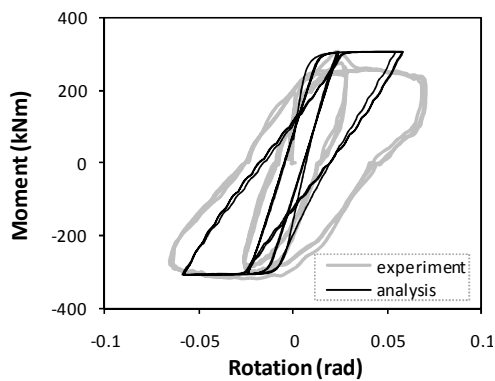
The numerical prediction is quite successful in terms of the settlement–rotation response (Figure 11b). Excessive uplift appears to take place indicated by the sharp edges of the settlement–rotation loops. As elucidated by Gajan et al. [2005], foundation rocking during large amplitude lateral loading leads to (permanent) loss of contact between the soil and the footing. The generated gap at the uplifted side is associated with a drastic reduction of the effective width of the foundation, leading to extensive soil yielding at the opposite side, further increasing the detached area of the foundation.



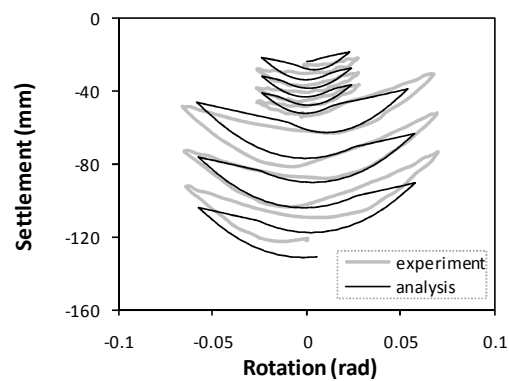
(a) Centrifuge testing set-up: Horizontal cyclic push



(b) Centrifuge testing set-up: Horizontal cyclic push



(c) Experimental vs. analytical moment–rotation loops



(d) Experimental vs. analytical settlement–rotation loops

Figure 3. Model validation against UC Davis Centrifuge Tests *on clay* – Cyclic lateral pushover testing of footings.

Overall, it may be claimed that despite some discrepancies, which mainly involve the response under low amplitude displacements, the numerical model reliably reproduces the experiments throughout the entire range of displacements capturing with sufficient accuracy the ul-

timate lateral capacity of the foundation as well as the progressively non-linear response in the moment–rotation plane, implied by the degradation of rotational stiffness with increasing rotation amplitude. Furthermore the analysis predicts the accumulation of permanent settlement underneath the footing and the predomination of uplifting with increasing the number of loading cycles.

3.2 Large-scale testing of a square footing on dense and loose sand

Aiming to verify the claim that, after being appropriately modified so as to encompass the pressured dependency of frictional materials (Equations 7 and 8), the presented numerical model may as well apply to sands, a series of large scale 1-g tests performed on footings upon sandy soil profiles are simulated and results are summarized in Figure 4 for both dense and loose sand specimens. The experiments were conducted at the ELSA facility in ISPRA (Italy) in the framework of the TRISEE research project and have been documented by Faccioli et al., [1999]. In detail report of their numerical simulations has been conducted by Anastasopoulos et al., [2011].

A remarkable agreement is observed between measured and calculated hysteresis loops produced during slow cyclic tests on dense sand (Figure 4a). Both loops evolve quite symmetrically. The numerical analysis effectively reproduces the lateral capacity of the system : $M_{ult} \approx 100$ kNm. Furthermore, it captures with sufficient accuracy both the initial stiffness of the system, and the gradual degradation of rotational stiffness with increasing rotation.

Contrarily to the uplifting behavior of the footing on dense sand (evident by the S-shaped loops of Figure 4a), the foundation on loose sand is obviously subjected to substantial irrecoverable sinking within the soil. This is justified by both the numerical model and the experimental results, which show clearly larger energy dissipation.

The analysis has been successful in simulating the experimentally observed mobilization of the foundation capacity. In very good accord with the measured value, the predicted ultimate moment of the system is $M_{ult} \approx 40$ kNm in the negative loading direction. It should be noted that the asymmetry of response in the test, attributable to some irregularity in the input displacement, cannot be reproduced in the analysis. Yet, the general comparison between analytical and experimental results is judged as very satisfactory.

4 DEALING WITH SCALE EFFECTS: SIMULATION OF 1-G REDUCED SCALE TESTS

It is well known that the strength of sands highly depends on the applied stress [Bolton, 1986]. Thus, physical modeling in reduced scale results in misreproduction of the soil strength due to the underestimation of the distribution and evolution of the applied effective stress field, this being admittedly the most important shortcoming of 1-g testing against centrifuge modeling.

When performing numerical simulations of reduced-scale experiments on sand, it is essential to account for such scale related variations in the soil strength profile. This may be achieved simply by inputting a pressure dependent relationship for the soil friction angle, which may be determined with reference to shearbox test results, instead of a constant value of φ (Figure 5a). The scale factor N is unavoidably introduced in the calculation of the apparent φ , so as to achieve stress–strength similarity for any pair of homologous points between the model and the prototype (Figure 5b).

Hence, reduced scale effects may be incorporated in the herein presented constitutive model by modification of Equation (7), so as any soil element in the FE model (in prototype scale) to have the same strength with its homologous point in the physical model (model scale):

$$\sigma_v = \sqrt{3} \left(\frac{\sigma_1^2 + \sigma_2^2 + \sigma_3^2}{3} \right) \sin \varphi (\sigma_v) \quad (9)$$

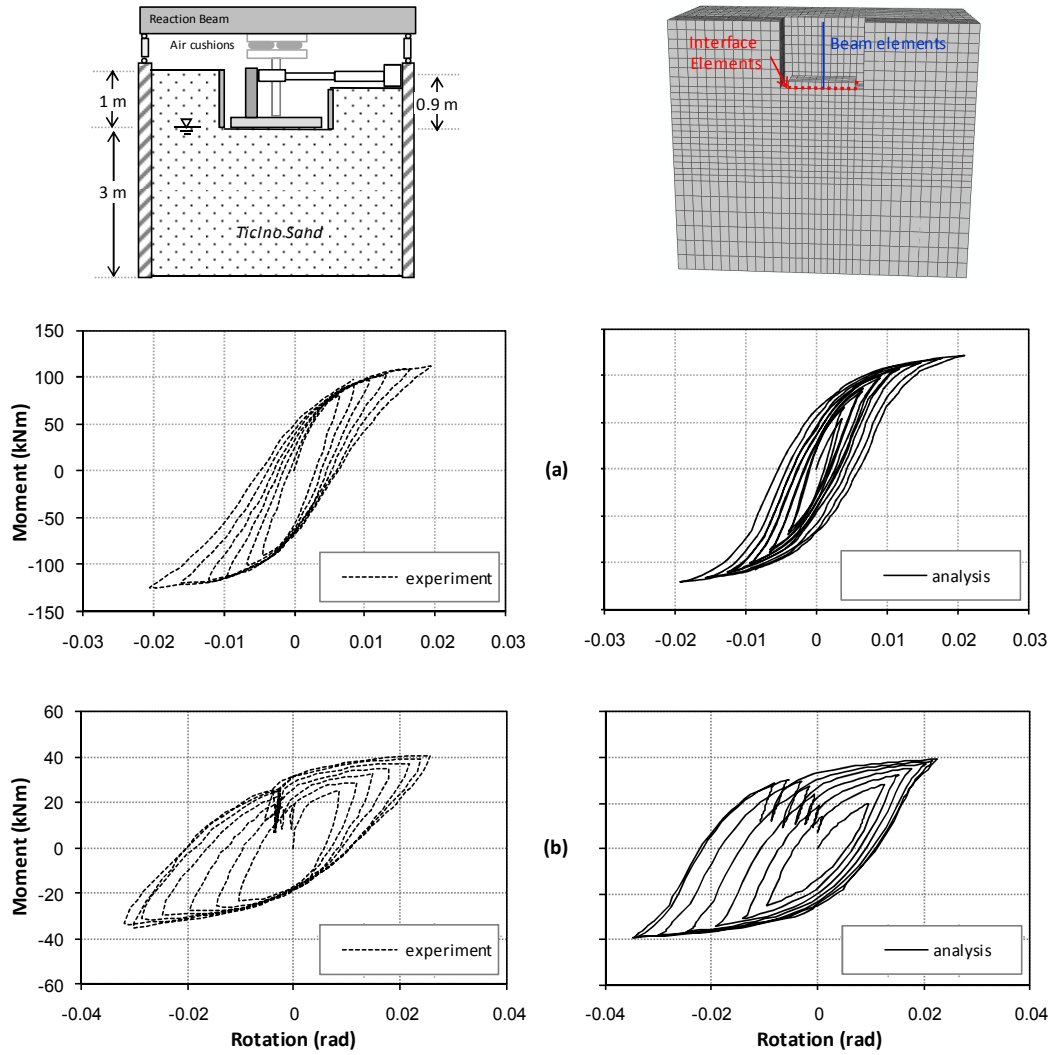


Figure 4. Model validation against 1-g large scale tests *on sand*. Comparison of cyclic response in terms of foundation moment - rotation loops for (a) dense sand; and (b) loose sand.

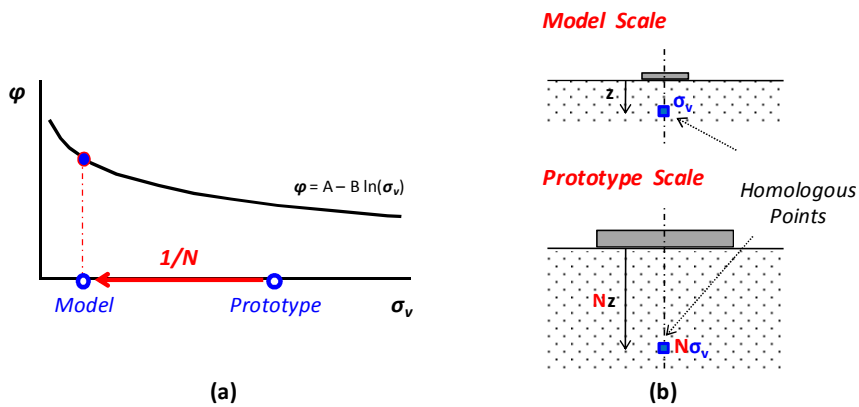


Figure 5. Effect of reduced scale modeling on the reproduction of the prototype soil strength distribution: (a) friction angle is a function of effective stress, and hence (b) for any pair of homologous points between prototype and scaled down model, the vertical stress in the model is N times lower than in the prototype and therefore the effective friction angle is somewhat larger.

A series of small scale experiments on foundations of various sizes and safety factors, which have been conducted at the Laboratory of Soil Mechanics of NTUA and are documented in a companion paper (Drosos et al., 2011), were simulated numerically in order to verify the ability of the presented numerical method in capturing scale effects. The experimental campaign involved three rigid 1-dof systems supported upon a layer of dense sand through three distinctively different shallow foundations: (i) the so called *large* foundation ($FS_V = 7.3$) was designed in accord with current capacity design practice; (ii) the *medium* foundation ($FS_V = 3.5$) was unconventionally designed to allow uplifting and yielding mechanisms to take place; and (iii) the *small* foundation ($FS_V = 2.1$) represents a seriously under-designed foundation.

4.1 Monotonic Loading

Figure 6 compares the numerically computed against the measured response of the three foundations to monotonic horizontal pushover loading in terms of moment–rotation and settlement–rotation curves.

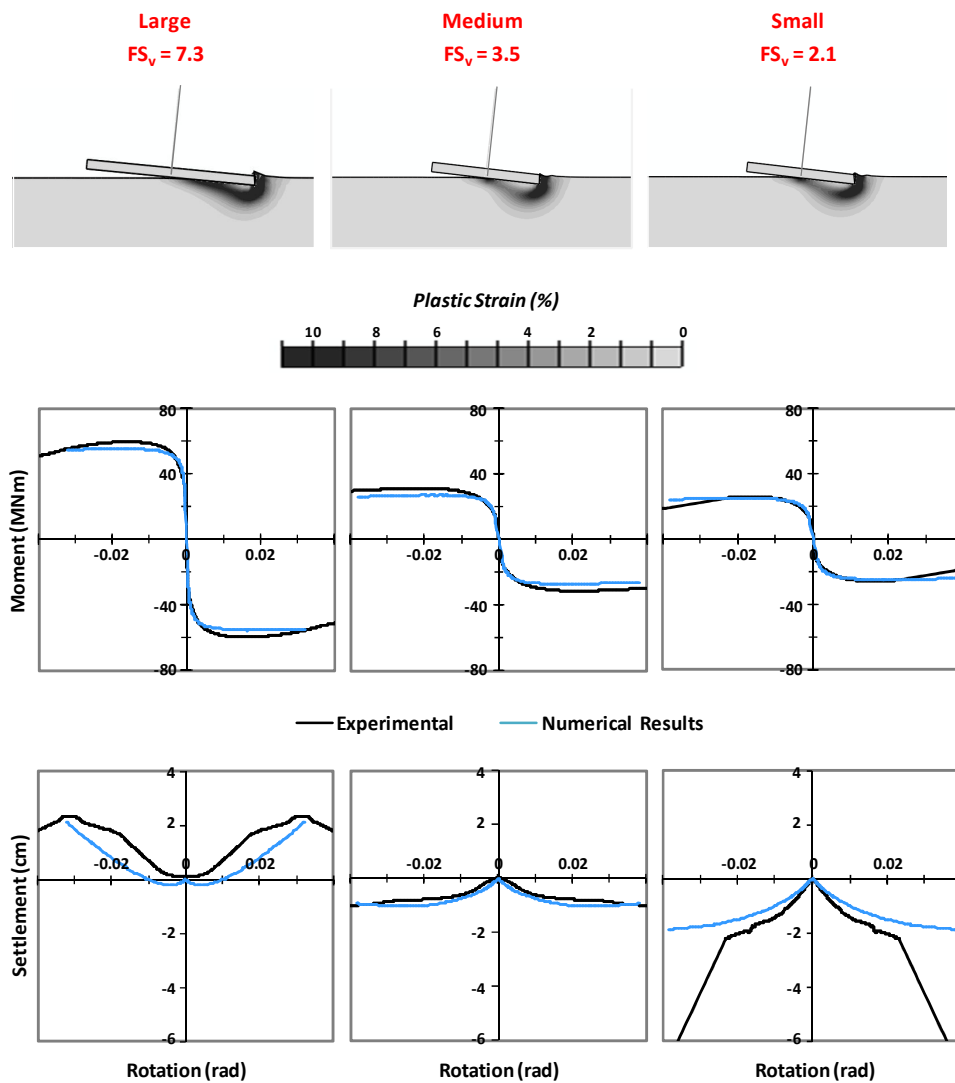


Figure 6. Model validation against 1-g reduced scale tests ($N = 20$). Monotonic horizontal pushover tests results in terms of moment–rotation and settlement–rotation curves and comparison with the FE analysis results for the three different foundation sizes considered: the large foundation ($FS_V = 7.3$); the medium foundation ($FS_V = 3.5$) and the small foundation ($FS_V = 2.1$).

Naturally, moment capacity appears as a decreasing function of the foundation size. Furthermore, in accord with the design, the lightly loaded large foundation demonstrates an uplift dominated response and, as shown by the corresponding settlement–rotation curve, its centre appears to move upwards straight after the application of loading revealing that more than half of the foundation area loses contact with the supporting soil. The opposite appears to be the case for the two smaller foundations, where the behavior is mostly associated with soil yielding owing to the relatively lower bearing capacity. Hence, the centre of the medium and the small foundations move downwards (settle) with increasing displacement at a rate which presumably increases with reducing FS_V .

The numerical method predicts with sufficient accuracy the rocking stiffness (gradient of the M – θ curve) and reproduces generally well the moment–rotation response of all three foundations despite the slight underestimation of the ultimate moment capacity for the two larger ones. Equally satisfactory in general terms is the comparison between numerically predicted and measured response in the settlement–rotation plane. Some discrepancies refer to the numerical prediction of the soil–foundation system stiffness, indicated by the gradient of the w – θ curve, which is somewhat underestimated in the case of the large foundation and contrarily somewhat over-predicted in the case of the small one. Nevertheless, the numerical method appears to reproduce the general attributes of response to this type of loading with sufficient reliability.

4.2 Cyclic Loading

The three structure–foundation systems were also subjected to cyclic pushover tests. The loading sequence included a series of displacement cycles of increasing amplitude divided for convenience into three loading packets. Figure 7 compares the experimental results with the results of the respective numerical simulations in terms of moment–rotation and settlement–rotation loops for all three foundations during the third loading packet, which involved large amplitude displacements (generally ranging from 10 to 50 cm in prototype scale).

As expected, non-linear material response, betrayed by the area enclosed in the moment–rotation loop becomes more significant with decreasing foundation size. Thus, uplifting dominates the response of the lightly loaded large foundation (observe the impressive 2 cm lift-off of its center during the last loading cycle in Figure 7a), yet giving place to soil yielding mechanisms as FS_V reduces. Some uplifting, although much less than in the case of the large foundation, may be traced in the settlement–rotation response of the medium foundation (Figure 7b) while the small foundation demonstrates pure "sinking" response, implied by the downwards movement of its center on every half-cycle of loading.

Comparison between analytical and experimental results manifests the effectiveness of the numerical method in capturing the details of rocking response, namely the ultimate lateral capacity, the degradation of stiffness with increasing rotation and the interchange between uplift and yielding mechanisms as well as their relation to the relative weight (i.e. FS_V). Interestingly, the agreement between analysis and experiment becomes surprisingly good in the case of the small foundation when material non-linearity is significant. Furthermore, the numerical method gives excellent predictions of the total accumulation of settlements under the foundations as well as the rate of settlement per cycle. However, it should be mentioned that the comparison was less satisfactory for the two previous loading packets (which are not shown here), where the three systems were subjected to smaller displacements, partly because of the simplicity of the constitutive model and also due to the inaccuracies associated with reduced scale testing in the small strain domain.

5 SUMMARY AND CONCLUSIONS

The paper has presented a comprehensive validation of the simplified constitutive model of Anastasopoulos et al., [2011] with regard to the non-linear rocking response of shallow foundations. Employed in the simulation of different large scale experiments conducted on clayey and sandy soil profiles, as well as in the simulation of small scale experiments on sand, the presented numerical methodology proved capable of reliably reproducing all the different aspects of shallow foundation rocking response regardless of the supporting soil material or the possible

effect of physical modeling scale. More specifically, the most important conclusions may be summarized as follows:

- The Von Mises failure criterion of the constitutive model can be considered appropriate for clay under undrained conditions.
- The extended normal-pressure-dependent Von Mises failure criterion, employed to render the model applicable to sand, constitutes a simplified approximation of real sand behavior.
- Despite its inherent simplifications and as far as the problem of rocking of a shallow foundation is considered, the proposed numerical model has been shown to yield quite satisfactory results *for both clayey and sandy soils*. Through the validation presented herein, the model was found capable of capturing with reasonable engineering accuracy the details (ultimate capacity, stiffness degradation with increasing rotation, hysteretic response, settlement–uplifting in relation to the rotation amplitude and the number of loading cycles) of such a complex problem where multiple types of non-linearity are combined.
- Furthermore, the numerical method was appropriately modified so as to account for scale effects when reproducing reduced scale experiments and confidence on its validity was strengthened by successful simulations of a series of small-scale experiments on the monotonic and cyclic non-linear response of footings of varying safety factors.
- Being easily implemented in commercial FE codes and requiring but only the knowledge of soil strength (S_u for clays and ϕ for sand) and small-strain stiffness (G_o or V_s) the model is believed to provide a practically applicable solution, not restricted to simple superstructures, and not to be solely used by numerical analysis specialists.

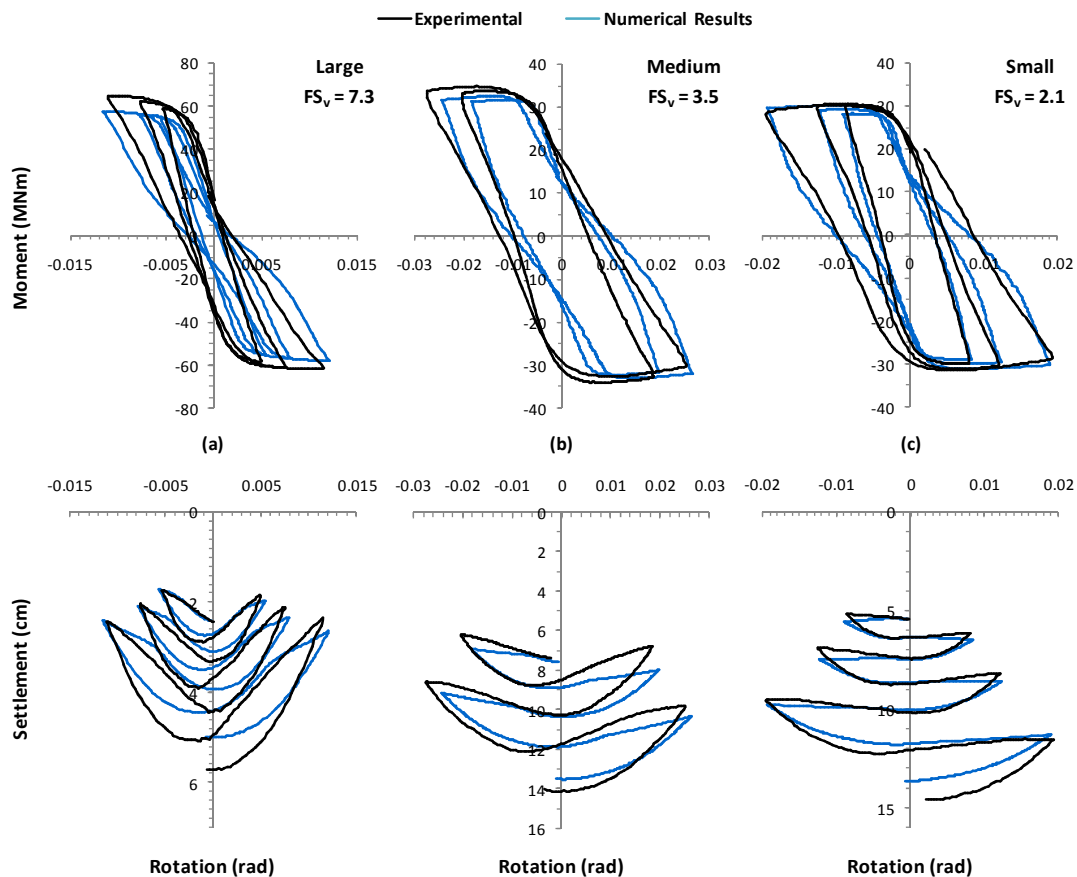


Figure 7. Model validation against 1-g reduced scale tests ($N = 20$). Cyclic horizontal pushover tests results in terms of moment–rotation and settlement–rotation curves and comparison with the FE analysis results for the three different foundation sizes considered: (a) the large foundation ($FS_v = 7.3$); (b) the medium foundation ($FS_v = 3.5$), and (c) the small foundation ($FS_v = 2.1$).

6 ACKNOWLEDGMENT

The research presented in this paper was funded by the European Research Council (ERC) Program "IDEAS, Support for Frontier Research – Advanced Grant", under Contract number ERC–2008–AdG 228254–DARE.

7 REFERENCES

- Anastasopoulos I., Gazetas G., Loli M., Apostolou M., Gerolymos N. (2010), Soil Failure can be used for Earthquake Protection of Structures, *Bulletin of Earthquake Engineering*, Vol. 8(2), pp. 309–326.
- Anastasopoulos I., Gelagoti F., Kourkoulis R., Gazetas G. (2011), Simplified Constitutive model for Simulation of Cyclic Response of Shallow Foundations: Validation against Laboratory Tests, *Journal of Geotechnical and Geoenvironmental Engineering*, ASCE (in press).
- Chatzigogos C.T., Pecker A., Salencon J. (2009), Macroelement modeling of shallow foundations, *Soil Dynamics and Earthquake Engineering*, Vol. 29(6), pp. 765–781.
- Dafalias Y.F., & Manzari M.T. (2004), Simple plasticity sand model accounting for fabric change effects. *ASCE Journal of Engineering Mechanics*, 130(6), pp. 622–34.
- Drosos V., Georgarakos T., Loli M., Anastasopoulos I., and Gazetas G. (2011), Non-linear Soil–Foundation Interaction : An Experimental Study on Sand, *Proceedings of the 4th Japan–Greece Workshop*, Kobe, October 2011.
- Faccioli E., Paolucci R., and Vanini M., eds (1999), *TRISEE : 3D Site Effects and Soil-Foundation Interaction in Earthquake and Vibration Risk Evaluation*, European Commission Publications.
- Gajan S., Kutter B.L., Phalen J.D., Hutchinson T.C., Martin G.R. (2005), Centrifuge modeling of load-deformation behavior of rocking shallow foundations, *Soil Dynamics and Earthquake Engineering*, 25, pp. 773–783.
- Gajan S. & Kutter B.L. (2009), "Contact interface model for shallow foundations subjected to combined loading", *Journal of Geotechnical and Geoenvironmental Engineering*, ASCE, 135(3), pp. 407–419.
- Gazetas G., Anastasopoulos I., Apostolou M. (2007), Shallow and Deep Foundations under Fault Rupture or Strong Seismic Shaking, *Earthquake Geotechnical Engineering*, Pitilakis K., Editor, Springer : Berlin, pp. 185–210.
- Harden C., Hutchinson T., and Moore M. (2006), Investigation into the effects of foundation uplift on simplified seismic design procedures, *Earthquake Spectra*, 22(3), pp. 663–692.
- Houlsby G.T. & Puzrin A.M. (2006), *Principles of Hyperplasticity*, Springer : Berlin.
- Martin G. R. & Lam I. P. (2000), "Earthquake Resistant Design of Foundations : Retrofit of Existing Foundations", *Proceedings of GeoEng 2000 Conference*, Melbourne, pp. 19–24.

A Simplified Method to Assess the Toppling Potential of Ground Motions: Application to Rocking–Isolated Frame Structures

F. Gelagoti, R. Kourkoulis

Soil Mechanics Laboratory, National Technical University, Athens, Greece

ABSTRACT: This paper aims to explore the limitations associated with the design of "*rocking–isolated*" frame structures. According to this novel seismic design concept the foundation is intentionally under-designed (so as to present lower moment capacity than the corresponding column), with the intention to bound the inertia loading that may be transmitted to the superstructure. Yet, decreasing footing dimensions increases the risk of toppling. Motivated by the need to address this issue in design, this paper proposes the peak spectral displacement of an earthquake record as a conservative upper-bound estimate of displacement demand. The adequacy of the measure is validated through comparison with published analytical and numerical results. Finally the paper attempts an investigation on the record characteristics affecting the overturning potential of ground motions, concluding that the impact pulse velocity and the number of cycles exceeding the toppling acceleration play prominent role.

1 INTRODUCTION

Recorded accelerations during strong earthquakes over the last 20 years very often overly exceeded code provisions: in the 1994 Northridge earthquake ($M_s = 6.8$) the maximum recorded P.G.A. exceeded 0.90 g; the 1995 Kobe earthquake ($M_s = 7.2$) produced maximum recorded acceleration of $a = 0.85$ g, while the 2007 Niigata-ken Oki earthquake produced an acceleration of $a = 1.20$ g. Such events have demonstrated that non-linear foundation response is indeed inevitable during strong seismic shaking. In fact, ensuring elastic foundation response may even be totally undesirable since enormous ductility demands would be imposed on the superstructure. On the other hand, allowing "plastic hinging", in the form of foundation uplift could be beneficial for the superstructure as it would bound the inertial forces transmitted to it [Psycharis and Jennings, 1983; Yim & Chopra, 1984; Martin & Lam, 2000; Pecker & Pender, 2000; Faccioli et al., 2001; Kutter et al., 2003; Harden and Hutchinson, 2006; Gajan and Kutter, 2008; Kawashima et al., 2007; Apostolou et al., 2007; Paolucci et al., 2008; Chatzigogos et al., 2009; Anastasopoulos et al, 2010].

The potential effectiveness of the mechanisms of foundation uplifting on frame structures has recently been investigated by Gelagoti et al (2011) for a simple 2-storey 1-bay frame (Fig. 1). Since foundation plastic "hinging" is mainly in the form of rocking and uplifting of the footing, the proposed design concept is termed *rocking isolation*, following the terminology proposed by [Mergos and Kawashima, 2005].

The authors compared the seismic performance of a conventionally designed structure (with square footings of $B = 1.7$ m) to a specific rocking-isolation alternative (with smaller footings of $B = 1.4$ m, Fig. 1). In this latter case footings were designed so that their moment capacity (M_{ult}) is smaller than that of the corresponding column. Hence, when the earthquake demand exceeds the footing capacity of the foundation, uplift is promoted. In all cases examined the Safety Fac-

tor against vertical loads was adequately high ($FS_v > 6$) so as foundation rocking prevails and soil yielding is impeded.

Through static pushover and nonlinear dynamic time-history analysis (using an ensemble of 24 strong motion records), the performance of the rocking-isolated alternative was found to be advantageous in very strong seismic shaking, well in excess of the design limits: it survives the earthquake demand sustaining non-negligible but repairable damage to its beams and non-structural elements (infill walls, etc.). Further decrease of foundation width (and subsequently further reduction of the foundation moment capacity) was shown to provide even more effective rocking isolation, yet at the expense of augmented foundation rotation or increased risk of frame toppling.

Motivated by the need to estimate a safe lower-bound dimension of rocking-isolated frame footings this paper aims to develop a simplified yet conservative procedure to estimate the maximum credible earthquake displacement demand (δ_{dem}). This demand may subsequently be combined with the (known) displacement capacity of the rocking superstructure to assess the minimum allowable footing dimensions that would ensure structural integrity of the superstructure.

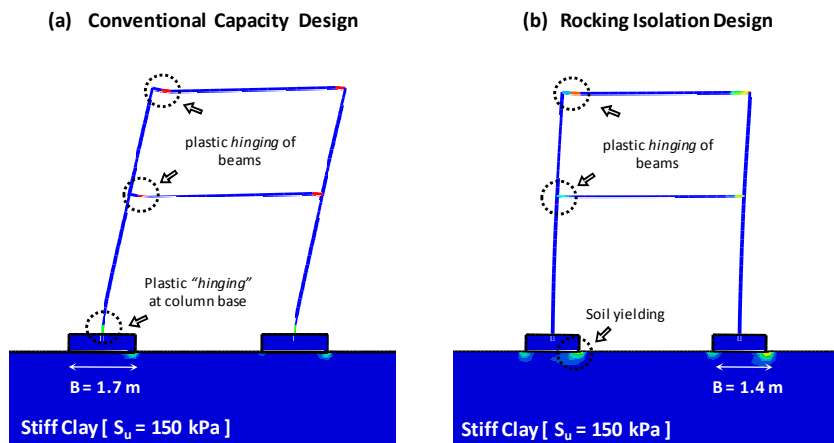


Figure 1: (a) Schematic illustration of the “rocking-isolation” concept that was thoroughly investigated at *Gelagoti et al (2010)*: Plastic Strains contours superimposed with deformed mesh when the two frames are excited by the extremely strong Takatori (Kobe, 1995) record. The conventionally designed frame collapses (plastic hinges are formed at the base of the two columns), while the rocking-isolation alternative survives despite the severity of the excitation.

Recalling that the apparent period of a rocking system changes constantly during shaking, rising from zero (in the case of a rigid block glued to its base) to infinity at the state of incipient toppling (Fig. 2), T_{eff} can neither be known a-priori nor can it be accurately estimated by means of conventional iterative procedure (Makris and Konstantinidis; 2003). Following this reasoning, in this research the peak spectral displacement SD_{max} is proposed as a conservative measure of the *upper bound* displacement demand (i.e. independent of T_{eff}). It is noted that SD_{max} is only proposed as an index of the maximum anticipated seismic displacement demand, knowing that this will not necessarily develop during shaking.

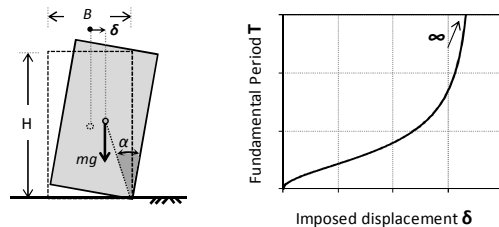


Figure 2. Evolution of the apparent natural period T with imposed displacement δ during rocking of a rigid block on rigid base. At the state of incipient toppling, T tends to infinity.

The validity and limitations of this simplified approximation are investigated in the following sections for two classes of rocking bodies: (i) a rigid-block on a rigid-base, and (ii) a nonlinear frame structure on inelastic soil.

2 VALIDATION OF THE APPROACH: RIGID BLOCK ON RIGID BASE

The issue of earthquake-induced rocking of *rigid blocks* on *rigid base* has been thoroughly investigated [Housner, 1963; Psycharis & Jennings, 1983; Koh et al., 1986; Makris & Roussos, 2000; Apostolou et al., 2007], and quite invariably it was demonstrated that overturning is rather unpredictable – *if not chaotic* – even for idealized cycloidal pulses as excitation. Hence, attempting to accurately quantify the toppling potential of a seismic motion (for a given *rigid block*) utilizing the simplified SD_{max} criterion would be overly optimistic and is by no means attempted herein. Instead, the present study aims to propose SD_{max} only as a *conservative upper-bound* of earthquake displacement demand δ_{dem} , for which toppling will not take place. The exploration presented in this paragraph refers to a rigid block on a rigid base subjected to (a) cycloidal (sinus and cosine) pulses, and (b) Ricker wavelets.

2.1 Rigid block excited by sinus and cosine pulses

A rigid block of width B and height H (Figure 2) is characterized by its angle $\alpha = \tan^{-1}(B/H)$ and the frequency parameter p :

$$p = \sqrt{3g/4R} \quad (1)$$

where $R = \sqrt{(\frac{B}{2})^2 + (\frac{H}{2})^2}$. The latter, which can be seen as a measure of the dynamic characteristics of the block, decreases with the size of the block. *Zhang & Makris [2001]* investigated analytically the transient rocking response of free-standing rigid blocks subjected to trigonometric (sine and cosine pulses) base excitation. Their rigorous analytical results are used herein as a comparison with the SD_{max} approach estimations. A relatively “small” block of $p = 2.14$ rad/s and $\alpha = 0.25$ rad is used as an illustrative example. The block is excited by one-cycle sinus (Fig. 3a) and cosine pulses (Fig. 3b) of amplitude a and cyclic frequency ω_p . The non-dimensional toppling acceleration $a_p/\alpha g$ is plotted as a function of normalized excitation frequency ω_p/p . The predictions of the simplified SD_{max} approach (distinct markers) are compared with the results of the exact analytical solution (shaded areas indicate toppling of the block).

It can be seen that both in the rigorous and the simplified approach, the non-dimensional toppling acceleration $a_p/\alpha g$ increases exponentially with ω_p/p ; this reveals that $a_p/\alpha g$ increases with excitation frequency *and* block dimensions ($1/p \propto \sqrt{R}$). In fact for the sinus pulse, the SD_{max} approach yields conservative results for the whole frequency range. However, for the cosine pulse, although conservative for lower and higher values of the frequency ratio ($\omega_p/p \leq 1.8$ and $\omega_p/p \geq 4.3$) it becomes marginally unconservative for intermediate frequencies ($1.8 < \omega_p/p < 4.3$). However this “unsafe region” is of reduced practical interest for relatively large systems such as low rise frames where p values normally range between $0.6 < p < 1$, and consequently the ratio ω_p/p is always greater than 4 for pulse periods $T_p < 1.6$ s (i.e., almost the complete earthquake period range).

2.2 Rigid block subjected to Ricker pulses

Gerolymos et al. (2005) based on dynamic time-history results, employed artificial neural networks to derive closed-form analytical expressions for predicting the overturning acceleration a_p of a rigid block subjected to Ricker pulses as a function of its geometric properties: Figure 4 depicts the comparison of the simplified SD_{max} - based prediction with the numerical solution of *Gerolymos et al. (2005)* for (i) a medium-size block of $p = 3.14$ rad/s and $\alpha = 0.25$ rad, simulating an *electrical transformer* ; and (ii) a large-size block of $p = 0.76$ rad/s and $\alpha = 0.30$ rad, simulating a *slender building*. Evidently, in accord with our previous observation, the larger the

dimensions of the rocking body, the greater the degree of conservatism of the SD_{max} -based method, whereas for very high frequency motions the simplified procedure underpredicts the toppling capacity by a factor greater than 1.5.

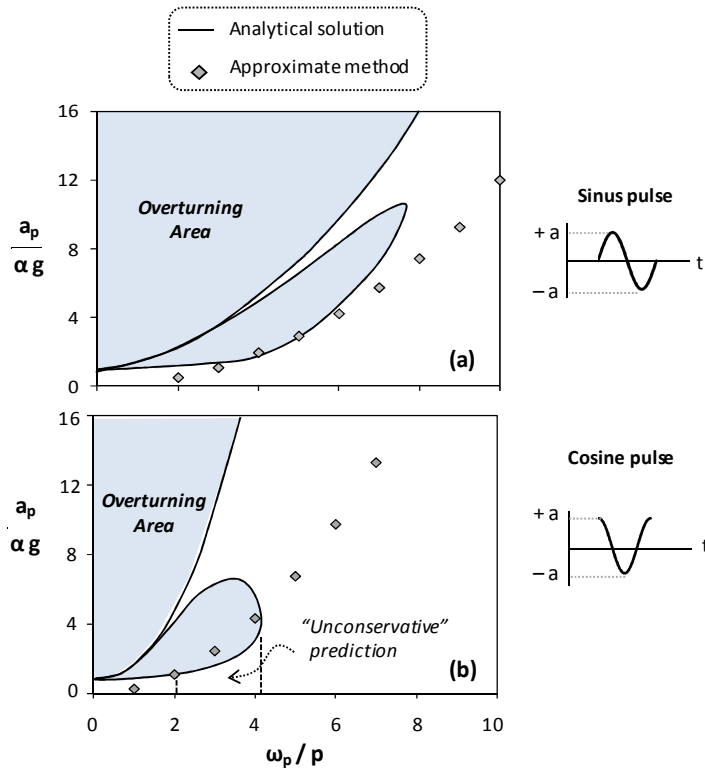


Figure 3. Non-dimensional toppling acceleration of a rigid body rocking on a rigid base: Comparison of the simplified method (based on the maximum spectral displacement SD_{max}) with the rigorous analytical solution of Zhang & Makris (2001) for two idealized excitation pulses: (a) one-cycle sinus, and (b) one-cycle cosine. Case study: rigid block of $p = 2.14$ rad/s and $\alpha = 0.25$ rad.

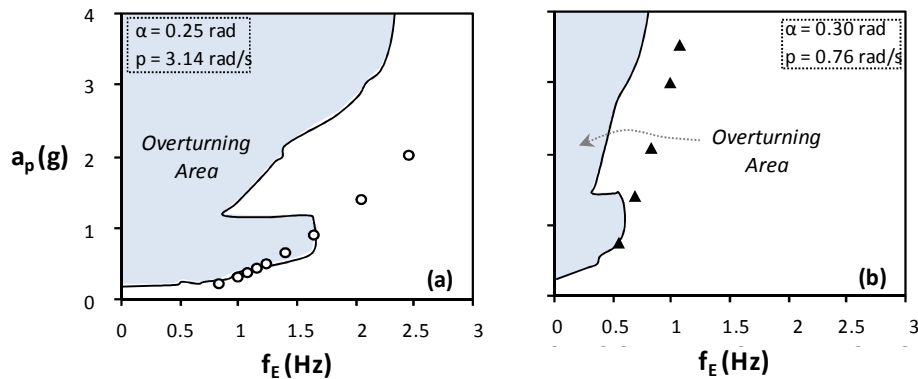


Figure 4. Toppling acceleration a_p of a rigid body rocking on a rigid base when excited by Ricker pulses of various f_E : Comparison of a_p estimated by the simplified method with the numerical solution of Gerylmos *et al.* [2005], plotted as a function of excitation frequency f_E for: (a) a medium-size block (electrical transformer) of $p = 3.14$ rad/s and $\alpha = 0.25$ rad, and (b) a large-size block (slender building) of $p = 0.76$ rad/s and $\alpha = 0.30$ rad

3 VALIDATION OF THE APPROACH: 2-STOREY FRAME ON INELASTIC SOIL

Having gained confidence on the results of the SD_{max} approach when implemented to estimate the toppling capacity of a rigid block on a rigid base, this section further verifies its effectiveness for the case of the 2-storey frame founded on nonlinear soil, subjected to both Ricker pulses and actual seismic records. To this end time history non-linear FE analyses had been conducted for the example frame (of Fig. 1) founded on footings of $B = 1.10$ m. Based on the $M-\theta$ response of the two footings (Fig. 5), the toppling rotation is $\theta_{ult} = 0.143$ rad, corresponding to a toppling displacement at the center of mass of the frame $\delta_{topl} = 71$ cm (ignoring frame's flexibility). Hence, according to the simplified approach, any motion with $SD_{max} < \delta_{topl}$ should not provoke toppling of the frame.

To validate this, the FE model have been subjected to amplitude-scaled excitations with SD_{max} marginally lower than the toppling displacement δ_{topl} of the frame (e.g., $SD^- = 0.9 \delta_{topl}$). In order to investigate the possible safety margins of the proposed methodology, the input motions are also scaled to $SD_{max} = 1.1 \delta_{topl}$ ($= 78$ cm), denoted SD^+ .

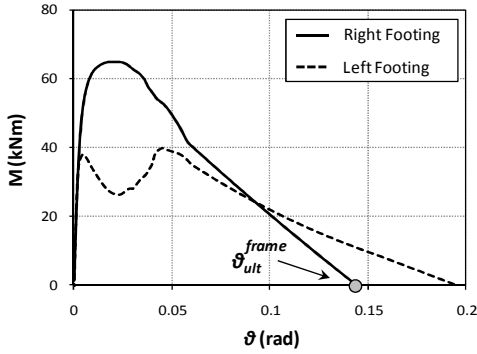


Figure 5. $M-\theta$ response of the two frame footings. [Results correspond to the frame of Figure 1 assuming foundation width of $B=1.1$ m]

3.1 Frame subjected to Ricker pulses

Ricker pulses of seven different characteristic frequencies, $f_E = 0.40, 0.50, 0.65, 0.85, 1.00, 1.25,$ and 1.50 Hz, have been used whose amplitude was sequentially increased until toppling of the frame. The minimum acceleration amplitude of each motion which provokes failure of the F.E. model is considered to be the “actual” (rigorously computed) toppling acceleration a_p . Fig. 6b, plots a_p as a function of normalized frequency ω_p/p of the system, and compares it to the predicted $(a_p)_{SD}$ toppling acceleration. Evidently, for all frequencies examined, the simplified approach yields a reasonably conservative prediction, while the margin of safety increases with increasing ω_p/p .

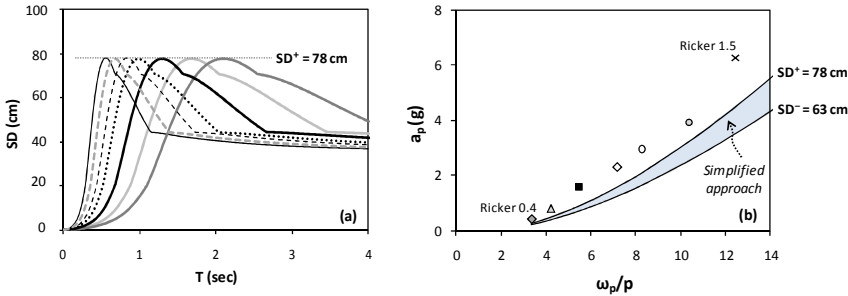


Figure 6. Comparison of simplified method with dynamic time history analysis of the frame on nonlinear soil subjected to Ricker pulses of various dominant frequencies f_E : (a) displacement response spectra SD of scaled Ricker pulses (to produce max $SD^+ = 78$ cm), (b) comparison of FE computed toppling acceleration a_p with the predicted $(a_p)_{SD}$ as a function of non-dimensional excitation frequency ω_p/p .

3.2 Real Records

18 recorded earthquake motions from the US, Europe, and Asia are utilized as excitation of the frame. The records were selected so as to enable us to capture the effects of various parameters, such as PGA and PGV, SA and SD, frequency content, duration, number of strong motion cycles. As previously, the validity of the SD_{\max} prediction is verified through dynamic nonlinear time-history analysis of the frame, where all input motions have been scaled at SD^+ (Fig. 7a) and SD^- values respectively. (Table 1). The produced Spectral Accelerations of the scaled accelerograms are displayed in Fig. 7b.

Quite encouragingly when the imposed displacement amplitude is SD^- – i.e a mere 10% lower than the toppling displacement ($SD^- = 0.9\delta_{ult}$) – toppling is avoided for all records. It is interesting to note that even for the SD^+ scaled seismic motions ($SD^+ = 1.1\delta_{ult}$), in most cases the frame will not topple. Yet, in only 2 (and admittedly highly amplified) of the records examined, the SD^+ scaled ground motion will produce overturning of the frame. Although this observation does not question the applicability of the simplified approach (since the imposed SD is 10% higher than the toppling displacement δ_{ult}) a more detailed insight into the factors affecting the toppling potential of a seismic excitation is attempted in the next section.

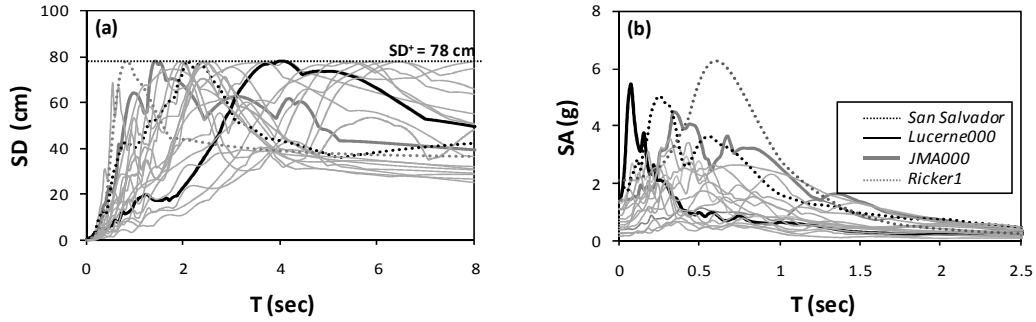


Figure 7: (a) displacement and (b) acceleration response spectra of actual acceleration time histories recorded during devastating earthquakes scaled *appropriately* to achieve $SD = 78$ cm. Four ground motions are distinguished and are further discussed.

4 INVESTIGATION OF THE TOPPLING POTENTIAL OF A GROUND MOTION

It is well known that a number of factors affect the toppling potential of a seismic motion [Makris & Roussos, 2000; Apostolou et al., 2007]. Aiming to better quantify it, a destructiveness measure is proposed herein, which is termed as the *cumulative impact pulse velocity* and is defined as:

$$V_{imp,max} = \max |V_{imp}| = \max \left| \int_0^{t_{tot}} (a - a_{yield}) dt \right| \quad (2)$$

where t_{tot} is the total duration of the ground motion, a the motion acceleration and a_{yield} is the minimum acceleration that when applied pseudostatically to the footing may provoke uplift. An approximate yet simple way to calculate a_{yield} is:

$$a_{yield} = \frac{(SA)_D M_{ult}^{footing}}{M_{RD}^C} \quad (3)$$

where $(SA)_D$ is the design spectral acceleration of the frame, $M_{ult}^{footing}$ is the overturning moment capacity of the footing, and M_{RD}^C is the bending strength of the corresponding column. The effect of the aforementioned measure on the toppling potential of ground motions is inves-

tigated in the sequel for the example frame with footing width $B = 1.1$ m. For this case $a_{yield} = 0.15 g$.

Figure 8 compares the Lucerne-000 record (Landers, 1992) with the GIC-090 record (San Salvador, 1986), both scaled to $SD^+ = 78$ cm. Although the Lucerne record contains a large number of peaks that exceed the yield acceleration a_{yield} (Fig. 8a), it does not contain a large impact velocity pulse $V_{imp,max}$ (Fig. 8b), and is therefore not leading to appreciable foundation rotation (Fig. 8c). In stark contrast the San Salvador record, despite boasting a considerably smaller number of strong motion cycles (and duration), is characterized by a substantially larger $V_{imp,max}$ (2.04 m/s compared to 0.78 m/s of Lucerne). Therefore it produces constant accumulation of rotation and eventually causes toppling of the structure. The time histories of V_{imp} reveal the key disparity between the two records. The effect of a clearly recognizable pulse produces a prominent "impact" on the structure, dragging it definitely beyond its equilibrium position. Depending on the amplitude of this *velocity impact pulse*, the increase of rotation following loss of equilibrium may bring about toppling of the structure. This effect is obvious on the time history of footing rotation θ for the San Salvador record: the large *impact velocity pulse* at $t = 1.4$ s produces a large rotation value $\theta \approx 0.08$ rad. Although this rotation alone is undeniably far lower than the toppling rotation $\theta_{ult} = 0.186$ rad, it causes an irrecoverable deviation from the initial equilibrium position while the subsequent strong motion cycles generate further accumulation of θ until, ultimately, toppling. The picture is significantly altered in case of the Lucerne record. Despite its multitude of strong motion cycles substantially exceeding a_{yield} , none of them boasts the kinematic characteristics (asymmetry *and* low frequency, i.e. large duration) to produce a large enough V_{imp} . As a result, the produced footing rotation θ fluctuates around zero, while the residual rotation remains relatively small.

The previous comparative example suggests that $V_{imp,max}$ may reveal certain characteristics of a seismic motion, mainly related to the existence of impact velocity pulses. However, it is still not adequate for the complete description of the toppling potential of a strong earthquake motion. For this purpose, the JMA-000 record (Kobe, 1995) is compared with a Ricker 1 pulse (i.e. $f_E = 1$ Hz). As shown in Fig. 9, the Ricker 1 pulse (scaled with respect to PGA) describes sufficiently the prevailing strong motion pulse of the JMA record.

In the context of the SD_{max} approach, the two ground motions are scaled to $SD^+ = 78$ cm. As shown in Fig. 9a, the Ricker 1 requires larger scaling ($PGA = 2.2 g$) to produce the same maximum spectral displacement with the JMA record (whose $PGA = 1.4 g$). Despite the fact that its *impact pulse velocity* $V_{imp,max} = 2.1$ m/s (Fig. 9b) is substantially larger than that of the scaled JMA record (of $V_{imp,max} = 1.87$ m/s), Ricker 1 is clearly inadequate to provoke toppling. The rotation $\theta \approx 0.09$ rad generated by the first pulse of Ricker 1 (Figure 9c) is recovered during the next (of opposite direction) cycle of motion. Due to the lack of subsequent strong motion pulses, the loss of equilibrium does culminate in toppling. On the other hand, the JMA record contains a prevailing strong motion cycle (at $t = 8$ s) which generates similar footing rotation θ as Ricker 1, however, its subsequent strong motion cycles which exceed a_{yield} produce gradual accumulation of θ ultimately resulting in toppling, which reveals that the number of cycles exceeding a_{yield} play an important role in the toppling potential of the ground motion.

4.1 The paradox of the Chi-Chi Record

The preceding discussion focused on the safety margin provided by the simplified SD_{max} approach, revealing that a *Factor of Safety* of the order of 1.1 may be considered adequate for real seismic motions. In reality, however, such *tremendous* seismic motions (e.g. the devastating JMA record scaled up at 1.4 g) have never been recorded and cannot possibly be considered realistic, especially for design purposes. This observation is of particular importance, since it implies that toppling can be quite *improbable* for real seismic motions, even in case of occurrence of *extremely strong earthquakes* (such as the ones deliberately selected for analysis), and even for *extremely under-designed* footings ($B = 1.1$ m).

Although the selected records cover a wide range of seismic motions, none of them is charac-

terized by fling-step effects — a different category of near-source effects, associated with large permanent displacement rather than a large velocity pulse. As shown in the examples of Figure 10a, such ground motions are characterized by excessively large spectral displacements. For example, the TCU-068 records (Chi-Chi, Taiwan 1999) yield SD_{max} of the order of several meters, i.e. almost an order of magnitude larger than δ_{ult} . With such large SD_{max} , it would be expected that the structure would easily be lead to toppling. To unravel the response of the system when subjected to this special category of near-source seismic motions, additional analyses are conducted utilizing the original records (without any scaling). Quite remarkably, even for the very extreme case of the TCU-068(NS) record (Fig. 10a), the footing experiences almost negligible rotation θ (Fig. 10b), and the structure is not toppling.

As paradox as this may appear, it is explainable on the basis of the acceleration time history. Despite the large SD_{max} , the yield acceleration a_{yield} is only slightly exceeded, and not for a long duration. This means that both V_{imp} and t_{yield} , and consequently TPi , are not large enough to provoke toppling. This implies that the long-period (almost quasi-static) component of the seismic motion, which is responsible for the excessive SD_{max} , is not really exceeding a_{yield} and, therefore, cannot lead to toppling. As clearly seen in Fig. 10a, the acceleration pulses that do exceed a_{yield} are of much higher frequency, and are not associated with the large SD_{max} of the record. This example reveals the notable conservatism of the simplified approach, for such special cases of near source seismic motions characterized by fling-step effects.

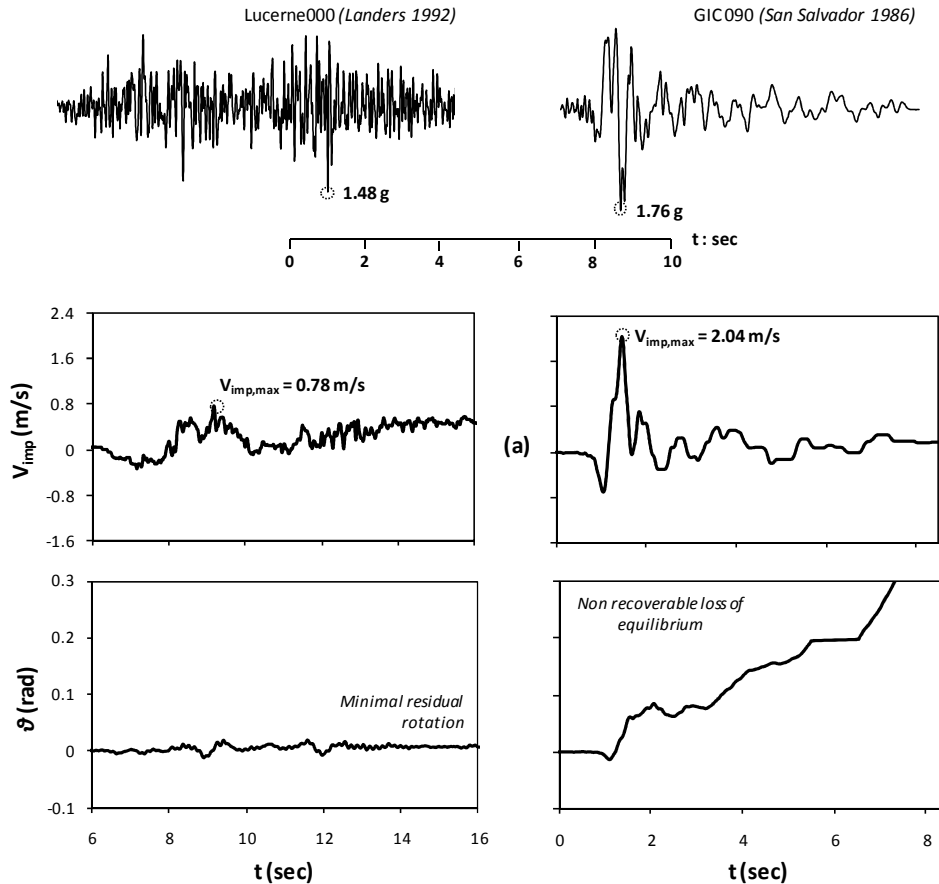


Figure 8. Nonlinear dynamic time history analysis — comparison of the effects of the Lucerne-000 (left column) with the GIC-090 (right column) record, both scaled to $SD^+ = 78$ cm : (a) time histories of “impact velocity” V_{imp} (bold black line), and (b) time histories of footing rotation θ .

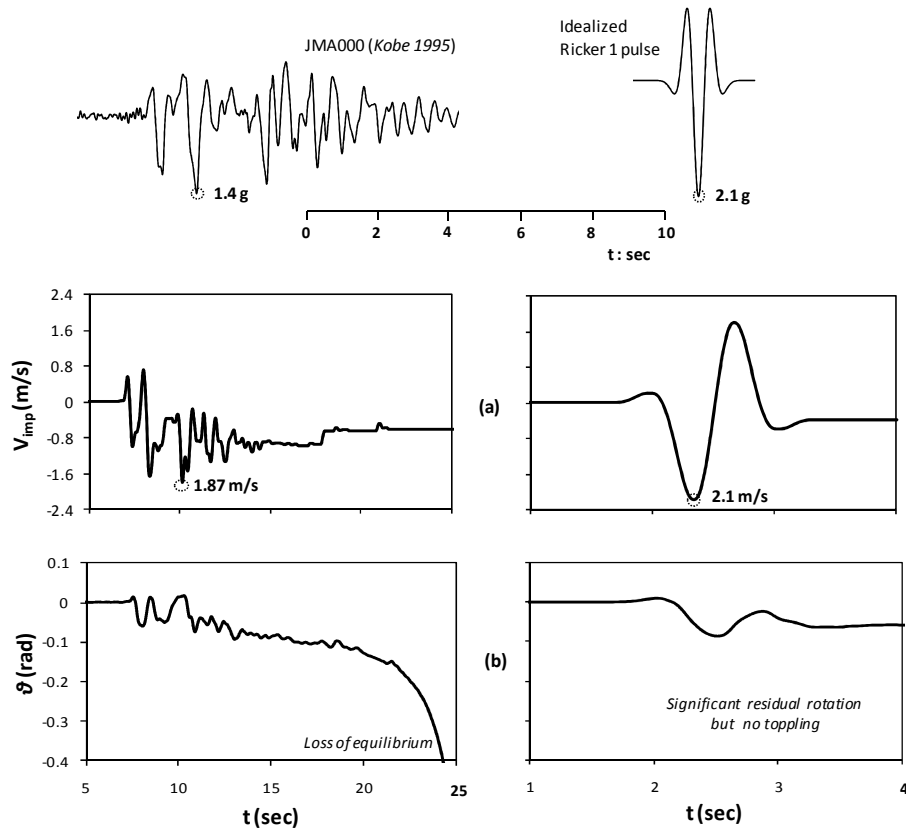


Figure 9. Nonlinear dynamic time history analysis – comparison of the effects of JMA-000 record with the Ricker 1 pulse both scaled to $SD^+ = 78$ cm : (a) time histories of “impact velocity” V_{imp} (bold black line and (b) time histories of footing rotation θ .

5 ACKNOWLEDGEMENT

The financial support for this paper has been provided under the research project “DARE”, which is funded through the European Research Council’s (ERC) “IDEAS” Programme, in Support of Frontier Research–Advanced Grant, under contract/number ERC–2–9–AdG228254–DARE.

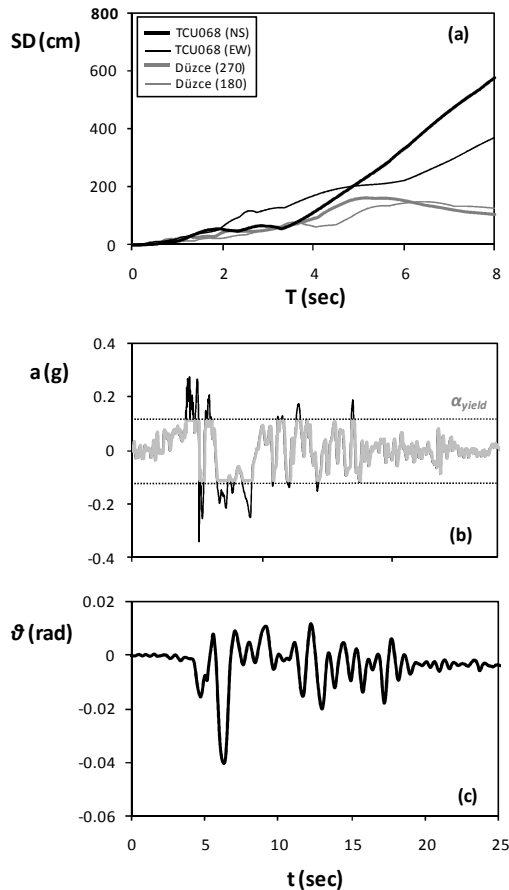


Figure 10. (a) Displacement response spectra of near-source motions characterized by fling-step effects. Nonlinear dynamic time history analysis of the frame subjected to seismic excitation with the TCU-068 (NS) record (Chi-Chi, Taiwan 1999) : (b) acceleration time history (the grey-shaded line represents the portion of the acceleration time history which lies below the yield acceleration α_{yield} – only a very small portion of the record exceeds α_{uplift} ; (c) time history of footing rotation θ .

6 REFERENCES

- ABAQUS, Inc. (2009), ABAQUS user's manual, Providence, R.I.
- Anastasopoulos I., Gazetas G., Loli M., Apostolou M, Gerolymos N. (2010), Soil Failure can be used for Earthquake Protection of Structures, *Bulletin of Earthquake Engineering*, 8, pp. 309–326.
- Anastasopoulos I. Gelagoti F., Kourkoulis R., Gazetas G. (2011) Simplified Constitutive Model for Simulation of Cyclic Response of Shallow Foundations : Validation against Laboratory Tests, *Journal of Geotechnical and Geoenvironmental Engineering*, ASCE (*in print*).
- Apostolou M., Gazetas G., Garini E. (2007), Seismic response of slender rigid structures with foundation uplifting, *Soil Dynamics and Earthquake Engineering*, 27 (7), pp. 642–654.
- Chatzigogos C.T., Pecker A., Salencon J. (2009), Macroelement modeling of shallow foundations, *Soil Dynamics and Earthquake Engineering*, Vol. 29, No. 6, pp. 765–781.
- Faccioli E, Paolucci R, Vivero G. Investigation of seismic soil– footing interaction by large scale cyclic tests and analytical models. *Proc. 4th International Conference on Recent Advances in Geotechnical Earthquake Engineering and Soil Dynamics*, Paper no. SPL-5, San Diego, California; 2001.

- Gajan S., Kutter B.L. (2008), Capacity, settlement, and energy dissipation of shallow footings subjected to rocking, *Journal of Geotechnical and Geoenvironmental Engineering*, ASCE, 134 (8), pp 1129-1141.
- Gelagoti F., Kourkoulis R., Anastasopoulos I., and G. Gazetas (2011), Rocking Isolation of Frames Founded on Isolated Footings, *Journal of Earthquake Engineering and Structural Dynamics* (*in print*)
- Gerolymos N., Apostolou M., Gazetas G. (2005), Neural network analysis of overturning response under near-fault type excitation, *Earthquake Engineering and Engineering Vibration*, 4 (2), pp. 213-228.
- Harden, C., Hutchinson, T. (2006), Investigation into the Effects of Foundation Uplift on Simplified Seismic Design Procedures, *Earthquake Spectra*, 22 (3), pp. 663–692.
- Housner G.W. (1963), The behavior of inverted pendulum structures during earthquakes. *Bulletin of the Seismological Society of America*, 53 (2), pp. 404–417.
- Kawashima K., Nagai T., Sakellarakis D. (2007), Rocking Seismic Isolation of Bridges Supported by Spread Foundations, *Proc. of 2nd Japan-Greece Workshop on Seismic Design, Observation, and Retrofit of Foundations*, April 3-4, Tokyo, Japan, pp. 254–265.
- Koh A.S., Spanos P., Roesset J.M. (1986), Harmonic rocking of rigid block on flexible foundation, *Journal of Engineering Mechanics*, ASCE, 112 (11), pp. 1165–1180.
- Kutter B.L, Martin G., Hutchinson T.C., Harden C., Gajan S., Phalen J.D. (2003), *Status report on study of modeling of nonlinear cyclic load–deformation behavior of shallow foundations*, University of California, Davis, PEER Workshop; March.
- Makris N., Konstantinidis D. (2003), The rocking spectrum and the limitations of practical design methodologies, *Earthquake Engineering & Structural Dynamics*, 32 (2), pp. 265–289.
- Makris, N., Roussos, Y. (2000), Rocking response of rigid blocks under near source ground motions, *Géotechnique*, 50 (3), pp. 243–262.
- Martin, G., R., and Lam, I. P. (2000). Earthquake Resistant Design of Foundations : Retrofit of Existing Foundations, *Proc. GeoEng 2000 Conference*, Melbourne.
- Paolucci R., Shirato M., Yilmaz M.T. (2008), Seismic behaviour of shallow foundations: Shaking table experiments vs numerical modelling, *Earthquake Engineering and Structural Dynamics*, Vol. 37, pp. 577–595.
- Pecker, A., & Pender, M.J., (2000), Earthquake Resistant Design of Foundations : New Construction, Invited paper, *GeoEng2000*, Vol 1, pp. 313-332.
- Psycharis I., Jennings P. (1983), Rocking of slender rigid bodies allowed to uplift. *Earthquake Engineering and Structural Dynamics*, 11, pp. 57–76.
- Yim C.S., Chopra A.K. (1984), “Earthquake response of structures with partial uplift on Winkler foundation”, *Earthquake Engineering and Structural Dynamics*, Vol. 12, pp. 263-281.
- Zhang J., Makris N. (2001), Rocking response of free-standing blocks under cycloidal pulses. *Journal of Engineering Mechanics*, ASCE, 127 (5), pp. 473–483.

Rocking of Inelastic Frame on Two-Layered Inelastic Soil

R. Kourkoulis, F. Gelagoti, V. Founta

Soil Mechanics Laboratory, National Technical University, Athens, Greece

ABSTRACT: The paper studies the response of a simple rocking-isolated 1-bay 2-storey frame on two-layered soil profile consisting of a stiff surface layer overlying a weak homogeneous soil stratum. Analyses were conducted employing the finite element code ABAQUS and involved monotonic and cyclic push-over tests and dynamic time-history analyses. It was shown that the existence of even a shallow surface layer of depth equal to the footing width enhances the seismic performance of the frame-foundation system by reducing the residual settlements and limiting the extent of damage in the structural members.

1 INTRODUCTION

According to the present capacity design principles, the foundation is designed so as to behave elastically even under extreme earthquake shaking. This is typically achieved by imposing conservative factors of safety against all possible “failure” modes such as mobilization of bearing-capacity, uplifting and/or sliding on the supporting ground. Nevertheless, a growing population of researchers suggest the need to relax some of the aforementioned criteria and allow for a design that accounts for, or even promotes inelastic action at the foundation level. Following this reasoning, the idea of “rocking isolation” [Mergos and Kawashima 2005] has recently been proposed as an alternative seismic design philosophy in which soil failure is not only not prohibited but is rather used as a “fuse”: the foundation is deliberately “*under-designed*” to promote rocking, thus limiting the inertia forces transmitted onto the superstructure. The potential effectiveness of such a design scheme has been explored analytically by, among others [Anastasopoulos et al., 2010] and experimentally [Anastasopoulos, 2010; Drosos et al., 2011] for an idealized *RC* bridge pier, and for idealized 2-storey *RC* frame structures [Gelagoti et al., 2011a; 2011b].

For the particular frame examined by Gelagoti (2010) which was founded on clay with undrained shear strength $S_u = 150$ kPa, it was testified that the new design method was beneficial in terms of settlement and floor drift especially in case of an earthquake far exceeding the limits set by the current design codes. The new design method was proven to be particularly effective when a safety factor against vertical loads of greater than $FS_v \approx 5$ is ensured: foundation rocking prevails against soil yielding thus reducing the residual settlement and rotation of the footing. Still, however, for lower FS_v values, collapse may be avoided –although at the cost of increased distortion.

Despite this quite encouraging outcome, question still remains as to the generalization potential of the results to less idealized cases, such as practical applications where the exact soil properties cannot be a priori guaranteed thus jeopardizing the applicability of rocking isolation. In an effort to overcome this obstacle, this paper investigates the potential of *shallow* soil improvement, a concept commonly applicable in geotechnical engineering as a means to increase

soil strength and reduce settlements. The adequacy of shallow only mitigation stems from the nature of foundation rocking which mobilizes only a shallow stress bulb within the soil layer.

2 METHODOLOGY AND NUMERICAL MODELING

A rather extreme scenario is considered hereafter in order to examine the adequacy of shallow soil improvement. It is tactically assumed that the frame investigated by *Gelagoti et al (2010)* is founded on soil of undrained shear strength $S_u = 50$ kPa yielding a mere $FS_v \approx 2.6$ instead of $FS_v \approx 5$ (when $S_u = 150$ kPa) which was found to be necessary in order to promote efficient up-lifting. The effect of applying shallow soil improvement on the low FS_v profile is subsequently examined by parametrically varying its depth d (expressed as a ratio of the foundation width B). The following sections compare the behavior of the frame under various loading scenarios, considering the $FS_v = 5$ condition as the target scenario. In case of two-layered profiles, the improved layer's strength has been considered equal to $S_u = 150$ kPa, while the underlying one was maintained at $S_u = 50$ kPa (Figure 1).

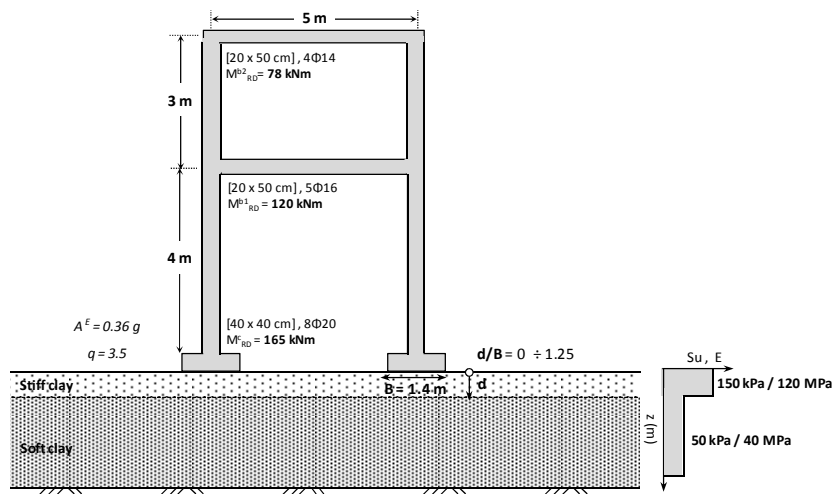


Figure 1. Geometry and member properties of the problem analyzed

Analyses have been performed utilizing the FE code ABAQUS (Figure 2). Soil is modeled with nonlinear quadrilateral continuum elements, assuming plane strain conditions. The soil foundation interface is modeled using special interface elements which allow both detachment and sliding. The seismic excitation (i.e acceleration time history) is applied at the base of the model. Free field boundaries are used at the two lateral boundaries of the model. Nonlinear soil behavior is modeled through a simple kinematic hardening model with Von Mises failure criterion, and associated flow rule. The model capability to effectively capture the rocking response of foundations has been validated against centrifuge model tests by Anastasopoulos et al. (2011). Non linear 2-D beam elements have been used for the modeling of RC beams and columns of the frame. The reinforced concrete constitutive model was the same as the one used for the soil, after proper adaptation, to simulate the non-linear moment–curvature response of the superstructure reinforced concrete members. In order to effectively capture the RC sections behavior, the model parameters are calibrated against moment-curvature relationship computed through section analysis in the X-tract 2000 software in accordance with the details of Vintzi-laiou et al. (2007).

3 EFFECT OF SOIL IMPROVEMENT ON THE FOOTING'S BEARING CAPACITY

A series of initial vertical monotonic push-down tests were performed in order to calculate the safety factor against vertical load for all the subsequent analyses, including those on homogeneous soil as well the layered profiles to be discussed in the following sections. As explained previously, foundation rocking (and hence rocking-isolation) may materialize through the reduction of foundation dimensions. However, even once foundation rocking is ensured, the latter will respond to strong ground shaking either trough uplifting from the supporting soil when the factor of safety against vertical load FS_v is large, or by sinking due to excessive soil yielding in case of lower FS_v values. This may result in large residual displacements possibly unacceptable for the design. Evidently, ensuring an adequately large FS_v in order to promote uplifting, presumes that soil properties are known; a rather overoptimistic assumption in engineering practice. Shallow soil improvement provides a reasonable means of overcoming the ambivalence that such uncertainties cause to design by ensuring well known soil properties within the top soil layer. Based on the reasoning of the previous section, it is rational to expect that although the improved properties of the top layer are not adequate to increase the global factor of safety against vertical loads, they will definitely assist the desired uplifting response of the shallow foundation.

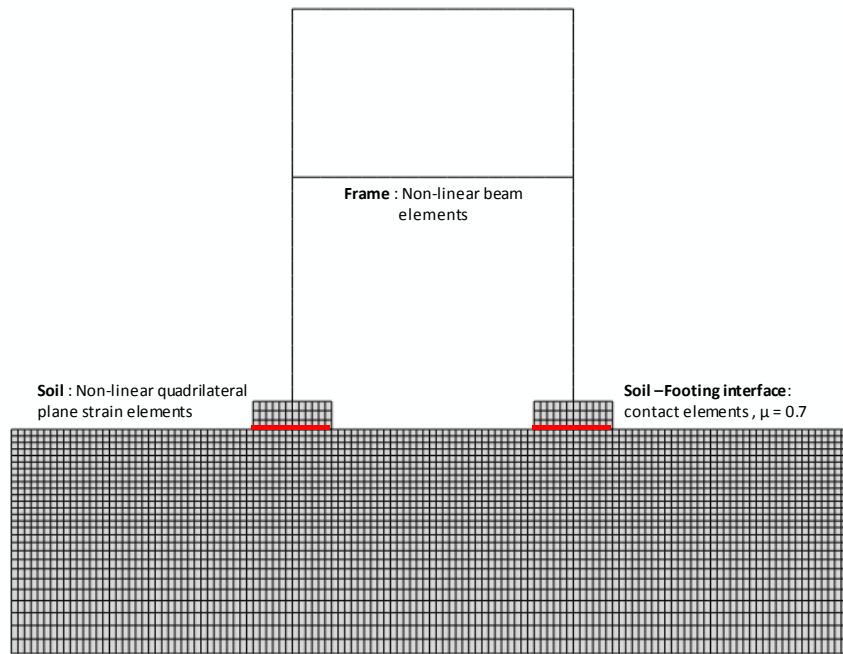


Figure 2. Finite element model

Figure 3 shows the corresponding safety factors versus the thickness of the improved surface layer for the soil profiles discussed previously. As expected, increasing the depth of the improved layer results in increased foundation capacity. It seems that a significant increase in safety factor for vertical loads takes place even when the thickness of the improved layer is relatively small. The rate of increase of FS_v is initially high, but gradually decreases for larger values of the d/B ratio. This drop in increase rate can be explained by the fact that the stress bulb produced by vertical loading is enclosed within the improved layer (for $d/B > 1$) and thus further increase of the depth of the improved layer has no influence on the failure load.

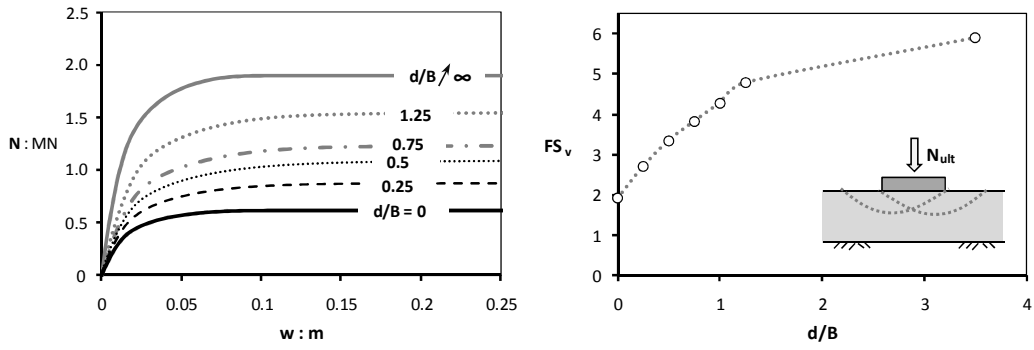
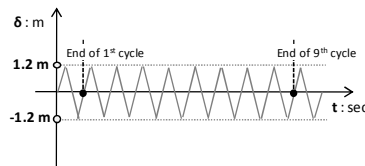
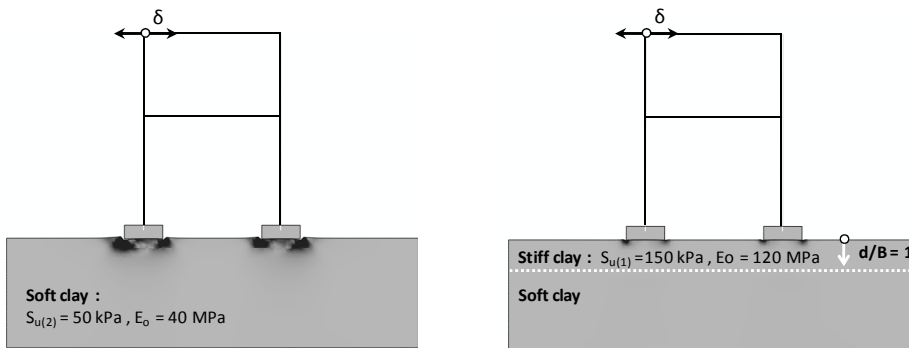


Figure 3. Evolution of Foundation Bearing Capacity and Safety factor against vertical loads with increasing depth of mitigation zone



(a) After the 1st cycle of loading



(b) After the 9th cycle of loading

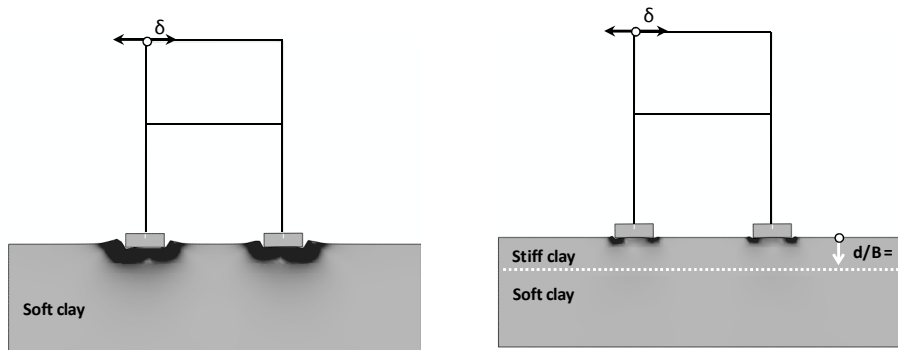


Figure 4. Frame subjected to slow cyclic horizontal loading: comparison of the distribution of plastic deformations produced after (a) the first and (b) the ninth cycle of loading

4 FRAME SUBJECTED TO LATERAL LOADING

4.1 Response to monotonic and Cyclic Loading

Initially, the models have been subjected to slow cyclic displacement-controlled push-over loading in the horizontal direction. Displacement is imposed on the upper left node of the frame, and consists of 10 cycles of amplitude $\delta = 1.2$ m. This value corresponds to 75% δ_u , where δ_u is the toppling displacement of the particular frame.

Figure 4 compares the response after the 1st and after the 9th cycle in terms of contours of produced plastic strains for the two examined systems: (a) homogeneous soil with $S_u = 50$ kPa and (b) two-layered with a surface layer of thickness $d/B = 0.5$ and undrained shear strength $S_{u1} = 150$ kPa. Apparently, the existence of the improved zone drastically reduces the plastification underneath the footings (Fig. 4a) while it limits the rate of settlement accumulation. Even after the 9th cycle of loading, plastification is restricted within the mitigation zone without penetrating the underlying weak soil stratum.

4.2 Response to moderately strong seismic shaking

The aim of these analyses was to determine the response of the system under different seismic excitations and, through this procedure, estimate the adequate soil improvement depth. Initially, the frame was subjected to relatively moderate seismic excitations (i.e. within its design limits). In this case, interest is mainly focused in serviceability after the end of the earthquake. Therefore, parameters such as the irrecoverable deformation of the foundation are expected to be crucial in assessing design effectiveness. The response of the frame on improved soil (of depth $d/B = 0.5$ and 1.0) is compared to its response when founded on:

- (a) the unimproved homogeneous soil profile of $S_u = 50$ kPa ($FS_v = 3$) and
- (b) the “target” case of a competent profile of $S_u = 150$ kPa ($FS_v \approx 5$).

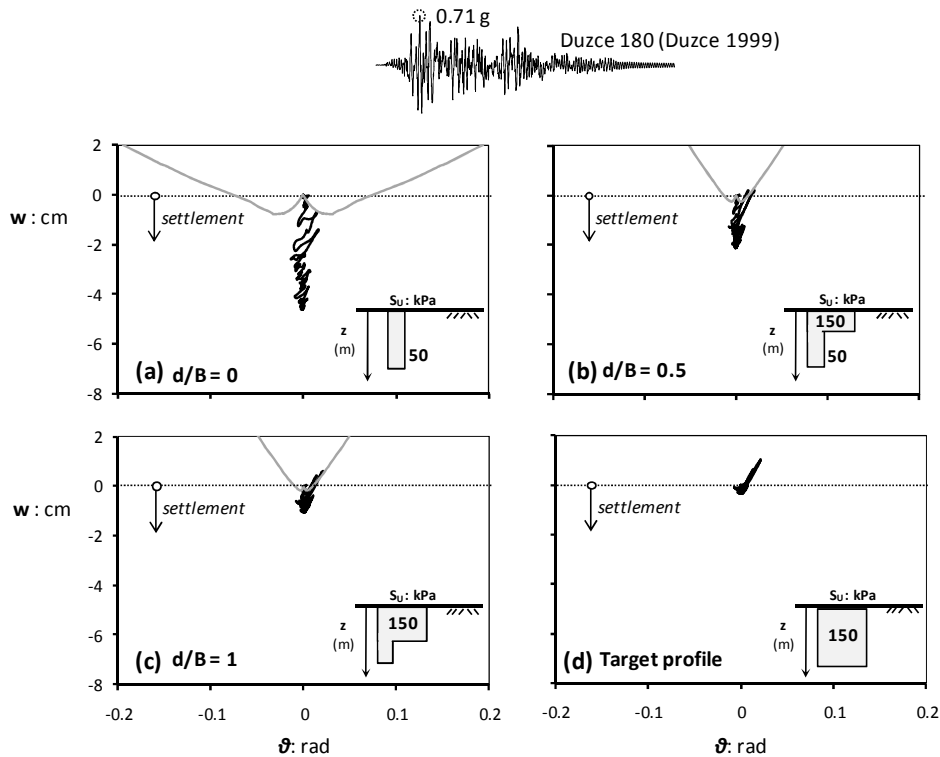


Figure 5. Frame excited by the Duzce 1999 record: comparison of vertical displacement versus rotation ($w-\theta$) loops for the case of (a) homogeneous $S_u = 50$ kPa, (b) two layered profile

$d/B = 0.5$, (c) two layered profile $d/B = 1$; and (d) homogeneous $S_u = 150$ kPa.

Figure 5 compares the evolution of settlements as a function of rotation angle of the left footing for the four systems examined, when the model is subjected to the Duzce180 record (Duzce, Turkey 1999 earthquake). Indeed, the response of the $FS_v \approx 3$ footing deviates substantially from the target $FS_v \approx 5$ response: the footing accumulates settlement w during each strong motion cycle, reaching a peak value of 4.5 cm instead of a mere 0.5 cm in the high FS_v case. Such a high unanticipated settlement under the design earthquake definitely questions the serviceability of the frame and should be avoided. Quite encouragingly, it is seen (Figs. 5b and c) that the use of an improved layer of depth only $d/B = 0.5$ significantly reduces the settlements, yet not approaching the minimal settlement developed in the target homogeneous profile. The desired behavior is better captured when the improved crust's depth increases to $d/B = 1$ (Figure 6c), which practically creates the necessary conditions to ensure a rather efficient uplifting response of the foundation.

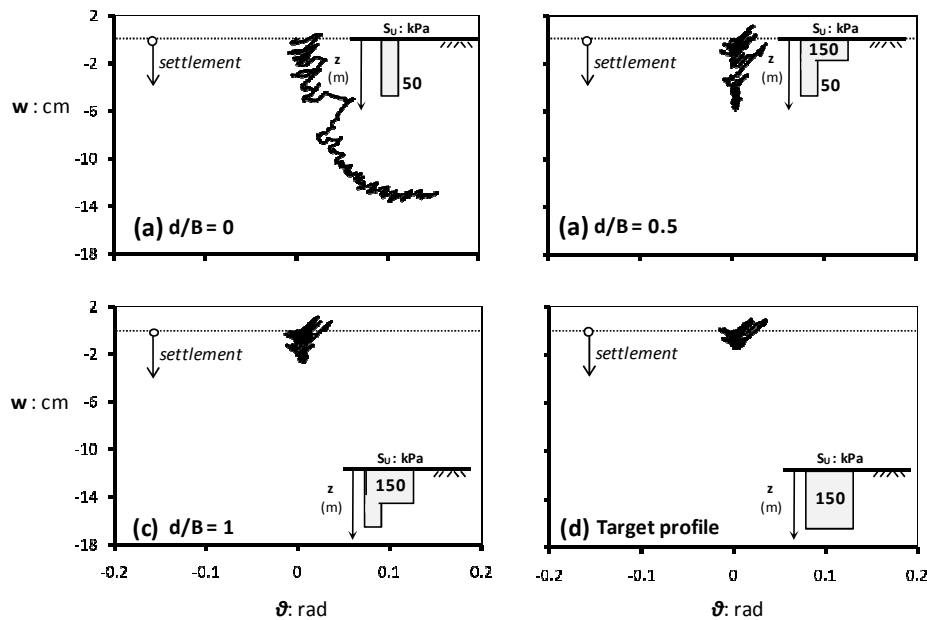


Figure 6. Frame excited by the Tabas 1981 record: comparison of vertical displacement versus rotation ($w-\theta$) loops for the case of (a) homogeneous $S_u = 50$ kPa, (b) two layered profile $d/B = 0.5$, (c) two layered profile $d/B = 1$; and (d) homogeneous $S_u = 150$ kPa.

4.3 Response to very strong seismic shaking

The effectiveness of shallow mitigation becomes palpably more impressive in case of the frame subjected to the Tabas (Tabas, Iran 1981) which overly exceeds the structure's design spectrum. The record is characterized by a multitude of strong motion cycles while its PGA exceeds 0.81 g. The evolution of settlements as a function of the rotation angle when the frame is founded on improved soil is illustrated in Figures 7b and c. In case of the weak ($FS_v = 3$) profile, the under-designed footings of the frame accumulate severe differential settlement (reflected in the developed rotation) which gradually causes the frame to practically collapse. Apparently, the sequence of many strong motion cycles produces significant plastification extending to large soil depths which, in turn, brings about irrecoverable foundation (and structural) distortion. The beneficial effect of using an improved surface layer with depth ratio just $d/B = 0.5$ in preventing the collapse of the building becomes obvious: it limits extent of soil yielding and aborts the development of permanent rotation which is responsible for the distortion of the superstructure (Figure 7b). The behavior is further improved when the improvement depth is d/B

= 1. The foundation response tends to imitate that of the target ($FS_v \approx 5$) profile. Although the rocking-induced residual settlement of the foundation is higher than in the homogeneous $S_u=150$ kPa profile (3cm instead of 2cm), it is considered as a relatively fair price to pay.

5 SUMMARY & CONCLUSIONS

The dynamic response of the system has been simulated employing nonlinear dynamic time history analysis. A quite comprehensive database of 20 recorded time-histories was used as input to assess the seismic performance of the systems under different earthquake scenarios. The selected records incorporate the effect of a wide range of strong-motion parameters such as *PGA*, *PGV*, *SA*, *SV*, frequency content, number of strong motion cycles, duration.

Figure 7 displays comparative collective results of the settlement for the left footing. Obviously, the use of a surface layer of depth only $d/B = 0.5$, significantly reduces the residual settlement for all seismic excitations although the target behavior of the homogeneous $S_u = 150$ kPa case is not perfectly imitated. Further increase of the soil improvement depth to $d/B = 1$ further reduces the residual settlements while the foundation behavior resembles that achieved in case of the target profile.

It is concluded that the use of a shallow improved soil layer of depth $d/B = 1$ is able to reduce the risk of settlement associated with uncertainties in the proper estimation of soil properties. The use of the improved surface layer has a favorable effect for the majority of the examined seismic records limiting settlement and damage in structural members.

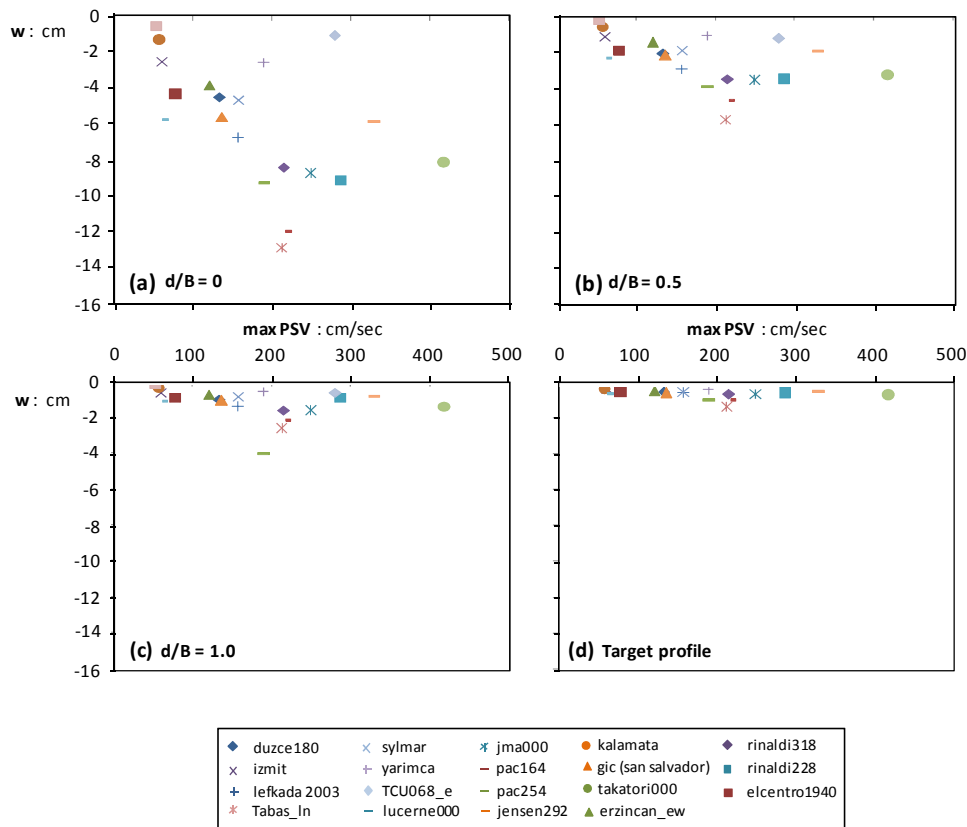


Figure 7. Conclusive results. Comparison of the residual settlement for all investigated earthquake scenarios for all the examined scenarios: (a) homogeneous $S_u = 50$ kPa , (b) two layered profile $d/B= 0.5$, (c) two layered profile $d/B= 1$; and (d) homogeneous $S_u= 150$ kPa .

6 ACKNOWLEDGEMENT

The financial support for this paper has been provided under the research project “DARE”, which is funded through the European Research Council’s (ERC) “IDEAS” Programme, in Support of Frontier Research–Advanced Grant, under contract/number ERC–2–9–AdG228254–DARE to Professor G. Gazetas.

REFERENCES

- Anastasopoulos I. (2010), “Beyond conventional capacity design : towards a new design philosophy”, In : *Soil–Foundation–Structure Interaction*, Orense R.P., Chouw N., Pender M.J. (editors), CRC Press, Taylor & Francis Group : New York.
- Anastasopoulos I., Gazetas G., Loli M., Apostolou M, Gerolymos N. (2010) “Soil failure can be used for seismic protection of structures”, *Bull. Earthquake Eng.* Vol.8, pp. 309-326
- Anastasopoulos I., Gelagoti F., Kourkoulis R., G. Gazetas, (2011) “Simplified Constitutive Model for Simulation of Cyclic Response of Shallow Foundations : Validation against Laboratory Tests”, *Journal of Geotechnical and Geoenvironmental Engineering*, ASCE (in print)
- Drosos V., Georgarakos T., Loli M., Anastasopoulos I., Zarzouras O., and Gazetas G. (2011), “Soil–Foundation–Structure Interaction with Mobilization of Bearing Capacity : An Experimental Study on Sand”, *Journal of Geotechnical and Geoenvironmental Engineering*, ASCE (submitted for possible publication).
- Gelagoti F. (2010), “Metaplastic Response and Collapse of frame-Foundation Systems, and the Concept of Rocking Isolation” Doctoral Thesis, NTUA.
- Gelagoti F., Kourkoulis R., Anastasopoulos I., and Gazetas G. (2011a) “Rocking Isolation of Frame Structures Founded on Isolated Footings”, *Earthquake Engineering and Structural Dynamics* (in print)
- Gelagoti F., Kourkoulis R., Anastasopoulos I., and Gazetas G. (2011b), “Rocking–isolated Frame Structures : Margins of Safety against Toppling Collapse and Simplified Design Approach”, *Soil Dynamics and Earthquake Engineering* (in print)
- Mergos, P. E., Kawashima, K. (2005). "Rocking isolation of a typical bridge pier on spread foundation." *Journal of Earthquake Engineering*, 9(2): pp 395-414.
- Vintzilaiou E., Tassios T.P., Chronopoulos M. (2007) “Experimental validation of seismic code provisions for RC columns”, *Engineering Structures*, 29, pp1153-1164

Destructiveness of Earthquake Ground Motions: “Intensity Measures” versus Sliding Displacement

Ev. Garini & G. Gazetas

Soil Mechanics Laboratory, National Technical University, Athens, Greece

ABSTRACT: The scope is to estimate qualitatively and quantitatively the potential destructiveness of earthquakes on structures characterized by inelastic response. To this end, earthquake records are utilized studying several seismological parameters as destructiveness indices of earthquake shaking. We employ twenty six widely acknowledged indices, such as the Arias intensity, the Housner intensity, the destructiveness potential factor, the acceleration spectrum intensity, the specific energy density etc. A large number (eighty nine) of earthquake records are selected, paying particular attention to include ground motions with strong near-fault characteristics: forward directivity and fling. Apart from the seismological parameters, sliding displacement on an inclined plane is utilized as an additional destructiveness index representative of the inelastic response of structural systems. In particular, we adopt the Newmark’s model of a rigid block resting on an inclined surface (governed by the Coulomb friction law) subjected to seismic excitation. The results are presented in form of sliding displacement versus each one of the seismic indexes. By comparison we conclude to specific indices which can describe satisfactorily the inelastic response.

1 INTRODUCTION–SCOPE OF STUDY

For systems whose deformation involves restoring mechanisms with a dominant linear component, the viscous-elastic response spectra, S_A S_V S_D , of a particular accelerogram provide an efficient indication of its potential to cause unacceptable amplitudes of deformation in various structures (as a function of their elastic fundamental period). However, for systems with strongly nonlinear and/or inelastic restoring mechanisms, elastic response spectra are often inadequate descriptors of the damage potential. This is absolutely true in cases where no elastic component of restoring mechanism is present, such as with systems which rely solely on friction for lateral support. An example in structural engineering is the (flat) friction–isolated structures. In geotechnical engineering, gravity retaining walls and slopes rely primarily on frictional interfaces (rather than elasticity) for lateral seismic support. In general, ductile structures designed to respond mainly in the inelastic region, have restoring force–displacement relationships which resemble the frictional mechanism.

An abstraction has been inspired by the above applications. To assess the potential of an accelerogram to inflict large irrecoverable deformation on highly inelastic systems, the seismic behavior of two idealized systems is explored. They are to be thought of as analogues of actual inelastic systems: (a) the sliding of a rigid block on a horizontal base, and (b) sliding of a rigid block on an inclined ($\geq 25^\circ$) base, [called Newmark’s sliding in the geotechnical literature]. These two systems are characterized by a rigid–plastic symmetric (a), or asymmetric (b), restoring–force–displacement relationships obeying Coulomb’s friction law, as presented in Figure 1. The supporting base of each system is subjected to a particular ground motion under investigation, and the size of the resulting inelastic/nonlinear response serves as an index of the damage

that this motion can inflict on the corresponding class of inelastic systems—the “destructiveness” potential of the motion.

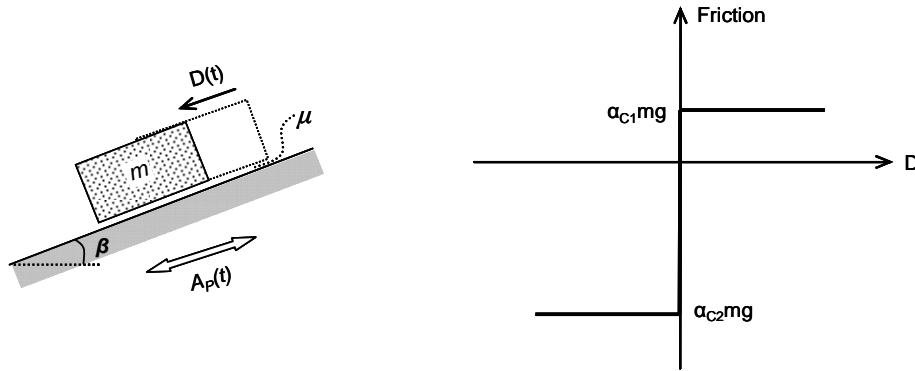


Figure 1. Schematic representation of the Newmark 1965 sliding-block analogue and friction force as a function of slip displacement.

2 TYPES OF DESTRUCTIVENESS INDICES

2.1 Newmark's asymmetric sliding response

The analysis of the behavior of a block on horizontal or inclined base which is subjected to motion $A(t)$ parallel to the plane is obtained from elementary rigid body kinematics along with Newton's second law of motion. The critical acceleration(s) which must be exceeded for slippage to be initiated are simply:

$$A_{C1} = (\mu \cos \beta - \sin \beta) g \quad (1)$$

$$A_{C2} = (\mu \cos \beta + \sin \beta) g \quad (2)$$

in which A_C = the critical acceleration for sliding in either direction of the symmetric system; μ = the (constant) coefficient of friction; A_{C1} and A_{C2} are the critical accelerations for downhill and uphill sliding respectively, for the asymmetric system of a plane inclined at an angle β . Usually $A_{C1} \ll A_{C2}$ and as a result sliding takes place only downhill.

Whenever the base acceleration exceeds A_C or A_{C1} (or, rarely, A_{C2}) slippage of the block takes place with respect to the base. This slippage lasts only momentarily, thanks to the transient nature of earthquake shaking; it terminates as soon as the velocities of the base and the block equalize. And the process continues until the motions of both the block and the base eventually terminate. The maximum and/or the permanent amount of slippage is taken as the damage of the idealized system (analogue).

2.2 Intensity indices

Numerous parameters of a ground motion have been proposed over the years to serve as indices of the “damage potential” of a ground motion. Such indices are often called “Intensity Measures” (IM). Several such IM are tested herein against the amount of slippage induced by a ground motion. Specifically, the examined indices include: the Arias intensity (I_A), the Housner intensity (I_H), the RMS acceleration; or velocity; or displacement (A_{RMS} , V_{RMS} , D_{RMS}), the characteristic intensity (I_C), the specific energy density (S_E), the cumulative absolute velocity (CAV), the sustained maximum acceleration and velocity (SMA and SMV respectively), acceleration and velocity spectrum intensity (ASI and VSI), the acceleration parameter A_{95} , the predominant period (T_P), the mean period (T_{mean}), the significant duration (D_{sig}), the destructiveness potential factor (P_D), and the ratio V_{max}^2/A_{max} of the peak velocity squared divided by PGA. Next all these parameters are presented in detail:

- Arias Intensity, I_A , is proportional to the integral of the squared ground acceleration $A(t)$ time history:

$$I_A = \frac{\pi}{2g} \int A^2(t) dt \quad (3)$$

- Housner Intensity, I_H , is the integral of the pseudo-velocity spectrum over the period range [0.1 s, 2.5 s] :

$$I_H = \int_{0.1}^{2.5} S_V(T, \xi = 5\%) dT \quad (4)$$

where $S_V(T, \xi)$ is the pseudo-velocity response spectrum (Housner, 1952).

- RMS acceleration, A_{RMS} , is the square root of the mean acceleration:

$$A_{RMS} = \sqrt{\frac{\int A^2(t) dt}{T_D}} \quad (5)$$

where T_D is the length of the record and $A(t)$ is the acceleration time history.

- RMS velocity, V_{RMS} , is the root mean square of velocity:

$$V_{RMS} = \sqrt{\frac{\int V^2(t) dt}{T_D}} \quad (6)$$

where T_D is the length of the record and $V(t)$ is the velocity time history.

- RMS displacement, D_{RMS} , is the root mean square of displacement:

$$D_{RMS} = \sqrt{\frac{\int D^2(t) dt}{T_D}} \quad (7)$$

where T_D is the length of the record and $D(t)$ is the displacement time history.

- Characteristic Intensity, I_C , is defined as:

$$I_C = (A_{RMS})^{3/2} \sqrt{T_D} \quad (8)$$

where T_D is the length of the record.

- Specific Energy Density, S_E , is calculated from the expression:

$$S_E = \frac{\beta_s \rho_s}{4} \int V^2(t) dt \quad (9)$$

where $V(t)$ is the ground velocity time history, β_s is the wave velocity and ρ_s is the mass density of the recording site (Sarma, 1971).

- Cumulative Absolute Velocity, CAV, is defines as:

$$CAV = \sum_{i=1}^N H(PGA_i - A_{\min}) \int_{t_i}^{t_{i+1}} |A(t)| dt \quad (10)$$

where $A(t)$ is the ground acceleration, N is the number of 1-second time windows in the time series, PGA_i is the PGA (in g) during time window i , t_i is the start time of time window i , A_{\min} is an acceleration threshold (user-defined, but usually taken as 0.025g) to exclude low amplitude motions contributing to the sum, and $H(x)$ is the Heaviside step function (unity for $x > 0$, zero otherwise).

- Sustained Maximum Acceleration, SMA, is the third highest absolute peak in the acceleration time history, proposed by Nuttli (1979).
- Sustained Maximum Velocity, SMV, is the third highest absolute peak in the velocity time history, proposed by Nuttli (1979).
- Acceleration Spectrum Intensity, ASI, is calculated as:

$$ASI = \int S_A(5\%, T) dT \quad (11)$$

where $S_A(5\%, T)$ is the spectral acceleration for 5% damping and T is natural period [see Kramer (1996)].

- Velocity Spectrum Intensity, VSI, is calculated from:

$$VSI = \int S_V(5\%, T) dT \quad (12)$$

where $S_V(5\%, T)$ is the spectral pseudo-velocity for 5% damping and T is natural period [see Kramer (1996)].

- Acceleration parameter A_{95} is the level of acceleration which contains up to 95% of the Arias Intensity [Sarma & Yang (1987)].
- Predominant Period, T_P , evaluated using the 5% damped acceleration response spectrum, and corresponds to the period of the maximum spectral acceleration, as long as $T_P > 0.20$ sec.
- Mean Period, T_{mean} , is defined based on the Fourier amplitude spectrum. The mathematical expression is:

$$T_{mean} = \frac{\sum \left(\frac{C_i^2}{f_i} \right)}{\sum C_i^2} \quad (13)$$

where C_i is the Fourier amplitude for each frequency f_i within the range 0.25–20 Hz.

- Significant Duration, D_{signif} , is the interval of time between the accumulation of 5% and 95% of Arias Intensity.
- Destructiveness Potential Factor, P_D , is the ratio between the Arias Intensity I_A and the square of the number of zero crossings per second of the accelerogram v_0^2 :

$$P_D = \frac{I_A}{v_0^2} = \frac{\pi}{2g} \frac{\int A^2(t) dt}{v_0^2} \quad (14)$$

as introduced by Araya & Saragoni (1984) and by Crespellani et al (2003).

3 GROUND MOTIONS

A large number (99) of recorded ground motions are utilized for this test. The selection was such as to cover many of the well known accelerograms from earthquakes of the last 30 years, and to include motions bearing near-fault characteristics: directivity and fling effects. Table 1

lists these records along with their PGA, PGV, and PGD values. Each accelerogram imposed with its recorded sign (normal polarity) and with opposite sign (reverse polarity).

Table 1. List of significant earthquake records bearing the effects of ‘directivity’ and ‘fling’, utilized as excitations in this study.

Record Name	PGA [g]	PGV [m/s]	PGD [m]
Fukiai	0.763	1.232	0.134
JMA-0°	0.830	0.810	0.177
JMA-90°	0.599	0.761	0.199
Nishi Akashi-0°	0.509	0.357	0.091
Nishi Akashi-90°	0.503	0.356	0.109
Shin Kobe-NS	0.422	0.688	0.169
Takarazuka-0°	0.693	0.682	0.274
Takarazuka-90°	0.694	0.853	0.167
Takatori-0°	0.611	1.272	0.358
Takatori-90°	0.616	1.207	0.328
No 4-140°	0.485	0.374	0.202
No 4-230°	0.360	0.766	0.590
No 5-140°	0.519	0.469	0.353
No 5-230°	0.379	0.905	0.630
No 6-140°	0.410	0.649	0.276
No 6-230°	0.439	1.098	0.658
No 7-140°	0.338	0.476	0.246
No 7-230°	0.463	1.093	0.447
No 9 Differential Array-270°	0.352	0.712	0.458
No 9 Differential Array-360°	0.480	0.408	0.140
Lucerne-0°	0.785	0.319	0.164
Lucerne-275°	0.721	0.976	0.703
Joshua Tree-0°	0.274	0.275	0.098
Joshua Tree-90°	0.284	0.432	0.145
Pacoima Dam-164°	1.226	1.124	0.361
Pacoima Dam-254°	1.160	0.536	0.111
Erzincan (Station 95)-EW	0.496	0.643	0.236
Erzincan (Station 95)-NS	0.515	0.839	0.312
Los Gatos Presentation Center-0°	0.563	0.948	0.411
Los Gatos Presentation Center-90°	0.605	0.510	0.115
Saratoga Aloha Avenue-0°	0.512	0.412	0.162
Saratoga Aloha Avenue-90°	0.324	0.426	0.275
Karakyr-0°	0.608	0.654	0.253
Karakyr-90°	0.718	0.716	0.237
Jensen Filtration Plant-22°	0.424	0.873	0.265
Jensen Filtration Plant-292°	0.592	1.201	0.249
L.A. Dam-64°	0.511	0.637	0.211
L.A. Dam-334°	0.348	0.508	0.151
Newhall Firestation-90°	0.583	0.524	0.126
Newhall Firestation-360°	0.589	0.753	0.182
Pacoima Dam (downstream)-175°	0.415	0.456	0.050
Pacoima Dam (downstream)-265°	0.434	0.313	0.048
Pacoima Kagel Canyon-90°	0.301	0.379	0.095
Pacoima Kagel Canyon-360°	0.432	0.452	0.069
Rinaldi-228°	0.837	1.485	0.261
Rinaldi-318°	0.472	0.627	0.166
Santa Monica City Hall-90°	0.883	0.403	0.102
Santa Monica City Hall-360°	0.369	0.232	0.059
Sepulveda VA-270°	0.753	0.848	0.186
Sepulveda VA-360°	0.939	0.766	0.149

Simi Valley Katherine Rd–0°	0.877	0.409	0.053
Simi Valley Katherine Rd–90°	0.640	0.378	0.051
Sylmar Hospital–90°	0.604	0.744	0.165
Sylmar Hospital–360°	0.843	1.027	0.256
TCU 052–EW	0.350	1.743	4.659
TCU 052–NS	0.437	2.186	7.319
TCU 065–EW	0.450	1.298	1.820
TCU 065–NS	0.554	0.876	1.254
TCU 067–EW	0.487	0.973	1.953
TCU 067–NS	0.311	0.536	0.849
TCU 068–EW	0.491	2.733	7.149
TCU 068–NS	0.353	2.892	8.911
TCU 075–EW	0.324	1.143	1.692
TCU 075–NS	0.254	0.360	0.414
TCU 076–EW	0.335	0.706	1.223
TCU 076–NS	0.416	0.617	0.662
TCU 080–EW	0.968	1.076	0.186
TCU 080–NS	0.902	1.025	0.340
TCU 084–EW	0.986	0.923	0.910
TCU 084–NS	0.419	0.486	0.966
TCU 102–EW	0.297	0.870	1.478
TCU 102–NS	0.168	0.705	1.062
Duzce–180°	0.312	0.474	0.285
Duzce–270°	0.358	0.464	0.176
Sakarya–EW	0.330	0.814	2.110
Yarimca–60°	0.231	0.906	1.981
Yarimca–330°	0.322	0.867	1.493
Tabas–LN	0.836	0.978	0.387
Tabas–TR	0.852	1.212	0.951
National Geographical Institute–180°	0.392	0.566	0.206
National Geographical Institute–270°	0.524	0.753	0.116
Geotechnical Investigation Center–90°	0.681	0.793	0.119
Geotechnical Investigation Center–180°	0.412	0.602	0.201
Institute of Urban Construction–90°	0.380	0.441	0.173
Institute of Urban Construction–180°	0.668	0.595	0.112
Bolu–0°	0.728	0.564	0.231
Bolu–90°	0.822	0.621	0.135
Duzce–180°	0.348	0.600	0.421
Duzce–270°	0.535	0.835	0.516

4 ANALYSES RESULTS

At this point, the results here are for the asymmetric sliding system, as shown in Figure 1. Figure 2 illustrates the correlation between Arias intensity and slippage. Figure 3 demonstrates slippage, D , according to the peak acceleration, velocity and displacement values for all the 99 ground motions. Next, at Figure 4 sliding response is depicted in correlation with the potential destructiveness factor, P_D .

Figures 5-9 pictured asymmetric sliding versus the rest Intensity Measures (IM). Furthermore, Table 2 presents the correlation index, R^2 , between asymmetric sliding response, D , and each IM, covering the parametric range of our study.

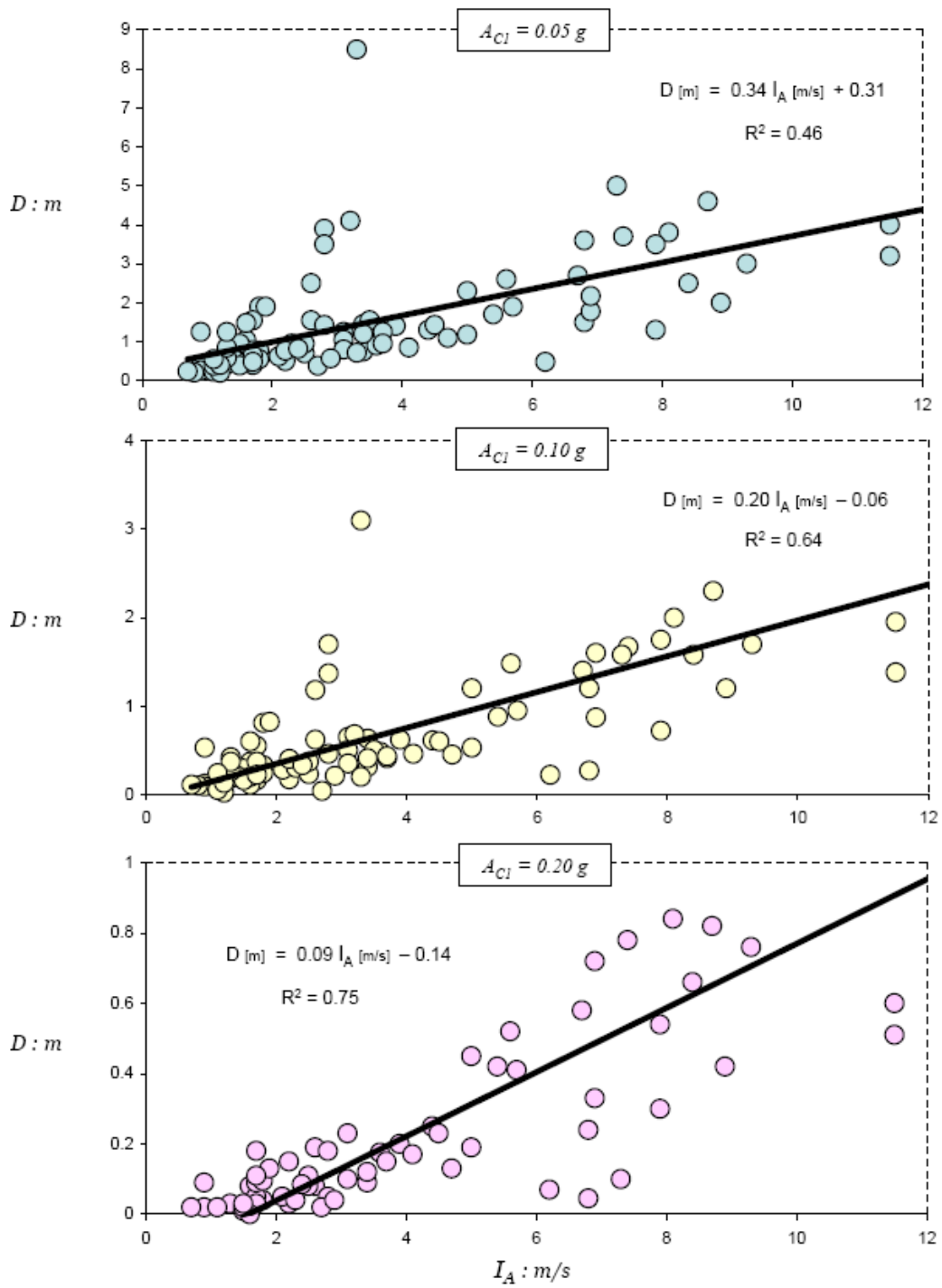


Figure 2. Correlation between the Arias Intensity, I_A , of the records utilized as excitation in our study and the triggered sliding displacement, D , for three values of critical acceleration A_C . A linear trend line is plotted for each case, with the correlation index, R^2 , stated.

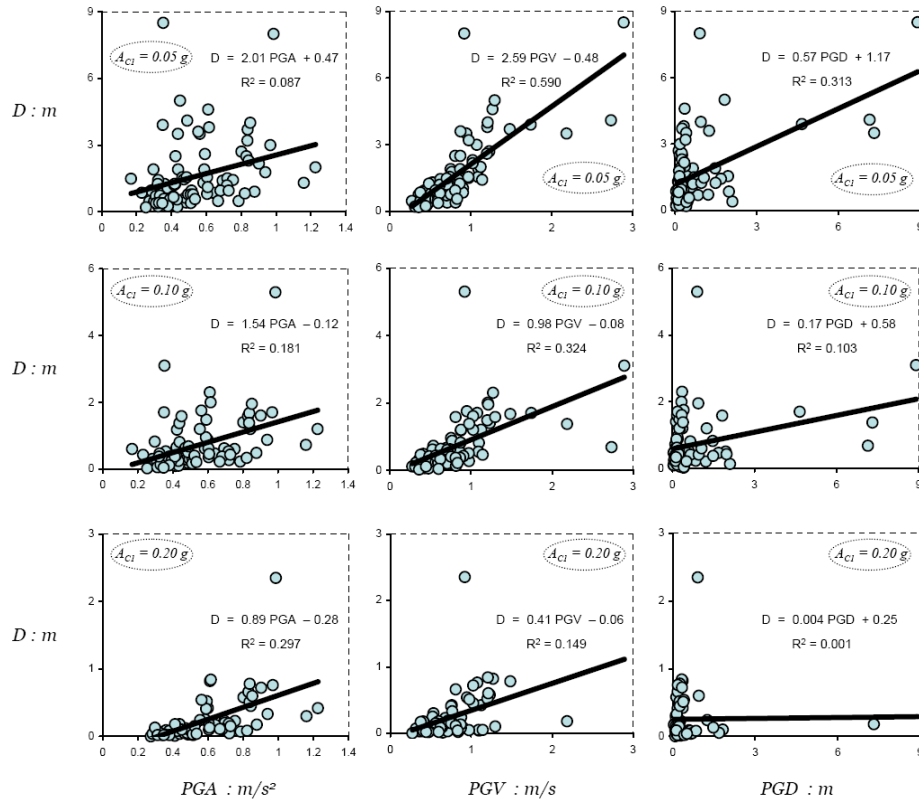


Figure 3. Slippage, D , with respect to the most widely used ground motion characteristics: (a) peak ground acceleration–in the first column from the left, (b) peak ground velocity–in the second column, and (c) peak ground displacement–in the last column to the left.

Table 2. Correlation index, R , between asymmetric sliding response, D , and seismic indices of destructiveness, covering the parametric range of our study.

Correlation Index, R	$A_{C1} = 0.05g$	$A_{C1} = 0.10g$	$A_{C1} = 0.20g$
Peak Ground Acceleration, PGA	0.09	0.18	0.29
Peak Ground Velocity, PGV	0.59	0.32	0.15
Peak Ground Displacement, PGD	0.31	0.10	0.001
Arias Intensity, I_A	0.46	0.64	0.75
Destructiveness Potential Factor, P_D	0.58	0.73	0.69
Housner Intensity, I_H	0.52	0.67	0.71
RMS Acceleration, A_{RMS}	0.23	0.25	0.24
RMS Velocity, V_{RMS}	0.54	0.26	0.12
RMS Displacement, D_{RMS}	0.07	0.03	0.004
Spectral Displacement at $T=1$ sec, $S_{D/(T=1s)}$	0.36	0.53	0.61
Spectral Displacement at $T=2$ sec, $S_{D/(T=2s)}$	0.61	0.61	0.45
Spectral Displacement at $T=3$ sec, $S_{D/(T=3s)}$	0.31	0.19	0.05
Spectral Displacement at $T=4$ sec, $S_{D/(T=4s)}$	0.23	0.08	0.00
Characteristic Intensity, I_C	0.39	0.51	0.55
Specific Energy Density, S_E	0.49	0.23	0.07
Cumulative Absolute Velocity, CAV	0.44	0.51	0.52
Sustained Maximum Acceleration, SMA	0.16	0.23	0.29
Sustained Maximum Velocity, SMV	0.53	0.36	0.16
Acceleration Spectrum Intensity, ASI	0.08	0.17	0.30
Velocity Spectrum Intensity, VSI	0.53	0.68	0.73
Acceleration Parameter, A_{95}	0.11	0.19	0.27
Predominant Period, T_P	0.17	0.15	0.14
Mean Period, T_{mean}	0.15	0.07	0.002
Significant Duration, D_{sig}	0.001	0.003	0.006

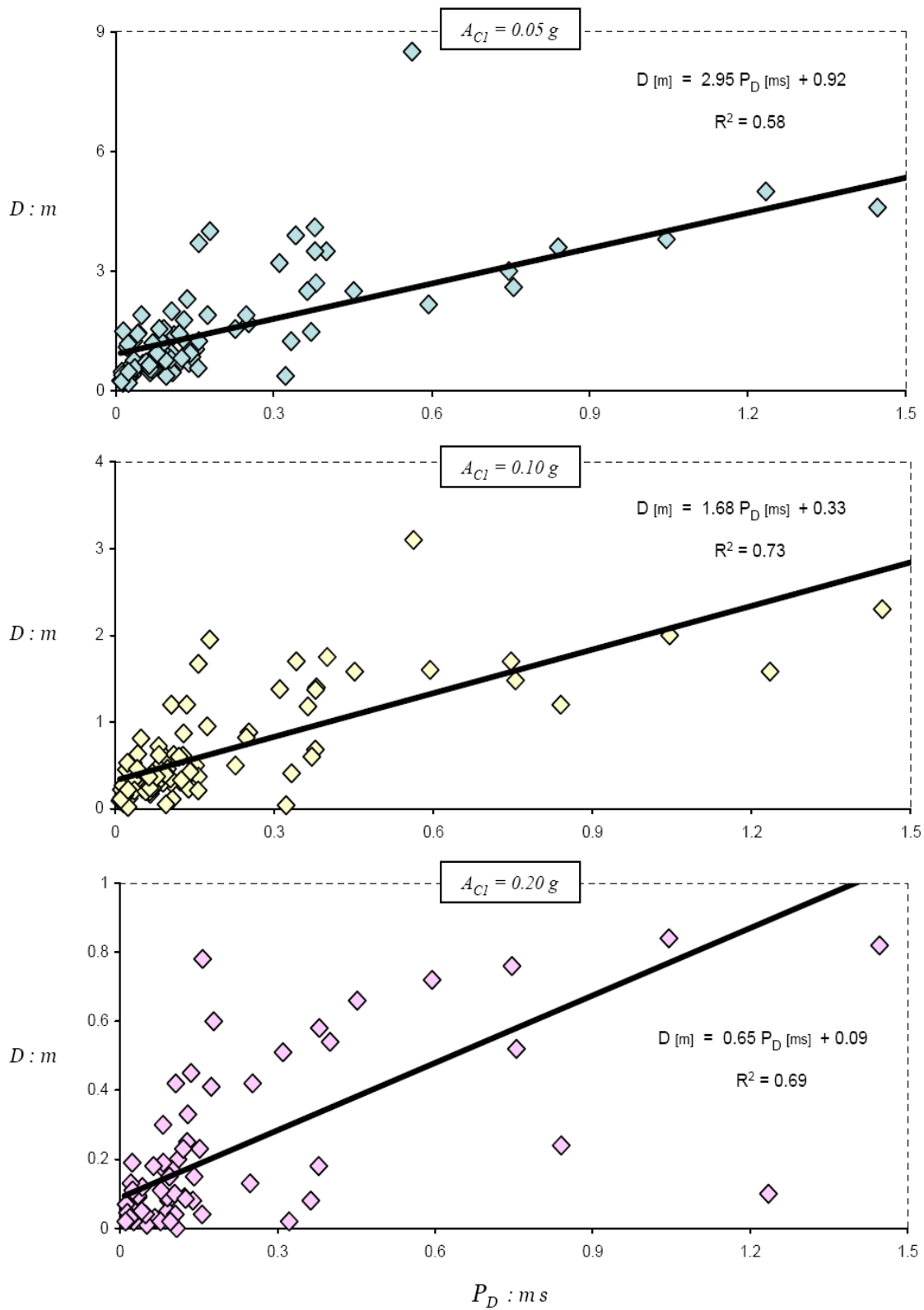


Figure 4. The influence of potential destructiveness factor P_D (as defined by Araya & Saragoni, 1984) on sliding displacement D , for three levels of critical yielding acceleration A_C : 0.05 g, 0.1 g, and 0.2 g.

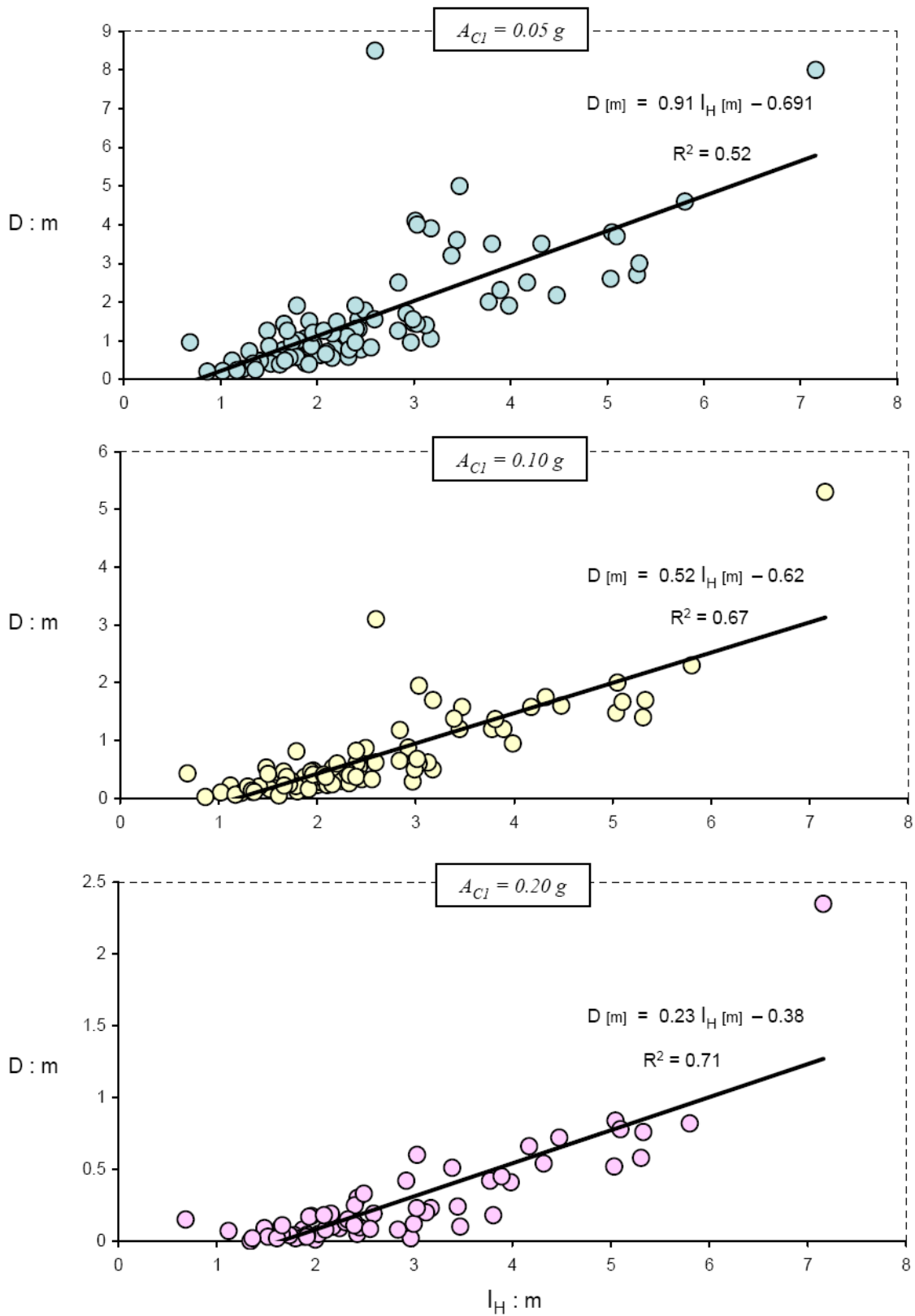


Figure 5. Correlation between the Housner Intensity, I_H , of the records utilized as excitation in our study and the triggered sliding displacement, D , for three values of critical acceleration A_C . A linear trend line is plotted for each case, with the correlation index, R^2 , stated.

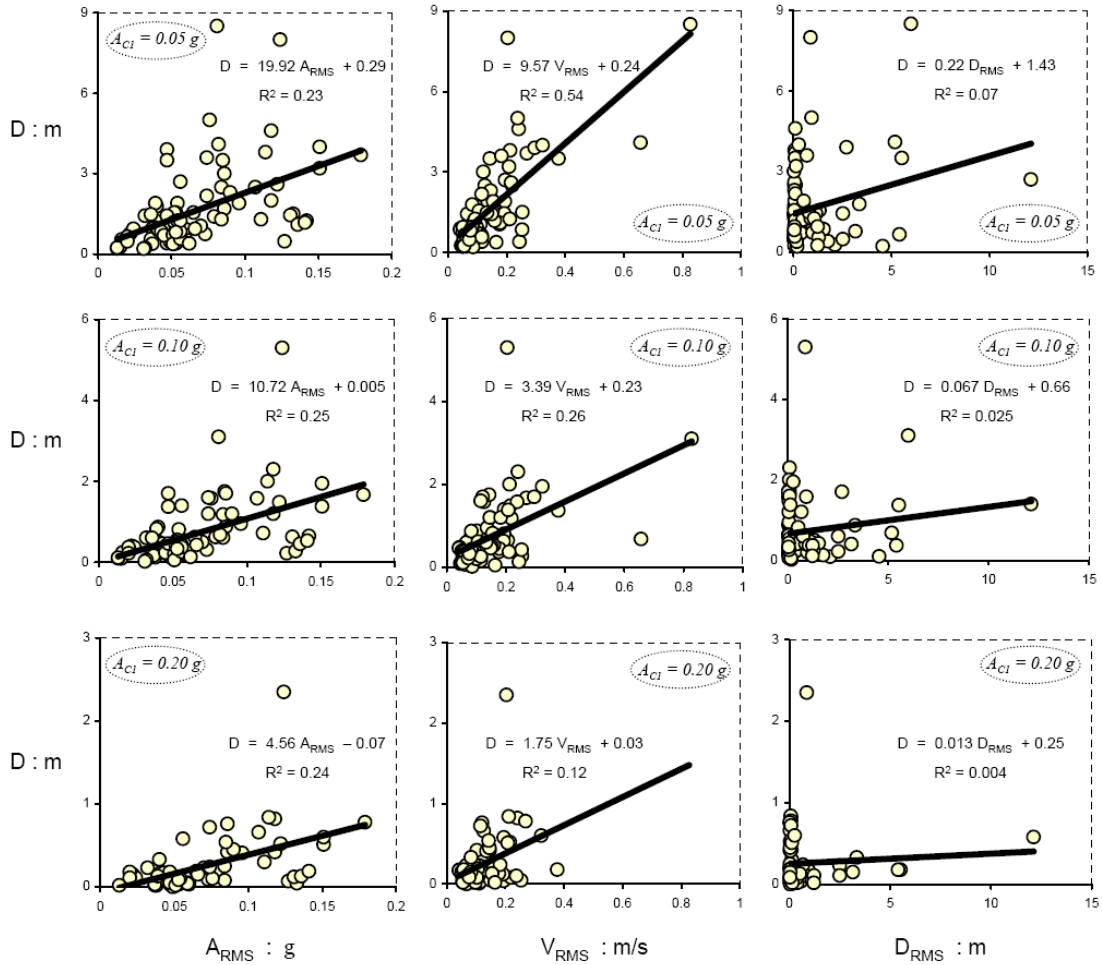


Figure 6. Slippage, D , in connection with the Root Mean Square values: (a) RMS acceleration–in the first column from the left, (b) RMS velocity–in the second column, and (c) RMS displacement–in the last column to the left.

5 CONCLUSIONS

As an index of the structural response of yielding systems we adopt the Newmark's model of a rigid block resting on an inclined plane with Coulomb friction interface subjected to seismic excitation. For the latter, 99 actual accelerograms, many of which bear the effects of near-fault forward directivity or fling step, are utilized unscaled. The resulting sliding displacements are then correlated with 26 widely used "intensity measures" (or "indices of destructiveness potential"), such as the peak ground acceleration, the peak ground velocity, peak ground displacement, the Arias intensity, the Housner intensity, the destructiveness potential factor, the acceleration spectrum intensity, the specific energy density, and others. The conclusions are drawn regarding the performance of each index vis-à-vis the ensemble of sliding displacements, as summarized in Table 2.

For small ratios of A_{C1} , the intensity indices that provide the best correlation with the induced sliding displacement are in descending order: the spectral displacement at period of 2 seconds ($S_{D(T=2s)}$), the destructiveness potential factor (P_D), and the peak ground velocity (PGV). For large ratios of A_{C1} , best correlations present the Arias intensity (I_A), the Housner intensity (I_H), and the velocity spectrum intensity (VSI).

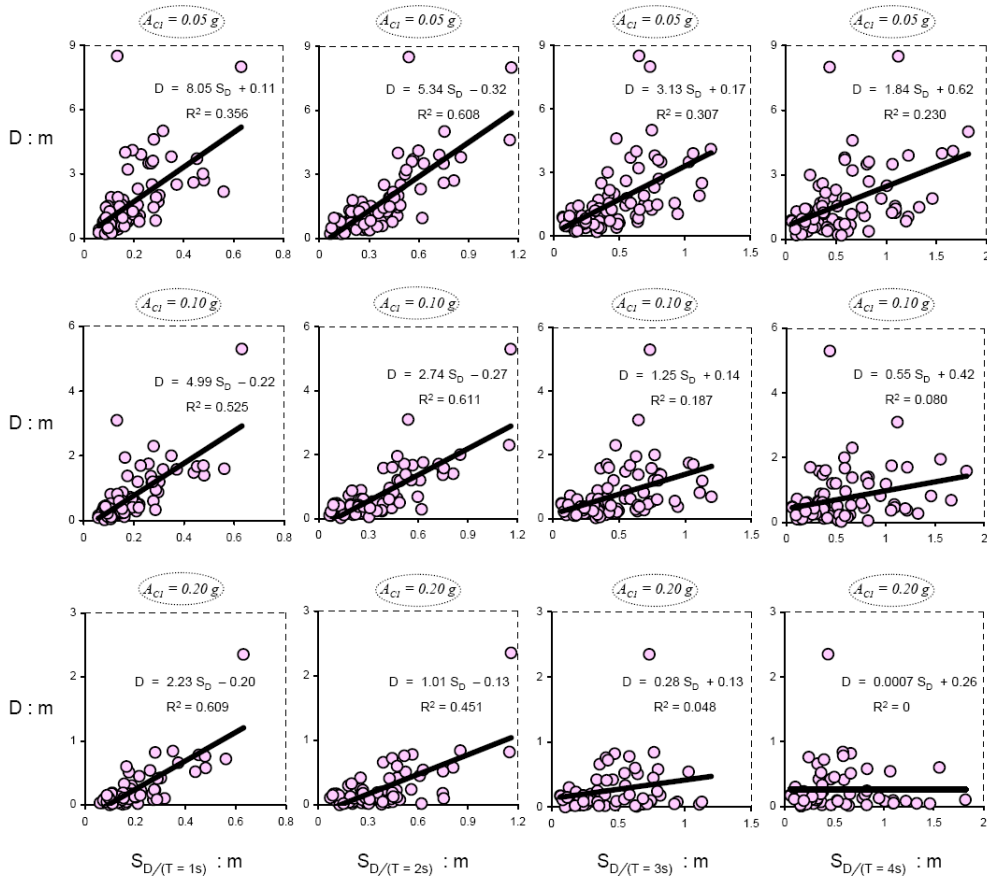


Figure 7. Correlation of slippage, D , with its corresponding spectral displacement at four different periods, T : for period of 1, 2, 3, and 4 seconds.

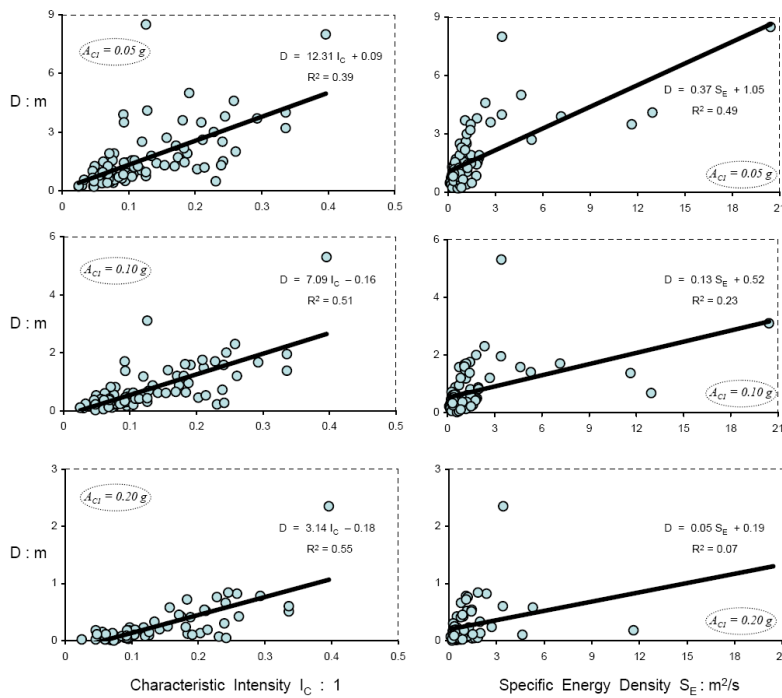


Figure 8. Influence of the dimensionless parameter of characteristic intensity, I_C , on slippage, D , at the left hand-side and effect of specific energy density, S_E , at the right. Observe the poor correlation of the induced slippage with the energy density value of each earthquake event.

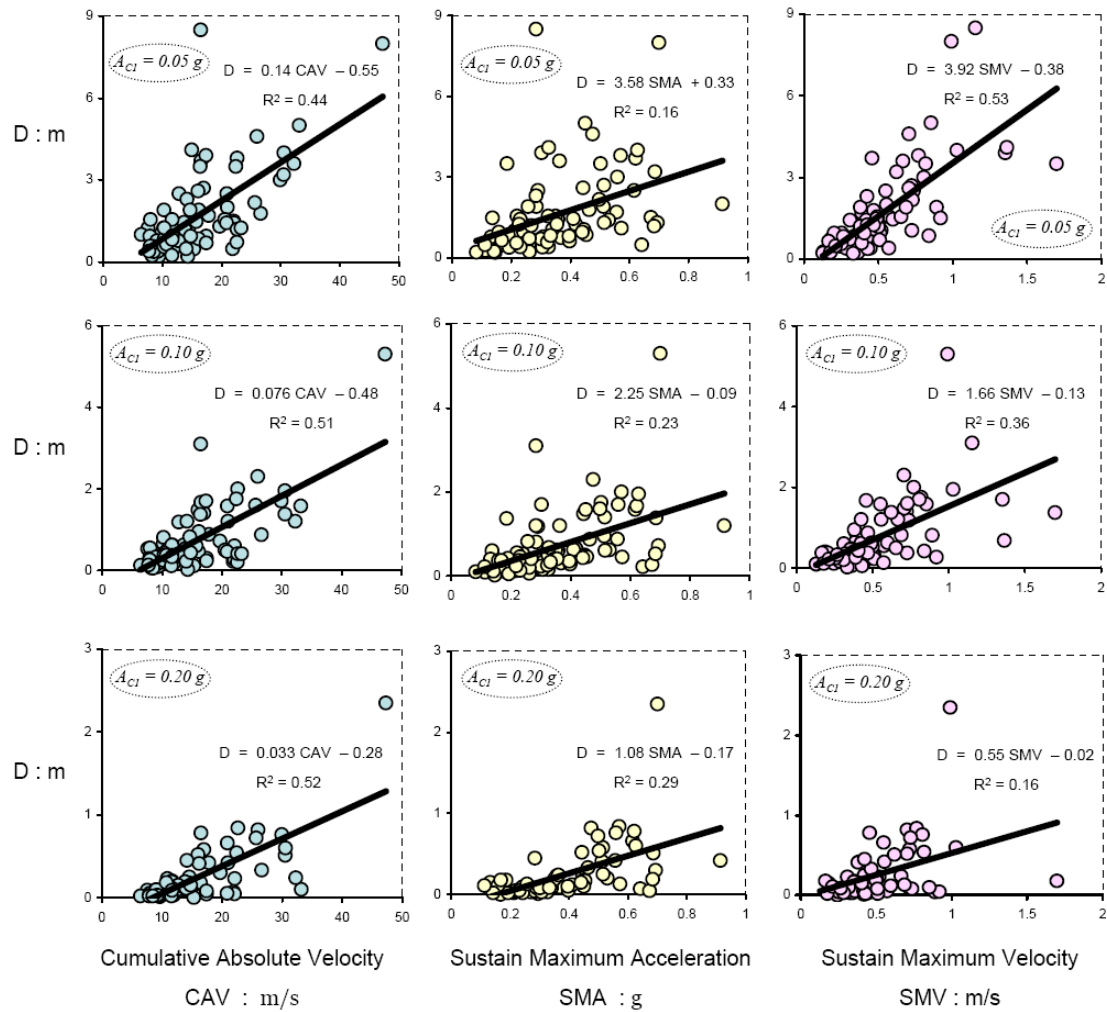


Figure 9. Slippage, D , as a function of : (a) the cumulative absolute velocity–in the first column from the left, (b) the sustained maximum acceleration–in the second column, and (c) the sustained maximum velocity–in the last column to the left.

6 ACKNOWLEDGEMENTS

The financial support for the work outlined in this paper has been provided under the collaborative research project “PERPETUATE”, under contract number ENV.2009.3.2.1.1.

7 REFERENCES

- Arias, A. 1970. A measure of earthquake intensity. *Seismic Design for Nuclear Power Plants* (ed. R.J. Hansen), MIT Press, Cambridge, Massachusetts, 438-483.
- Bommer, J. J. & Martinez, P. 1999. The effective duration of earthquake strong motion. *Journal of Earthquake Engineering*, 3(2), 127-172.
- Gazetas, G., Garini, E., Anastasopoulos, I. & Georgarakos, T. 2009. Effects of near-fault ground shaking on sliding systems. *J. Geotech. Geoenviron. Engng*, ASCE 135(12), 1906-1921.
- Garini, E., Gazetas, G. & Anastasopoulos, I. 2010. Asymmetric ‘Newmark’ sliding caused by motions containing severe ‘directivity’ and ‘fling’ pulses. *Géotechnique*, Vol.60, doi: 10.1680/geot.2010.60.00.1
- Hancock, J. & Bommer, J. J. 2005. The effective number of cycles of earthquake ground motion. *Earthquake Engineering & Structural Dynamics*, 34, 637-664.

- Newmark, N. M. 1965. Effects of earthquakes on dams and embankments, *Géotechnique* 15(2), 139-160.
- PEER Strong Motion Database. 2002. <http://peer.berkeley.edu/smcat/data.html>.
- Rathje, E. M., Faraj, F., Russell, S. & Bray, J. D. 2004. Empirical relationships for frequency content parameters of earthquake ground motions. *Earthquake Spectra*, 20(1), 119-144.
- Sarma, S. K. & Yang, K. S. 1987. An evaluation of strong motion records and a new parameter A95. *Earthquake Engineering & Structural Dynamics*, 15(1), 119-132.
- Housner, G.V. 1952. Spectrum intensities of strong motion earthquakes. *Proceedings of the Symposium on Earthquake and Blast Effects on Structures*, EERI, Oakland California, 20–36.

